UNIVERSITÉ DE GENÈVE
Section de Physique

Département de Physique Nucléaire et Corpusculaire

FACULTÉ DES SCIENCES
Prof. Xin Wu
Prof. Martin Pohl

Enlightened Top Quark: Measurements of the $t\bar{t}\gamma$ Cross Section and of its Spectrum in Transverse Energy of the Photon in the Single Lepton Channel at $\sqrt{s} = 7$ TeV in 4.59 fb^{-1} of pp Collision Data Collected with the ATLAS Detector

Thèse

Présentée à la Faculté des Sciences de l'Université de Genève pour obtenir le grade de docteur ès Sciences, mention Physique.

Par
Gaetano Αϑανὰσιος Barone

d'Italie et de Grèce

Thèse N° 4807

Genève
Atelier d'impression ReproMail
2015

UNIVERSITÉ
DE GENÈVE

FACULTÉ DES SCIENCES

Doctorat ès sciences
Mention physique

Thèse de *Monsieur Gaetano Athanassios BARONE*

intitulée :

"Enlightened Top Quark: Measurements of the $t\bar{t}\gamma$ Cross Section and of its Spectrum in Transverse Energy of the Photon in the Single Lepton Channel at $\sqrt{s}$ = 7 TeV in 4.59 fb^{-1} of *pp* Collision Data Collected with the ATLAS Detector"

La Faculté des sciences, sur le préavis de Monsieur X. WU, professeur associé et directeur de thèse (Département de physique nucléaire et corpusculaire), Monsieur M. POHL, professeur ordinaire et codirecteur de thèse (Département de physique nucléaire et corpusculaire), Monsieur T. GOLLING, professeur associé (Département de physique nucléaire et corpusculaire) et Monsieur T. CARLI, docteur (Département de physique, CERN - Organisation Européenne pour la Recherche Nucléaire, Meyrin, Suisse), autorise l'impression de la présente thèse, sans exprimer d'opinion sur les propositions qui y sont énoncées.

Genève, le 13 juillet 2015

Thèse - 4807 -

Le Décanat

N.B. - La thèse doit porter la déclaration précédente et remplir les conditions énumérées dans les "Informations relatives aux thèses de doctorat à l'Université de Genève".

Abstract

The top-photon electromagnetic couplings can be probed via the analysis of the production of top quark pairs ($t\bar{t}$) in association with a photon (γ). A dataset of events with final-states containing jets, missing transverse momentum, one isolated electron or muon and an energetic photon is selected out of 4.59 ± 0.08 fb^{-1}, of proton–proton collisions at a centre-of-mass energy of 7 TeV recorded by the ATLAS detector at the CERN Large Hadron Collider. In total 140 and 222 $t\bar{t}\gamma$ candidate events are observed in the electron and muon channels, respectively. They are to be compared to an expectation of 79 $\pm$ 26 and 120 $\pm$ 39 background events in the single-electron and single-muon channels respectively.

A first observation of $t\bar{t}\gamma$ state, combining both electron and muon channels, is reported, with $t\bar{t}\gamma$ events being separated by 5.3 standard deviations from the background only hypothesis. The $t\bar{t}\gamma$ production cross section times the branching ratio (BR) of the single-lepton decay channel, as well as its spectrum in transverse energy of the photon, are measured in a fiducial phase-space within the detector acceptance.

The measured cross section is $\sigma_{t\bar{t}\gamma} \times \mathrm{BR} = 63 \pm 8(\mathrm{stat.})\,^{+17}_{-13}\,(\mathrm{syst.}) \pm 1\,(\mathrm{lumi.})\,\mathrm{fb}$ per lepton flavour, which is in good agreement with the leading-order theoretical calculation normalised to the next-to-leading-order theoretical prediction of 48 ± 10 fb.

Acknowledgements

I would like to express my sincere gratitude to my two thesis supervisors Xin Wu and Martin Pohl for the opportunity given to me. The direction and motivation for the research presented in this thesis were underpinned by several physics discussions that I had with both of my supervisors.

I would like to thank the members of the jury Tancredi Carli and Tobias Goldling, for their carful reading of the thesis and for providing comments which have lead to extremely interesting discussions both before and during the defence.

Special thanks to my collaborators of the ATLAS Inner Detector, Semiconductor Tracker and of the Top group. Among the many people involved in the Inner Detector and Semiconductor Tracker activities some need to be mentioned by name: Dave Robinson, Steve McMahon, Saverio D'Auria and Alex Kastanas. From the Top group I would like to thank the past and present conveners, Alison Lister and Tancredi Carli, for giving me the opportunity to strengthen the confidence of the results thanks to ideas that emerged from conversations that took place both within the framework of the collaboration and privately. From the closest collaborators on the same subject the discussions with Andrey Loginov and Johannes Erdmann have motivated me to expand the bounds of the research being carried out.

My co-workers at Department of Particle Physics cannot be forgotten from the acknowledgments, they have been of great support and help, thus creating unbreakable friendly bonds.

My peers with whom I've begun the studies in physics, evolving from co-students to closest friends, have always demonstrated great support to me and to each other, for that and for all the good moments I thank you. From all of the discussions about physics, statistics and the meaning of everything a special bond was born with Pierre and Elisabeth, their unprecedented support stands out. I would like to express a special thought to all of my friends who now live only in our memories.

Catherine Blanchard and Nathalie Chaduiron deserve to be acknowledged for their help with all the administrative work needed in order to perform this research.

Finally, Sergio Gonzalez Sevilla deserves my deepest gratitude, it has been a pleasure to work with Sergio. From one side, sharing of his profound knowledge of the detector and of the physics processes involved in this analysis have been fundamental for my deeper understanding of the subject presented in this thesis and for many others. On the other side, his view of the greater picture without loosing any attention to the detail have been fundamental in many aspects.

Table of contents

Résumé

Le quark top (t) joue un rôle important dans la compréhension de la nature à haute énergie, sa masse étant comparable à l'échelle d'énergie du mécanisme de brisure spontanée de la symétrie électrofaible. Des phénomènes physiques inconnus, qui apparaissent à des énergies inaccessibles expérimentalement, peuvent induire des déviations des propriétés observables du quark top par rapport à celles prévues par le Modèle Standard (MS) de la physique des particules. Cette hypothèse se concrétise dans plusieurs modèles théoriques, qui engendrent des couplages anormaux entre le quark top et les bosons porteurs de la force électrofaible (W, Z, γ). Par exemple, des excitations du quark top ($t^\star$) ou le quark lui-même, sous l'hypothèse qu'il ne serait pas une particule fondamentale mais un état lié, peuvent se désintégrer en produisant un photon ($t^\star \to t\gamma$).

Expérimentalement, les constantes de couplage électromagnétiques doivent être déterminées avec précision. L'analyse de la production des états liés de la paire top anti top avec un photon ($t\bar{t}\gamma$) permet la détermination des constantes de couplage électriques du vertex $t\gamma$. Plus précisément, l'observation de $t\bar{t}\gamma$ et la mesure de la section efficace de sa réaction de production, permettent d'inférer les valeurs des couplages $t\gamma$.

Cette thèse présente l'analyse de 4.59 ± 0.08 fb^{-1} de données de collisions entre protons (p) ayant une énergie au centre de masse de 7 TeV, recueillies par l'expérience ATLAS auprès du grand collisioneur à hadrons (LHC). Cette analyse a pour but d'observer l'état $t\bar{t}\gamma$ et de mesurer la section efficace de la réaction $pp \to t\bar{t}\gamma$ se désintégrant en des états finaux avec lepton ($\ell =$ electron ou muon), des gerbes hadroniques et un photon.

La majorité des collisions entre protons sont dominées par la production d'états dont l'énergie est inférieure à celle de $t\bar{t}\gamma$, et constituent un bruit de fond à la mesure. Le fait d'imposer des critères de sélection sur les données des collisions entre protons permet de réduire en grande mesure la contribution de ce bruit de fond. Toutefois, des contributions résiduelles polluent la richesse en $t\bar{t}\gamma$ des événements sélectionnés. Ces contributions sont principalement dues à la reconstruction de mésons (π^0, η^0 *etc.*) ou de leurs produits après désintégration ($\pi^0, \cdots \to \gamma\gamma$) sous forme de photons. Une contribution importante est aussi due à la reconstruction d'électrons sous forme de photons. Une pollution minoritaire est due à la reconstruction sous forme de $t\bar{t}\gamma$ des produits de désintégration des bosons vectoriels W et Z, ainsi que de leur états liées, également produits par collisions de protons.

Les hadrons, ou leur produits après désintégration, développent des gerbes de particules secondaires similaires à celles initiées par des photons (gerbes électromagnétiques). Toutefois, leurs

caractéristiques géométriques diffèrent. Les premières sont accompagnées d'une activité d'hadrons secondaires, absente dans les gerbes électromagnétiques. Cette activité secondaire a pour effet d'élargir latéralement la forme de la gerbe. Par conséquent, la distribution de la somme des impulsions des particules reconstruites dans un cône à rayon fixe a une forme différente pour des gerbes électromagnétiques et pour des gerbes hadroniques. L'inclusion de cette information dans un modèle statistique complexe permet de discriminer entre les photons et les hadrons.

La contribution de photons et d'électrons produits par le bruit de fond restant ne peut pas être distinguée de la contribution de photons associés à l'état $t\bar{t}\gamma$. Cependant, une soustraction de ce bruit est possible, pourvu qu'une estimation préalable en ait été faite. Pour éviter une dépendance de la modélisation à l'égard des simulations, ce bruit de fond a été déterminé (en grande partie) à partir des données mêmes. L'analyse d'ensembles de données statistiquement indépendantes de l'ensemble constituant la sélection des candidats au signal, a permis la détermination de ce bruit de fond.

Les incertitudes dues aux méthodes d'évaluation des bruits de fond, aux limitations des méthodes expérimentales, mais aussi celles dues à la modélisation du signal, sont inclues dans le modèle statistique. Ceci permet, d'une part d'évaluer correctement la propagation des incertitudes entre les paramètres modélisant chaque contribution et le signal, et d'autre part d'extraire la valeur de la section efficace.

La section efficace, ainsi que le spectre en énergie transversale du photon, ont été déterminés pour tout photon ayant une énergie transversale $E_{\mathrm{T}}(\gamma) > 20$ GeV dans un espace de phases défini par les propriétés du détecteur. L'espace de phases dans lequel la mesure est reportée a été formulé de façon à ce qu'il soit indépendant des modèles utilisés pour les simulations théoriques. Les coupures imposées à l'espace de phase correspondent aux valeurs accessibles avec les contraintes géométriques et cinématiques du détecteur. Elles excluent l'extrapolation du résultat à des régions non contrôlées expérimentalement.

Le résultat de la section efficace, multiplié par le Rapport de Branchement (RB) par saveur de lepton dans le canal des états finaux avec un électron ou un muon, est

$$\sigma^{\mathrm{fid}}_{t\bar{t}\gamma} \times \mathrm{RB} = 63 \pm 8(\mathrm{stat.})\,^{+17}_{-13}\,(\mathrm{syst.}) \pm 1\,(\mathrm{lumi.})\,\mathrm{fb}, \tag{1}$$

ce qui est en accord avec la prédiction théorique de 48 ± 10 fb. La probabilité que le bruit de fond reproduise la valeur mesurée a été exclue avec une précision de 5.3 σ, ce qui fait de cette mesure la première observation de l'état $t\bar{t}\gamma$.

Introduction

The top quark (t), discovered twenty years ago [1, 2], possesses a mass [3] close to the scale of the Electroweak Symmetry Breaking (EWSB) which underpins the modern understanding of particle physics. Undiscovered physical phenomena connected with the EWSB can manifest themselves through deviations from the predictions of the Standard Model (SM) in top quark observables. Hypothesised new phenomena, at a higher scale of that accessible by the experiment, can be modelled by effective theories. These models are based upon anomalous couplings of vector bosons (W, Z and photon) to the top quark that can be probed through precision measurements at lower scales.

The Electroweak (EW) couplings of the top quark to the vector bosons, in particular to the γ, are yet to be fully constrained by the experiment. Models with composite top quarks [4], or models with an exited top quark decaying radiativelly ($t^* \to t\gamma$), can be constrained by probes of the $t\gamma$ vertex. At hadron colliders, the $t\gamma$ vertex can be probed through the measurement of the top quark pair-production cross section in association with a photon ($t\bar{t}\gamma$). So far the experimental observation of the the $t\bar{t}\gamma$ state is yet to be determined, evidence of which was first reported [5] by the CDF Collaboration.

This thesis reviews the analysis of 4.59 ± 0.08 fb^{-1} of proton–proton (pp) collision data, recorded by the ATLAS detector and delivered by the Large Hadron Collider (LHC) at a centre-of-mass energy of $\sqrt{s} = 7$ TeV. The analysis aims at a first observation of the $t\bar{t}\gamma$ final-state and at the measurement of the cross section of the $pp \to t\bar{t}\gamma$ reaction in the single-lepton (electron, or muon) plus jets and plus photon final-state. Both the measurement of the $t\bar{t}\gamma$ production cross section times the Branching Ratio (BR) in the single-lepton decay channel and its spectrum as a function of the photon's energy in the transverse plane are reported in a phase-space within detector acceptance.

Proton–proton collisions produce final-states containing large amounts of collimated sprays of particles (jets), as well as energetic leptons and photons. Energy deposits in the detector of final-state particles are recorded and interpreted as complex sets of objects containing momentum and energy information for leptons, photons and jets. The bulk of pp collision-data delivered by the LHC are dominated by low energy interactions of quantum chromodynamics, which are of no interest in a $t\bar{t}\gamma$ cross section measurement. The request of stringent selection criteria reduces the size of data to a few hundred of candidate $t\bar{t}\gamma$ events. Among these, more than half do not come from $t\bar{t}\gamma$ production, but from other background processes. Production of W- and Z-bosons, as well as top EW production in association with a photon create indistinguishable final-states to the ones of $t\bar{t}\gamma$ production. Jets misidentified as leptons with additional radiation from jet fragmentation, as well as electrons from W- and Z-boson leptonic decays misidentified as photons, can also fake the $t\bar{t}\gamma$ response in the detector. Most of these background processes are estimated from data, without any model-dependent assumptions.

Moreover, hadrons, or hadron-decay products such as neutral mesons decaying into diphotons ($\pi^0, \eta^0 \to \gamma\gamma$), can be misidentified as photons of the final-state of this analysis. Both photons and hadrons, through their interaction with the detector, develop sprays of secondary particles (showers). The showers initiated from hadrons have a wider shape than the more collimated showers from photons or electrons. This characteristic is exploited in order to discriminate between the two types of detector responses.

The fraction of $t\bar{t}\gamma$ events is extracted out of the candidate events from the maximisation of a complex function (likelihood) modelling all contributions. The likelihood incorporates the measured probabilities for hadrons, or hadron-decay products, to be misidentified as photons, the probabilities for electrons to be misidentified as photons and the probabilities for other processes to have produce the same signature as $t\bar{t}\gamma$ production. Deterministic and stochastic biases, that are rooted from the limited knowledge of the detector, are also included into the likelihood model in terms of additional uncertainties.

Finally, the results are interpreted as probes of the $t\gamma$ vertex, and more specifically as probes to the top quark electric charge. These probes are used to constrain the generic picture of theoretical models that hypothesise new physics at a higher scale through deviations from the SM of the top quark's EW couplings.

The concepts discussed in this thesis are organised into chapters that incrementally expand the reader's understanding of the methodology used in the analysis. At first, in Chap. 1, the motivations for the study of the $t\gamma$ vertex, the top quark's electric charge, and their relation to a measurement of the $t\bar{t}\gamma$ cross section are reviewed. Chapter 2 overviews the experimental setup and techniques used to collect and interpret responses from the detector. These responses are then organised into sets of objects the definition of, and the selection criteria on, which are explained in Chap. 3. Based upon the detector capabilities, the phase-space in which the cross section is measured is determined in Chap. 4. The chapters following that are dedicated to explaining how the extraction of the $t\bar{t}\gamma$ cross section is performed from the selected set of candidate events. At first the statistical framework developed for this measurement is explained in Chap. 5. Then the extraction of the probabilities for processes other than $t\bar{t}\gamma$ production, including electrons misidentified as photons and jets misidentified as leptons are detailed in Chap. 6. The determination and extraction of uncertainties and systematic biases is discussed in Chap. 7. Finally the results, reported in a region defined by jets, a single lepton and an energetic photon, are given in Chap. 8. In particular, the probability of background fluctuations to the signal level is calculated in the same chapter. Both the cross section of the $t\bar{t}\gamma$ production process as well as its spectrum (as a function of the photon's energy on the transverse plane) are measured. Furthermore, both results are compared to the most recent next-to-leading order calculation from the theory. The chapter is concluded with some interpretative considerations, based on the results, on the $t\gamma$ couplings and on the theoretical models of unobserved physics phenomena.

CHAPTER 1

Motivations

In this chapter the motivations for the measurement of the top quark pair production in association with a photon are reviewed. The arguments discussed in this section are based on the well established Standard Model (SM) of particle physics.

Despite the top quark's (t) discovery [1, 2] ages twenty years nowadays, some of its properties are yet to be fully understood. Due to it's large mass [3] the top quark is speculated to play an important role in the Electroweak Symmetry-Breaking mechanism [6–8]. Moreover, the electroweak couplings of the top quark to vector gauge bosons (Z, W and photon) are yet to be determined experimentally. Precision measurements of the tZ, tbW and $t-$photon (γ) couplings can provide hints for new physics through deviations to their SM predictions. Several models [9–11] allow for top anomalous couplings with deviations from the SM values at the percent level [12]. Within this scheme the top quark's electric charge (Q_t), which is yet to be determined through direct observation, is speculated to play a special role, as several theoretical models allow for non standard $t\gamma$ couplings. For example, fourth generation models [10, 11] interpret the observed particle as a fourth generation quark with $Q_t = -4/3$, while the SM top quark would have a higher mass [1].

The top-quark's electric charge can be measured indirectly by the determination of the charges of the quark's decay products (lepton, W-boson and b-quark) [3, 13, 14]. Most recently ATLAS published a result of $Q_t = 0.64 \pm 0.02$ (stat) $\pm\, 0.08$ (syst) and excluded the hypothesis of a heavy quark of electric charge $Q_t = -4/3$ with more than eight gaussian standard deviations (8σ) [15].

However, this result does not preclude the theory from hypothesising non-standard top-photon coupling values. Models with integer quark charges can still achieve the correct sum of charges of the top quark decay products. Moreover, new phenomena, which may appear at a higher energy scale, can induce (small) deviations to the theoretical prediction of $t\gamma$ SM coupling values.

After a general introduction of the production mechanisms of the top quark at hadron colliders (Sec. 1.1.1), the theoretical motivations for a measurement of the top pair production in association with a photon ($t\bar{t}\gamma$) cross section are given in more detail. The mechanisms which allow for non standard coupling values are reviewed concentrating on two aspects: the fractional electric charge of the top quark (Sec. 1.2) and the relation between the hypothesised new phenomena and the

[1] It is worth mentioning that such hypothesis is supported by the fact that, experimentally, the b and $\bar{b}$ quarks were not distinguished, allowing an interpretation of the top decay via the $t \to W^+\bar{b}$ chain.

top-photon coupling (Sec. 1.3). Finally, the importance of higher order corrections, under the hypothesis of either standard or anomalous couplings, are scrutinised in Sec. 1.4.

1.1 Overview of $t\bar{t}\gamma$ process

This section overviews the production mechanism of the $t\bar{t}$ pair-production in association with a photon in proton–proton collisions. After a brief explanation of the top quark production (Sec. 1.1.1) and of its decay modes (Sec. 1.1.2), the sections focuses in the classification of the $t\bar{t}\gamma$ signature.

1.1.1 Production of $t\bar{t}$ pairs

Top quarks are produced in hadron colliders through Electroweak (EW) interaction ($pp \to W^\star \to tb$), so called single top, or in pairs ($t\bar{t}$) via either the strong interaction ($pp \to g \to t\bar{t}$) or EW interaction ($pp \to \gamma^\star(Z^\star) \to t\bar{t}$). Top quark pairs can be produced via two distinct strong interaction processes: quark-antiquark ($q\bar{q}$) annihilation (s-channel diagrams), and gluon gluon (gg) fusion [16] (in the t-,s- and u- channels), as shown in Fig. 1.1.

At the Large Hadron Collider (LHC) $t\bar{t}$ production occurs above threshold $x_{\text{th}} \simeq \frac{2m_t}{\sqrt{s}} \simeq 0.05$ at a centre-of-mass energy of 7 TeV. The lower threshold at the LHC, compared to that at the Tevatron ($x_{\text{th}} \simeq 0.2$, $\sqrt{s} = 1.96$ TeV) allows for a higher production rate of $t\bar{t}$ pairs. Therefore, measurements of phenomena with small cross sections, such as the $t\bar{t}\gamma$ production, are possible at the LHC.

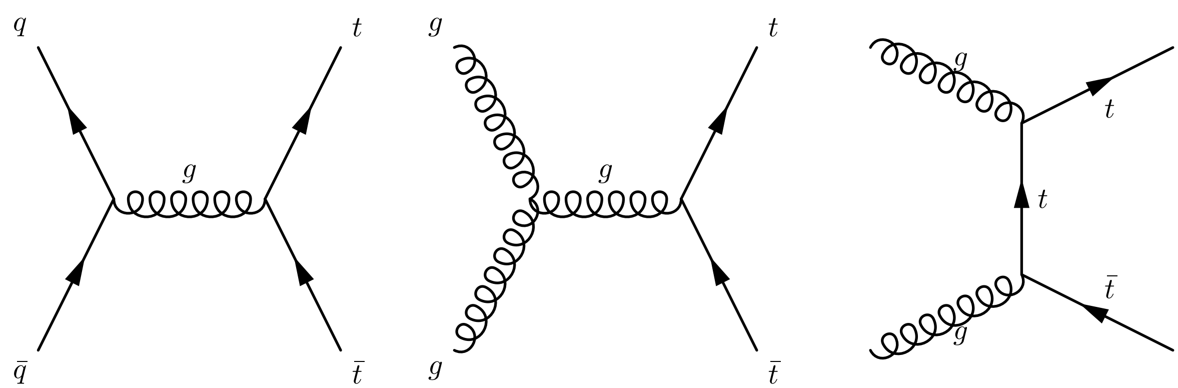

Figure 1.1: Representative leading-order Feynman diagrams of $t\bar{t}$ pair production via strong interaction. The s-channel $q\bar{q}$ annihilation is shown on the left, the s-channel gg fusion in the middle and the u-channel gg fusion on the right.

1.1.2 Top quark decays

In the SM the top quark decays to lighter quarks through weak interaction via $t \to Wq$. Since $|V_{t,b}| \simeq 1 \gg |V_{t,q}|$ [3] for any other quark q, this document assumes the top quark decays only through $t \to Wb$.

The W-boson can decay primarily in [3]: (i) lepton modes $W \to \ell\bar{\nu}_\ell$, with $\ell = (e, \mu, \tau)$; (ii) in all-hadronic modes with $W \to$ hadrons; (iii) rare decays such as $W \to \pi^\pm\gamma$, $W \to D_s^\pm\gamma$, etc. The total Branching Ratio (BR) for rare decays

$$\Gamma_{\text{Rare Decays}} = \sum_{i}^{\text{Rare Decays}} \Gamma_i/\Gamma(W^+ \to e^+\nu_e) \tag{1.1}$$

with Γ indicating the decay width, is found to be $\mathcal{O}(\Gamma_{\text{Rare Decays}}) < 10^{-3}$ [3]. From here onwards, these decay-modes are neglected. The W-boson decays allow to classify, therefore, the $t\bar{t}$ pair final states in the following modes:

- both W-bosons decay only into quarks, this is the so-called *all-hadronic mode*
- one W-bosons decays into quarks while the other decays into leptons, this is the so-called *semi-leptonic mode*
- both W-bosons decay into leptons, this is the so-called *dileptonic mode*.

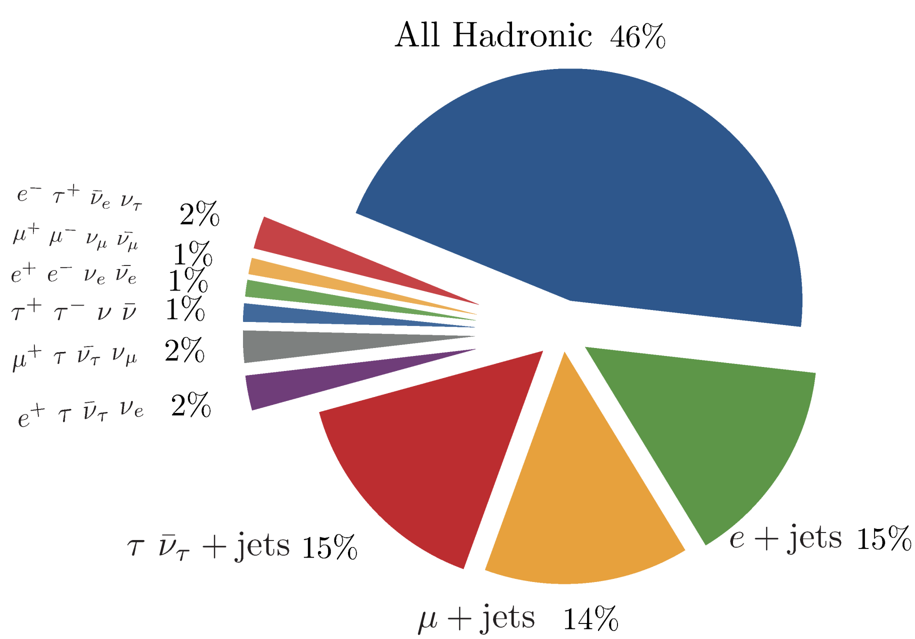

Figure 1.2: Branching ratios for all $t\bar{t}$ decay modes.

Figure 1.2 shows the BR for each $t\bar{t}$ decay mode. The experimental signature considered for the analysis presented in this thesis is in the *semi-leptonic* mode.

1.1.3 Production mechanisms of $t\bar{t}\gamma$

As in the region of $x_{\rm th} \simeq 0.05$ gg fusion dominates the $t\bar{t}$ production (90%), it is almost impossible a direct probe of the $t\gamma$ vertex via an off-shell photon $q\bar{q} \to \gamma^{\star} \to t\bar{t}$. Therefore, $t\bar{t}$ production with associated photon radiation ($t\bar{t}\gamma$) is the only process in which the vertex can be probed at the LHC realistically. In this process, the initial-state photon radiation is drastically decreased, thus enhancing the sensitivity to the $t\gamma$ vertex.

The $t\bar{t}\gamma$ production can be classified into two processes: the radiative top-quark production and the radiative top-quark decay.

- The **radiative top quark production** ($pp \to t\bar{t}\gamma$), illustrated in Fig. 1.3, represents the process where the top quarks decay through $t \to Wb$ and where the photon is radiated from the top quark prior to its decay.

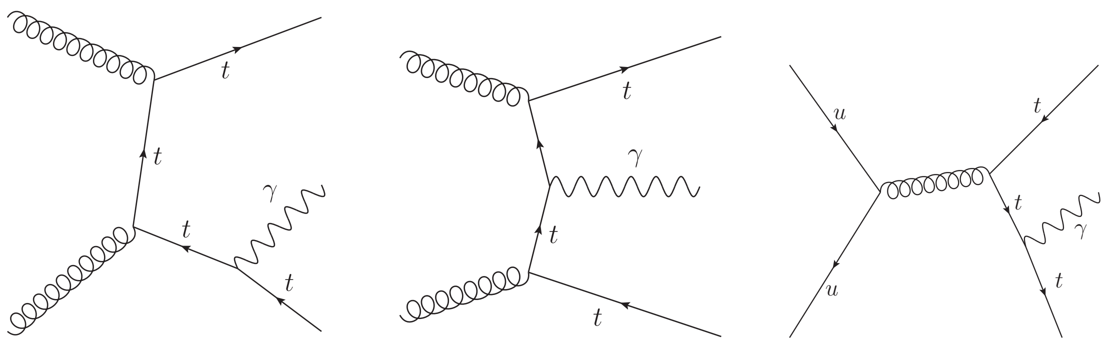

Figure 1.3: Some representative Feynman diagrams for the $t\bar{t}\gamma$ process classified as **radiative top quark production**.

- The **radiative top quark decay** ($pp \to t\bar{t}$), illustrated in Fig. 1.4, are the processes where a photon is radiated from the decay of an on-shell top quark ($t \to Wb\gamma$) or along the subsequent decay chain, *i.e.* from a radiatively decaying W ($W \to l\nu\gamma$ or $W \to q\bar{q}\gamma$), from the b-quark ($b \to b\gamma$), or from the decay products of the W-boson ($\ell \to \ell\gamma$ or $q \to q\gamma$).

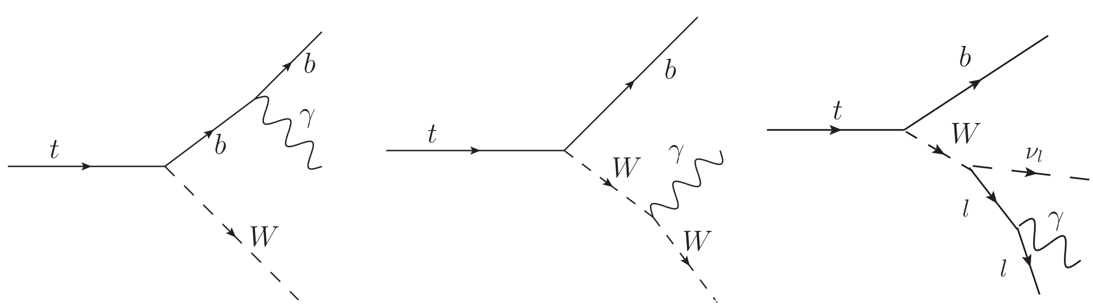

Figure 1.4: Some representative Feynman diagrams for the $t\bar{t}\gamma$ process classified as **radiative top quark decay**.

Radiative top-quark decays are not sensitive to the top charge and therefore they are of no interest in probing the $t\gamma$ vertex. Non-negligible interferences can arise from both production mechanisms, for example interferences between the photon radiated from the t-quark or from the b-quark (see Fig. 1.4). As these interference effects are not distinguishable experimentally, a cross section measurement cannot make a differentiation between the two.

Therefore, the inclusive cross section for both processes $pp \to t\bar{t}\gamma$ can be expressed through the factorisation theorem as a function of the *parton* cross section $\hat{\sigma}^{ij\to t\bar{t}\gamma}$, with the indices i and j running through all combinations of incoming constituents of the proton (partons: $q, \bar{q}, g$) [16]:

$$\sigma^{pp\to t\bar{t}\gamma}(s, m_t^2) = \sum_{i,j} \int_0^1 dx_i \int_0^1 dx_j f_i(x_i, \mu_{\mathrm{F}}^2) f_j(x_j, \mu_{\mathrm{F}}^2) \hat{\sigma}^{ij\to t\bar{t}\gamma} \left(\hat{s}_{ij}, m_t, \alpha_{\mathrm{S}}\left(\mu_{\mathrm{R}}^2\right)\right) \tag{1.2}$$

where $f_i(x_i, \mu_{\mathrm{F}})$ denotes the Parton Density Function (PDF) for the parton i, carrying a momentum fraction x_i of the incoming proton and parametrised at an arbitrary factorisation scale μ_{F}. The parton cross section $\hat{\sigma}^{ij\to t\bar{t}\gamma}\left(\hat{s}_{ij}, m_t, \alpha_{\mathrm{S}}(\mu_{\mathrm{R}}^2)\right)$ is a function of the centre-of-mass energy $\sqrt{\hat{s}_{ij}} = \sqrt{s x_i x_j}$ of the colliding partons, the top quark's mass m_t and the strong coupling constant α_{S} parametrised at a renormalisation scale μ_{R}. For values of $\mu_{\mathrm{R}}, \mu_{\mathrm{F}} \gg \Lambda_{\mathrm{S}}$, with $\mathcal{O}(\Lambda_{\mathrm{S}}) \simeq 200$ MeV, the calculation of $\hat{\sigma}$ can be solved via a perturbative expansion by calculating the Matrix-Element (ME) for the transition $\mathcal{M}(i, j \to t\bar{t}\gamma)$. The Feynman rules can be applied and $|\mathcal{M}(i, j \to t\bar{t}\gamma)|^2$ is obtained by summing over all degrees of freedom of colour and spin.

Numerical computations

Nowadays, computational developments allow, in most cases, for a high-precision numerical approximation of the first order diagrams via Monte Carlo simulation programs. However, for several processes, higher order corrections contribute non-negligibly to the perturbative expansion. The second order corrections contribute majorly to the normalisation of $\hat{\sigma}$, while the shapes of the differential spectra are correctly predicted by the leading order diagrams. Experiments typically normalise their leading order computation to the ratio of the second to the first order calculation provided by the theory, when available. Although Next-to-Leading-Order (NLO) simulation programs exist for the computation of the $t\bar{t}$ production cross section, such as `MC@NLO` [17–19], higher order corrections to $t\bar{t}\gamma$ production are still being discussed by theory, as it is shown in Sec. 1.4.

Stochastic evolution of the parton density functions

Due to collinear gluon radiation from the outgoing parton, the integral in the right-hand part of Eq. 1.2 is not solvable by perturbative expansion. However, the Dokshitzer-Gribov-Lipatov-Altarelli-Parisi (DGLAP) equation [20–22] guaranties that solutions exits. They are valid for any value of momentum fraction x and at any fixed factorisation scale. The DGLAP equation provides the stochastic evolution of a parton density with loss of energy, e.g. through gluon emission. For each parton a probability density function of energy loss (splitting function) is assigned and it was shown [20–22] that DGLAP correctly describes the leading-logarithmic approximation of any order of the perturbative expansion.

Approximations for parton density functions

Suitable parametrisations of the PDF allow for high precision approximations, via global fits to data (see Fig. 1.5). The CTEQ [23] and the MSTW [24–26] Collaborations extract parametrised PDFs from collider and fixed target experiments. The time evolution of the PDF is susceptible to corrections due to soft gluon emissions or $q\bar{q}$ loop corrections which are non-perturbative. An iterative procedure [27], based on the Sudakov form factor method [28], can be applied on the splitting functions, introduced in the above paragraph. Iterations are performed up to a cut-off value. Initial-state radiation has also to be taken into account. In simulation programs the same iterative procedure is used for the initial-state parton emission. The application of this procedure with simulation programs is referred as the Parton Shower (PS) technique and it lifts the requirement to an exact solution to the DGLAP equation.

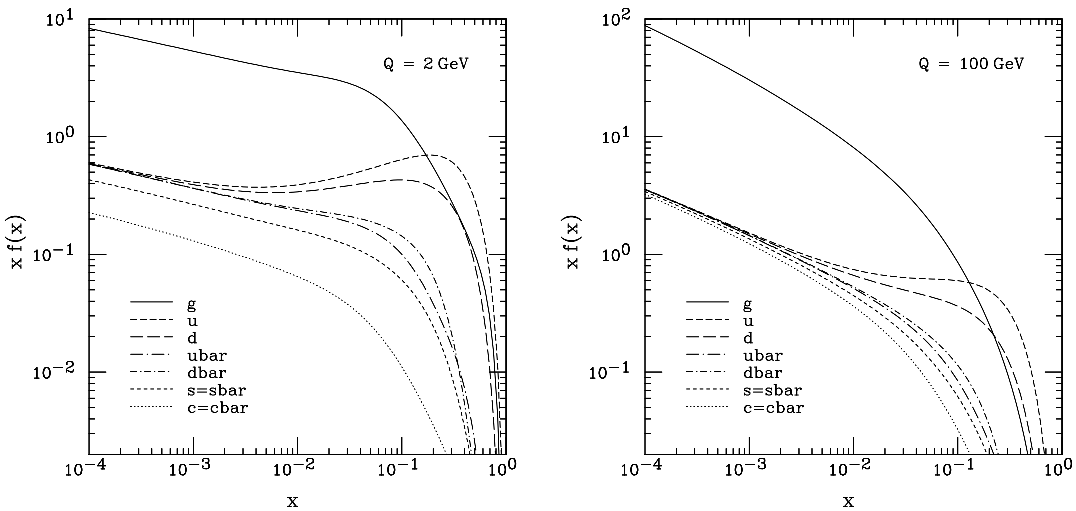

Figure 1.5: Parton Density Functions (PDF) as measured by the CTEQ Collaboration as a function of the parton to proton momentum fraction x. The left plot shows the PDFs evaluated at $\mu_{\rm F} = 2$ GeV while the right plot shows the PDFs evaluated at $\mu_{\rm F} = 100$ GeV [29].

Matching computations of the time evolution of the cross section and computations of the ME can lead to overlapping final-states inducing a double-counting. Matching of the final states produced by the PS and the ME are usually based on momentum and angular separations between objets and by using a cone algorithm. The event acceptance depends on the correct association of ME partons, within a cone of arbitrary radius, with jets produced by the parton shower. This procedure is referred to as the MLM [30]. Other matching schemes exits such as the Catani-Krauss-Kuhn-Webber [31], for which the assignment of the ME partons to jets is done using a clustering algorithm.

1.2 Integer charge quarks models

The fractional nature of the electric charge of quarks has intrigued, since a long time, both experiment and theory. Several models have tried to propose integer values introducing non-standard $q\gamma$ couplings, and some are still compatible with the experimental results.

The top quark charge (Q_t) is experimentally determined by the sum of charges of $t\bar{t}$ decay products [32–34], however, it relies on the assumption that quarks have a fractional charge.

Integer Charge Quark (ICQ) models, introduced at first by M. Y. Han and Y. Nambu [35] in 1965, can achieve the correct sum of charges hypothesising a non-fractional charge for Q_t. In the absence of a direct measurement of the quark charge those models have continued to thrive. The reader will find such hypothesis, nowadays, being close to science-fiction. However, situating the first ICQ models historically in the developing Quantum Chromodynamics (QCD) picture may give more insights on their validity.

1.2.1 Early integer charge quark models

ICQ models came into existence during the mid sixties, when QCD was not yet a well-established theory. The baryon masses were explained in 1964 by the up-to-then hypothesised fractionally-charged nucleon constituents (quarks) [36, 37] through the three-flavour symmetry $SU(3)_{\text{flavour}}$. The quark spin was, later that year, introduced through the $SU(2)_{\text{spin}}$ symmetry acting on the two states of spin 1/2 [38]. The paradoxical, at that time, fractional aspect of the electric charge was yet to be confirmed.

The combination of those two groups $SU(2)_{\text{spin}} \times SU(3)_{\text{flavour}}$ in a $SU(6)$ symmetry correctly predicted the proton to neutron ratio of magnetic moments. The quark model, however, in order to predict the baryon masses imposed on multi-particle states of quarks to be symmetric under commutation of fields, contradicting the spin-statistics theorem [39]. The introduction of a hidden degree of freedom (colour), allowed for the quarks to be in a symmetric spin-state while correctly predicting the baryon masses. Evidence of colour can be easily seen in $e^+e^- \to q\bar{q}$ reactions when compared to $e^+e^- \to \ell\bar{\ell}$. In particular, the ratio of cross sections of hadron-production to lepton-production in e^+e^- collisions

$$\mathcal{R} = \frac{\sigma_{e^+e^-\to q\bar{q}}}{\sigma_{e^+e^-\to \ell\bar{\ell}}} \tag{1.3}$$

should be proportional to the square sum of all quark charges, given the fact that in presence of colour (c)

$$\mathcal{M}(e^+e^- \to q\bar{q}) = \sum_{c=1}^{3} \mathcal{M}_c(e^+e^- \to q_c\bar{q}_c), \tag{1.4}$$

it follows that

$$\mathcal{R} = \frac{1}{3}\left(\sum_c Q_{q_c}\right)^2 . \tag{1.5}$$

The former equation holds for fractional charges of q [40] and has been confirmed by early experiments [41, 42]. Early quark-models postulated the existence of an additional quantum number: the *triality* [43], involving higher order Lie-group symmetry [44]. However, no experimental evidence was seen. The ICQ model was then introduced as a solution for (i) the fractional electric charge, (ii) the above mentioned contradiction with the spin statistics theorem and (iii) the fact that simple dynamics on the quark model did not allow for the realisation of only zero *triality* states at lower energies.

The so-called "three-triplet ICQ model" hypothesised three sets of quark-triplets described by a double $SU(3)$ symmetry group. One group ($SU(3)'$) described the flavour permutations while the second ($SU(3)''$) introduced a **visible** three-valued colour-charge, with quarks retaining the integrity of their electric charge. While the colour-charge would be visible, the binding-energy involved in hadron formation (referred as *super-strong* interaction) would be at higher scale, speculated to be close to the Electroweak Symmetry Breaking (EWSB) scale [45]. The lowest energy-states, *i.e.* $SU(3)''$ singlet states, would commute according to $SU(3)'$ and the energy-scale involved in these interactions would be $\simeq$GeV. This would correspond to the known *strong* interaction involving baryons and mesons. The quark electric charge would be dependent on the quark's colour index, for example, for each colour index the up quark would have electric charge $(1, 0, 0)$ and the down quark a charge $(0, -1, -1)$ respectively. Table 1.1 shows a comparison between the three-flavour quark model and the three-triplet ICQ model.

Property	**Quark model**	**ICQ**
Isospin	$(\frac{1}{2}, -\frac{1}{2}, 0)$	$(\frac{1}{2}, -\frac{1}{2}, 0)$, $(0, -1, -\frac{1}{2})$ and $(1, 0, \frac{1}{2})$
Hypercharge	$(\frac{1}{3}, \frac{1}{3}, -\frac{2}{3})$	$(1, 1, 0)$, $(0, 0 - 1)$ and $(0, 0, -1)$
Electric charge	$(\frac{2}{3}, -\frac{1}{3}, -\frac{1}{3})$	$(1, 0, 0)$, $(0, -1, -1)$ and $(1, 0, 0)$

Table 1.1: Comparison of quantum numbers for the quark model and the three triplet model introduced by Hand and Nambu (labelled ICQ) [35–37].

In this picture, the correct sum of Eq. 1.5 can be achieved using integer quark charges: following the up quark (down quark) example one obtains $\mathcal{R} = 4/3$ $(1/3)$ for both integral and fractional charge hypotheses. This model allowed for the $SU(3)''$ group to be gauged if quarks had fractional charges, therefore, it could be identified with the Greenberg's model [46]. The connection between fractional quark-charge and $SU(3)_{\text{colour}}$ was made explicit [47], in 1966. This development lead to the abandonment of the ICQ models.

1.2.2 Gauged integer charge models

Measurements of the differential cross sections of $e^+e^- \to e^+e^-\pi^0 + \text{X}$ and $e^+e^- \to e^+e^-K_s^0 + \text{X}$ [48] performed at the Large Electron Positron (LEP) Collider at CERN in 2001 showed large discrepancies with respect to the SM prediction, as shown in Fig. 1.6.

In order to solve the observed discrepancy, new theoretical developments occurred. These developments included the re-consideration of ICQ models.

Renormalisable gauged ICQ models [49] appeared in allready since 1973. In 2004 they were associated to be originating from a broken-symmetry [50] of $SU(3)''$. They were used to fit the discrepancies of the observed π^+, K_s^0 p_{T} spectra. It is worth mentioning that ICQ is not the only hypothesis that can explain such discrepancies, however, no direct experimental disproof for integer quark charges has been ever presented.

1.3 Anomalous $t\bar{t}\gamma$ couplings

Hypothesised new phenomena at a scale (Λ) higher than the one accessible by the current experiments are often described by effective theories $(\mathcal{L}_{\text{eff}})$ with higher dimension operators (O) as extensions to the Standard Model Lagrangian $(\mathcal{L}_{\text{SM}})$:

$$\mathcal{L}_{\text{eff}} = \mathcal{L}_{\text{SM}} + \left[\sum_i^{\infty} \frac{C_i}{\Lambda} O_i + h.c.\right], \tag{1.6}$$

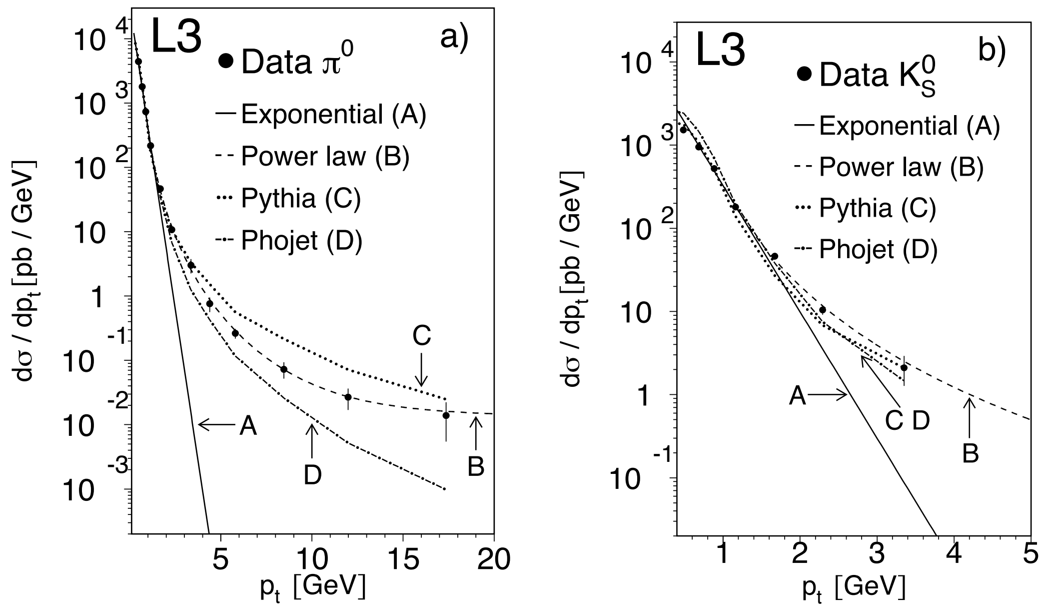

Figure 1.6: The differential cross section of π^0 (K_s^0) for rapidity $|y| < 0.5$ ($|y| < 1.5$) production at LEP as measured by the L3 Collaboration is shown on the left (right) [48]. Data are compared to MC predictions from the SM (lines labelled C and D), to an exponential fit (line labelled A) and to a power low fit (line labelled B). High-p_{T} regions are not well reproduced by simulations.

with C_i being constant pre-factors. The leading contributions of $\mathcal{L}_{\mathrm{eff}}$ impose to the $t\bar{t}\gamma$ vertex $\Gamma_\mu^{t\bar{t}\gamma}$ which, at tree level, in the SM is $\Gamma_\mu^{t\bar{t}\gamma} = -ieQ_t\gamma_\mu$, with e being the proton charge and γ_μ the Dirac matrices.

Ten form-factors $F(\hat{s}^2)$, as a function of the invariants of type $\hat{s}^2 = (p_t + \bar{p}_t)^2$, can describe a most general Lorentz-invariant of the $\Gamma_\mu^{t\bar{t}\gamma}$ vertex [51], which in a low-energy limit, can be assumed as couplings of dimension-four and -five operators. For on-shell production of γ, or assuming massless fermions, or when both top quarks are on-shell, the problem is reduced by five degrees of freedom, and a most general effective $t\bar{t}\gamma$ vertex can be written as [12]:

$$\Gamma_\mu^{t\bar{t}\gamma}\left(\hat{s}^2, q, \bar{q}\right) = \\ -ie\left\{\gamma_\mu\left[F_{1,\mathrm{V}}^\gamma(\hat{s}^2) + \gamma_5 F_{1,\mathrm{A}}^\gamma(\hat{s}^2)\right] + \frac{g_{\mu\nu}}{2m_t}(p_t + \bar{p}_t)^\nu\left[iF_{2,\mathrm{V}}^\gamma(\hat{s}^2) + \gamma_5 F_{2,\mathrm{A}}^\gamma(\hat{s}^2)\right]\right\} \quad (1.7)$$

where $p_t, \bar{p}_t$ are the four-momenta for the t and $\bar{t}$ respectively, and $g_{\mu\nu} = \frac{1}{2}\{\gamma_\mu, \gamma_\nu\}$. $F_{1,\mathrm{V}}^\gamma$ and $F_{1,\mathrm{V}}^\gamma$ are the $t\bar{t}\gamma$ vector and axial-vector form-factors. The form-factors $F_{2,\mathrm{V}}^\gamma$ and $F_{2,\mathrm{A}}^\gamma$ are proportional to the magnetic (g_t) and electric dipole-factors (d_t^γ)

$$F_{2,\mathrm{V}}^\gamma = Q_t\frac{g_t - 2}{2} \qquad , \qquad F_{2,\mathrm{A}}^\gamma = \frac{2m_t}{e}d_t^\gamma \quad (1.8)$$

and they contribute only at higher order corrections (in one-loop corrections they are $\mathcal{O}(10^{-3})$) [52]. At tree level and for the SM, $F_{1,\mathrm{V}}^\gamma = Q_t$ and the remainder form-factors are equal to zero.

At high partonic centre-of-mass energies ($\sqrt{\hat{s}} \gg m_t^2$) the unitarity of the S-matrix, via $|\mathcal{M}|^2 \leq \mathrm{Im}(\mathcal{M})$, imposes that anomalous axial and vector-axial couplings have to correspond asymptotically to the SM values of the couplings, hence they must have a momentum dependance to ensure such correspondence. Theory, typically, imposes such condition in loop observables by the implementation of a cut-off Λ in the anomalous couplings, for which the deviations drop to zero abruptly at $\sqrt{\hat{s}} = \Lambda$. Instead, in order to explore the unitarity constraint with k^2 dependance dipole form-factors were used [12] for the restriction of the deviations from the SM couplings ($\Delta F^{\gamma}_{i,\mathrm{V,A}}$):

$$\Delta F^{\gamma}_{1,\mathrm{V,A}}(k^2) = \frac{\Delta F^{\gamma}_{1,\mathrm{V,A}}(0)}{(1+\frac{k^2}{\Lambda^2})^2} \tag{1.9}$$

Based on the unitarity constraint of the processes $t\bar{t} \to t\bar{t}$, $t\bar{t} \to W^+W^-$ and $t\bar{t} \to ZH$, bounds on $|\Delta F_1|$ and $|\Delta F_2|$ were deduced as a function of Λ:

$$|\Delta F^{\gamma}_{1,\mathrm{V,A}}(0)| \leq \frac{96\pi}{\sqrt{6}G_\mathrm{F}\sin^2\theta_\mathrm{W}\Lambda^2} \tag{1.10}$$

$$|\Delta F^{\gamma}_{2,\mathrm{V,A}}(0)| \leq \frac{128\sqrt{2}\pi m_t}{\sin^2\theta_\mathrm{W}G_\mathrm{F}\Lambda^3}. \tag{1.11}$$

Figure 1.7 shows the evolution of such limits as a function of $\hat{s}$ at fixed scales where the new phenomena are hypothesised. It can bee seen, indeed, that the allowed deviations vanish with large $\sqrt{\hat{s}}$, while at $\mathcal{O}(\Lambda \simeq$ TeV) larger are possible in regions of $\sqrt{\hat{s}}$ accessible by the LHC .

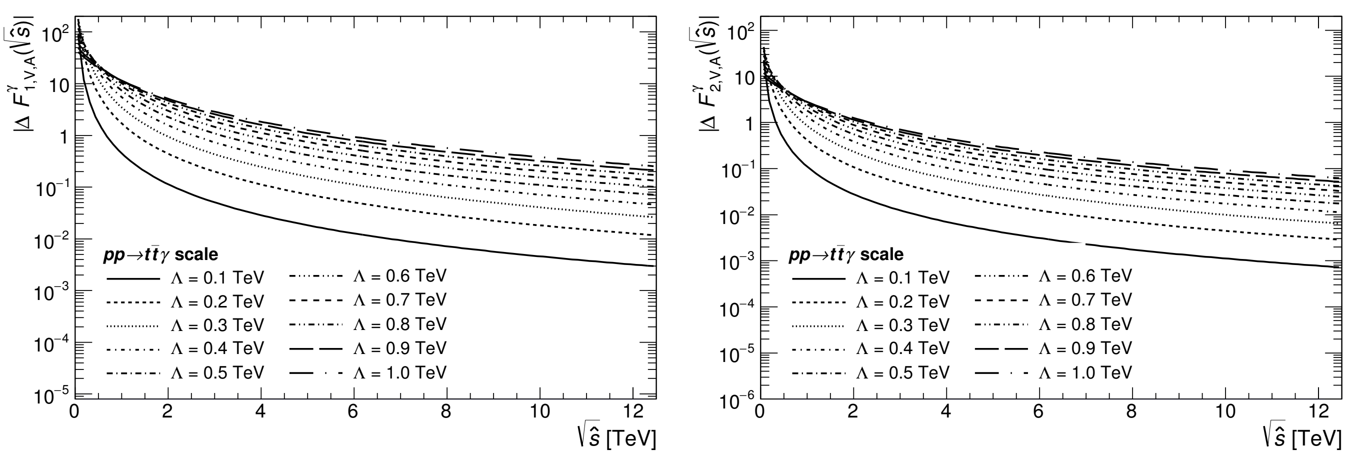

Figure 1.7: Evolution of the anomalous $t\bar{t}\gamma$ couplings as a function of the the partonic centre-of-mass energy ($\sqrt{\hat{s}}$). Allowed regions $|\Delta F^{\gamma}_{1,\mathrm{V,A}}|$ ($|\Delta F^{\gamma}_{2,\mathrm{V,A}}|$) are shown on the left (right). The unitarity of the S-matrix allows for deviations of the Standard Model couplings in the regions below the curves that are shown. The curves are parametrised with respect to the scale of new physics (Λ). Limits are deduced from Eq. 1.10 and Eq. 1.11, which are based on the theoretical calculation [12]. It can be seen that, asymptotically, with the increase of $\hat{s}$, deviations tend to null values, thus conserving the Matrix Element unitarity.

At present, stringent experimental limits on $\Delta F^Z_{1,\mathrm{A,V}}(0)$ for the $t\bar{t}Z$ vertex restrict the deviations to be of the percent level at the TeV scale. Similarly, anomalous magnetic and electric dipole form-factors for the $t\bar{t}\gamma$ vertex are restricted to [3, 12]:

$$-0.2 \leq F^{\gamma}_{2,\mathrm{V}}(0) \leq 0.5 \tag{1.12}$$

$$-4.5 \leq F^{\gamma}_{2,\mathrm{A}}(0) \leq 4.5 \tag{1.13}$$

However, $F^{\gamma}_{1,\mathrm{V}}$ and $F^{\gamma}_{1,\mathrm{A}}$ are yet to be constrained by the experiment.

As introduced in Sec. 1.1, the LHC provides a good framework for the study of the $t\gamma$ couplings compared to $p\bar{p}$ colliders. As can be seen in Fig. 1.8, in $p\bar{p}$ colliders the domination of initial-state photon radiation from the colliding quarks makes a discrimination between different values of $\Delta F^{\gamma}_{1,\mathrm{V}}$ impossible. Moreover, even hypothesising a null electric charge for the top quark ($\Delta F^{\gamma}_{1,\mathrm{V}} = 2/3$ in the left hand-side distribution of Fig. 1.8), the differential spectrum with respect the photon transverse momentum in $p\bar{p}$ collisions shows almost no differences in $t\bar{t}\gamma$ production with respect to the SM coupling values. On the contrary, at pp colliders, where gg production dominates and initial-state radiation is suppressed, the discrimination is more prominent.

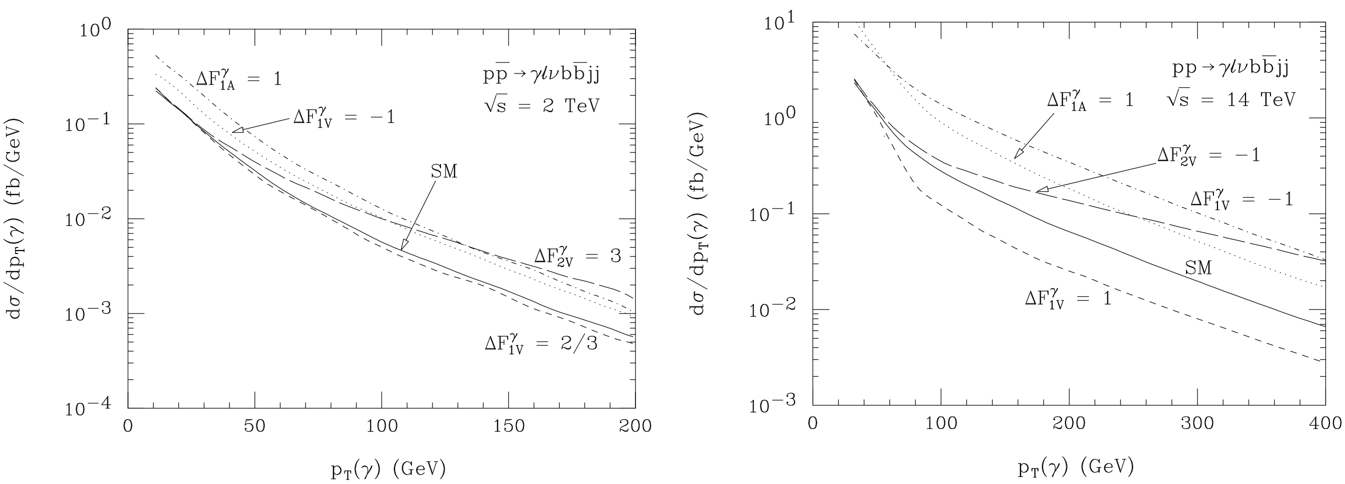

Figure 1.8: Differential cross section spectra of $t\bar{t}$ production in association with a photon in the single-lepton channel as a function of the photon transverse momentum $p_{\mathrm{T}}(\gamma)$ for $p\bar{p}$ collisions at $\sqrt{s} = 2$ TeV (left) and pp collisions at $\sqrt{s} = 14$ TeV (right) [12]. The continuous curve labelled "SM" corresponds to the Standard Model prediction of the $t\bar{t}\gamma$ cross section, while the dotted and dashed curves correspond to the $t\bar{t}\gamma$ cross section with anomalous $t\bar{t}\gamma$ couplings. For each curve only, one coupling is allowed to deviate and the labels $\Delta F^{\gamma}_{1(2),\mathrm{V}}$ ($\Delta F^{\gamma}_{1(2),\mathrm{A}}$) indicate the differences with respect to the SM of the vector (axial-vector) form-factors $F^{\gamma}_{1(2),\mathrm{V}}$ ($F^{\gamma}_{1(2),\mathrm{A}}$). For $p\bar{p}$ collisions the curve labelled $\Delta F^{\gamma}_{1,\mathrm{V}} = 2/3$ corresponds to a null electric charge for the top quark. In that case, because of the overwhelming photon production from initial-state radiation, it can be seen that the differences with respect to the SM prediction are small.

1.4 Next-to-leading order calculations and their interpretations

This section reviews the theory status of higher order QCD computations of $\hat{\sigma}_{t\bar{t}\gamma}$ and how this may affect the interpretation of the measurement.

1.4.1 Next-to-leading order calculation in the *Born* approximation

A first NLO calculation [53], performed using the *Born* approximation for top quarks (*i.e.* considered as stable particles), proved the importance of the second order corrections to $t\bar{t}\gamma$ production compared to a Leading-Order (LO) prediction. The authors showed that for values of $\mu_{\rm F}$ and $\mu_{\rm R}$ close to m_t, the k-factor $= \sigma^{\rm NLO}_{t\bar{t}\gamma}/\sigma^{\rm LO}_{t\bar{t}\gamma}$ is $\simeq 1.5$, as shown in Fig. 1.9.

As explained in Sec. 1.1, the sensitivity to the production cross section, *i.e.* to the $t\gamma$ vertex, is dependent on stringent cuts imposed between the photon and the final state decay products from the t. Because of the approximation of stable top quarks used in this first calculation, the cross section retains a strong dependence to its kinematical definition. Furthermore, cuts, between the top quark decay-products and the photon, should be imposed in order to decrease contributions from radiation from leptons, W-bosons and jets, see Fig. 1.10. Therefore, this calculation cannot be used for a direct comparison with experimental data, as the cross section definition, and its inference to the $t\gamma$ couplings, will strongly depend on the choice of such cuts.

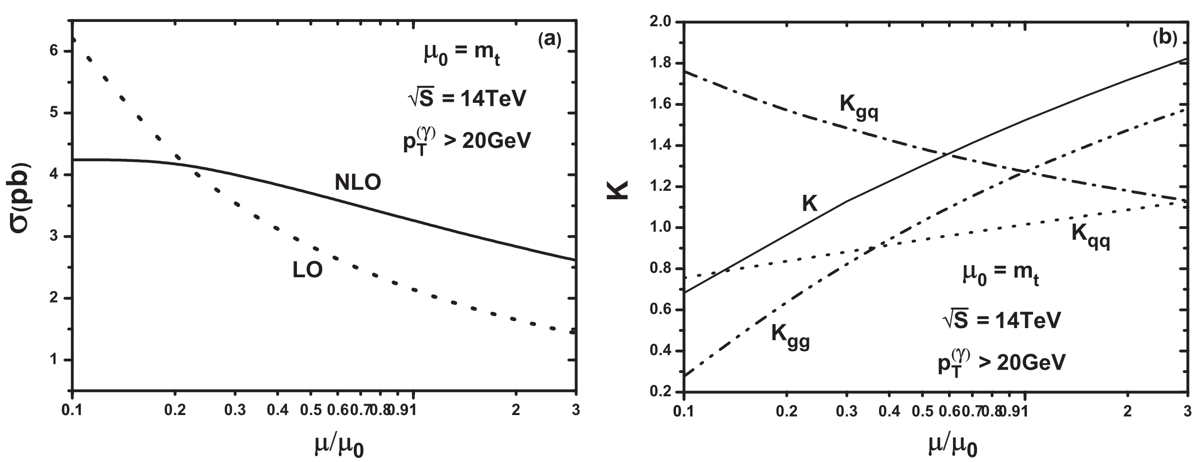

Figure 1.9: A comparison of the NLO and LO cross sections for $t\bar{t}\gamma$ production at the LHC is shown on the left, while on the right the k-factor is shown as a function of the renormalisation and factorisation scales [53]. K labels the inclusive k-factor from all processes contributing to the reaction, while K_{gg}, K_{qq} and K_{gq} label the k-factor of the individual processes. It can be seen that second order QCD corrections are dominant with respect to the LO component. In particular for $\mu_{\rm F} = \mu_{\rm R} \simeq m_t$ the correction is of about 1.5. These results were obtained for $\sqrt{s} = 14$ TeV, but the interpretation at $\sqrt{s} = 7$ TeV is similar [54].

1.4.2 Next-to-leading order calculation in the narrow-width approximation

A recent NLO calculation [56] was performed assuming top quarks being unstable particles. This calculation was able to overcome the challenge of non-factorisable QCD corrections that appear

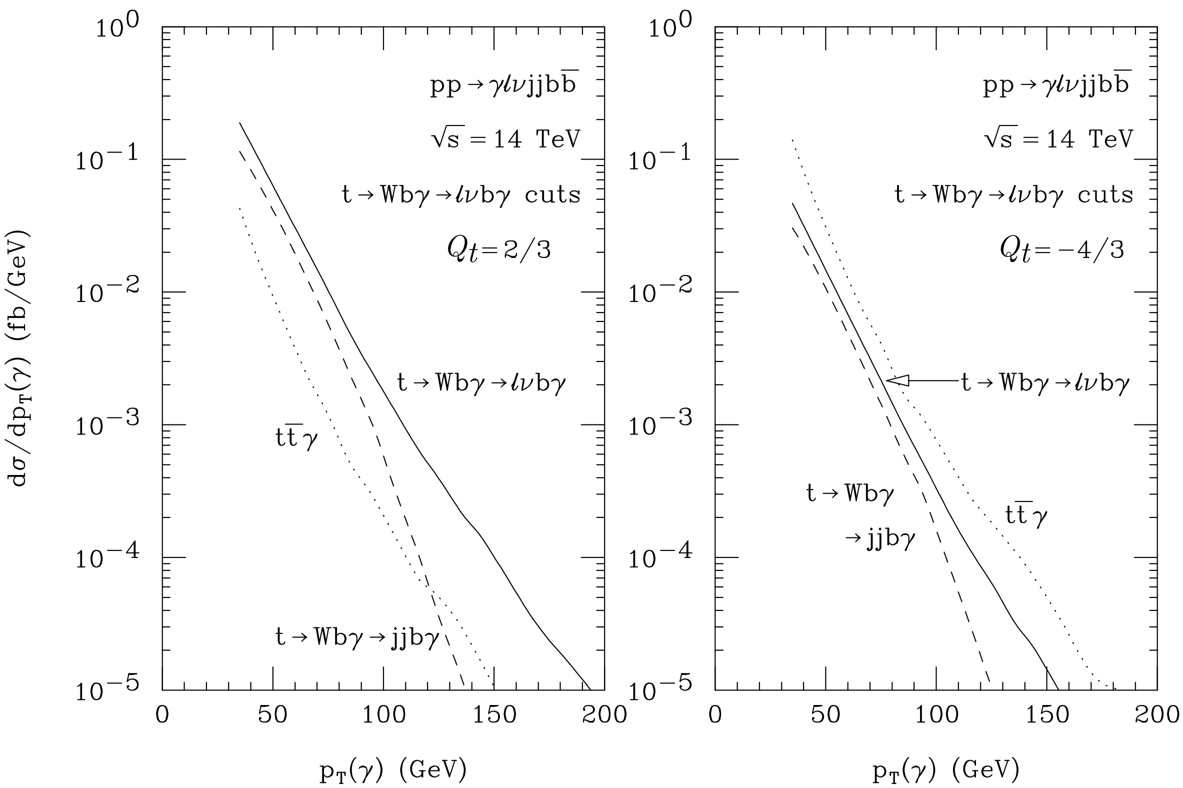

Figure 1.10: Differential $t\bar{t}\gamma$ cross section as a function of the photon transverse momentum for two electric charges of the top quark, $Q_t = 2/3$ (left) and $Q_t = -4/3$ (right) [55]. The calculation was performed at LO for pp collisions at $\sqrt{s} = 14$ TeV. The dotted line represents the $t\bar{t}\gamma$ total contribution including the interferences between the production $t \to Wb\gamma$ and decay $t\bar{t}\,(t \to Wb \to) \to \ell\nu jj\gamma$ cross sections. Individual contributions to the production cross section for $t \to Wb\gamma \to \ell\nu b\gamma$ and $t \to Wb\gamma \to jjb\gamma$ are shown with a solid and a dashed line respectively. The left-hand side distribution assumes $q_t = 2/3$ while the right-hand side distribution assumes $q_t = 4/3$.

between the top quark and its decay products. Advancements in the understanding of those corrections [57–59], which were proven to be suppressible, allowed for a NLO calculation to be less dependent on the kinematical definition of the cross section. While this result [56] includes NLO corrections to the $t\bar{t}\gamma$ cross section at the LHC for a centre-of-mass energy of $\sqrt{s} = 14$ TeV, a dedicated calculation [54] at $\sqrt{s} = 7$ TeV has been performed in the muon channel ($pp \to t\bar{t}\gamma \to b\mu^+\nu_\mu\bar{b}jj\gamma$), see Fig. 1.11. Cuts and event selection applied for this dedicated calculation are similar to the ones in the measurement subject of this thesis, see Sec. 4.4.

The k-factor was determined with a twenty percent uncertainty, where the leading contributions arise from variations (of a factor of two) around the choice of renormalisation scale. However, the dependance on the kinematical cuts on the photon and on the top decay products are strongly reduced. The k-factor is considered to be stable within the systematic uncertainties of the calculation, as shown in Fig. 1.11.

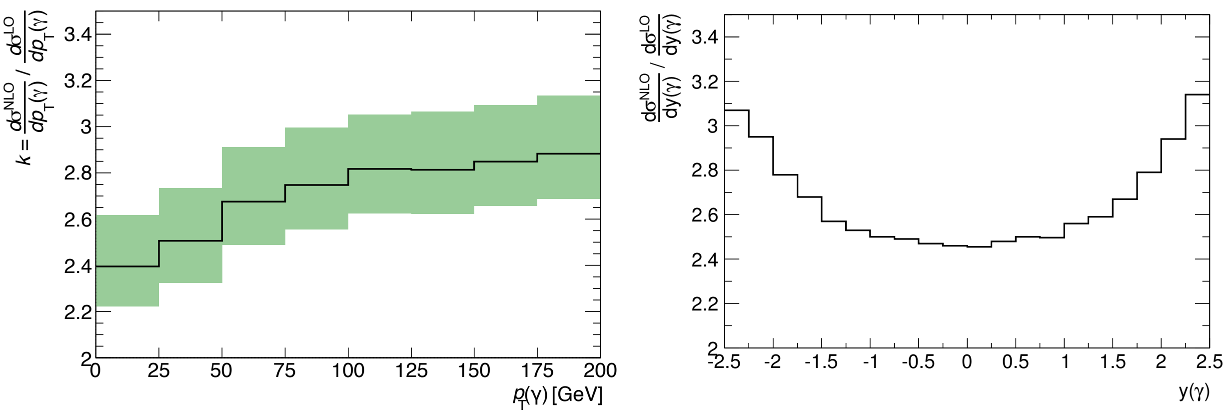

Figure 1.11: k-factor $\sigma^{\mathrm{NLO}}_{t\bar{t}\gamma}/\sigma^{\mathrm{LO}}_{t\bar{t}\gamma}$, with $\mu_{\mathrm{R}} = 2m_t$ and $\mu_{\mathrm{F}} = \sqrt{\hat{s}}$, as a function of photon transverse momentum (left) and of the photon rapidity (right) for pp collisions at $\sqrt{s} = 7$ TeV [54]. The uncertainty, from scale variations, is overlaid as a band on the k-factor as function of the transverse momentum.

1.5 Summary

The top quark, because of its large mass, decays before producing bound states, therefore it allows for a unique possibility to probe directly the quark-photon vertex. The measurement of the $t\bar{t}\gamma$ production cross section paves the way for a direct probe of the $t\gamma$ vertex. A direct measurement of the top quark's electric charge would allow to increase the confidence in the exclusion of ICQ models. Furthermore, (small) deviations from the SM prediction of the top-EW couplings can provide hints of new phenomena appearing at a higher scale of that accessible by the experiment. The comparison of experimental data with the NLO theoretical prediction of the $t\bar{t}\gamma$ cross section is the starting point of this programme.

CHAPTER 2

The experimental setup and its performance

This chapter is meant as a quick description of the experimental setup used in this measurement for the reader who is not familiar with the detector components and its nomenclature.

Section 2.1 describes the accelerator complex and the beam parameters of the Large Hadron Collider at CERN. Section 2.2 briefly explains the different detection techniques used in the ATLAS experiment. Section 2.6 is devoted to the review of the data acquisition and processing. Section 2.7 reviews the detector operations during the run 1 period (2010-2013) and the detector performance is overviewed in Sec. 2.8. In the last two sections a more detailed emphasis is given to data quality monitoring and performance of the silicon micro strip detector, as the author was directly involved in these activities [60].

2.1 The accelerator complex

The ATLAS experiment is located at an interaction point (IP) of the Large Hadron Collider (LHC) [61]. The LHC itself is a two-ring-superconducting-proton (ion) accelerator situated at the European Centre for Nuclear Research (CERN) in Geneva, Switzerland. The LHC is part of a wide accelerator complex hosted by CERN.

2.1.1 Pre-accelerators

Before protons are accelerated to a centre-of-mass energy ($\sqrt{s}$) of the order of 7 TeV by the LHC ring, a range of pre-accelerators is used to bring the proton energy in steps close to the TeV threshold. Figure 2.1 illustrates the complex accelerator system and the LHC experiments situated at CERN. Hydrogen gas is ionised and accelerated by linear accelerators, such as the Linac1 and the Linac2. The ions passing through Radiofrequency (RF) conductor cavities are accelerated to about 50 MeV. A small circular accelerator system, the Proton Synchrotron Booster (PSB), accelerates protons up to 1.4 GeV which are then injected into the Proton Synchrotron (PS). The PS subsequently injects protons to the Super Proton Synchrotron (SPS) where they reach gradually an energy of 450GeV. Clockwise and anticlockwise injector systems feed those protons into the LHC .

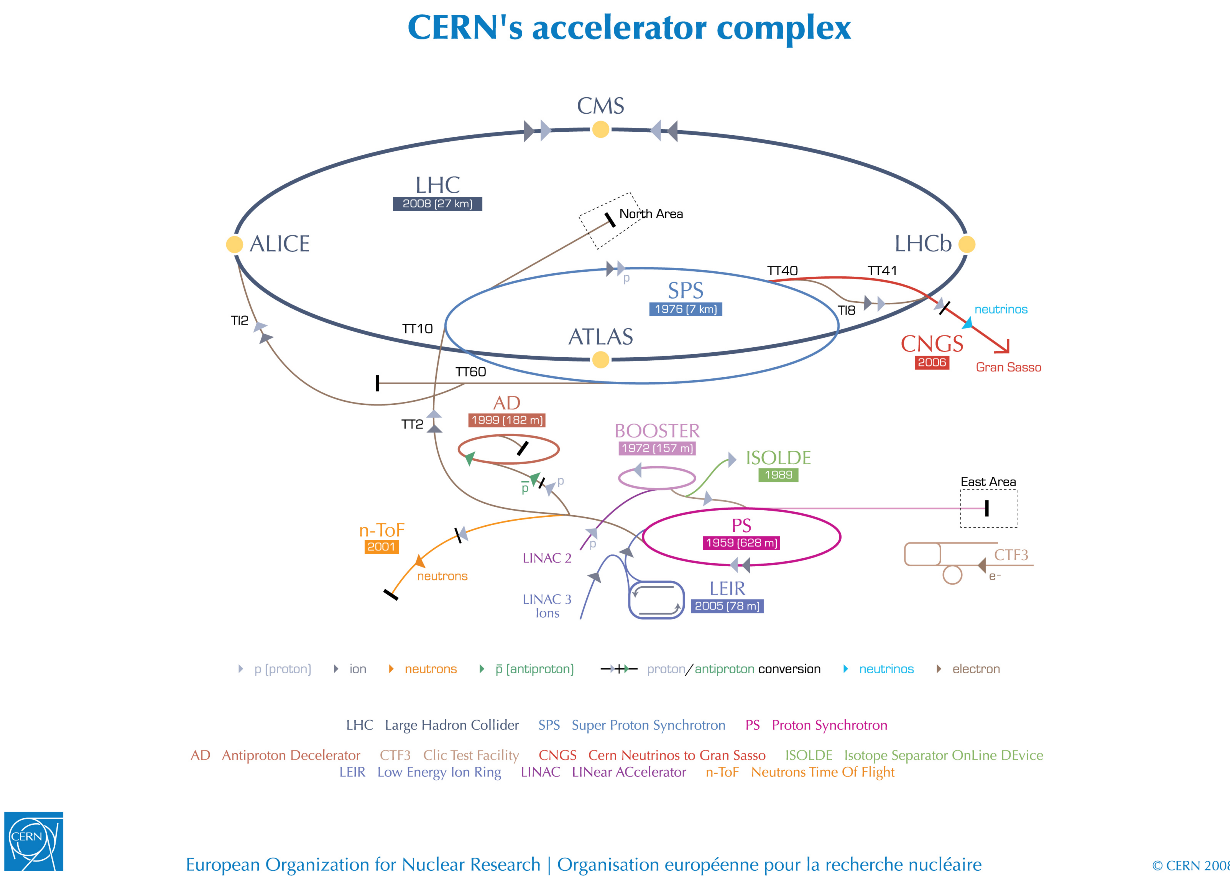

Figure 2.1: Overview of the accelerator complex at CERN [62].

2.1.2 The Large Hadron Collider

The LHC consists of 1232 liquid helium cryogenic dipole magnets filling two thirds of a circle of approximatively 27 km circumference, the rest comprising beam focusing quadrupole magnets, and accelerating cavities. The ring is divided in eight straight sections and in eight arced sections. A cross section view of a dipole element is shown in Fig. 2.2. The underground tunnel excavated for the Large Electron Positron (LEP) now hosts the LHC. Lying on molasse and limestone rock beads for, respectively, 90% and 10% of its length, the tunnel is situated between 100 m and 45 m underground with a 1.4% inclination gradient pointing towards Geneva. Two transfer tunnels link the LHC to the remainder of the CERN accelerator complex. Technical aspects are detailed elsewhere [63]. For a bunched gaussian-distributed beam containing N_{b} particles per bunch, interacting at a frequency f_{rev}, and accelerated at speeds of γ_{r}, the instantaneous luminosity (L_{Lumi}) can be defined as [61]:

$$L_{\mathrm{Lumi}} = \frac{N_{\mathrm{b}}^2 n_{\mathrm{b}} f_{\mathrm{rev}} \gamma_{\mathrm{r}} F}{4\pi \varepsilon_{\mathrm{n}} \beta^{\star}} \tag{2.1}$$

where the normalised transverse emmitance (ε_{n}) and the beta function at the point of collision ($\beta^{\star}$) characterise the geometrical properties of the beam. The luminosity is corrected by a geometrical factor F which depends on the angle formed by the opposite direction of the two colliding beams (θ_{c}), on the longitudinal (transverse) gaussian width of the colliding beams at the IP σ_z ($\sigma^{\star}$).

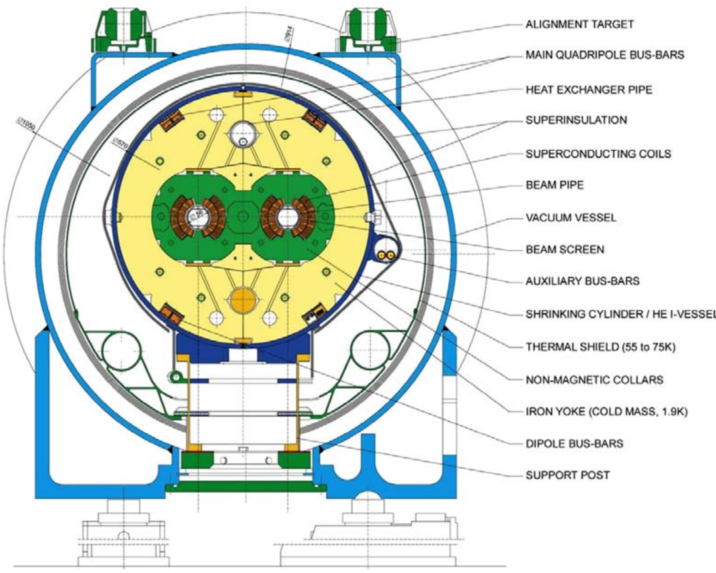

Figure 2.2: Cross section view of a dipole element of the LHC [61].

The total amount of data recorded by the experiments, situated in the IP s of the ring, depends upon the choice of those parameters. Design and typical operating values for those parameters are shown on Tab. 2.1.

	Year		**Design**
Parameter	**2011**	**2012**	
Beam energy	3.5 TeV	4 TeV	7 TeV
$\beta^\star$	1.0 m	0.6 m	0.55 m
$1/f_{\mathrm{rev}}$	50 ns	50 ns	25 ns
n_{b}	1380	1374	2808
$< N_{\mathrm{b}} >$	1.45×10^{11} protons	1.65×10^{11} protons	1.10×10^{11} protons
Intial ε_{n}	2.5 mm mrad	2.5 mm mrad	3.75 mm mrad
$L_{\mathrm{Lumi}}^{\mathrm{max}}$	$3.7 \times 10^{33}\mathrm{cm}^{-2}\mathrm{s}^{-1}$	$7.7 \times 10^{33}\mathrm{cm}^{-2}\mathrm{s}^{-}1$	$1.0 \times 10^{34}\mathrm{cm}^{-2}\mathrm{s}^{-1}$
Stored beam energy	110 MJ	140 MJ	362 MJ

Table 2.1: Overview of proton proton beam parameters of the LHC during the machine operations of 2011 and 2012. Paramters are compared with respect to their design values [61, 64, 65].

2.2 Detector overview

The ATLAS detector is composed of a range of sub-systems which, ordered from the inside out: (i) the Inner Detector, which is the innermost tracker for charged particles,(ii) a calorimetry system, comprised of an electromagnetic calorimeter and a hadronic calorimeter measuring respectively energy deposits of particles originated from Electromagnetic (EM) and from hadronic showers and (iii) an outermost Muon Spectrometer measuring muon trajectories escaping the calorimeter system. Figure 2.3 shows a schematic view of the detector and its different components and a detailed description of the ATLAS experiment can be found elsewhere [66].

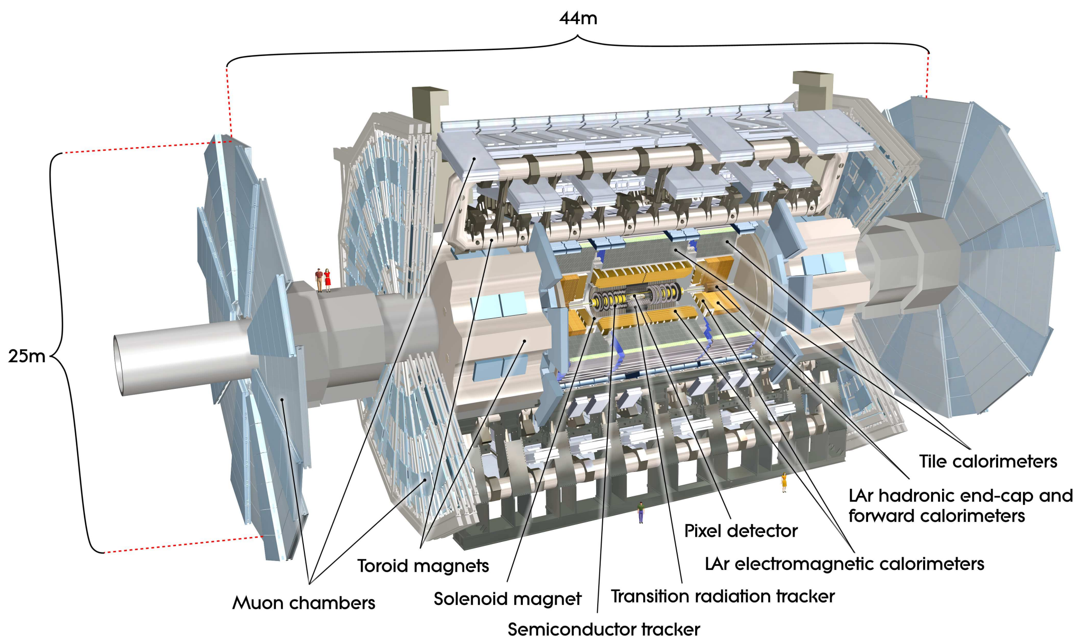

Figure 2.3: Artist's overview of the ATLAS detector and its sub-systems.

ATLAS uses a right-handed coordinate system with its origin at the nominal IP in the centre of the detector and the z-axis along the beam pipe. The x-axis points from the IP to the centre of the LHC ring, and the y-axis points upward. Cylindrical coordinates (r, φ) are used in the transverse plane, φ being the azimuthal angle around the beam pipe. The pseudorapidity (η) is defined in terms of the polar angle θ as $\eta = -\ln \tan(\theta/2)$. Transverse momentum and energy are defined as $p_{\mathrm{T}} = p \sin\theta$ and $E_{\mathrm{T}} = E \sin\theta$ respectively.

2.3 Inner Detector

The Inner Detector (ID) [67], submersed in a 2 T solenoidal field, includes the subsystems closest to the interaction point.

It is comprised, as shown in Fig. 2.4, by a gaseous Transition Radiation Tracker (TRT), and two silicon trackers: the pixel detector (PIXEL) and the semiconductor tracker. Overall, the total material budget is of about 0.4 radiation lengths (X_0) in the central region, and of 1.5 X_0 in the forward region. The ID provides momentum measurement and interaction vertex reconstruction.

2.3.1 The PIXEL detector

High granularity tracking detectors near the IP are crucial for a good tracking performance in environments with high track multiplicity, such as the collisions at the LHC. The PIXEL detector

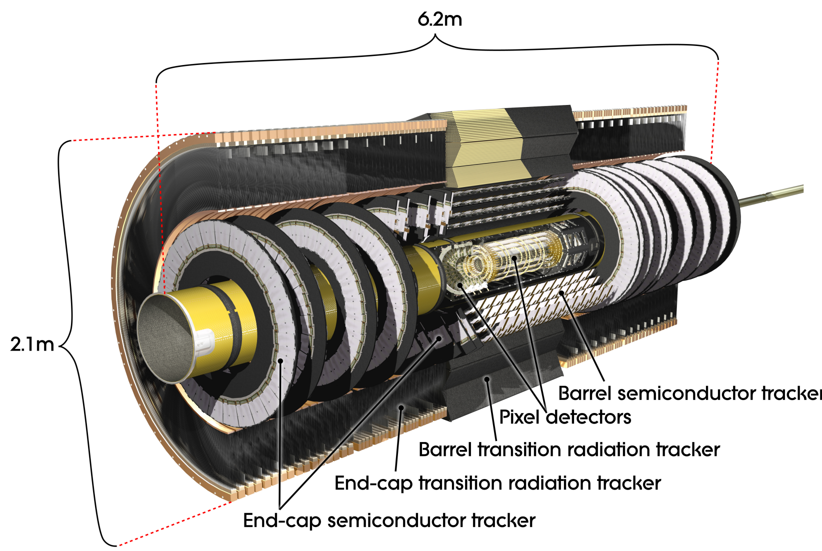

Figure 2.4: Overview of the ATLAS Inner Detector [67].

consists of 1744 silicon pixel modules, of unit size of 62.4 mm × 21.4 mm, arranged in 3 barrel layers and 3 disks in each of the two end-caps, providing around 80 million read-out channels. The detector spans radially, covering distances in the range from $r = 50.5$ mm to $r = 150$ mm. Typical position resolution equals to 10 μm in the $r - \varphi$ plane and 115 μm along the z direction for the barrel for the end-cap disks respectively.

Ionisation, from charged particles traveling through the material, produces pairs of electrons and holes which, under the influence of an electric field, are collected by electrodes producing an electric pulse. In each module, sixteen radiation-hard bump-bonded chips convert the collected charge into binary information. The read-out occurs when the pulse-height exceeds a tuneable threshold (time-over-threshold technique).

Hits recorded in the barrel (end-cap) provide three (two) track measurements. The PIXEL detector contributes to the global track reconstruction with pattern recognition. Vertex reconstruction benefits from the closeness of the detector to the interactions, thus reducing the uncertainty of the measurement of the impact parameter of the track [1].

2.3.2 The Semiconductor Tracker

An area of 61m^2 of silicon with 6.2 million readout channels composes the Semiconductor Tracker (SCT). Its 4088 silicon micro-strip modules are arranged in 4 barrel layers and 18 disks, 9 in each of the two end-caps. The barrel is made of 2112 modules and has a coverage in pseudorapidity $|\eta| < 1$, while the end-caps are made of 1976 modules covering $1.1 < |\eta| < 2.5$.

The barrel modules consist of two pairs of identical, single-sided, p-on-n silicon micro strips sensors with 80 μm strip-pitch glued back-to-back to a base-board (see Fig. 2.5). A stereo-angle of 40 mrad between sides provides three dimensional point information with space-point resolution of ~ 16 μm in the r, φ coordinates and ~ 580 μm in the z. The end-cap modules are very similar but

[1] The track impact parameter is defined as the minimum distance of a track to the reconstructed interaction vertex and its measurement is a crucial input for the algorithms identifying heavy-flavoured jets and τ leptons.

comprise wedge-shaped sensors. The operational temperature, nominally at -7 °C, is maintained by C_3F_8 evaporative cooling shared with the PIXEL sensors.

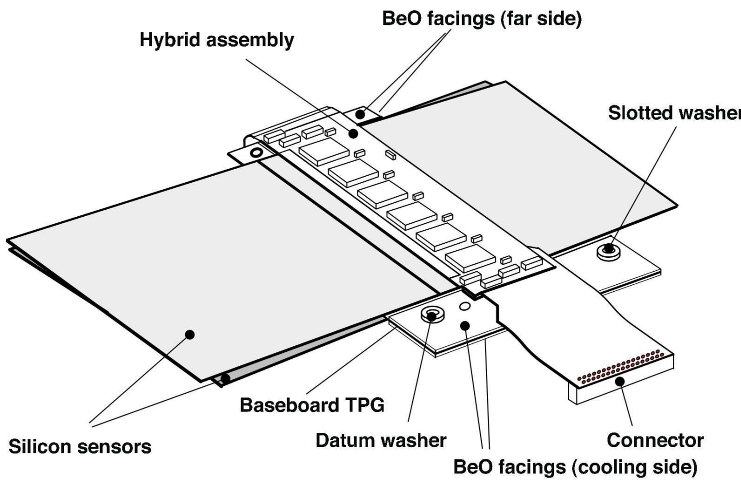

Figure 2.5: Overview of a barrel module of the SCT [66].

2.3.3 The Transition Radiation Tracker

The TRT [68] consists of roughly 3×10^4 proportional drift tubes (so called *straws*) covering the radial range from $r = 563$ mm to $r = 1066$ mm. Each straw, see Fig. 2.6, has a diameter of 4 mm and a length of 114 cm. It consists of an anode made of a gold-plated tungsten wire, which is read-out from each side. The anode is surrounded by a non flammable gas, which consists of a mixture of Xe and CO_2, with 70% and 20% partial pressures respectively, with the remainder 10% being CF_4.

The gas and wire are enclaved in a thin inner aluminium layered cathode, providing an electrical resistance less than 300 Ω/m. The inner layer is linked to an identical outer layer by carbon fibre mounts. Carbon fibres guarantee good mechanical properties and reduce the effective resistance to about 20 Ω/m.

The TRT is laid out such that charged particles with $p_{\mathrm{T}} > 0.5$ GeV and with $|\eta| < 2.0$ cross more than 30 straws. Charged particles interact through ionisations with the gas-mixture. Electrons and positive ions drift to the anode and cathode respectively. Differences in the arrival times between the ions and the electrons determine the drift-time, thus extracting position information. The collected charge from wire is sampled in twenty-four time bins of 3.12 ns width and it is compared to a threshold of 300 eV. Drift-time measurements provide tracking information with a spatial resolution of about 130 μm.

Polypropylene fibres in the barrel, and foils in the end-caps, sandwiched between the straws, provide transition radiation photons when a charged particle crosses the straw-polypropylene boundary. These photons have a typical energy of 5 to 30 keVand produce cascade electrons. The collected charge is compared to a separate higher threshold of 6 keV. The proportionality between the recorded high-threshold pulse and the $\gamma = E/m$ of the particle crossing the detector allows for discriminating between minimum ionising particles (electrons) and charged hadrons [69].

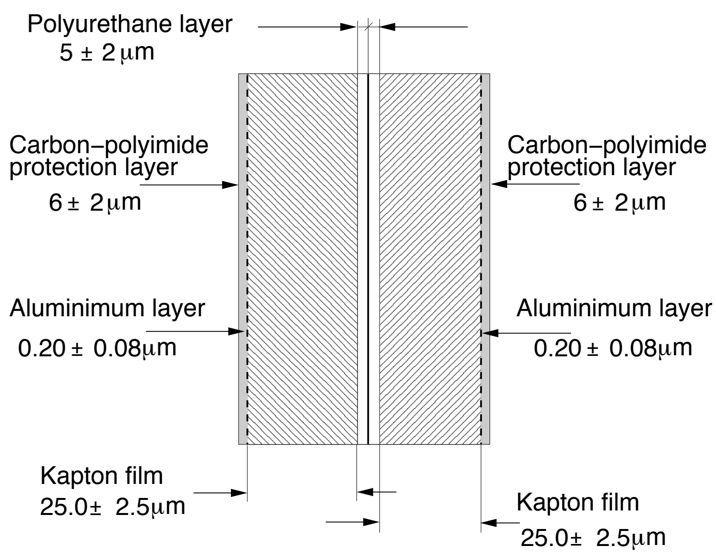

Figure 2.6: Overview of a TRT straw [68].

Figure 2.7 shows the high threshold TRT fraction of hits with respect the γ factor.

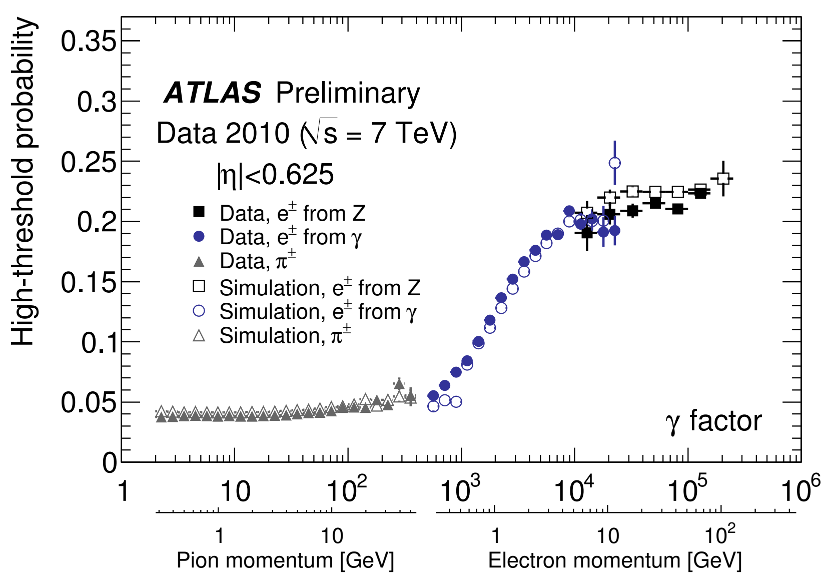

Figure 2.7: The high-threshold hit probability against the reconstructed particle's γ factor is shown for the barrel region ($|\eta| < 0.625$). Data is compared to simulated pions and electrons. The determination of γ is performed using the reconstructed transverse momentum of the incoming track and the assumed mass of the particle [69].

The particle identification capabilities can be seen as the high-threshold probability follows a turn on curve. While electrons demonstrate a rapid increase of the high-threshold probability with the increase of γ from $600 \rightarrow 5000$, pions, because of their larger mass, populate regions in γ below 103. Ionisation contributes majorly from $< \frac{dE}{dx} >$ in low γ regions ($\gamma < 103$). Gradually, the high-threshold probability associated to a pion track increases because of the rise of $< \frac{dE}{dx} >$ with increased momentum.

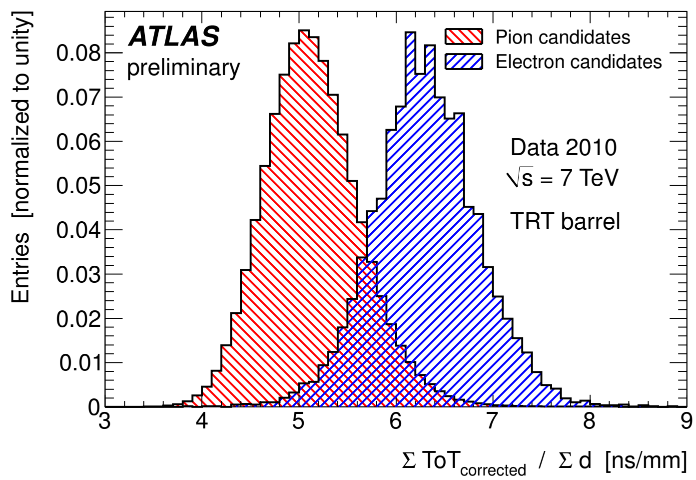

Figure 2.8: The particle identification capabilities of the TRT based on the Time-over-Threshold (ToT) techniques are demonstrated [69]. The distributions show the period of time ($\sum \mathrm{ToT}_{\mathrm{corrected}}$) during which the pulse-height exceeds the 300 eV threshold divided by the transverse particle trajectory length in the straws ($\sum d$). It can bee seen that the distribution for pion candidates peaks at lower values with respect to electron candidates.

The TRT has also demonstrated particle identification capabilities by timing, in time-bins of 25 ns, the pulse-height being the 300 eV threshold, see Fig. 2.8. Indeed, the Time-over-Threshold (ToT) is correlated with the maximum pulse-height. The ToT is dependent on uncorrelated systematics to $< \frac{dE}{dx} >$ of the incoming particle (primarily due to differences in the track-to-wire distances) and the ToT measurement is subject to corrections based on the η of the particle [69].

2.4 Calorimeters

2.4.1 Generalities

Calorimeters provide energy and position measurements for neutral and charged particles trough energy deposits in absorbing materials. Incoming particles interacting with the material develop showers of secondary particles with gradually reduced energy. Detection is based on the ionisation and scintillation processes which are originated from the secondary particles produced in the showers. Length and density of the interacting material are designed such that the incoming particles deposit all of their energy in their path. Showers developed in the material can be of two types, depending upon the particle originating them. Above the thresholds of *Compton* and *photoelectric* production, electromagnetic showers are generated by charged particles, radiating photons via *bremsstrahlung*, by photons, and by neutral mesons decaying into diphotons (e.g. $\pi^0, \eta^0, \rightarrow \gamma\gamma$), producing electron-positron pairs. Hadronic showers are initiated by hadron production, *i.e.* by successive inelastic nuclear interactions of mesons and baryons. Neutral mesons, such as π^0, will loose, on average, 1/3 of their energy in electromagnetic showers.

ATLAS uses non-compensating sampling calorimeters spanning from $r = 4.2$ to $r = 6.65$ m [66]. The non-compensating aspect of the calorimeter is determined by the fact that the ratio of the detector response for electromagnetic showers to hadronic showers for the same initial particle energy is greater than one. Alternating layers of passive and active material guarantee its sampling capabilities. Longitudinal segmentation allows for the extraction of position information, while lateral segmentation allows for the determination of the shower characteristics. The ATLAS calorimeter has a full φ-coverage around the beam axis and it is divided in barrel and end-cap regions.

Both electromagnetic and and a hadronic calorimeters constitute the overall calorimetry system which covers a range of $0 < |\eta| < 4.9$. The Electromagnetic Calorimeter (ECAL) is the closest to the interaction point followed by the Hadronic Calorimeter (HCAL). In the barrel region ($0 < |\eta| < 1.8$) the ECAL is complemented by a set of pre-samplers which increase the discrimination between pions and photons. The following two paragraphs explain in more details the characteristics of each system.

2.4.2 Electromagnetic Calorimeter

The ECAL [70] covers 22 and 24 radiation lengths (X_0) in the barrel and end-caps respectively. Based upon the intrinsic linear behaviour, its stability over time and its radiation-hardness, the ECAL uses Liquid Argon (LAr) as active material. Lead is used instead as the absorber medium. Charge is collected by copper-sheathed kapton electrodes, which are centred in each layer and have a typical 2 kV potential difference with respect to the medium. Each layered module is stacked in an accordion-shaped geometry ensuring a full coverage in azimutal ranges.

The calorimeter is characterised by three finely segmented η layers. In particular, the first layer ($|\eta| < 1.4$) is segmented with strips of size $\Delta\eta \times \Delta\varphi = 0.0031 \times 0.1$ covering 4.3 X_0, while the middle ($1.4 < \eta < 1.475$) layers granularity is $\Delta\eta \times \Delta\varphi = 0.0023 \times 0.025$ covering 16 X_0. The third's layer segmentation is coarser ($\Delta\eta \times \Delta\varphi = 0.05 \times 0.025$).

This fine fragmentation allows, by determining the position of the EM cluster in the first and second layers, for a precise determination of the η-direction of the photon. The improved resolution aids the particle identification algorithms to discriminate hadrons, which have wider showers, against electrons and photons which have narrower shower-shapes. Figure 2.9 shows an overview of the longitudinal and transverse segmentation of the ECAL.

2.4.3 Hadronic calorimeter

The ATLAS hadronic calorimeter (HCAL) [66] is composed of the following subsystems (i) the **Tile** hadronic calorimeter, covering $|\eta| < 1.7$; (ii) the **Hadronic end-cap** calorimeter, covering $1.5 < |\eta| < 3.2$; and the (iii) **Forward** calorimeter which is integrated in the cryostats housed in the end-caps, covering up to $|\eta| = 4.5$.

The Tile calorimeter

The Tile calorimeter (Tile) [66], placed directly after the ECAL, is a sampling calorimeter with steel and scintillating tiles as absorbing and active materials respectively. It consists of a barrel region covering $|\eta| < 1.0$ and two extended barrel regions, each covering ranges of $0.8 < |\eta| < 1.7$.

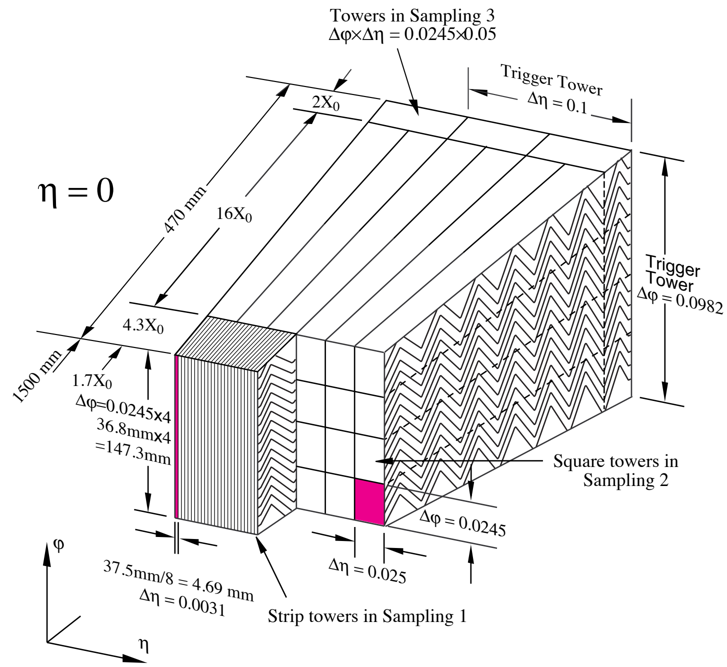

Figure 2.9: Overview of a barrel module of the liquid argon electromagnetic calorimeter [70].

Extending in radii from $r = 2.28$ m to $r = 4.25$ m, it is divided in 64 modules and segmented in three layers covering, respectively, 1.5, 4.1 and 1.8 (1.5, 2.6, and 3.3) interaction lengths (λ_0) for the barrel (extended barrel). Scintillation photons are read-out from each module by two opposite sided Photomultiplier Tubes (PMT), which are connected to the modules via wavelength shifting fibres.

The Hadronic End-cap calorimeter

The Hadronic End-cap Calorimeter (HEC) [66] consists of two wheels, situated at each end-cap, Extending from $|\eta| = 1.5$ and up to $|\eta| = 3.2$ the HEC overlaps with the Tile Calorimeter. This overlap increases the material density in the transition region between the end-caps and the forward Calorimeters. Each wheel consists of 32 modules shaped in wedges. A total of four in-depth layers of modules constitute each wheel. Parallel copper plates, having a typical thickness of 25 (50) mm, encase the active material and collect the deposited charge in the inner (outer) wheels. The active material is LAr, and it fills spaces of 8.5 mm in width between each copper plate.

The Forward Calorimeter

The Forward Calorimeter (FCal) [66] is situated in the forward-most segments of the system, specifically into the end-cap cryostats, thus reducing radiation in the Muon Spectrometer. The FCal uses LAr as active material, but, because of geometrical size limitations, a higher density design is used (covering 10 λ_0). A modular design allows for a combination of electromagnetic shower and hadronic shower measurements. A copper-made first module measures electromagnetic deposits, while the remainder two modules, made of tungsten, are sensitive to hadronic activity.

Concentric electrode rods, parallel to the beam axis, are arranged within a metal matrix acting as the frame for each module. Due to the matrix arrangement gaps, as small as 0.24 mm, are created, they are filled with the active material. This architecture avoids unnecessary build-up of ions.

2.5 Muon Spectrometer

A precise (and independent from the ID) momentum resolution for hight-p_{T} muons escaping the inner most detector layers is of capital importance for a rapid response trigger. Therefore, the Muon Spectrometer (MS) is tailored for this purpose. The detection method is based on bending muon tracks in a large superconducting toroidal magnetic system [66]. Toroidal barrel and end-cap magnet systems bend muons with $|\eta| < 1.4$ and $1.6 < |\eta| < 2.7$ respectively. Both the solenoidal magnetic filed, and the toroidal system bend muons in the transition region between barrel and end-caps ($1.4 < |\eta| < 1.6$). The usage of a toroidal system has the advantage that it provides an field orthogonal to the particle trajectory, thus, minimising multiple scattering which degrades the momentum resolution.

Radiation hardness and the busy environment of the LHC motivate the choice of a high rate and high granularity detector. The MS, of which a sketch can be seen in Fig. 2.10, makes use of the following systems: (i) monitored drift tube chambers, (ii) cathode strip chambers, (iii) resistive plate chambers and (iv) thin gap chambers.

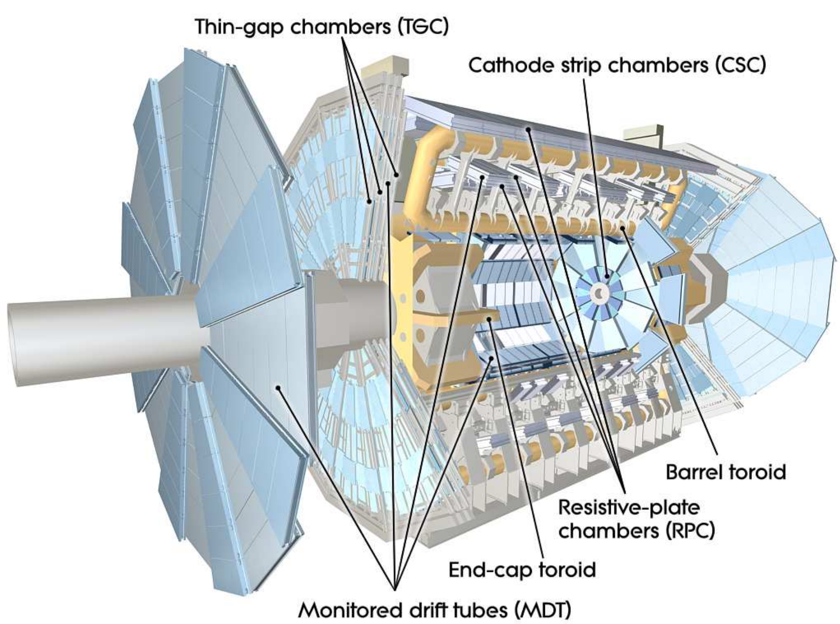

Figure 2.10: Artistic cutaway illustration of the Muon Spectrometer system and its components [66].

Monitored Drift Tube Chambers

The Monitored Drift Tube Chambers (MDTs) [66] consist of 1150 tubular layers separated by mechanical spacers. They are used for precision tracking and they have full coverage in φ. They can determinate the coordinate in the bending plane with a precision of typically 35 μm. The MDT cover ranges of $|\eta| < 2.7$.

Cathode Strip Chambers

The Cathod Strip Chambers (CSCs) [66] consist of 32 multi-wire proportional chambers with the wires oriented radially. Strip-segmented cathode wires allow for fast response times (typically 40 ns). CSCs provide coordinate measurements along both the bending plane, with 40 μm resolution, and along the orthogonal plane, with 5 mm precision. The CSCs cover ranges of $2.0 < |\eta| < 2.7$.

Resistive Plate Chambers

The Resistive Plate Chambers (RPCs) [66] are made of parallel electrode plates filled with gas and consist of 606 chambers. RPCs are used notably to provide trigger information, because of their rapid response time, but they also provide a second tracking coordinate. The RPCs cover ranges of $|\eta| < 1.05$.

Thin Gap Chambers

The Thin Gap Chambers (TGCs) [66] consist of 3588 multi-wire chambers. The TGCs are used primarily for triggering high-p_{T}muons, but they also contribute to track measurements. The TGCs cover ranges of $1.05 < |\eta| < 2.7$.

2.6 Data acquisition and trigger techniques

Unlike specific purpose experiments, data collected by ATLAS have to serve a wide range of analyses aims. As explained in Sec. 2.1.1, the LHC delivers collisions at a high rate of which only about 10 Hz are of interest in the experiment's physics programme, while the remainder portion, originated from lower energy Quantum Chromodynamics (QCD) interactions, is of a lesser interest. These two reasons call for a Data Acquisition System (DAQ) system capable of handling high rates and combining information from all the subsystem's responses. A crucial role is played by a trigger system capable of identifying, in short time and efficiently, events of interest. Both DAQ and Trigger [66] are briefly introduced in this section.

2.6.1 Trigger system

The ATLAS trigger is based on a multi-layered decision tree and it aims to a rate reduction from the 40 MHz of bunch cross rate to a few hundreds of Hz written to disk [66], as shown on Fig. 2.11.

The first trigger layer, named Level 1 (L1), conveys signals from 1600 point-to-point readout links from the calorimeters and the MS to custom-made electronic boards. Selection criteria, mainly based on the muon transverse momentum and energy deposits in the calorimeters, identify Regions-of-Interest (RoI) within the detector (through the corresponding η-φ coordinates). The decision is based on a predefined logic which makes use of all the information transferred to the electronic boards and sets of trigger chains (menus) are constructed. Due to the high throughput rate for certain menus, a random data rejection can be applied (pre-scaling) keeping, thus, only the fraction $\frac{1}{f_{\text{pre-scale}}}$ of data, with $f_{\text{pre-scale}}$ being an arbitrary constant parameter. The L1 makes a decision whenever to reject the event or to convey the information to the next level in 2.5 μs, on average it reduces the data rate to about 75 kHz.

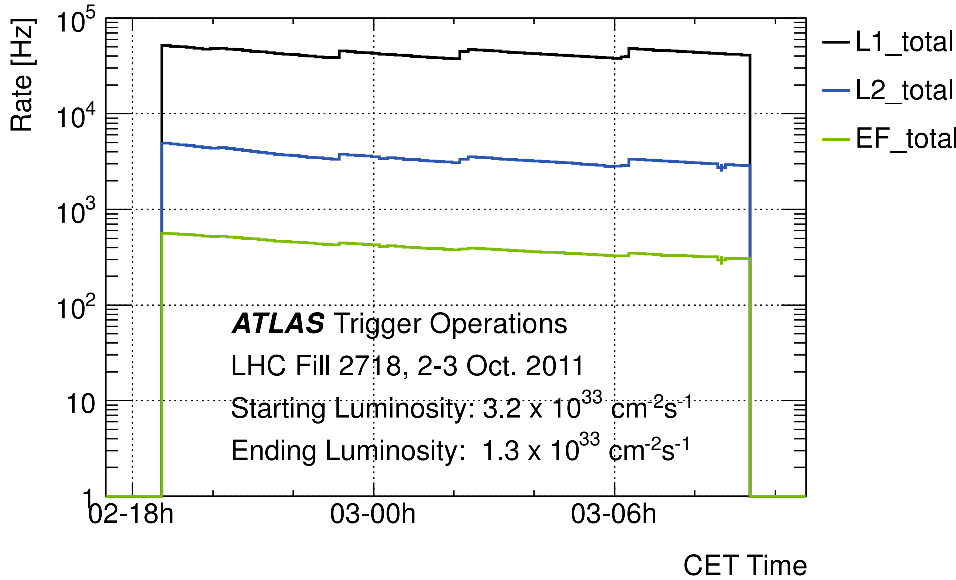

Figure 2.11: Data trigger output and recording rate at ATLAS at an instantaneous luminosity of $3.2 \times 10^{33}\text{cm}^{-2}\text{s}^{-1}$ [71].

Once an RoI has been identified, the L1 transfers the recorded data (containing at this stage only geometrical coordinates and information on the feature that caused the Trigger to fire) to detector specific electronics for further processing. Detector specific Read Out Drivers (ROD) transfer the full detector information to custom made electronic buffers. Subsequently, the buffers transfer, at slower speeds, data to computer farms situated on the surface. A software based decision is made at this stage, this is the second decision layer. The higher trigger level, using information (with full detector granularity) from all systems, creates event-based data-sets. Data throughput is reduced to about 3.5 kHz in approximately 40 ms.

A more complex decision, using the full event characteristics and tracking information, is made by the final trigger layer, so-called Event Filter (EF). The data collection rate is reduced to a few hundreds of Hz. Collected event information, organised in detector runs and blocks of recorded luminosity within the runs, is transferred to large computing farms where offline reconstruction algorithms refine the event data.

2.6.2 Data organisation

Event data is organised in sets based upon the trigger information used or upon their usage purpose. The data-sets are called *streams* and they are divided into the general purpose sets such as the “calibration”, “physics”, “debug” and “express” *streams*, and specific purpose such as the ID *stream*. The “calibration” *stream* contains information used for detector performance. The "express" *stream* contains about 10% of all trigger menus and it is used for data quality analysis. "Physics" *streams* are organised in exclusive sets based on the trigger menus that seeded their construction. An illustration of stream specific recording rates is shown in Fig. 2.12.

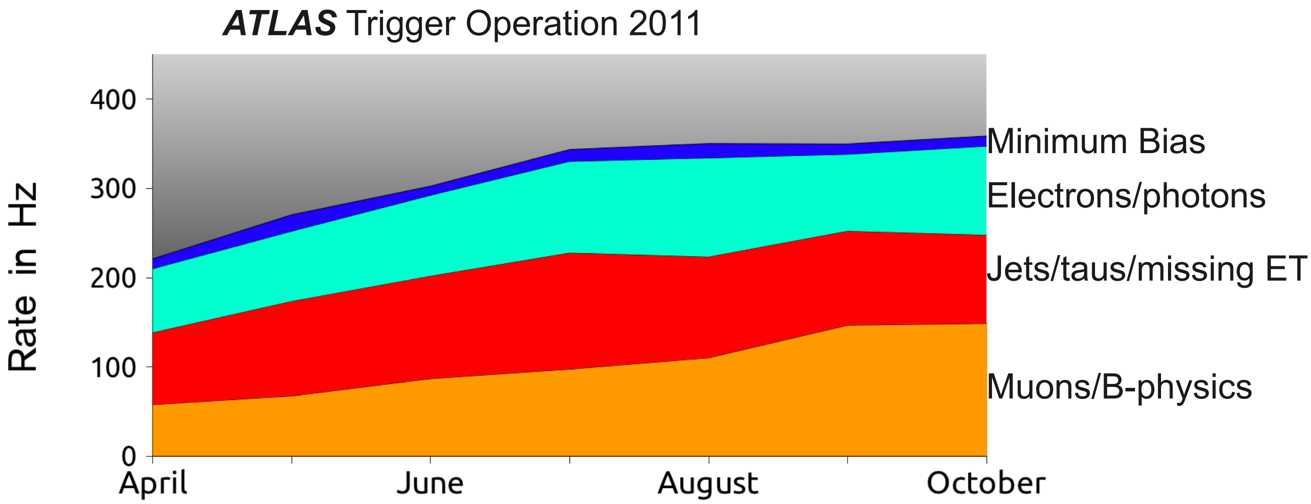

Figure 2.12: Event Filter *stream* recording rates, averaged over the periods for which the LHC declared stable beams [71].

2.7 Operations

The LHC's first run started in 2010 and ended in 2013; data-taking periods were spaced by technical stops and technical shutdowns. Technical stop period usually started at the end of the year and ended around spring, signalling the start of a new data-taking period with different beam settings (see Tab. 2.1). The accelerator machine delivered proton–proton collision at a centre-of-mass energy of $\sqrt{s} = 7$ TeV and $\sqrt{s} = 8$ TeV for the years 2010-2011 and 2012 respectively. Short runs of proton-Lead, proton-Iron, Iron-Iron and Lead-Lead were also part of theLHC's programme and those types of collisions were delivered at the end of each scheduled *pp* data-taking period. Figure 2.13 left shows the total integrated luminosity of *pp* collisions delivered by the accelerator and recorded by the ATLAS detector during the years 2011-2012. The instantaneous luminosity can be expressed as a function of the number of inelastic interactions per bunch crossing μ [73]:

$$L_{\mathrm{Lumi}} = \frac{\mu n_{\mathrm{b}} f_{\mathrm{rev}}}{\sigma_{\mathrm{inel}}} \tag{2.2}$$

where σ_{inel} is the *pp* total inelastic cross section per bunch crossing. The number of inelastic collisions per bunch crossing is also referred in this document as pile-up. The detector records responses from multiple collisions happening in the same bunch crossing ("in-time pile-up"), but also from signal remnants from previous bunch crossings ("out-of-time pile-up"). Several methods exist for measuring μ or $\mu/\sigma_{\mathrm{inel}}$ and for distinguishing the detector response from in-time collisions

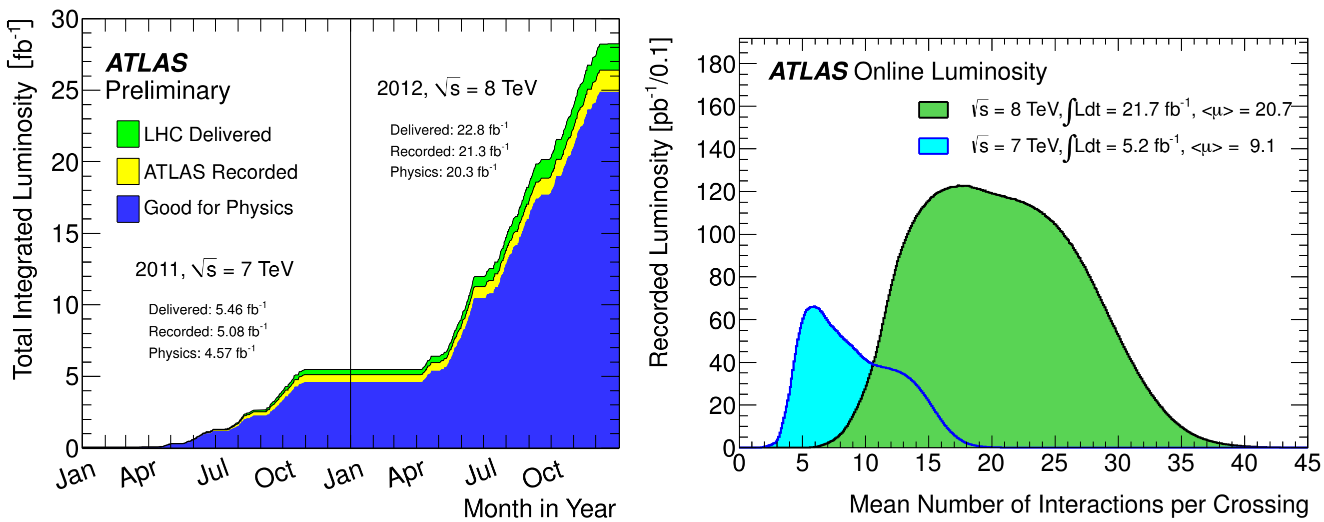

Figure 2.13: On the left, the cumulative luminosity versus time delivered to (green), recorded by ATLAS (yellow), and certified to be good quality data (blue) during stable beams and for pp collisions at 7 and 8 TeV centre-of-mass energy in 2011 and 2012, is shown. The delivered luminosity accounts for the luminosity delivered from the start of stable beams until the LHC requests ATLAS to put the detector in a safe standby mode to allow a beam dump or beam studies. The recorded luminosity reflects the DAQ inefficiency, as well as the inefficiency when the stable beam flag is raised, but the tracking detectors undergo a ramp of the high-voltage and, for the pixel system, turning on the preamplifiers, so-called *warm-start*. The data quality assessment shown corresponds to the "All Good" efficiency shown in Tab. 2.2. The luminosity shown represents the 7 TeV and 8 TeV luminosity calibration. [72]. On the right, the the luminosity-weighted distribution of the mean number of interactions per crossing (μ) for the 2011 and 2012 data is shown. This shows the full 2011 and 2012 *pp* runs [73].

and out-of-time responses. Referenced documentation [73] can provide the reader with more details on the detector components used for this purpose.

A less precise determination of μ can by achieved by using tracking information, of which an example is shown in Fig. 2.14. This method was used as an indicator of the tracking performance when compared to dedicated measurements of μ.

Recorded data are scrutinised by collaborators and a quality assessment is made. Only the portion of data passing stringent quality requirements, which are associated to DAQ and subsystem performance, are flagged as "good" for further analysis. Table 2.2 shows the portion of good data recored by the experiment with respect to the total integrated luminosity delivered by the LHC.

The next two sections are dedicated to an overview of the operations and performance of the SCT subsystem.

2.7.1 SCT operational experience

More than 99% of the 6.3 million strips were functional and available for tracking in all data taking periods. Constant work of shifters and experts during data taking and technical stop periods was crucial in maintaining this high efficiency [60]. The SCT crew consisted of a shifter present any time in the ATLAS Control Room with a turn over of 8 hours and a pool of experts being on call

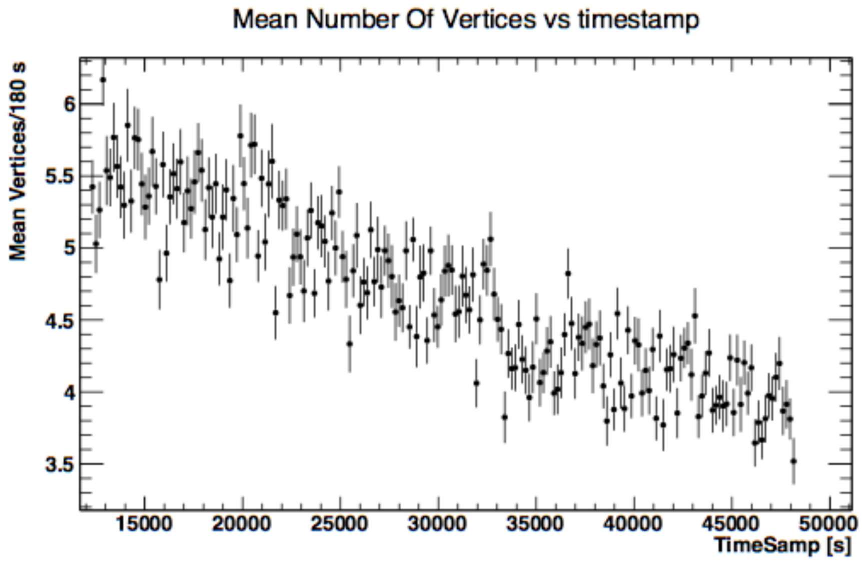

Figure 2.14: Measurement of μ versus the event time stamp during an ATLAS run. The number of in-time collisions was determined by reconstructing, the primary collision vertices. The measurement was performed on-line, *i.e.* progressively as events were recorded, from the "express" *stream*. This quantity was used for on-line data quality monitoring.

	Sub system								
Year	PIXEL	SCT	TRT	LAr	Tile	MDT	RPC	CSC	TGC
2011	99.8	99.6	99.2	98.7	99.2	99.4	98.8	99.4	99.1
2012	99.9	99.1	99.8	99.1	99.6	99.6	99.8	100.0	99.6

Table 2.2: Fraction of good quality data delivered by the subsystems during data tanking periods in *pp* collisions for 2011 and 2012 ($\sqrt{s}$ = 7 TeV and $\sqrt{s}$ = 8 TeV respectively). Runs taken between March 13th and October 30th 2011 correspond to $\int L_{\mathrm{Lumi}}dt$ = 5.23 fb^{-1} [74]. Runs recorded between April 4th and December 6th 2012 correspond to $\int L_{\mathrm{Lumi}}dt$ = 21.3 fb^{-1} [75]. Numbers are shown in percent.

in weekly blocks.

The semiconductor tracker (SCT) DAQ has proved to be highly reliable with excellent data taking efficiency. There are two potential sources of inefficiency: (i) errors from the front-end ASICs, for which data were flagged as "non-usable" for tracking purposes,(ii) and a BUSY signal from the SCT Readout Drivers (RODs) preventing ATLAS from taking data. The operation issues that impacted on data taking efficiency and data quality were as follows, listed in order from the most to the least significant:

1. **High occupancy and high rates.** In 2012 the SCT operated with a pile-up of up to ~ 30 interactions per bunch crossing and an occupancy reaching $\sim 1\%$. The high occupancy and rate exposed shortcomings in the DAQ processing and decoding of the data which lead to an increasing rate of BUSYs. Although this was the most significant issue impacting on data taking efficiency, it was mitigated by introducing the ability to disable the source of the busy ROD, reconfigure the

affected modules, and then to re-integrate the ROD without interruption to ATLAS data taking.

2. **High leakage current.** A (small) number of the SCT modules were assembled using sensors from a different vendor (CiS) compared to the majority (Hamamatsu) [76]. A small but significant fraction of those sensors exhibited high leakage currents at high luminosities, correlated with high noise levels. It is suspected that intense radiation may ionise nitrogen gas surrounding the silicon and the corresponding accumulated charge on the oxide may be responsible for the increase in current. Between data taking periods, the bias was decreased to 5 V with respect to the nominal value of 50 V and the high noise and currents were eventually mitigated by reducing the potential difference down from the nominal 150 V but keeping it above the depletion voltage of the sensors (typically > 90 V).

3. **Humidity affecting optical transmitters.** The optical transmitters (TXs) used by the RODs to broadcast the commands and triggers to the front-end modules have been problematic in all data taking so far. Individual channel deaths within the 12-channel Vertical-Cavity Surface-Emitting Laser array (VCSEL) lead to a loss of data from modules, until the TX was replaced or repaired. Early failures were due to the ingress of humidity to the VCSELs, which were addressed by introducing dry air to the racks. Humidity-resistant VCSEL arrays were installed afterwards.

4. **Single event upsets.** Single Event Upsets (SEUs) can corrupt front-end chip registers, leading to high or low noise from that chip, or to desynchronisation of the chips with the rest of ATLAS. In 2011, an automatic reconfiguration of individual modules was implemented and invoked when a desynchronisation was detected. In addition and in order to target noise-invoked SEU issues, a global reconfiguration of all modules, with negligible dead-time, was invoked every 30 minutes. With these measures, the fraction of the ~ 8000 data links giving errors was typically at $\sim 0.2\%$.

The increase of ROD BUSYs, as discussed in item 1, and the significant increase of leakage current of a portion of the modules at high luminosity, as discussed in item 2, were dominant in 2012 while items 3 and 4 dominated up to 2011.

2.8 Data quality and performance

2.8.1 SCT data quality and performance

Data Quality needs to be optimised during operations. The SCT has its own monitoring tool developed as an analysis software algorithm that can be run both online and offline.

- **Online**: by running the full track reconstruction it ensures tracking and DAQ quality is within the accepted range. It also allows for rapid investigation of problems during data taking.
- **Offline**: the monitoring tools ensure that, after every run, only the portion of data that satisfy strict quality criteria are selected.

This quality assessment is done by monitoring track quantities including track parameters, number of reconstructed vertices, number of tracks associated to reconstructed vertices and hit-map distributions and track. Strict quality cuts are applied based on that information and data are precluded from analysis in luminosity blocks corresponding to periods of 2 minutes of data taking on average. Each defect in tracking has a correspondence with a detector defect assigned when a portion of modules are unable to deliver reliable data. A detector defect is set if 0.1% of the modules are unable to deliver good quality data based on error and noise rates.

The intrinsic hit efficiency is among the tracking parameters constantly monitored:

$$\varepsilon = \frac{N_{\text{hits}}}{N_{\text{hits}} + N_{\text{holes}}} \tag{2.3}$$

where N_{hits} is the number of hits on any given track (with transverse momentum higher than 1 GeV) and N_{holes} is the number of holes on each track. A hole on a track is defined as an intersection of the track trajectory with an active detector element where no hit is found recorded [67]. The intrinsic hit efficiency for 2012 is shown in Fig. 2.15. For an average hit efficiency lower than 99.5% in a region, either barrel or end-cap, data are not cleared for analysis. As expected, a small decrease in the hit efficiency was observed in 2012 with respect to early data taking. The higher track multiplicity, due to the increase of the average number of collisions per bunch crossing increases the probability of tracks sharing hits thus reducing the efficiency artificially. In nominal data taking the SCT hit efficiency was above 99.7%.

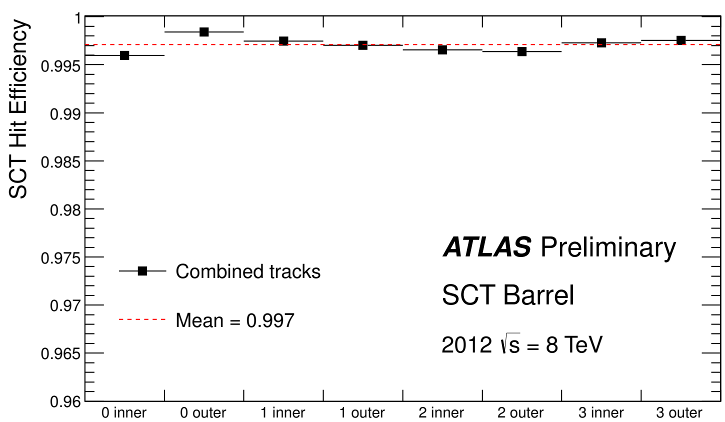

Figure 2.15: Intrinsic SCT hit efficiency from combined tracking for each side (inner or outer) of each barrel layer from a typical run (206573) in 2012 with $\sqrt{s} = 8$ TeV [77]. Each track is required to have at least 7 silicon hits.

The noise occupancy (NO), which is defined as the probability to record a hit only due to noise, is also a closely measured quantity both online and offline by the monitoring tool in empty bunches. Throughout all data taking, the SCT noise occupancy remained significantly lower than the design specification of NO $< 5 \times 10^{-4}$.

A low data rejection was achieved as shown in Tab. 2.2. A slight decrease of the total data cleared for analysis is observed in 2012 with respect to 2011 due to the increase of issues, discussed in the above section, being related to the rise of the delivered luminosity by the LHC . Throughout all data taking periods the SCT collected and cleared a portion greater than 99% of the data delivered by the LHC .

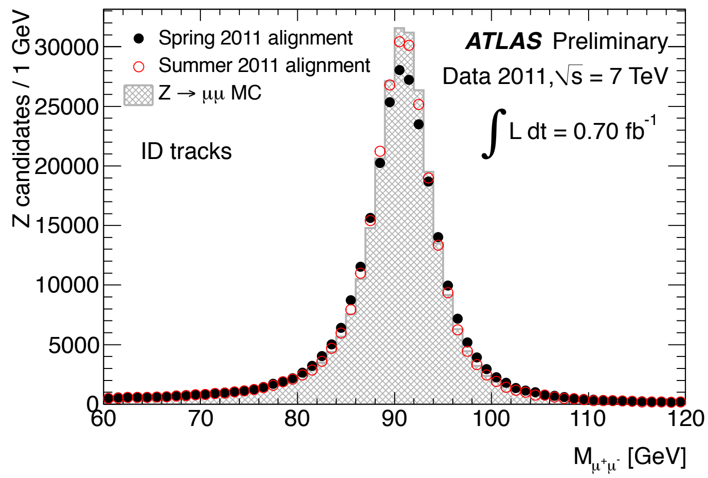

Figure 2.16: Invariant mass distribution of $Z \to \mu\mu$ decays [78], where the mass is reconstructed using track parameters from the Inner Detector. Ideal alignment performance based on simulations is compared to observed performance of data processed with spring 2011 alignment and data processed with updated alignment constants.

Alignment is performed with cosmic and collision data by minimising the χ^2 of track hit residuals. For collision data, tracks with $p_{\mathrm{T}} > 15$ GeV are selected from a jet trigger in order to minimise multiple scattering effects. Particularly for high momentum tracks, where multiple scattering plays a less prominent role, remaining misalignment effects can be assessed by looking at hit residual distributions from the reconstructed invariant mass of well-known resonances (for example Z-boson decays). Excellent agreement was found in the residual distributions for both barrel and End Cap [79]. The resolution in the $Z \to \mu^+\mu^-$ invariant mass distribution from tracks reconstructed with the full Inner Detector, which is shown in Fig. 2.16, is very close to the expectation from simulation.

2.8.2 Irradiation damage in the strip detector

Irradiation of silicon sensors results in damage in the silicon bulk and the dielectric layers, with main effects being the increase in leakage current of the sensor, the change in the effective doping concentration and a change in the inter-strip capacitance. A measurement of the leakage current during off beam periods was made, and then, under the assumption that all high voltage currents originate from the current in the silicon bulk, the measurements were normalised to $T_{\mathrm{ref}} = 0°\mathrm{C}$ (common factor for all LHC experiments).

The measured current was found to be in agreement [81] with the Hamburg/Dortmund model simulated using FLUKA and including self annealing effects based on the different measured sensor temperatures. A conversion of the integrated luminosity for both $\sqrt{s} = 7$ TeV and $\sqrt{s} = 8$ TeV to 1 MeV neutron equivalent fluence to each barrel layer was made from simulations on minimum bias events of protons colliding at $\sqrt{s} = 7$ TeV. The increase in the leakage current, shown in Fig. 2.17, was observed to be correlated with the increase in luminosity as expected and excellent agreement between data and predictions is observed over the three years of operations. This indicates that the observed HV currents are mostly due to bulk generation current and also that the leakage

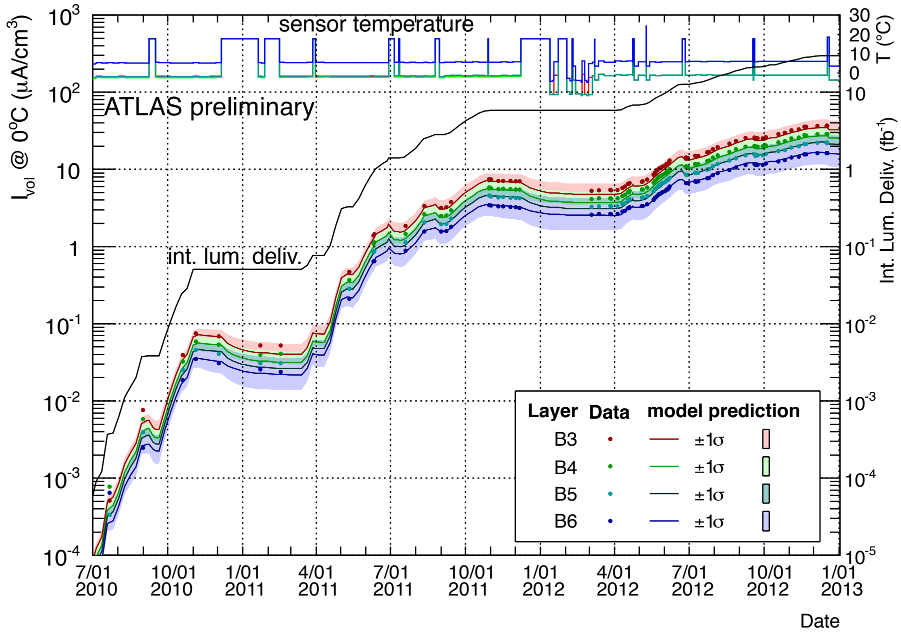

Figure 2.17: Measured leakage current for four SCT barrel layers [80]. The predicted leakage currents by the Hamburg /Dortmund model [81] are shown (solid lines) while the associated bands show the 1 σ statistical and systematic uncertainty. On the top of the plot the measured sensor temperatures are shown.

current modelling incorporating self-annealing effects are well applicable. Although a significant increase in leakage current is observed, the change in depletion voltage so far is negligible and the SCT remains far from type inversion.

CHAPTER 3

Physics objects definition

Proton–proton collisions produce final states containing large amounts of collimated sprays of particles, as well as leptons and photons. The interaction of these particles with the detector produce energy deposits in the wide range of ATLAS subsystems. Hits in tracking chambers and energy deposits in calorimeters are the starting point for complex algorithms that build unified sets of objects corresponding to the underlying properties of the measured particles. This chapter explains how the responses from several subsystems are reconstructed into sets of physics objects.

The reconstructed objects often have a complex definition, however the precision with which they correlate to the underlying physics quantities must be determined. This is achieved with complex simulation programs, embedded with extremely detailed detector description. These programs have to give an accurate and complete description of all the processes involved in proton-proton collisions. The interaction with matter is simulated with the `GEANT4` [82] program.

Moreover, the bulk of *pp* collision-data delivered by the Large Hadron Collider (LHC) are dominated by low energy interactions of quantum chromodynamics, which are of no interest to a $t\bar{t}\gamma$ cross section measurement. Therefore, stringent selection requirements must be imposed to the collected data, in order to decrease the contribution from background processes.

At first, in Sec. 3.1, the data considered in the measurement of the $t\bar{t}\gamma$ cross section are described. Then, Sec. 3.2 and Sec. 3.3, explain how events from $t\bar{t}\gamma$ and $t\bar{t}$ production are simulated. Section 3.4 describes the simulation of processes other than $t\bar{t}$ production.

Section 3.5 explains and defines what are the reconstructed quantities, in use by this measurement. The selection criteria upon them and their comparison with simulations is detailed from this point onwards. Finally Sec. 3.8 defines the observable quantities used to discriminate between prompt-like objects (electrons or photons) and hadrons.

3.1 Dataset

The analysis presented in this thesis is based on the full ATLAS dataset collected during the year 2011. Only the portion of good data, expressed in terms of integrated luminosity $\mathcal{L} = dataset \int L_{\mathrm{Lumi}} dt$, so-called *lumi-blocks*, taken with good data quality conditions as defined by the Top Working Group [83][1]are taken into account in the selection requirements. The selected *lumi-blocks* correspond to an integrated luminosity of $\mathcal{L} = 4.59 \pm 0.08$ fb^{-1}.

Up to 17 interactions per bunch crossing were recorded with a typical mean value lying between 8 and 9. Table 3.1 shows the run range for each portion of data considered (Period), the luminosity and the single lepton triggers used.

This analysis uses centrally-produced derived `ROOT`-formatted [84] and ordered in ensembles of data (n-tuples). The n-tuples are produced using the `ATHENA` reconstruction framework [85] used by ATLAS. Data are divided into exclusive sets (streams) based on the trigger information used. `Electron` and `Muon` streams, triggered, respectively, by deposits in the Electromagnetic Calorimeter and in the Muon Spectrometer are used for the selection of signal candidate events. The `JetTauEtMiss` stream, containing events triggered by deposits in the Hadronic Calorimeter, is used for the derivation of background processes.

Period	**Run range**	$\mathcal{L}$ [pb^{-1}]	**Electron trigger**	**Muon trigger**
B-D	177986 - 180481	176.2	`EF_e20_medium`	`EF_mu18`
E - H	180614 - 184169	937.7	`EF_e20_medium`	`EF_mu18`
I	185353 - 186493	333.2	`EF_e20_medium`	`EF_mu18`
J	186516 - 186755	223.5	`EF_e20_medium`	`EF_mu18_medium`
K	186873 - 187815	583.3	`EF_e22_medium`	`EF_mu18_medium`
L - M	188902 - 191933	2 401.8	`EF_e22vh_medium1` or `EF_e45_medium1`	`EF_mu18_medium`

Table 3.1: Data sample used in this analysis. Data is split into Periods ranging from B to M. The associate run-range, based on an unique run identifier, is shown under the column Run range. The right-hand-most columns indicate the trigger, see Sec. 2.6, used for the electron and muon channels. The label `EF` indicates that the trigger selection is applied at the Event Filter (EF) level while the the label `eXX` (`muXX`) indicates the minimum E_{T} (p_{T}) requirement (in GeV) for the trigger to fire. The labels `v` and `h` indicate a variable threshold and the request of isolation requirements. The label `medium` represents the identification criterion that is applied at EF level [86].

3.2 Simulation of $t\bar{t}\gamma$ production

Events of top and anti-top quark pair-production ($t\bar{t}$) with an associated photon are simulated from proton-proton collisions at $\sqrt{s} = 7$ TeV. The $t\bar{t}$ state is allowed to decay in the single-lepton channel ($\ell\nu_\ell q\bar{q}' b\bar{b}\gamma$) as well as in the dilepton channel ($\ell\nu_\ell\ell'\nu_{\ell'} b\bar{b}\gamma$)[2]. The signal simulation is performed using two independent Leading-Order (LO) Matrix-Element (ME) Monte Carlo (MC) generators: `WHIZARD v1.93` [87, 88], and `MadGraph v5.1.5.12` [89]. Both MC generators use the CTEQ6L1 Parton Density Function (PDF) [29] and include full interference effects between radiative top quark production and and radiation off top quark decay products, see Sec. 1.1.2.

[1]The TopReconstruction Group is responsible for defining the portion of good data to be used top-related physics analyses. In particular a "Good Run List (GRL)" is defined and used.

[2]Here and here only $\ell = (e, \mu, \tau)$.

Even-though the measurement is performed in the single -electron or -muon channel only, the simulation of events in the dilepton channel or in the single-τ channel is necessary for the correct definition of the phase-space in which the measurement is performed. Experimentally, events from the dilepton channel and from the single-τ channel can leak into the measured phase-space.

The choice of two independent ME generators is motivated by the study of the systematic uncertainties associated to the extracted cross section. Details upon how different simulation settings enter in the systematic uncertainty evaluation are given in Sec. 7.1.

In order to compare simulation-to-data candidate estimates, the computations from both programs are normalised according to the Next-to-Leading-Order (NLO) theoretical prediction, as detailed in Sec. 1.4.

3.2.1 The `WHIZARD` generator

The `WHIZARD` [87] MC generator was developed for automated calculations of ME at LO. For any given initial and any final state, the simulation program calculates the full ME. All contributing diagrams are taken into account using the Optimised Matrix Element Generator `O'Mega` [88]. The `O'Mega` algorithm is an optimised ME generator designed to compute helicity amplitudes by direct numerical evaluation in the most efficient way suited for the evaluation of cross section with massive particles. After collecting all common subexpressions in the sum over Feynman diagrams contributing to a given scattering amplitude at tree level, `O'Mega` constructs a symbolic representation of the factored scattering amplitude, resulting in an exponential, instead of a factorial, growth of matrix element complexity with the number of external particles.

Phase-space

The `WHIZARD` phase-space is defined as follows:

- The minimum transverse momentum of any outgoing parton x is set to $p_{\mathrm{T}}(x) > 10$ GeV.
- The minimum transverse energy for the photon is set to $E_{\mathrm{T}}(\gamma) > 8$ GeV. Fig. 3.1 shows respectively the photon E_{T} and η distributions at the generator level (before detector simulation).
- The invariant mass (m) between the photon and any quark (lepton) from the W-boson decay is required to be $m(\gamma, q) > 5$ GeV ($m(\gamma, \ell) > 5$ GeV), see Fig. 3.2.
- Low p_{T} and collinear divergencies are mitigated by cuts imposed between the quarks from the hadronically decaying W-boson (q_1, q_2) and the incoming gluons (g_1, g_2) of the process $g_1 g_2 \to t\bar{t}\gamma$. These cuts are: $m(q_1, q_2) > 5$ GeV, $m(g_1, q_1) > 5$ GeV, $m(g_1, q_2) > 5$ GeV, $m(g_2, q_1) > 5$ GeV, and $m(g_2, q_2) > 5$ GeV. Also, the invariant mass between any incoming gluon and the photon is required to be higher than 5 GeV.
- Similarly, for any incoming quark (Q_i, Q_j) of the process $Q_i\bar{Q}_j \to t\bar{t}\gamma$ it is required $m(Q_i, Q_j) >$ 5 GeV, for any $i, j =$ (u-, d-, c-, s- and b-quark). Also, the invariant mass between any incoming quark and the photon is required to be higher than 5 GeV.

The renormalisation scale is set to $2m_t$, and the factorisation scale is set to the partonic center-of-mass energy $\sqrt{\hat{s}}$, the values for the particle masses used are summarised in Tab. 3.2

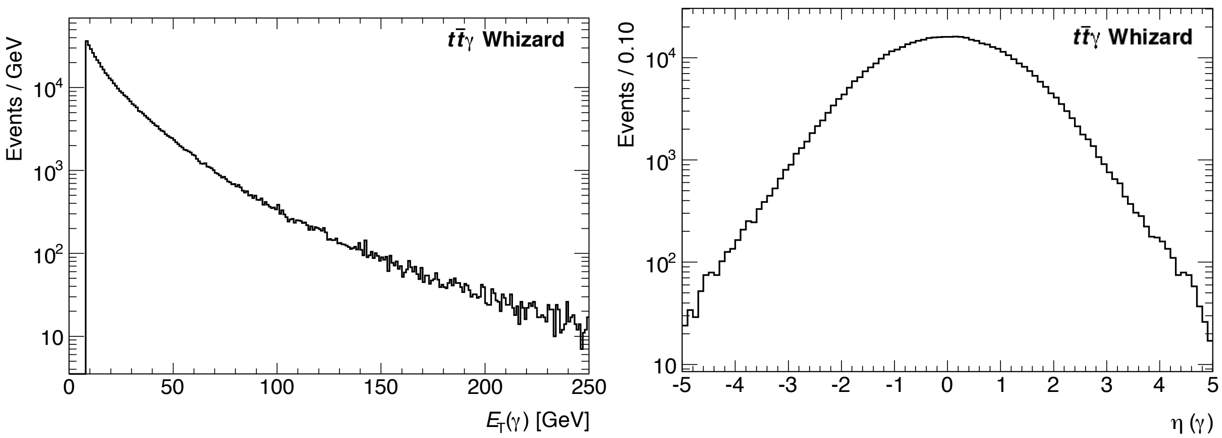

Figure 3.1: Left: photon E_{T} spectrum of the `WHIZARD` $t\bar{t}\gamma$ sample (generator level, before detector simulation) in logarithmic scale in the range [0 ; 250] GeV. Right: photon η distribution of the $t\bar{t}\gamma$ sample (generator level, before detector simulation) [86].

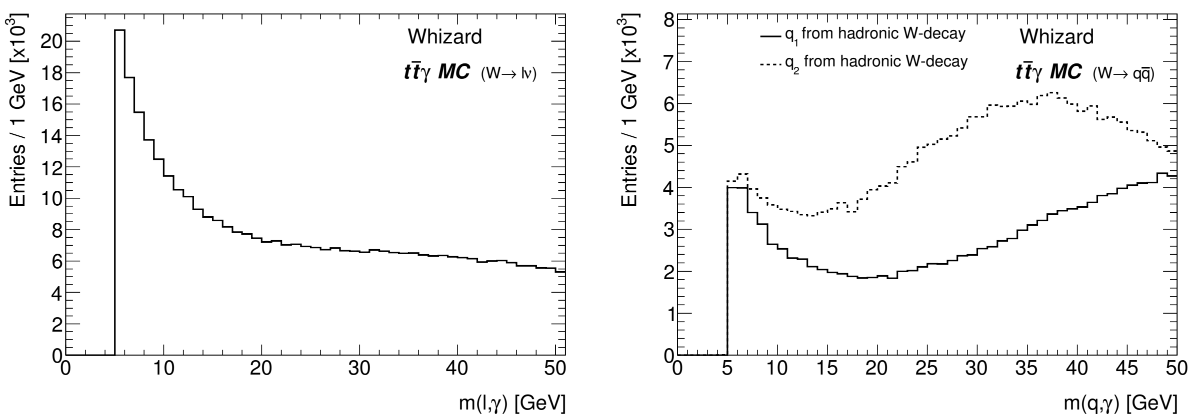

Figure 3.2: Invariant-mass distributions (generator level, before detector simulation) of the photon and charged lepton from the leptonic W-decay (left) and of the photon and both quarks from the hadronic W-decay (right). In the latter case, q_1 is the leading-quark from the W-decay [86].

Particle	Quarks			Leptons		
	light-quarks (u, d, c, s)	t-quark	b-quark	e	μ	τ
Mass [GeV]	0	172.5	4.2	0	0.105	1.776

Table 3.2: Particle masses definitions used in `WHIZARD` and `MadGraph` [86].

Figure 3.2 shows the invariant mass distributions between the photon and the decay products of the W-boson. In the case of the hadronically decaying W-boson, q_1 is the leading quark. Figure 3.3 shows the invariant mass distributions between the incoming quark (except $b/\bar{b}$) and the photon and between the incoming gluon and the quarks from the hadronic W-boson decay. Fig. 3.4 (top-left) shows the p_{T} distributions of the outgoing partons (other than the photon) produced in the ME. Figure 3.4 (top-right) shows the $\Delta R = \sqrt{(\Delta\varphi)^2 + (\Delta\eta)^2}$ distributions for the photon and

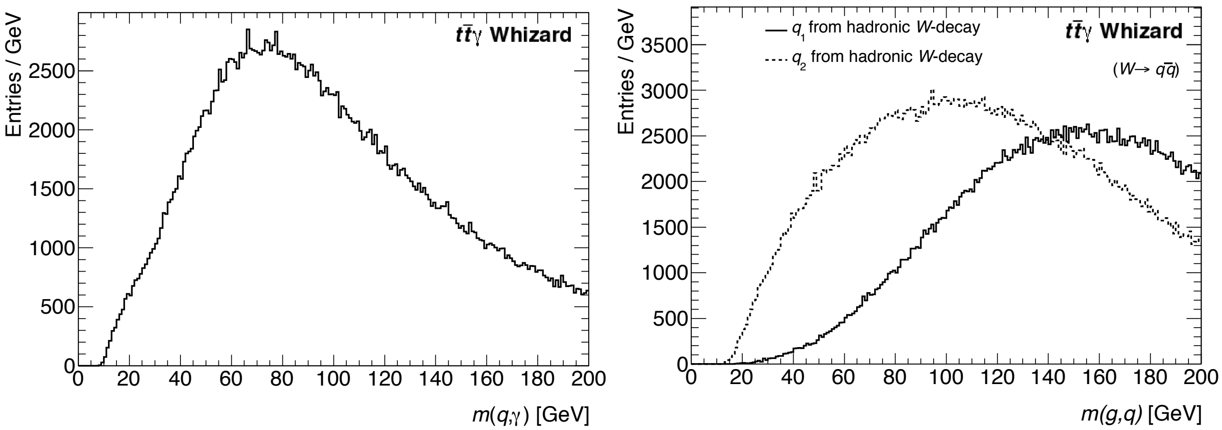

Figure 3.3: Invariant-mass distributions (generator level, before detector simulation) of the incoming quark (except $b/\bar{b}$) and the photon (left) and of each incoming gluon and each quark from the hadronically decaying W-boson decay (right). In the latter case, q_1 is the leading-quark from the W-decay [86].

the charged lepton from the leptonic-W and for the photon and the quarks from the hadronic-W. Effectively, the invariant mass cuts translate into a ΔR cut between the corresponding objects. Figure 3.4 (bottom) shows the invariant mass $m(l,\nu)$ of the decay product of the leptonic-W, and that of the three-body system $m(l,\nu,\gamma)$ for those events in which $m(l,\nu) < 70$ GeV. The reduction of the low mass tail after the inclusion of the photon in the invariant mass calculation $m(l,\nu,\gamma)$ clearly indicates the presence of a prompt-photon produced in the $t\bar{t}\gamma$ ME process after $(W \to l\nu \to l\gamma\nu)$ or during $(W \to l\nu\gamma)$ the leptonic W-decay.

`HERWIG` [90] and `JIMMY` [91] are used for the parton showering and underlying event simulation. Additional photon radiation in the fragmentation process is simulated with `PHOTOS` [92]. The cross section is, when summing over all three lepton flavours, 648 fb for the single-lepton (e, μ, τ) and 188 fb for the dilepton $t\bar{t}\gamma$ final states.

3.2.2 The `MadGraph` generator

The `MadGraph` program automatically generates the amplitudes for all the subprocess of $pp \to \ell\nu_\ell q\bar{q}' b\bar{b}\gamma$ and $pp \to \ell\nu_\ell \ell'\nu_{\ell'} b\bar{b}\gamma$. `MadGraph` uses the single-diagram-enhanced [89] method which, after the amplitude generation, creates the appropriate mapping between subprocesses for the integration over the phase-space. Any process dependent information is passed to a standalone code, so-called `MadEvent`, which allows the cross section calculation. Particle masses used by this program are described in Tab. 3.2. The renormalisation and factorisation scales are set to m_t. ME events were interfaced to two different Parton Shower (PS) programs (`HERWIG` and `PYTHIA`) and featured also varying QED radiation settings, as it will be explained in Sec. 7.1.

Phase-space

The phase-space used by the `MadGraph` generator is defined below:

- The minimum transverse momentum for any parton x but the b-quark is required to be $p_{\mathrm{T}}(x) > 15$ GeV.

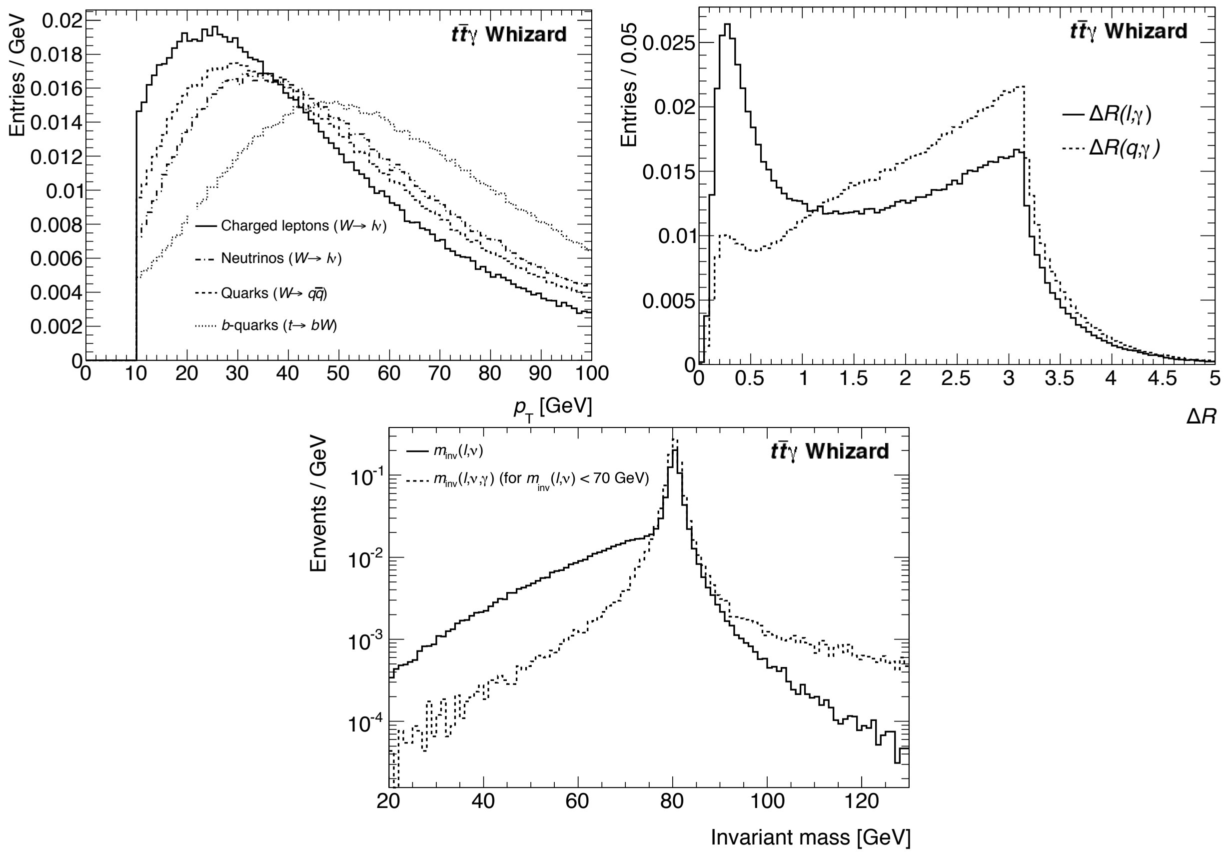

Figure 3.4: Top-left: p_T spectrum (generator level, before detector simulation) of the charged leptons and neutrinos from the leptonic W-decay, quarks from the hadronic W-decay and b-quarks from the top-quark decay in $t\bar{t}\gamma$ sample (top-left). Top-right: ΔR distributions between the charged lepton (from the leptonic-W) and the photon, and between the quarks (from the hadronic-W) and the photon (top-right). Bottom: invariant mass distributions $m(l,\nu)$ of the decay products of the leptonic-W and that of the three-body system $m(l,\nu,\gamma)$ for those events in which $m(l,\nu) < 70$ GeV (bottom). All distributions are normalised to unity [86].

- The minimum transverse momentum for any lepton ($\ell = e, \mu, \tau$) is required to be $p_T(\ell) > 15$ GeV.
- The minimum transverse momentum for the photon is required to be $p_T(\gamma) > 15$ GeV.
- Leptons and photons are required to have $|\eta| < 2.8$.
- Any quark, but the b-quark is required to have $|\eta| < 5.0$.
- In order to avoid collinear and infra-red divergencies a minimum angular separation is required between any set of outgoing particle i, j, $\Delta R(i,j) > 0.2$.

The cross section is 445 fb when summing over all three lepton flavours for the single-lepton and 131 fb for the dilepton $t\bar{t}\gamma$ final states.

3.2.3 On MadGraph and WHIZARD phase-spaces

The reader may have noticed that the phase-space defined by the WHIZARD generator mitigates collinear and low energy divergencies with invariant mass cuts between particles, while, the MadGraph generator uses angular cuts between particles. The two types of cuts are correlated, therefore equivalent, as:

$$\Delta R(i,j) > \text{arcos}\left(1 - \frac{m^2(i,j)}{2E_iE_j}\right) \tag{3.1}$$

where m is the invariant mass per particle pair i, j and E is energy for any particle. Nevertheless, the two phase-spaces are not identical and the volume defined by angular cuts is larger than the one defined by invariant mass cuts. This is of no problem as long as the detector acceptance (A) is smaller than both volumes *i.e.* $A \subseteq A_{\texttt{WHIZARD}} \subseteq A_{\texttt{MadGraph}}$. As the WHIZARD phase-space features a more stringent definition, this could be easily mitigated by imposing the WHIZARD cuts on the data selection. However, this is not a suitable solution for the following two reasons.

At first, imposing generator-dependent cuts on the data will define a cross section completely model-dependent, and moreover, the result will be extrapolated to a region where no measurement is defined. On the other hand, the invariant mass cuts featured by WHIZARD are on non-detectable particles, *i.e.* quarks and gluons, and therefore they are, by definition, impossible to apply on data.

The solution is, again, two-fold. As the result described in this document is reported within the detector phase-space (so-called fiducial measurement), the definition of the MC phase-space does not affect directly the result. In this case, an ill-defined generator acceptance will mostly drive the error on the measurement, and these effects will show up in the efficiency calculations as event migrations to, and from, the detector defined phase-space.

On the other hand, it is of great interest to ensure that the cross section uncertainty will not dependent greatly of this potential mis-modelling. Therefore, an estimation of the size of the discrepancy of the two generator acceptances is needed. Because MadGraph utilises angular cuts between particles, defining a phase-space larger than the detector's acceptance (see Sec. 3.5), the relation $A \subseteq A_{\texttt{MadGraph}}$ holds by construction. Therefore, it is only necessary to measure the differences between the two simulation programs.

The method used for the determination is briefly described in the following. The kinematic spectra in p_{T}, η and φ of particles generated by either simulation program are used to build four-vector binned probabilities (templates). The spectra are determined before detector simulation, in order to be independent of detector smearing and resolution effects. The particle's kinematic properties are determined by extrapolating the information from the templates outside the ranges defined by both generator cuts. The extrapolation uses ensemble tests based on random numbers (pseudo-experiments). The shape of the four-vector templates is mainly driven by the steeply falling momentum spectrum of the particle under consideration, as φ distributions are flat and the η coverage is large at generator level. An approximation could be made at this point. The p_{T} spectrum can be approximated by a Poisson distribution, of which the slope parameter would be intrinsic to each MC generator. However, a full numerical approximation was chosen instead, which includes bin-by-bin migrations. Up to 10^5 pseudo-experiments were thrown in order to minimise the statistical uncertainty.

Out-of the newly-generated four-vectors, two-dimensional histograms between $\Delta R(i,j)$ and the $m(i,j)$ of any pair of particles (i,j) show the relation between the two type of cuts for each phase-space definition. Figure 3.5 shows the results obtained using the WHIZARD generator as input, while Fig. 3.6 shows the results obtained using the MadGraph generator as input. It can be

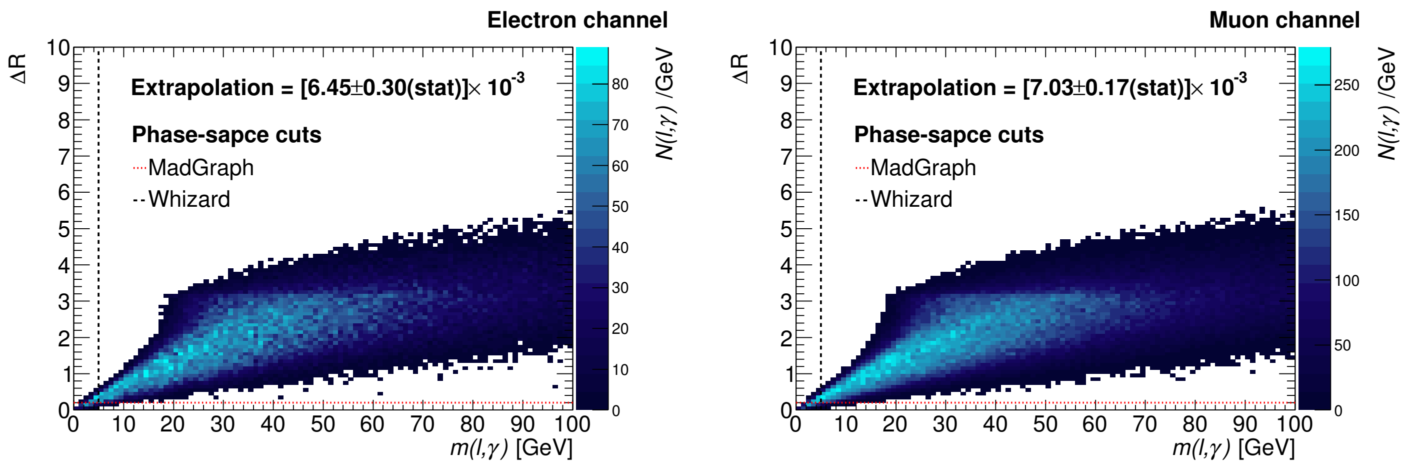

Figure 3.5: Relation between ΔR and invariant mass (m) between the lepton and the photon, as obtained from pseudo experiments, for the `WHIZARD` generator. The plot on the left shows results for electrons and on the right for muons. The dashed line indicates the generator level ΔR cut between the lepton and the photon, while the dotted line indicates the generator level invariant mass cut between the lepton and the photon.

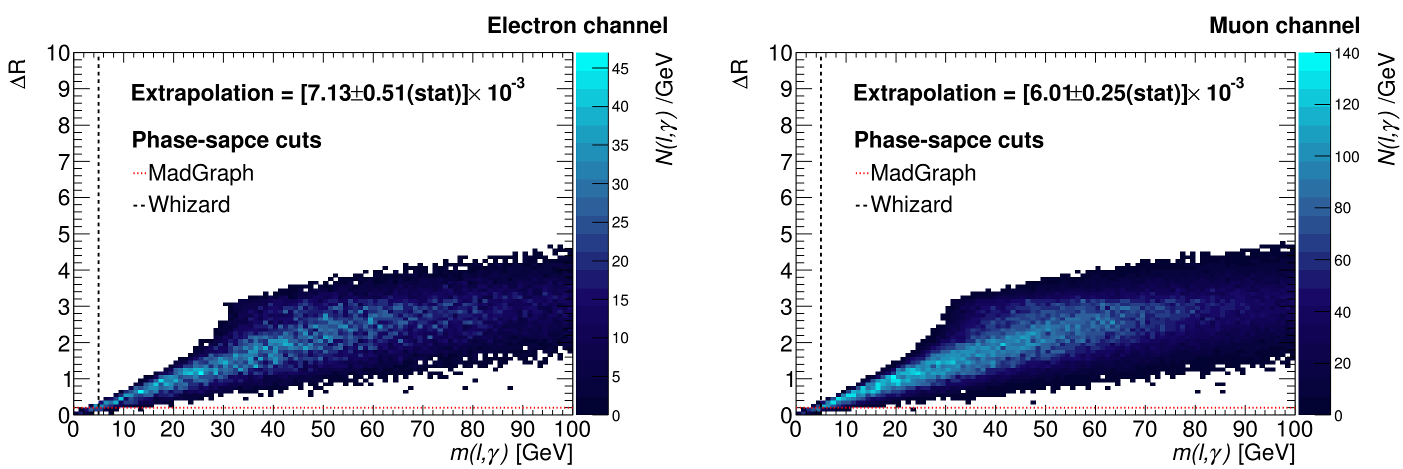

Figure 3.6: Relation between ΔR and invariant mass (m) between the lepton and the photon, as obtained from pseudo experiments, for the `MadGraph` generator. The plot on the left shows results for electrons and on the right for muons. The dashed line indicates the generator level ΔR cut between the lepton and the photon, while the dotted line indicates the generator level invariant mass cut between the lepton and the photon. This result is meant as a "closure" test of the method and numbers are in agreement with the results of Fig. 3.5.

seen that the relationship between angles and invariant mass is mainly linear but the spread of the distributions differs for the two simulation programs. The percentage of non-generated phase-space (labeled "Extrapolation" in Fig. 3.5) of `WHIZARD` is the fraction of events with $\Delta R(i,j) < 0.1$ and $m(i,j) < 5$ GeV to the total. The extrapolation fractions obtained form `MadGraph` were used as a cross-check for the method. The resulting extrapolation is lower than 1%, detailed results are shown in Tab. 3.3.

Generator input	**Electron channel**	**Muon channel**
`WHIZARD`	$(0.65 \pm 0.03)\%$	$(0.70 \pm 0.02)\%$
`MadGraph`	$(0.71 \pm 0.05)\%$	$(0.60 \pm 0.03)\%$

Table 3.3: Extrapolation factors as determined from pseudo experiments using inputs for `WHIZARD` and `MadGraph`. Numbers are split between the electron channel and the muon channel. Uncertainties are statistical only. For a given generator, no differences are expected between channels as the cross section is the same. Numbers extracted from `MadGraph` are meant as a "closure" test of the method.

In conclusion, the effect of the phase-space difference between the two generators is small when measuring a cross section within detector acceptance. The 1% extrapolation is included as systematic uncertainty on event migrations from, and to, the measured phase-space, as it is discussed in Sec. 7.1.

3.3 Simulation of $t\bar{t}$ pair production

Inclusive $t\bar{t}$ pair production, without a specific requirement for a photon in the final state, is simulated using the `MC@NLO` [93] ME simulation program which interfaced to `HERWIG` for the PS simulation. This sample used the CTEQ6.6 [94] PDF set. QED radiation off charged particles is handled by the `PHOTOS` simulation program. The phase-spaces of `WHIZARD` (or `MadGraph`) and of `MC@NLO` generators may overlap, therefore, a possible double-counting of final states is possible. This is avoided by removing *post*-generation overlapping events from either simulation program. This affects only simulation-to-data comparisons and not the cross section measurement. The latter being performed in a fiducial region and the background estimation being deduced from data any residual MC dependence is thus avoided.

Additional $t\bar{t}$ samples have been generated using different MC event generators with various settings in order to evaluate systematic uncertainties associated with the signal modelling. See Sec. 7.1 for the different settings used for each program.

3.4 Simulation of processes other than $t\bar{t}$ production

Non-$t\bar{t}$ processes, with final states identical to that of $t\bar{t}\gamma$ production, have to be also simulated. They are referred here as background processes. In fact, they are processes which constitute a background to a $t\bar{t}$ cross section measurement, but featuring in addition at least a final-state photon. The simulated samples include the W and Z pair-production ($WW/ZZ/WZ$ so-called dibosons), the production of W and Z (referred hereafter as $W+$jets and $Z+$jets respectively) and the residual Electroweak (EW) top quark production (so-called "single top").

$W+$jets and $Z+$jets production are simulated with the `ALPGEN` [95] and `SHERPA` [96] event generators, both interfaced to `HERWIG` with CTEQ6L1 PDF set for the former and CT10 PDF set [97] for the latter. The simulation of $W+$jets ($Z+$jets) production, includes processes with

$W(Z)+b\bar{b}$, $W(Z)+c$, and $W(Z)+c\bar{c}$[3]. Diboson samples were generated with `HERWIG`. The single top quark production is simulated with `MC@NLO` (s-channel) and `ACERMC` (t-channel).

3.5 Physics object definition

3.5.1 Jets

Quarks and gluons hadronise producing bound states of quarks in form of baryons and mesons. These appear in the detector as collimated sprays of particles called jets (j). Jets are reconstructed from clustered energy deposits in the calorimeters. Individual clusters are combined form physics objects with characteristics correlated to the parton that originated the spray. The way of combining the energy-deposits into these physics objects defines what a jet is. In ATLAS calorimeter cells are grouped into sets of topologically connected clusters (topo-clusters) [99,100]. Topo-clusters are combined into jet-objects based on the p_{T} with a sequential clustering algorithm. In particular, starting from any energy deposit, clusters in close proximity to each other are merged into the jet object if the distance $d_{i,j}$ from the i-th and j-th jet satisfies the equation

$$d_{i,j} \leq \min(p_{\mathrm{T}}(j)^k, p_{\mathrm{T}}(i)^k)\frac{\Delta R(i,j)^2}{R^2}, \tag{3.2}$$

with[4] $k = -2$ and $R = 0.4$. This is the so-called anti-k_{T} jet algorithm [103]. The anti-k_{T} ensures collinear and infrared safety from divergencies and jets are typically symmetrical in η and φ coordinates.

The energy calibration is performed initially at the Electromagnetic (EM) scale. The energy loss in non-active regions of the calorimeters, due to their non-compensating aspect, is taken into account with a correction on the energy profile and longitudinal shower-depth. This correction is determined from simulations by measuring the response of single particles and by varying the longitudinal and transverse material budget. The minimum transverse momentum requirement is $p_{\mathrm{T}}(j) > 25$ GeV. From the combination of reconstructed tracks, calorimeter jets and primary vertices (PV) a discriminant variable, referred to as the jet-vertex fraction (JVF), is defined. The JVF is the jet's constituent transverse track-momentum contributing to each PV. It is formally defined as:

$$P_{\mathrm{JVF}}(\mathrm{PV}) = \sum_{\mathrm{i=1}}^{\mathrm{N_{matched}}} \frac{\mathrm{p_T^i(track,PV)}}{\mathrm{p_T(j)}} \tag{3.3}$$

where N_{matched} is the number of matched tracks to a given PV. The JVF is a measurement of the probability of any jet to be matched to a PV. A jet selection based on this discriminant is shown to be insensitive to the contributions from simultaneous uncorrelated soft collisions that occur during pile-up [104]. A selection requirement of $|P_{\mathrm{JVF}}(\mathrm{PV})| > 0.75$ is imposed upon the jet definition. The acceptance in pseudorapidity (η) is $|\eta| < 2.5$.

3.5.2 Electrons

Electron (e) candidates are defined as energy deposits in the Electromagnetic Calorimeter (ECAL) with an associated, well measured track in the Inner Detector (ID). Clusters are combined using a

[3]Jets with same flavour can induce an overlap between those samples [98]. A dedicated tool, so-called Heavy Flavor Overlap Removal (HFOR), was used to remove the overlap.

[4]The value of k defines other sequential clustering jet algorithm, for example $k = 0$ is used for the Cambridge-Aachen algorithm [101], mainly used for highly boosted objects, and $k = 2$ for the k_{T} algorithm [102].

sliding-window algorithm [105] using deposits in the $\eta-\varphi$ plane (towers) of size $\Delta\eta\times\Delta\varphi = 0.025\times 0.025$. Three-by-five-sized towers form a window which is varied across the $\eta-\varphi$ plane. Clusters are seeded from energy deposits in the towers higher than 5 GeV. An energy-loss correction, due to the material ahead of the calorimeter, is applied. This correction is determined based on simulations and test-beam measurements with varied material budged in front of the ECAL [106].

All electron candidates are required to have transverse energy $E_{\mathrm{T}}(e) > 25$ GeV and $|\eta_{cl}| < 2.47$, excluding the calorimeter crack-region $1.37 < |\eta_{cl}| < 1.52$, where η_{cl} is the pseudorapidity of the associated EM cluster.

Electrons are required to be isolated with respect to near-by hadronic activity. Both track-based and calorimeter-based isolation criteria are used. In particular $E_{\mathrm{T}}^{20}(e) < 4$ GeV and $p_{\mathrm{T}}^{30}(e) < 2.5$ GeV are required. The calorimeter-isolation $E_{\mathrm{T}}^{20}(e)$ is defined as the sum of transverse energy deposits in calorimeter cells within a cone of $R = 0.2$ around the electron energy-cluster. The track-based-isolation p_{T}^{30} is defined as the sum of all transverse momenta of $p_{\mathrm{T}} > 1$ GeV of tracks within a cone of $R = 0.3$ with respect to the electron, minus the electron track momentum.

3.5.3 Muons

Muon objects (μ) are reconstructed from tracks independently determined from the Muon Specrometer and the ID [107, 108]. The independent track segments are combined to a single track using ΔR matching criteria. The combination of ID hits and Muon Spectrometer (MS) hits are re-used as inputs to the track-fitting algorithm, which determines the combined-track parameters. Standalone tracks in either sub-systems are therefore discarded.

Muons are required to have $p_{\mathrm{T}}(\mu) > 20$ GeV and $|\eta(\mu)| < 2.5$. The longitudinal impact parameter of the track is demanded to be < 2 mm. Holes on track, see Eq. 2.3, are required to be zero and at least six silicon hits are required.

Isolation requirements reduce the reconstruction of near-by hadronic activity. In particular, $E_{\mathrm{T}}^{20}(\mu) < 4$ GeV and $p_{\mathrm{T}}^{30}(\mu) < 2.5$ GeV are required. The calorimeter-isolation $E_{\mathrm{T}}^{20}(\mu)$ is defined as the sum of transverse energy deposits in calorimeter cells within a cone of $R = 0.2$ around the muon track. The track-based-isolation $p_{\mathrm{T}}^{30}(\mu)$ is defined as the sum of all transverse momenta of $p_{\mathrm{T}} > 1$ GeV of tracks within a cone of $R = 0.3$ with respect to the muon, minus the muon track momentum. Furthermore, muon candidates within $R = 0.4$ with respect to pre-selected and calibrated jets are rejected. These isolation requirements are used to suppress the backgrounds originating from heavy-flavoured hadron decays [109].

3.5.4 Photons and photon identification

Photons (γ) are reconstructed with the same method as done for electrons. Energy deposits in the ECAL are clustered using the sliding-window algorithm. Photons are required to have a minimum transverse energy of $E_{\mathrm{T}}(\gamma) > 20$ GeV. All photon candidates are required to have $|\eta_{\mathrm{cl}}| < 2.37$, excluding the calorimeter crack-region [5]. For both electrons and photons, corrections to the energy scale in data and to the energy resolution in MC (energy smearing) are applied.

The photon identification is based on a set of rectangular cuts on the shower-shape of calorimeter variables. The selection cuts do not depend on the photon transverse energy but vary as a function of η to account for variations associated with the total thickness of material in front of

[5] In addition a so-called “photon cleaning” is performed. Liquid Argon (LAr) cells with noise bursts and dead-regions are discarded. A timing cut is imposed, in order to reject out-of-time pile-up candidates.

the EM calorimeter. Two sets of cuts, *loose* and *tight*, are defined [110]. In addition to tighter cuts on the *loose* shower-shape variables, the *tight* menu adds additional discriminating variables and it is optimised for unconverted and converted photon candidates separately. The different discriminant variables used in the photon identification are detailed below, while the cut values used in the *tight* menu are given in table 3.4.

		Range in pseudorapidity						
Variable	**Cut**	[0,0.6[	[0.6,0.8[	[0.8,1.15[	[1.15,1.37[	[1.52,1.81[	[1.81,2.01[	[2.01,2.37]
Unconverted photon candidates								
R_{had}	max	0.009	0.007	0.006	0.008	0.019	0.015	0.014
R_η	min	0.951	0.940	0.942	0.946	0.932	0.928	0.924
R_φ	min	0.954	0.95	0.59	0.82	0.93	0.947	0.935
w_{η_2}	max	0.011	0.011	0.011	0.011	0.011	0.011	0.013
$w_{s_{\text{tot}}}$	max	2.95	4.4	3.26	3.4	3.8	2.4	1.64
w_{s_3}	max	0.66	0.69	0.697	0.81	0.73	0.651	0.610
F_{side}	max	0.284	0.36	0.36	0.514	0.67	0.211	0.181
ΔE	max	92	92	99	111	92	110	148
E_{ratio}	max	0.63	0.84	0.823	0.887	0.88	0.71	0.78
Converted photon candidates								
R_{had}	max	0.008	0.007	0.005	0.008	0.015	0.016	0.011
R_η	min	0.941	0.927	0.930	0.931	0.918	0.924	0.913
R_φ	min	0.4	0.426	0.493	0.437	0.535	0.479	0.692
w_{η_2}	max	0.012	0.011	0.013	0.013	0.014	0.012	0.013
$w_{s_{\text{tot}}}$	max	2.8	2.95	2.89	3.14	3.7	2.0	1.48
w_{s_3}	max	0.697	0.709	0.749	0.78	0.773	0.672	0.644
F_{side}	max	0.32	0.428	0.483	0.51	0.508	0.252	0.215
ΔE	max	200	200	122	86	123	80	132
E_{ratio}	max	0.908	0.911	0.808	0.803	0.67	0.915	0.962

Table 3.4: *Tight* identification cuts for unconverted and converted photon candidates [110]. Upper and lower cuts are referred as “max” and “min” respectively. ΔE is given in MeV. See text for a description of the different variables.

Hadronic leakage variable

The hadronic leakage (R_{had}) is the total transverse energy deposited in the hadronic calorimeter normalised to the total transverse energy of the photon candidate. In the pseudorapidity range $0.8 < |\eta(\gamma)| < 1.37$ the energy deposited in the whole hadronic calorimeter is used, while for $|\eta(\gamma)| < 0.8$ and $|\eta(\gamma)| > 1.37$ only the leakage in the first layer of the hadronic calorimeter is used.

EM second (middle) layer variables

- $R_\eta(\gamma)$ (**middle η energy ratio**): ratio in $\eta(\gamma)$ of cell energies in a 3×7 rectangle in $\eta \times \varphi$ (measured in cell units) versus the sum of energies in a 7×7 rectangle, centred around the cluster seed, see Fig. 3.7.

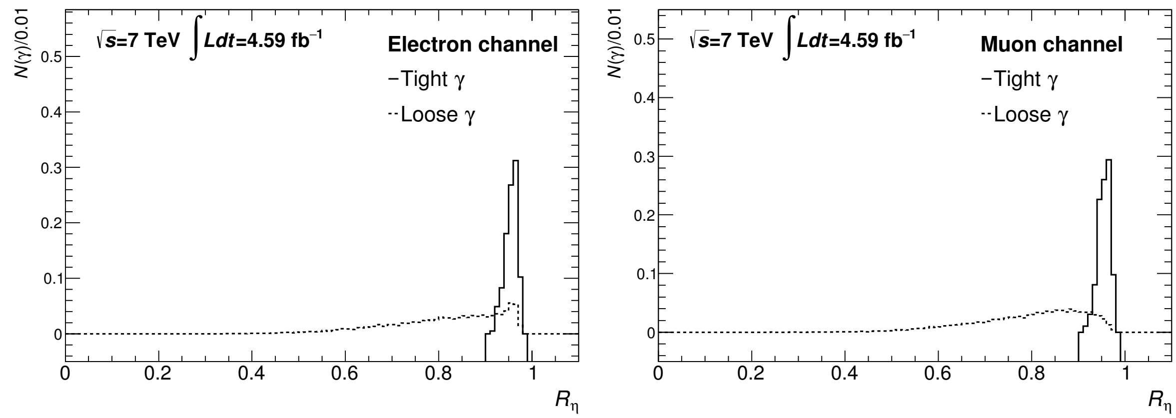

Figure 3.7: The $R_\eta(\gamma)$ distribution comparisons for *tight* photons (continuous line) with respect to *loose* photons (dotted line). The distributions are obtained from data and are normalised to their area. The left (right) plot shows distribution for the electron channel (muon) channel.

- $R_\varphi(\gamma)$ (**middle** φ **energy ratio**): ratio in φ of cell energies in a 3×3 rectangle in $\eta \times \varphi$ (measured in cell units) versus the sum of energies in a 3×7 rectangle, centred around the cluster seed, see Fig. 3.8.

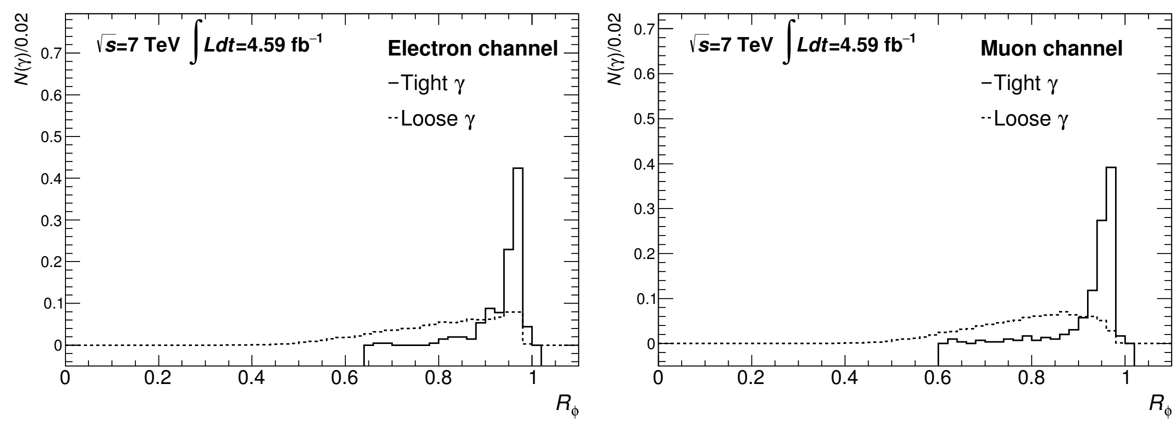

Figure 3.8: The $R_\varphi(\gamma)$ distribution comparisons for *tight* photons (continuous line) with respect to *loose* photons (dotted line).The distributions are obtained from data and are normalised to their area. The left (right) plot shows distribution for the electron channel (muon) channel.

- $w_{\eta_2}(\gamma)$ (**middle lateral width**): lateral width of the shower in the second layer of the EM calorimeter, using cells in a window $\eta \times \varphi = 3 \times 5$ (measured in cell units), see Fig. 3.9.

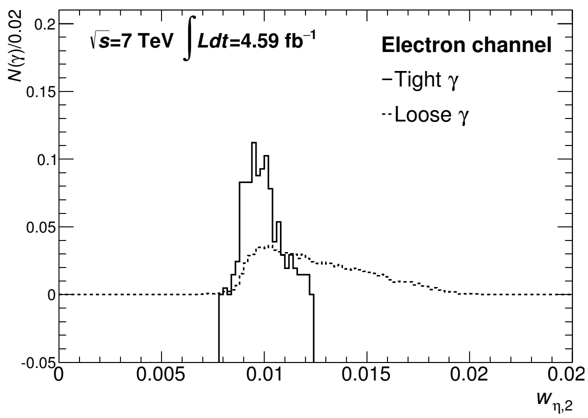

Figure 3.9: The $w_{\eta_2}(\gamma)$ distribution comparisons for *tight* photons (continuous line) with respect to *loose* photons (dotted line).The distributions are obtained from data and are normalised to their area. The left (right) plot shows distribution for the electron channel (muon) channel.

EM first (strip) layer variables

- $w_{s_{\rm tot}}(\gamma)$ (**total lateral width**): shower width in η in the first layer of the EM calorimeter using cells in a window $\Delta\eta \times \Delta\varphi = 0.0625 \times 0.2$ (corresponding approximately to 20×2 strip cells in $\eta \times \varphi$), see Fig. 3.10.

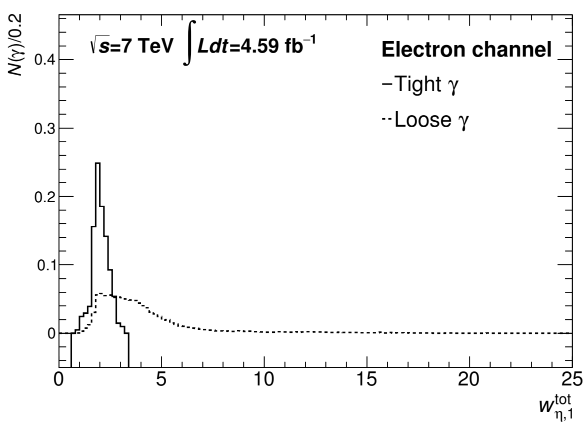

Figure 3.10: The $w_{s_{\rm tot}}(\gamma)$ distribution comparisons for *tight* photons (continuous line) with respect to *loose* photons (dotted line).The distributions are obtained from data and are normalised to their area. The left (right) plot shows distribution for the electron channel (muon) channel.

- $w_{s_3}(\gamma)$ (**front lateral width**): shower width in η in the first layer of the EM calorimeter using three strip cells around the maximal energy deposit, see Fig. 3.11.

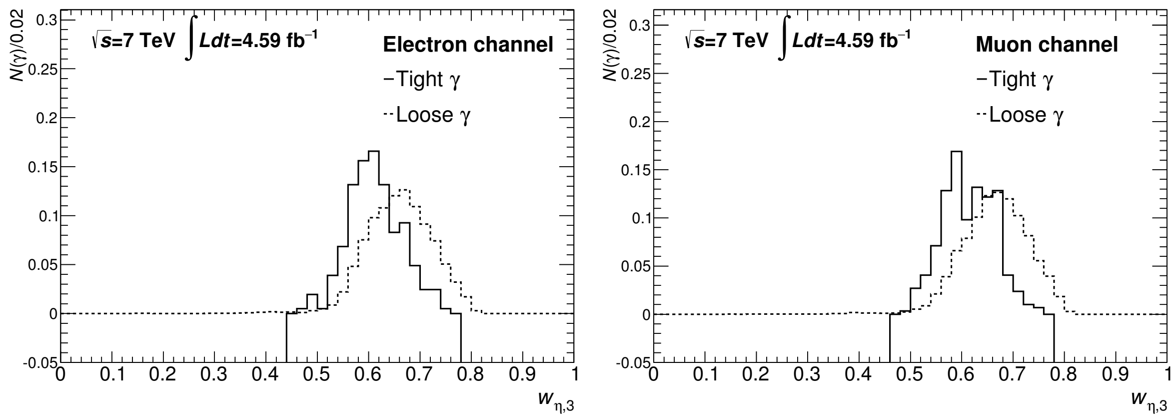

Figure 3.11: The w_{s_3} distribution comparisons for *tight* photons (continuous line) with respect to *loose* photons (dotted line).The distributions are obtained from data and are normalised to their area. The left (right) plot shows distribution for the electron channel (muon) channel.

- $F_{\mathrm{side}}(\gamma)$ (**front side energy ratio**): lateral containment of the shower along η. It is measured as the fraction of energy outside a core of three central strips but within seven strips, see Fig. 3.12.

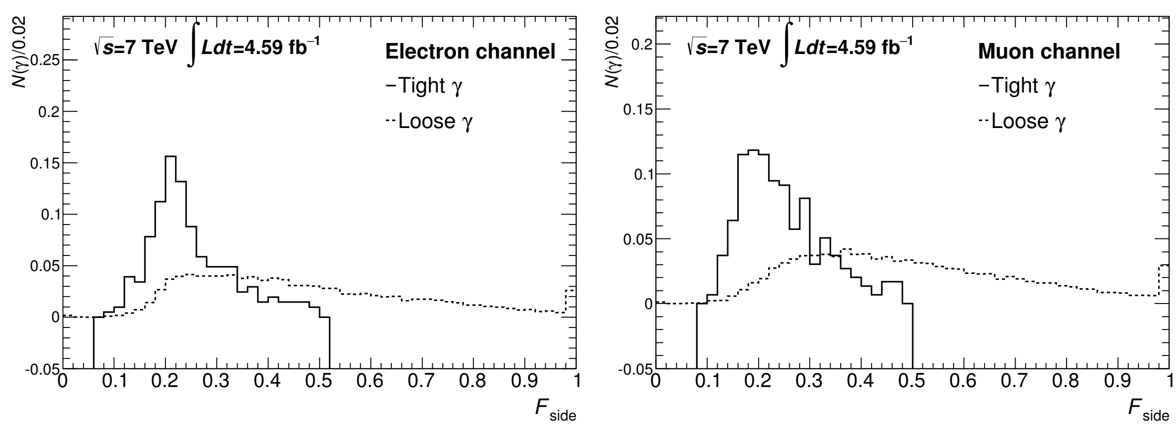

Figure 3.12: The F_{side} distribution comparisons for *tight* photons (continuous line) with respect to *loose* photons (dotted line).The distributions are obtained from data and are normalised to their area. The left (right) plot shows distribution for the electron channel (muon) channel.

- $\Delta E(\gamma)$ (**front second maximum difference**): difference between the energy associated with the second maximum in the strip layer, and the energy reconstructed in the strip with the minimal value found between the first and second maxima ($\Delta E = 1$ when there is no second maximum).

- $E_{\mathrm{ratio}}(\gamma)$ (**front maxima relative ratio**): ratio of the energy difference associated with the largest and second largest strip cell energy deposits over the sum of these energies ($E_{\mathrm{ratio}} = 1$ when there is no second maximum).

Appendix A contains plots illustrating the discrimination power of the shower shapes on data for converted and unconverted photons separately.

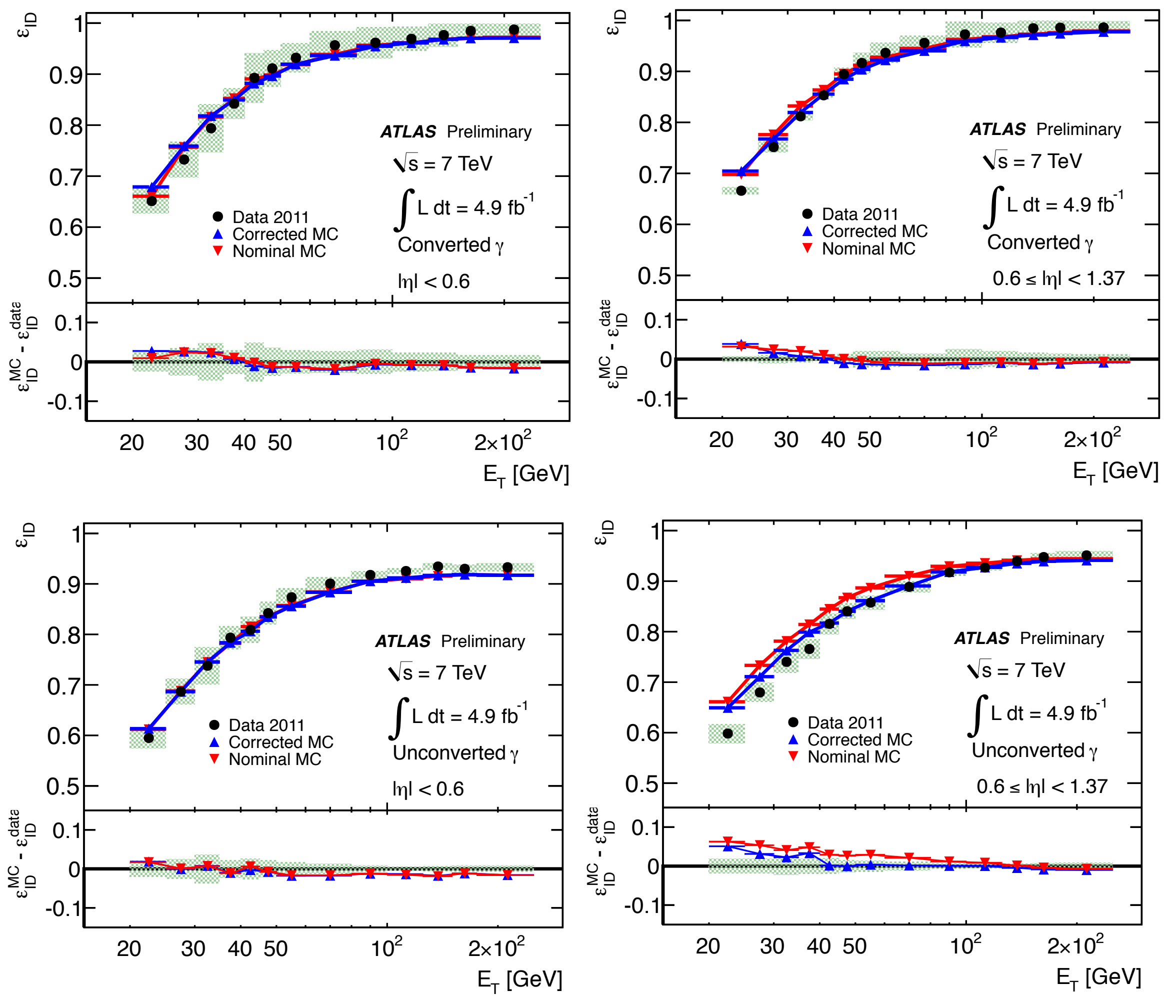

Figure 3.13: Photon identification efficiencies for 20 GeV $< E_{\mathrm{T}}(\gamma) <$ 300 GeV for two different η regions ($|\eta| < 0.6$ on the left and $0.6 < |\eta|1.37$ on the right).The plots on top (bottom) show the efficiency for converted (unconverted) photon candidates.The band corresponds to the stat$\oplus$sys uncertainty. For each figure the bottom plot shows the differences between data and simulations [111].

The minimum photon $E_{\mathrm{T}}(\gamma)$ value of 20 GeV is motivated by the validity of the so-called Fudge-Factors (FF), shifting factors used to correct for the discrepancies observed between the 2011 data and simulations in the photon discriminating variables. These shifting factors are obtained from the comparison of the means of the distributions of the shower shapes for simulations and data respectively. This method has been cross-checked with the minimisation of a χ^2 between data and simulations. These corrections do not account for shape differences in the shower-shapes distributions between simulations and data, see Fig. 3.13. Moreover, the are assumed to be the same for photons and hadrons. However, the data-to-simulation comparisons shows an increased agreement after the correction [111, 112].

3.5.5 Missing energy

Neutral weekly-interacting particles (here only neutrinos are considered) escape detection. An inference on the neutrino's kinematic properties can be deduced from the total momentum in the transverse plane [113]. The momenta sum in the transverse plane is imbalanced by the missing measurement of particles escaping detection. Calorimeter and MS information is used and the missing transverse momentum ($\boldsymbol{E}_{\mathrm{T}}^{\mathrm{miss}}$) is defined as the vectorial sum of all *missing* energies from reconstructed and calibrated physics objects (o_i) projected in the transverse plane

$$\boldsymbol{E}_{\mathrm{T}}^{\mathrm{miss}} = \sum_i \boldsymbol{E}_{\mathrm{T}}^{\mathrm{miss}}(o_i) \tag{3.4}$$

in the range $|\eta| < 4.9$. Calorimeter cells containing energy deposits due to noise and not associated with high-p_{T} objects are also included. Each term $\boldsymbol{E}_{\mathrm{T}}^{\mathrm{miss}}(o_i)$ is determined by the energy (and momentum) difference of reconstructed and calibrated objects with respect the energy deposits in calorimeter cells in the transverse plane [114]. The missing transverse momentum magnitude ($E_{\mathrm{T}}^{\mathrm{miss}}$) is defined as:

$$E_{\mathrm{T}}^{\mathrm{miss}} = \sqrt{(\boldsymbol{E}_{\mathrm{T,x}}^{\mathrm{miss}})^2 + (\boldsymbol{E}_{\mathrm{T,y}}^{\mathrm{miss}})^2} \tag{3.5}$$

where x, y denote the unit vectors defining the transverse plane.

3.6 Event selection criteria

In this section the event selection criteria are reviewed. The final state of the $t\bar{t}\gamma$ process in the single lepton channel is characterised by a high-p_{T} lepton (electron or muon), missing transverse momentum, jets with one or more b-jets and a photon. The lepton and missing transverse momentum are originated from the leptonic decay of the W-boson, the b-jets from the top-quarks decay, the other jets from the hadronic decay of the W-boson and additional jets, and the photon from the radiative emission in either the $t\bar{t}$ production or decay processes.

Events with data integrity errors in the ECAL calorimeter, and events in a time-window around around identified noise bursts, are rejected. The description of the selection criteria imposed follows. Cuts are listed in the order they are applied to data and to simulations.

- Events are separated into electron channel and muon channel, based upon the trigger fired.
- Events are required to contain a reconstructed primary vertex with at least five associated tracks.
- Reconstructed objects are ordered in sets using the definitions detailed in Sec. 3.5. Overlapping definitions are avoided applying the following criteria. The jet closest to an electron candidate is rejected if $\Delta R(e, j) < 0.2$ [109]. In addition, any jet within a cone $\Delta R = 0.1$ with respect to the reconstructed photon is also discarded to avoid double-counting photons being also reconstructed as jets.
- The event must contain at least one electron (muon) with $E_{\mathrm{T}}(e) > 25$ GeV ($p_{\mathrm{T}}(\mu) > 20$ GeV) matched to the appropriate trigger depending on the run period (see table 3.1). Electrons and muons are defined as explained in Sec. 3.5.2 and Sec. 3.5.3, respectively. They are labelled from here on as "good" leptons ($\ell = e, \mu$).

- The event is rejected if any other good lepton is reconstructed.

- In the electron channel a minimum $E_{\mathrm{T}}^{\mathrm{miss}} > 30$ GeV cut is imposed, while in muon channel events are required to have $E_{\mathrm{T}}^{\mathrm{miss}} > 20$ GeV [114].

- A W-transverse mass $m_{\mathrm{T}}(W) = \sqrt{2p_{\mathrm{T}}(\ell) \times E_{\mathrm{T}}^{\mathrm{miss}}(1 - \cos\varphi')} > 35$ GeV, where φ' is the azimuthal angle between the lepton direction and the missing transverse momentum, is required in the electron channel. In the muon channel the requirement is $E_{\mathrm{T}}^{\mathrm{miss}} + m_{\mathrm{T}}(W) > 60$ GeV.

- In both channels, at least four good jets with $p_{\mathrm{T}}(j) > 25$ GeV and $|P_{\mathrm{JVF}}| > 0.75$ are required.

- In order to reduce the acceptance of W+jets production, at least one jet should be originating from a b-quark. A jet is associated to a b-quark (b-tagged) using an algorithm as described briefly in the following.

  Due to its larger lifetieme the b quark decays at a distance from the primary vertex. This produces a displaced vertex which can be reconstructed and identified. The algorithms use as inputs the coordinates of the displaced vertex and the impact parameter of the track associated to the jet with respect to the primary vertex. Systematic biases are reduced by imposing weights on the secondary vertex reconstruction and on the impact parameter determination deduced from the fit. Typically, a jet originated from a b-quark will have a large impact parameter with positive sign. The sign is determined with respect to the jet track direction.

  The b-tagging algorithm used in this analysis is the *MV1* at a 70% b-jet identification efficiency working point [115, 116]. This algorithm relies on a neural network association of jet flavours and it uses inputs from other algorithms used by the Collaboration[6]. The output confidence level on each jet flavour is expressed in form of a weight for each jet. The *MV1* working point corresponds to a cut on the output weight greater than $\simeq 0.60$.

- Events are required to contain at least one good photon, *i.e.* fulfilling the *tight* identification menu, with $E_{\mathrm{T}}(\gamma) > 20$ GeV and $|\eta(\gamma)| < 2.37$.

- Events in which at least one jet is found within a cone of $R = 0.5$ around the photon direction are discarded.

- In the electron channel, the invariant mass of the electron and photon candidates is required to be outside a 5 GeV window around the Z-mass in order to suppress Z + jets events with one electron misidentified as a photon.

- In order to reduce photon radiation off leptons a $\Delta R(\gamma, \ell) > 0.7$ requirement is imposed.

The final selection yields a total of 140 and 222 events in the electron and muon channel respectively. Distributions in data for the N_{jets}, $E_{\mathrm{T}}^{\mathrm{miss}}$, the lepton (photon) E_{T} (p_{T}), and the photon η and φ under the full event selection criteria are in excellent agreement when compared to simulations, see Fig. 3.14 and Fig. 3.15. Additional data-to-simulation comparisons can be found in App. B.

[6] These are the IP3D, SV1 and JetFitterCombNN algorithms [117].

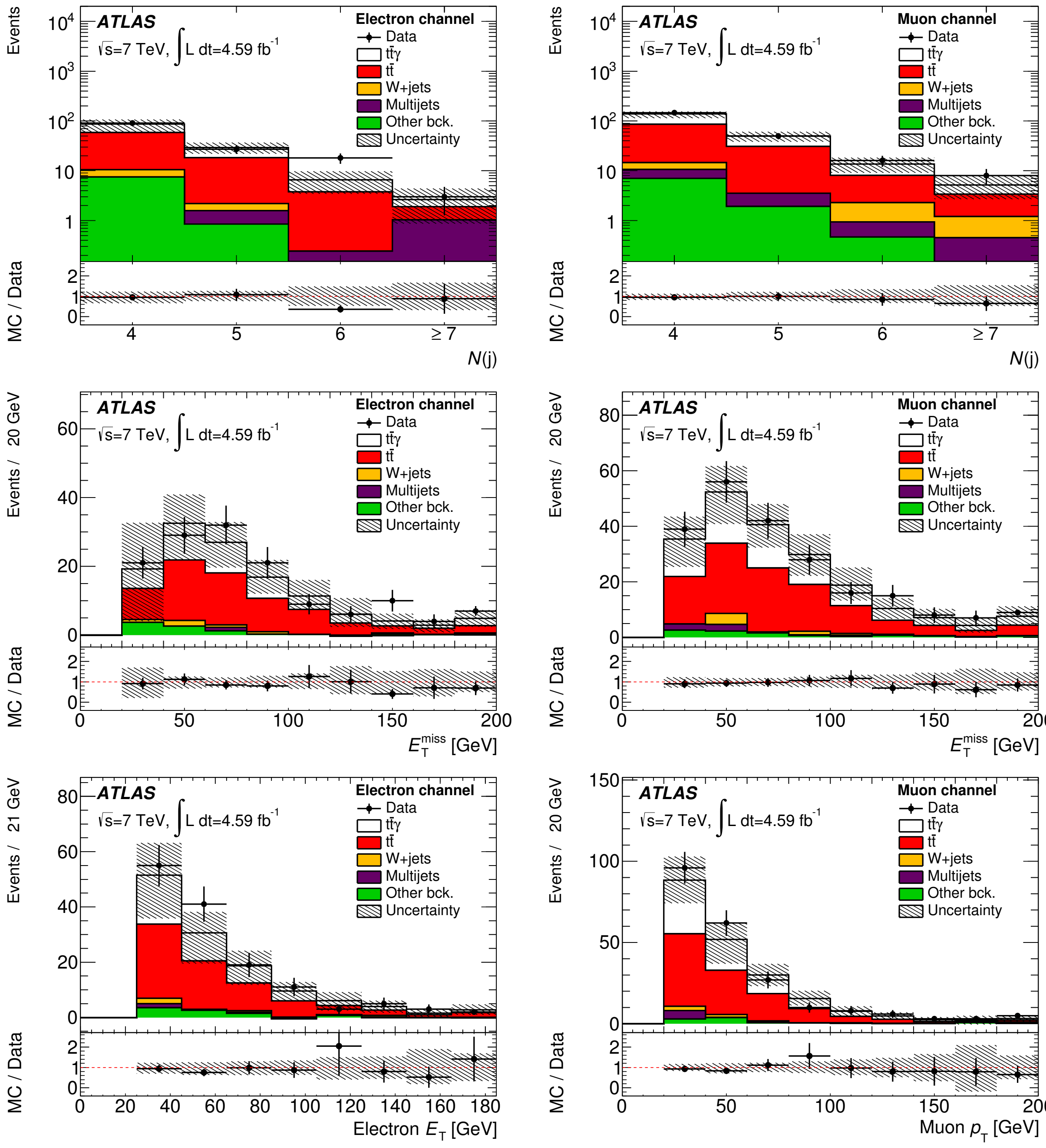

Figure 3.14: Distributions for the jet multiplicity (N_{jets}), the missing transverse energy ($E_{\mathrm{T}}^{\mathrm{miss}}$), the electron energy in the traverse plane ($E_{\mathrm{T}}(e)$) and the muon transverse momentum ($p_{\mathrm{T}}(\mu)$). Data (points) are compared to the expectation from simulations after full event selection. Distributions are shown separately for the electron (left) and muon (right) channels. The band labelled "Uncertainty" includes both, simulation based, statistical and systematic uncertainties (see Chap. 7). The entry "Other bck" includes the contributions from $Z+$jets, single top and dibosons. The last bin contains any overflow.

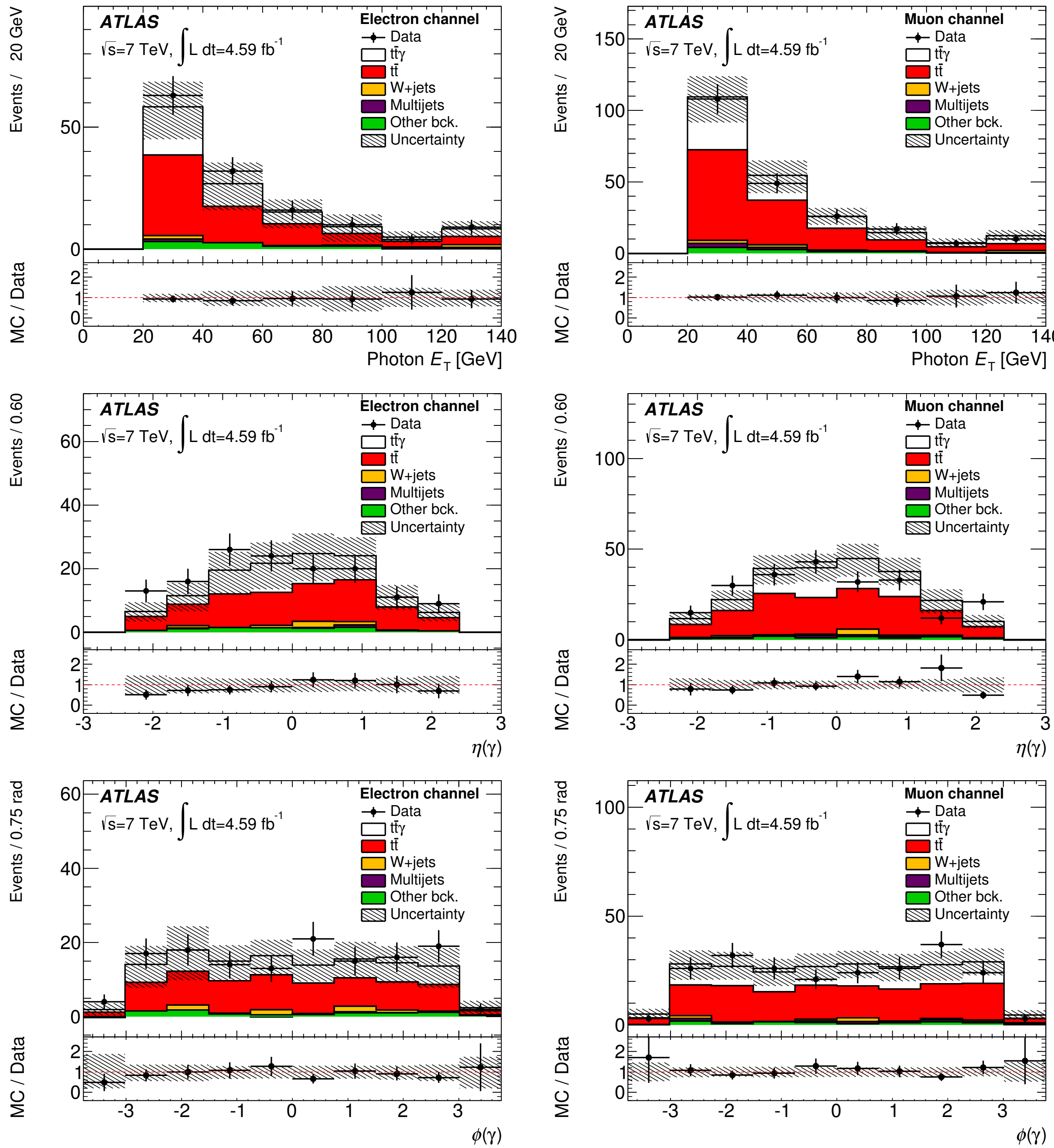

Figure 3.15: Photon kinematic variables. Data (points) are compared to the expectation from simulations after full event selection. Distributions are shown separately for the electron (left) and muon (right) channels. The band labelled "Uncertainty" includes both, simulation based, statistical and systematic uncertainties (see Chap. 7). The entry "Other bck" includes the contributions from $Z+$jets, single top and dibosons. The last bin contains any overflow.

However, for large jet multiplicities, typically ($N_{\text{jet}} \geq 5$) data-to-simulation comparisons show some differences, see Fig. 3.14 top. This is a known miss-modelling of high jet multiplicities in

MC@NLO [118]. As the estimation of processes other than $t\bar{t}\gamma$ production is derived from data, this miss-modelling does not affect the cross section measurement.

Although this selection cuts are primarily meant to reject background processes to $t\bar{t}$ production, they have a close correspondence with the cuts enhancing the $t\bar{t}\gamma$ production cross section, as explained in Sec. 1.1.2.

3.7 Kinematics of $t\bar{t}$ in association with a photon

An interesting digression off the main focus of the analysis is the study of the kinematic behaviour of the $t\bar{t}\gamma$ system. In a resolved scenario, *i.e.* when the top quark is not heavily boosted, the photon would take away some of the energy of the $t\bar{t}$ pairs. This could lead to a displacement of the resonant peak in the angular distributions of the photon and the $t\bar{t}$ pair, as well as a shift in the invariant mass distribution, whenever a photon is radiated off a top quark.

In order to study the event kinematics, an identification method of the final state particles, jets *etc.*, must be involved. Several methods exits, such as the Kinematic Likelihood fitter (KL) method [119] or *ad-hoc* defined algorithms. The KL fitter is a likelihood-based reconstruction algorithm capable of reconstructing event topologies using *Bayesian* methods. The algorithm's development was tailored for reconstructing $t\bar{t}$ events in the single-lepton channel, and has shown outstanding performances [119]. However, the application of this algorithm to the $t\bar{t}\gamma$ event topology stands two bottlenecks [119]. The algorithm uses resolution information from the reconstructed objects and it assigns weights to the reconstructed objects. The addition of the photon complicates the algorithmic weight assignment to neutrinos which also depends upon the definition used for the $E_{\mathrm{T}}^{\mathrm{miss}}$. The second shortcoming originates from the fact that the phase-space defined by the KL lacks a cut-based definition, adding a difficulty in the reproducibility of the phase-space.

3.7.1 *Ad hoc* algorithm

For those reasons, a simple *ad hoc* algorithm was developed. This algorithm does not out-stand the performance of the KL fitter or other *pseudo-top* algorithms used by the Collaboration, but it provides insights on the event kinematics.

The algorithm makes use of the b-tagging algorithm's response and also of the kinematic properties of the reconstructed jets, photons and lepton. The first step of the algorithm is the identification of the hadronic decaying W (called here also hadronic-W for simplicity). Jets that are not b-tagged are classified into two sets of pairs: one containing the two highest p_{T} jets and the other one containing the pair of jets having the highest magnitude of their four-vector sums. These two sets are not exclusive and their information is used at a later stage.

The next step involves the association of the b-jets in the event to top-quark decays. The identification uses the b-tagging information. A $t\bar{t}$ selection requires the event to contain at least one b-tagged jet, a classification must be made based b-tagged-jet multiplicity.

- $N(b-\mathrm{jet}) = 1$ Whenever the event contains only one b-jet, the identification of the second b-jet is based on the minimal angular separation. The jet with minimal angular separation with the lepton and with highest-$p_{\mathrm{T}}$is identified as a b-jet. The jet with highest-p_{T} and lowest $\Delta R(\ell, j)$ is identified the secondary b-jet. The performance of this step can be seen in the invariant mass distribution of a jet which is not b-tagged, but identified as a b-jet, shown in Fig. 3.16. It can be seen that the distribution peaks around the resonant invariant mass of a b-quark ($\simeq 5$ GeV). The width of the distribution can be used to determine a resolution uncertainty on the method.

- $N(b-\text{jet}) = 2$ For events containing exactly two b-tagged jets, both of them are associated as originating from a top quark decay.
- $N(b-\text{jet}) \geq 2$ In events where more than two jets are tagged as b-jets, only the two highest-p_{T} jets and with minimal $\Delta R(\ell, j)$ are associated as originating from the top quark decay.

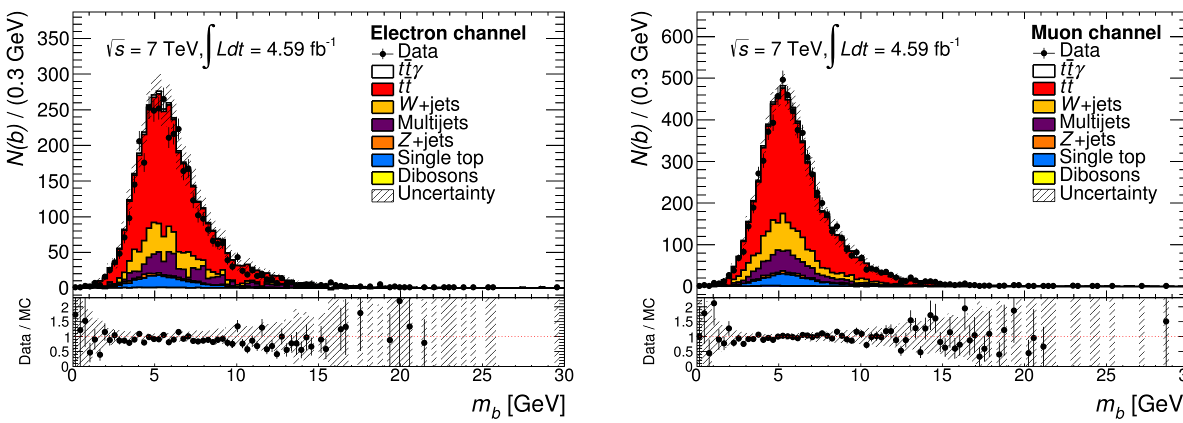

Figure 3.16: Invariant mass of a jet identified as originating from a b-quark, but not b-tagged. Distributions on the left (right) are for the electron (muon) channel. The band labelled "Uncertainty" includes sum in quadrature of the, simulation based, statistical and systematic uncertainties. The last bin includes any overflows.

The W decaying into a lepton and a neutrino (called leptonic-W for simplicity) is identified using the information from the $\boldsymbol{E}_{\text{T}}^{\text{miss}}$ and the lepton momentum. Two four-vectors are constructed from the identified objects: one is associated to the leptonic-W and the other one to the hadronic-W.
The four-vectors of the identified b-jets and the identified W-jets are merged based on their minimal angular separation into two top-quark four-vectors.

Figure 3.17 shows the transverse mass of the top quark identified from the hadronic-W while Fig. 3.18 shows the transverse mass of top identified from the leptonic-W. Both distributions peak around the top quark mass, while their spread is fairly large.

The distribution of the mass in the transverse plane of the $t\gamma$ system (Fig. 3.19) shows, although the small size of data, that indeed the peak of the distribution is displaced with respect to the top mass peak identified in Fig. 3.17 and in Fig. 3.19. Finally, the angular separation of the $t\bar{t}$ system, see Fig. 3.20, shows that the photons are emitted at high angles with respect to the $t\bar{t}$ pair.

3.7.2 Conclusions

Based on what was discussed in Sec. 1.3 and in Sec. 1.4, the angle of emission of the photon with respect to the $t\bar{t}$ system is sensitive to anomalous $t\gamma$ couplings and values of Q_t not predicted by theory. Therefore, this angular separation could discriminate between different values of the top charge and show hints of new phenomena.

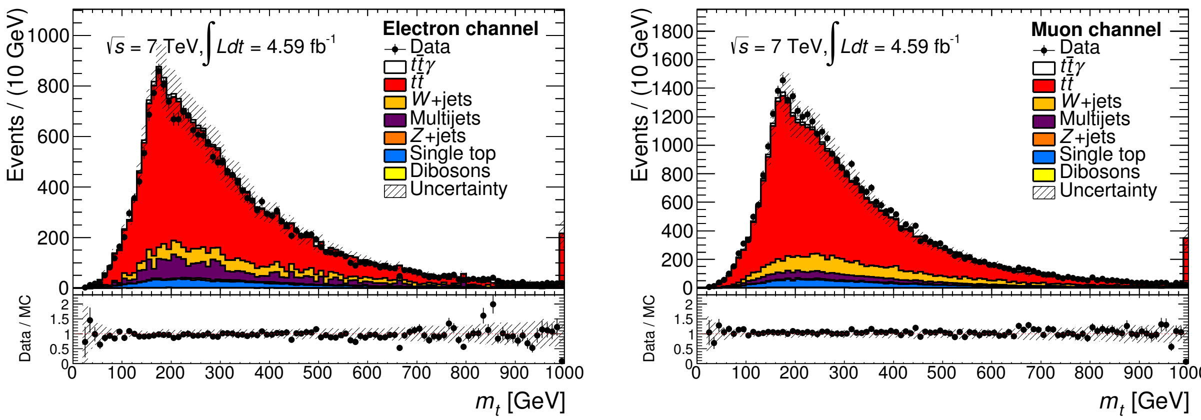

Figure 3.17: Transverse mass for the top-quark from hadronic W-boson decays. Distributions on the left (right) are for the electron (muon) channel. The band labelled "Uncertainty" includes sum in quadrature of the, simulation based, statistical and systematic uncertainties. The last bin includes any overflows.

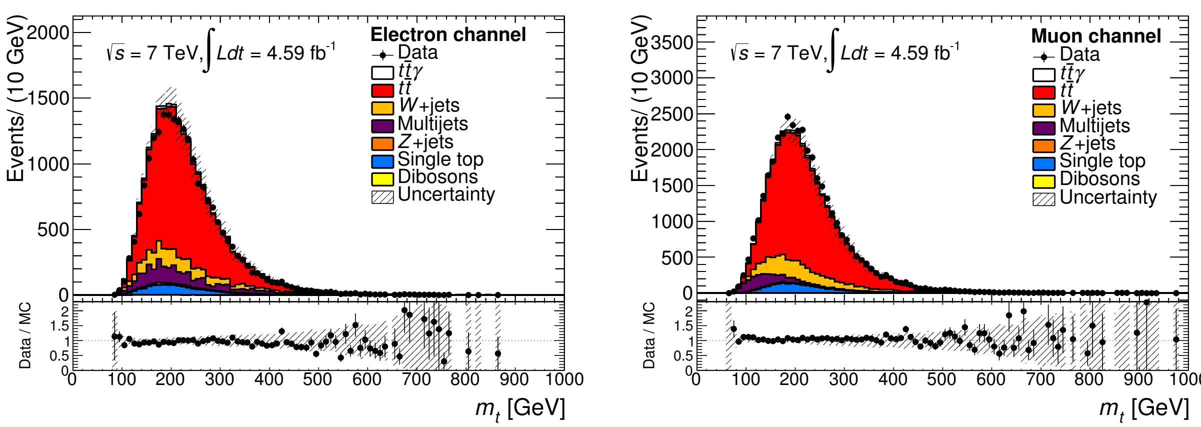

Figure 3.18: Trasnverse mass of the top-quark from W-boson leptonic decays. Distributions on the left (right) are for the electron (muon) channel. The band labelled "Uncertainty" includes sum in quadrature of the, simulation based, statistical and systematic uncertainties. The last bin includes any overflows.

The distributions shown in this section, show a good agreement with the prediction of the Standard Model (SM). All observed data candidates are within 1σ uncertainties of the simulated predictions.

Other than showing the agreement of the defined *pseudo-top* radiation with the SM expectation, the items discussed in this section cannot be used directly for the extraction of the cross section. In-fact, the photon candidates contain both signal prompt-photons, as well as hadrons, or hadron decay products, misidentified as photons. Therefore, one must determine a variable that can be used to discriminate between the two. The next section motivates the choice of this variable.

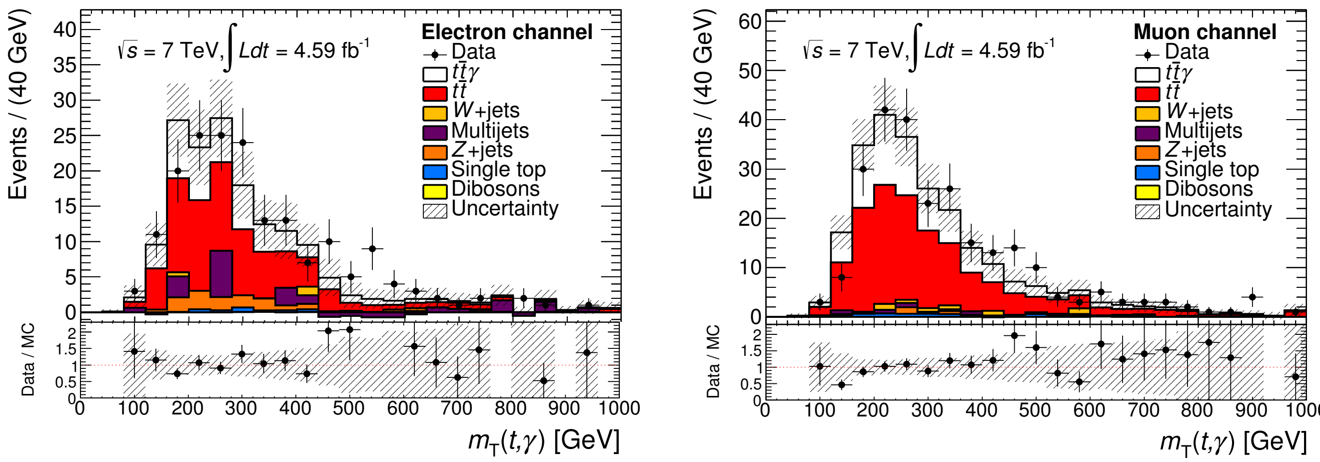

Figure 3.19: Transverse mass of the top-photon system. Distributions on the left (right) are for the electron (muon) channel. The band labelled "Uncertainty" includes sum in quadrature of the, simulation based, statistical and systematic uncertainties. The last bin includes any overflows.

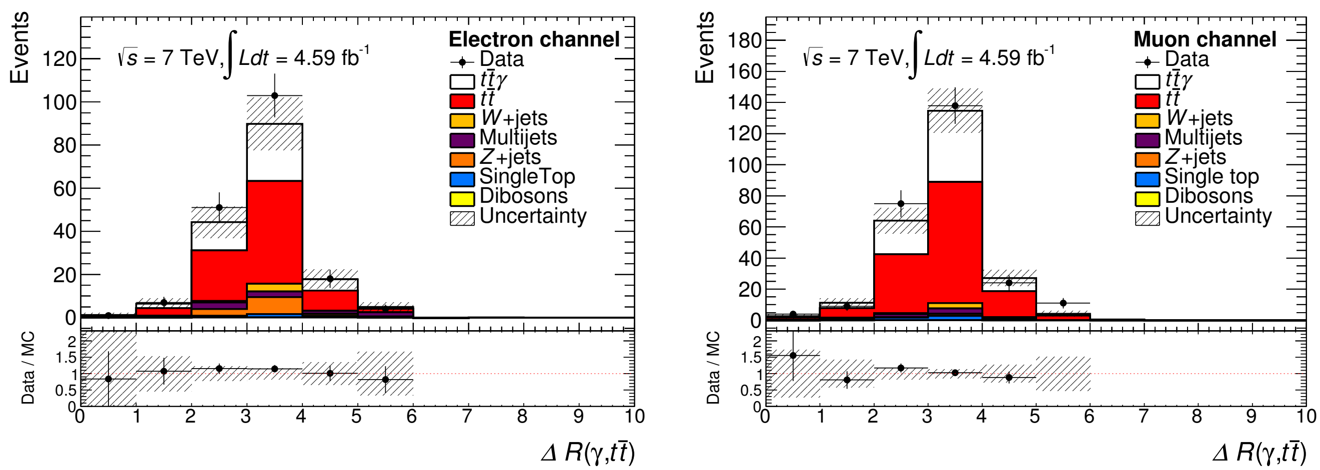

Figure 3.20: Angular distribution for the top-photon system. Distributions on the left (right) are for the electron (muon) channel. The band labelled "Uncertainty" includes sum in quadrature of the, simulation based, statistical and systematic uncertainties. The last bin includes any overflows.

3.8 Strategy and track isolation as discriminating variable

The $t\bar{t}\gamma$ cross section measurement is based on the template fit method, using as discriminating variable the track isolation $p_{\mathrm{T}}^{\mathrm{iso}}$ distributions for two different kind of photon candidates: prompt-photons and photons from the decay of high-p_{T} hadrons from jet fragmentation (*e.g.* π^0, η neutral mesons decaying to diphotons). The track isolation provides a good discrimination between prompt-photons and hadrons faking photons, and is favoured over other isolation criteria (*e.g.* calorimeter isolation with fixed cone) because of its smaller dependence with η (the calorimeter transverse isolation energy depends on the photon η due to the varying amount of material in front of the presampler) and its robustness against pile-up.

The $p_{\mathrm{T}}^{\mathrm{iso}}$ absolute track isolation is generally defined as the scalar sum of the transverse momenta of all selected tracks (ξ) in a cone $\Delta R < 0.2$ around the photon candidate minus the E_{T} of the photon candidate:

$$p_{\mathrm{T}}^{\mathrm{iso}} := p_{\mathrm{T}}^{20}(\gamma) = \left[\int_{0}^{0.2} dR \int_{p_{\mathrm{T}}(\xi)>1\ \mathrm{GeV}}^{\infty} d\xi\ p_{\mathrm{T}}(\xi, R) \right] - E_{\mathrm{T}}(\gamma) \tag{3.6}$$

For electron candidates, the tracks are required to have a transverse momentum $p_{\mathrm{T}} > 1$ GeV, a transverse impact parameter $d_0 \leq 1$ mm, a longitudinal impact parameter $z_0 \leq 1$ mm, at least six hits in the SCT and Pixel detectors and at least one hit in the B-layer (to avoid including tracks from conversions). Both d_0 and z_0 impact parameters are computed with respect to the primary vertex. The minimum p_{T}-cut minimises the effect of pileup and underlying events.

Contrary to electron candidates, the default $p_{\mathrm{T}}^{\mathrm{iso}}$ track isolation for photons is computed without a vertex constrain on the tracks, as in general the vertex associated with the photon is not known (or subject to large uncertainties). Since the signal isolation template for prompt-photons is extracted by extrapolating the electron template from $Z \to ee$ decays using the $t\bar{t}\gamma$ MC sample, a consistent definition of $p_{\mathrm{T}}^{\mathrm{iso}}$ for both electrons and photons is required in this case for consistency in the isolation definitions.

The photon track isolation is thus recomputed by excluding all tracks that fail a minimum $z_0 = 1$ mm cut, in the same way as it is done for electrons. Since only the total number of tracks that entered into the calculation of the photon $p_{\mathrm{T}}^{\mathrm{iso}}$ is known, but not the tracks themselves, permutations among all reconstructed tracks are performed in order to extract the subset of them that give rise to the original photon $p_{\mathrm{T}}^{\mathrm{iso}}$. Within the selected subset, the p_{T} of each track within the cone $\Delta R < 0.2$ not passing the z_0 requirement is subtracted from original track isolation of the photon candidate, see Fig. 3.21.

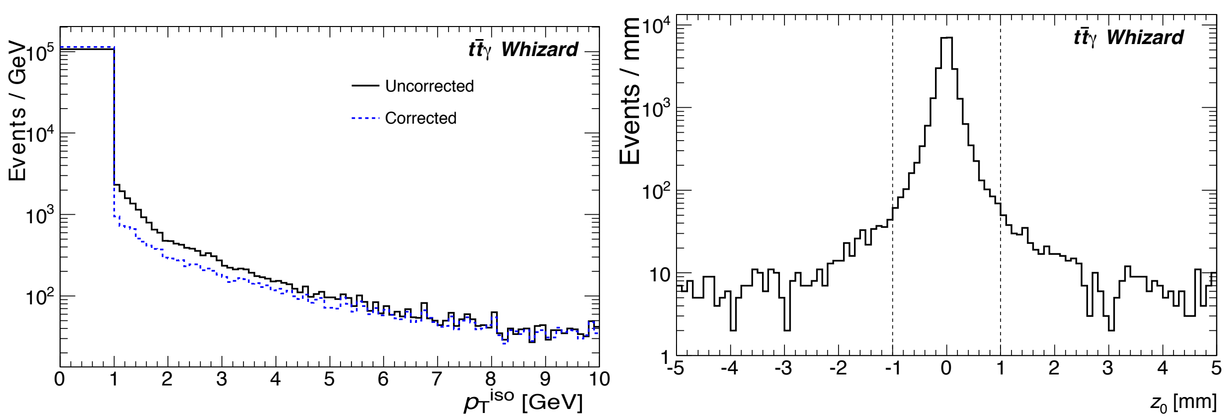

Figure 3.21: Comparison of the track isolation $p_{\mathrm{T}}^{\mathrm{iso}}$ for photons candidates (without any additional event selection) before and after correction by subtracting the transverse momentum of all tracks with $|z_0| > 1$ mm (left) and distribution of the longitudinal impact parameter for all tracks found within a cone $\Delta R = 0.2$ around the photon direction (right). Distributions are evaluated using `WHIZARD`. The vertical dashed lines in the right plot correspond to the cut applied to the z_0 distribution [86].

CHAPTER 4

Cross section definition

The phase-space in which the cross section is reported needs a definition. In order to compare the analysis results with any theoretical prediction, the cross section measurement is made within a fiducial phase-space defined from simulations of $t\bar{t}\gamma$ decays in the single-lepton (electron or muon) final state. This chapter gives the formal definition of, and the motivation for, the phase-space used. The prediction from theory is also reviewed and its projection, into the volume in which the measurement is performed, is calculated.

The chapter starts with Sec. 4.1, which defines, generally, the relation between the cross section and the number of observed $t\bar{t}\gamma$ events. A distinction is made between the cross section measurable within the detector phase-space and its extrapolation to larger regions. The construction of the phase-space follows. At first, the definition of the particles constituting the phase-space (based upon observable quantities) is given (Sec. 4.2), then the event selection criteria (closely following those applied on data) are applied (Sec. 4.2.5). At each step the correlation between the simulation-based definitions and the reconstructed quantities is reviewed.

Simulated events are categorised in exclusive ensembles which are based on the fulfilment (or not) of the definitions for both the simulation-level particles and the reconstructed quantities (Sec. 4.3). Consequently, the detection and reconstruction efficiency with respect to the phase-space is extracted.

The next-to-leading-order theoretical prediction is explained in Sec. 4.3, and its leading-order computation is compared to that of the $t\bar{t}\gamma$ simulation programs used by this analysis. In Sec. 4.5, the prediction of several models is projected into the fiducial phase-space.

4.1 General considerations

Considering two opposite oriented bunched beams of N_{b} colliding protons then the number of scattered events (dN_s) per unit time (dt) and unit volume (dV) is:

$$dN_s = \sigma L_{\mathrm{Lumi}} dV dt \tag{4.1}$$

where L_{Lumi} is the luminosity (see Eq. 2.1) of the two colliding beams. The proportionality constant σ is by definition the cross section. From Eq. 4.1 it is easy to see that σ has the dimension of an area. The proportionality constant must be related to the invariant amplitude $\mathcal{M}_{if}(pp \to \ell\nu_l q\bar{q}b\bar{b}\gamma)$ and the phase-space ($\Phi = Vt$) must be written in a Lorentz-invariant from. A n-body Lorentz-invariant phase-space Φ^n, where incoming particles (i) have four-momenta $\boldsymbol{p}_i$ and out-coming particles (f) with four-momenta $\boldsymbol{p}_f$, can be written as

$$d\Phi^{(n)} = (2\pi)^4\delta^{(4)}\left(\sum_i^{n_i}\boldsymbol{p}_i - \sum_f^{n_f}\boldsymbol{p}_i\right)\prod_j^n \frac{d^3p_j}{(2\pi)^3 2E_j} \tag{4.2}$$

which defines the integrated cross section over an arbitrary period of time:

$$d\sigma_{t\bar{t}\gamma} = \frac{1}{\int L_{\text{Lumi}}dt}\left|\mathcal{M}_{if}\left(pp \to \ell\nu_l q\bar{q}b\bar{b}\gamma\right)\right|^2 d\Phi^{(n)} \tag{4.3}$$

Reformulating Eq. 4.3 as a function of N_b background events and incorporating the phase-space element $\Phi^{(n)}$ into a geometrical and kinematic acceptance factor (A) one obtains the reduced cross section times the Branching Ratio (BR) :

$$\sigma_{t\bar{t}\gamma} \times \text{BR} = \frac{N - N_b}{A \cdot C \cdot \int L_{\text{Lumi}}dt} \tag{4.4}$$

where: $N_s = N - N_b$ is the number of $t\bar{t}\gamma$ observed data events with $\ell\nu_l q\bar{q}b\bar{b}\gamma$ final state ($\ell \equiv e, \mu$) and C is a detection efficiency correction, *i.e.* the fraction of recorded detector events over the total. It follows that a cross section measurement will depend on both C and A, therefore, the reproducibility of the result depends upon the correct definition of those constants. The acceptance defines the phase-space in which the result is reported and it is a measure of the extrapolation from the detector phase-space, to a theoretical phase-space defined by kinematic cuts imposed at simulation level. Cross sections with $A = 1$ are called *fiducial* (σ^{fid}) since the value is reported within the the geometrical (and kinematic) fiducial marks of the detector. A cross section with $A > 1$ will be referred in this document as a total cross section (σ^{tot}). One can easily express σ^{fid} as a function of σ^{tot}:

$$\sigma^{\text{fid}}_{t\bar{t}\gamma} \times \text{BR} = A \times (\sigma^{\text{tot}}_{t\bar{t}\gamma} \times \text{BR}) = \frac{N - N_b}{C \cdot \int L_{\text{Lumi}}dtL}. \tag{4.5}$$

The extrapolation from the phase-space in which the measurement is performed to the total phase-space can be subject to large theoretical uncertainties, ill-defined kinematic regions and simulation-induced model-dependencies. Figure 4.1 illustrates the level of the extrapolation down to the `WHIZARD` simulation defined phase-space for the photon and lepton transverse momenta respectively. It can be seen that the extrapolation reaches values as large as six times the size of the detector defined phase-space.

As a further example, the `WHIZARD` phase-space imposes cuts on invariant masses between quarks which are not a detector observable quantity. The exact extrapolation from the detector observable, a jet, to a quark, is not known and can only be defined using simulation programs.

As no experimental data can control the phase-space for $A > 1$ the measurement reported in this document is chosen to be evaluated at $A = 1$.

The advantage of a total cross section is that, from an experimentalist point of view, no theoretical prediction needs to be determined. Since the extrapolation is done to the simulation defined phase-space, the result can be directly compared with those values. This is also an advantage if two similar experiments want to compare their results to the theory predictions. If both

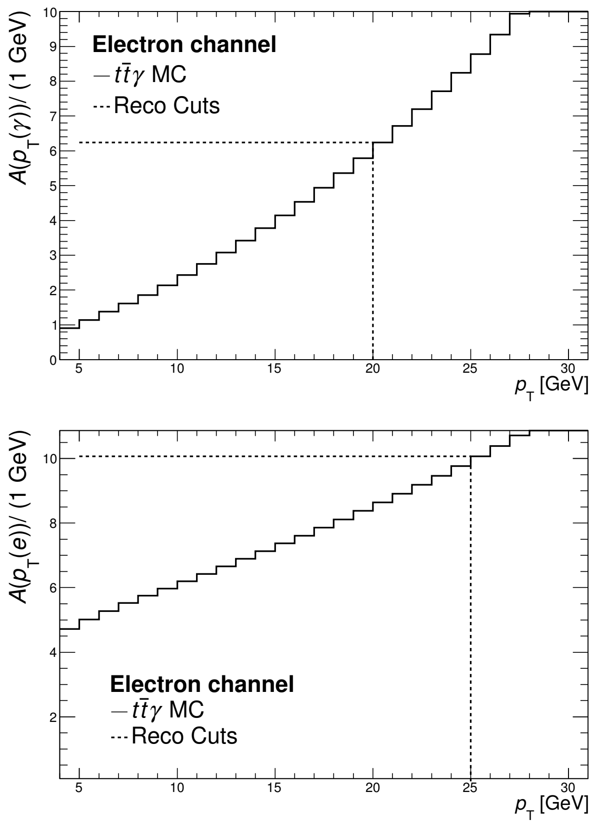

Figure 4.1: Extrapolation acceptance factors with respect to the `WHIZARD` phase-space for the photon (top) and the lepton (bottom) transverse momenta. The dotted line represents the minimum transverse energy requirement imposed on reconstructed objects. The results are separated into the electron channel (left) and muon channel (right) from $t\bar{t}\gamma \rightarrow \ell\nu_l q\bar{q}b\bar{b}\gamma$ decays.

experiments choose the same simulation program (with same settings), then a direct comparison between the two results is obvious. On the other hand, the disadvantage stands in the fact that the universality of the result is not easy to achieve. Extrapolating to other definitions of phase-spaces will be subject to corrections which are, from one side, difficult to determine and, from the other, not possible to confirm experimentally. The clear disadvantage of a fiducial measurement stands, from the point of view of the experimentalist, that the theoretical prediction has to be re evaluated within the phase-space defined by the experiment.

4.2 Particle and phase-space definitions

In this section the particles defining the phase-space are constructed. Each object is defined bearing in mind a close correspondence with detector-level observables and reconstructed objects.

The correlation of the kinematic properties between reconstructed objects and simulation-defined particles is reviewed. Detector resolution and smearing effects can degrade the correspondence between those quantities. The aim is to achieve a high correlation with small uncertainties between defined quantities and reconstructed objects, using tools which are not dependent upon the simulation programs used.

The particle definition is applied to both `WHIZARD` and `MadGraph` programs and the independence from those is shown. Objects are initially classified using the Particle Data Group Identification (PDGID) [3] numbering schemes stored in the High Energy Monte Carlo (HepMC) record [120], which traces the particle evolution throughout the simulation. *Ad hoc* algorithms further define each particle.

In what follows, only particles considered as detectable are considered, therefore the only final state particles with $c\tau > 10$ mm are considered. The definition follows closely recommendations enumerated in a recent workshop [121].

4.2.1 Leptons

Leptons are firstly classified based on their PDGID, then they are requested to not originate from hadron decays. These final state particles (*bare*) have lost part of their energy due to Quantum Electrodynamics (QED) radiation. Within the detector, *bare* leptons are indistinguishable from the Electromagnetic (EM) excitations surrounding them. Therefore, non negligible corrections can affect leptons which need to be taken into account. This is done by including in the definition photons radiated off leptons (*dressing*). Complex *dressing* algorithms exist, for example the anti-k_{T} algorithm can be used to re-cluster leptons with near-by photons. However, a simpler cut-based approach, easing the reproducibility of the result, has been used here.

The four-vector of a *bare* electron (or muon) with $p_{\mathrm{T}}(\ell) > 10$ GeV and $|\eta(\ell)| < 2.7$ is added to that of photons. These photons are requested to not originate from hadrons and must be within a cone of $\Delta R(\ell, \gamma) < 0.1$. Although the detector response for muons is calibrated using Monte Carlo (MC), their momentum depends upon the radiation cut-off defined in simulation; therefore, muons are also dressed. The muon momentum change due to the *dressing* is small, as they radiate less than electrons.

Infra-red divergencies are mitigated by the 8 GeV minimum transverse energy requirement on the photon, determined prior to event generation.

The minimum $p_{\mathrm{T}}(\ell)$ requirement for the lepton to be dressed ensures that soft particles, originated from hadron decays, are not associated with high-E_{T} photons. The $p_{\mathrm{T}}(\ell) > 10$ GeV is considered to be sufficiently lower than reconstruction-level momentum cut. The stability of the choice is tested by raising this requirement to 15 GeV. The differences with respect to the default $p_{\mathrm{T}}(\ell > 10 \text{ GeV})$ to that of $p_{\mathrm{T}}(\ell) > 15$ GeV are of the order of 0.2% and of 0.03% for the electron and muon channel respectively. The combination of the minimum traverse energy and momentum for the photon and the lepton, respectively, mitigates also collinear divergencies.

A good lepton is defined as such if the dressed object has $p_{\mathrm{T}}(\ell) > 20$ GeV and $|\eta(\ell)| < 2.5$.

A comparison between the lepton defined in the generator phase-space, the lepton as defined here and the reconstructed leptons is shown in Fig. 4.2. A good agreement is observed between reconstructed and defined particles. The large extrapolation to the generator phase-space is clear. The electron transverse momentum cut at reconstruction level is 5 GeV higher than at the particle level, leading to a small extrapolation. The reason for this extrapolation is motivated by a common phase-space definition for the electron and muon channels.

A closer inspection between the defined and reconstructed lepton, see Fig. 4.3, shows an excellent correlation between the two quantities. Detector resolution does not increase the spread between the two definitions and it remains roughly constant across the entire p_{T}-range. Additional plots and tables can be found in Appendix C.

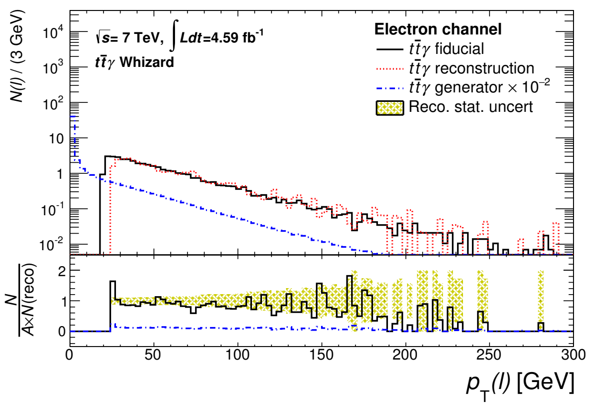

Figure 4.2: Comparisons of the lepton's transverse momentum as defined at particle level (labelled "fiducial" and drawn with continuos line), at reconstruction level objects (labelled "reconstruction" and drawn with a dotted line) and in `WHIZARD` (labelled "generator" and drawn with a dashed line). Left distributions are for electrons while distributions on the right are for muons.

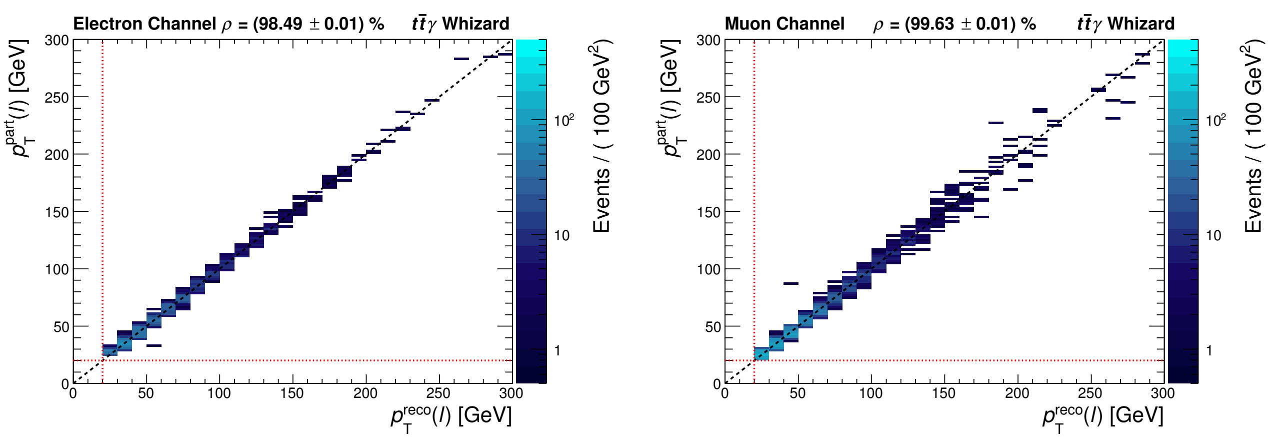

Figure 4.3: Correlation histogram between reconstructed (x-axis) and particle level (y-axis) $p_{\mathrm{T}}(\ell)$. The dotted vertical line shows the reconstruction level cut, while the dotted horizontal line shows the cut at particle level. For both leptons (electrons shown on the left and muons on the right) a correlation above 98% is observed and the spread between the two quantities remains along the diagonal.

4.2.2 Jets

Sprays of bound states (jets) are the observable manifestation of the theoretical concepts of quarks and gluons. Therefore, a jet definition in the phase-space in which the measurement is extrapolated to is needed. Jets (j) are clustered with the anti-k_{T} algorithm [103] with a radius parameter of $R = 0.4$. Muons and neutrinos (ν_ℓ) are not considered in the clustering. Good jets are required to have a $p_{\mathrm{T}}(j) > 25$GeV, $|\eta(j)| < 2.5$. Figure 4.4 compares the $p_{\mathrm{T}}(j)$ for reconstructed jets to particle-level jets to the generator-level quarks. The comparison between the particle level objects and the reconstructed ones is in excellent agreement. Although some discrepancies are visible in

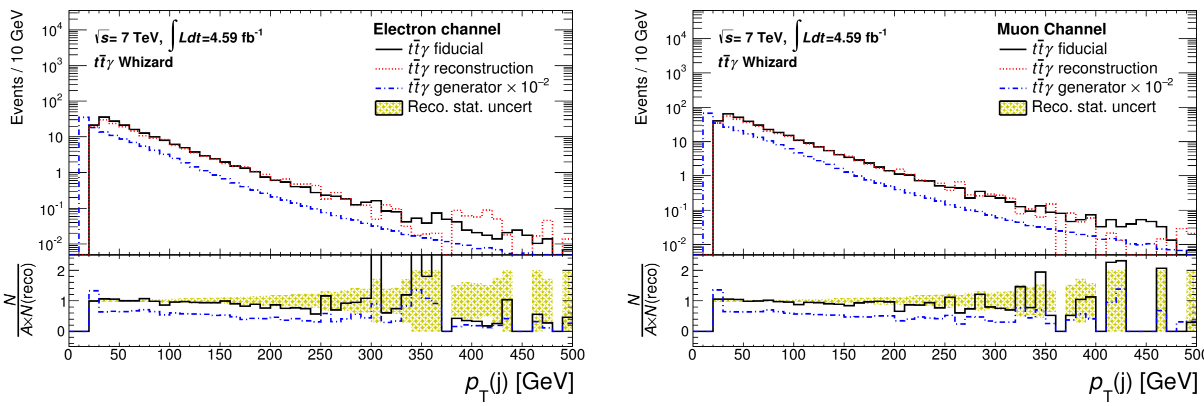

Figure 4.4: Comparisons of the jet's transverse momentum as defined at particle level (labelled "fiducial" and drawn with continuos line), at reconstruction level objects (labelled "reconstruction" and drawn with a dotted line) and in `WHIZARD` (labelled "generator" and drawn with a dashed line). For each distribution, the ratio with respect to the reconstructed distribution times the acceptance is drawn on the bottom pad. The plot on the left (right) shows distributions for the electron (muon) channel.

the high-p_T region, they remain within statistical uncertainties.

As for leptons, an excellent correlation between particles and reconstructed objects is observed, see Fig. 4.5.

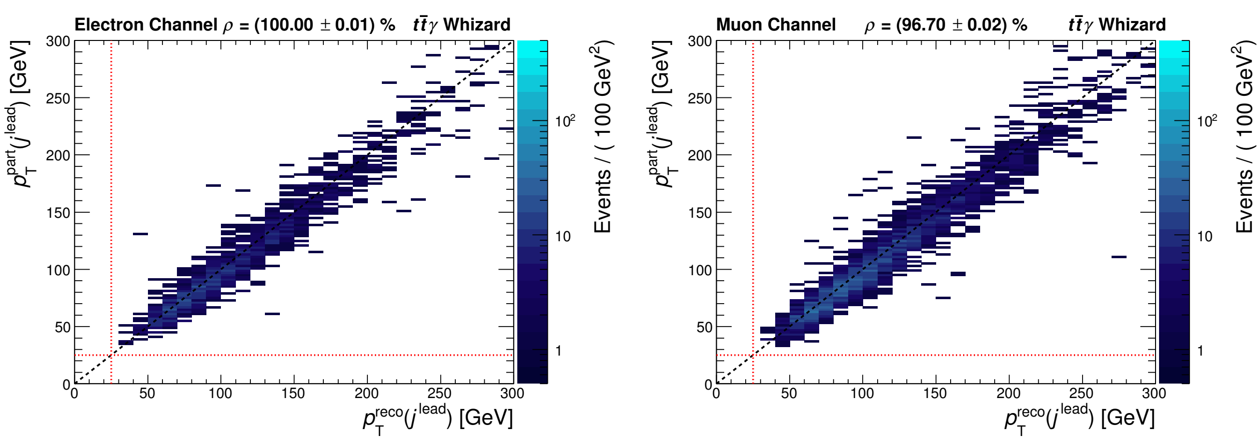

Figure 4.5: Correlation histogram between reconstructed and particle level $p_T(j)$. The dotted vertical line shows the reconstruction level cut, while the dotted horizontal line shows the cut at particle level. The plot on the left (right) shows distributions for the electron (muon) channel.

The valence of the quark at the origin of a jet needs determination. This needs to be done only for the b-flavour. An angular-based matching between jets and b-flavoured quarkonia is performed in order to identify b-jets. More specifically, if any good jet is associated to b-flavoured hadron (α) of any lifetime with $p_T(\alpha) > 5$ GeV within a cone of $\Delta R(j, \alpha) < 0.4$, then the jet is considered to be a b-jet. The minimum p_T requirement on hadrons ensures *infra*-red safety.

4.2.3 Photons

Photons are required not to be originated from hadron decays. Photons used for *dressing* leptons are discarded, as they are by definition part of the lepton. Good photons are required to have $E_{\mathrm{T}}(\gamma) > 20$ GeV and $|\eta(\gamma)| < 2.37$. Figure 4.6 shows the comparison between photons as defined above and reconstructed objects, as-well as a comparison with photons defined at generator level. It can be clearly seen that the extrapolation from the detector phase-space to the generator level phase-space is large. Moreover, some shape differences are also visible. These differences can be associated with low-E_{T} photons emitted by hadrons, or also photons radiated from leptons. The comparison between reconstruction and particle levels shows an excellent agreement.

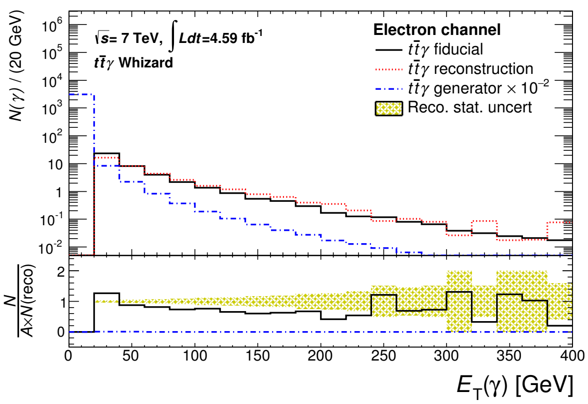

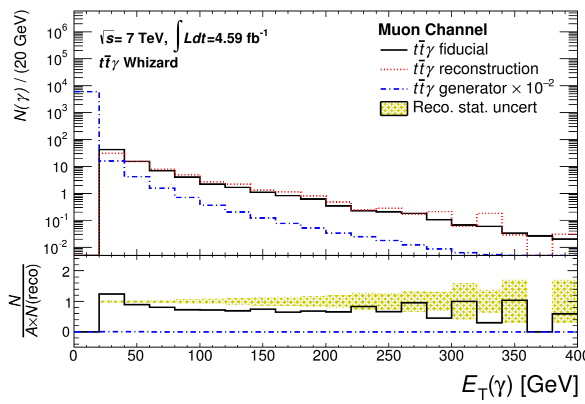

Figure 4.6: Comparisons of the photon's transverse energy as defined at particle level (labelled "fiducial" and drawn with continuos line), at reconstruction level objects (labelled "reconstruction" and drawn with a dotted line) and in `WHIZARD` (labelled "generator" and drawn with a dashed line). For each distribution, the ratio with respect to the reconstructed distribution times the acceptance is drawn on the bottom pad. The plot on the left (right) shows distributions for the electron (muon) channel.

Figure 4.7 shows a very good correlation between the particle level photons and the reconstructed objects. The larger spread of the distribution in low- and medium-E_{T} ranges is due to the different isolation requirements on the two. Infact, at the analysis level the photon is defined upon the track isolation template, see Sec. 5.3. Although the signal simulated samples contain in vast majority real photons, at reconstruction level a small amount of hadrons can still fulfil the photon identification requirements. The occasional entries off the diagonal in this histogram are due to this residual hadrons passing reconstruction level cuts, while at particle level photons originating from hadron decays are rejected. The next section discusses this point.

On the photon isolation

The theoretical calculation defines the photon using the *infra*-red safe *Frixione* prescription [122]. This prescription requires the re-clustering of the photon imposing angular and minimum momentum requirements between photons and near-by partons. This prescription acts effectively as a cut in the photon isolation. The choice not to define the photon in this manner is motivated by the following.

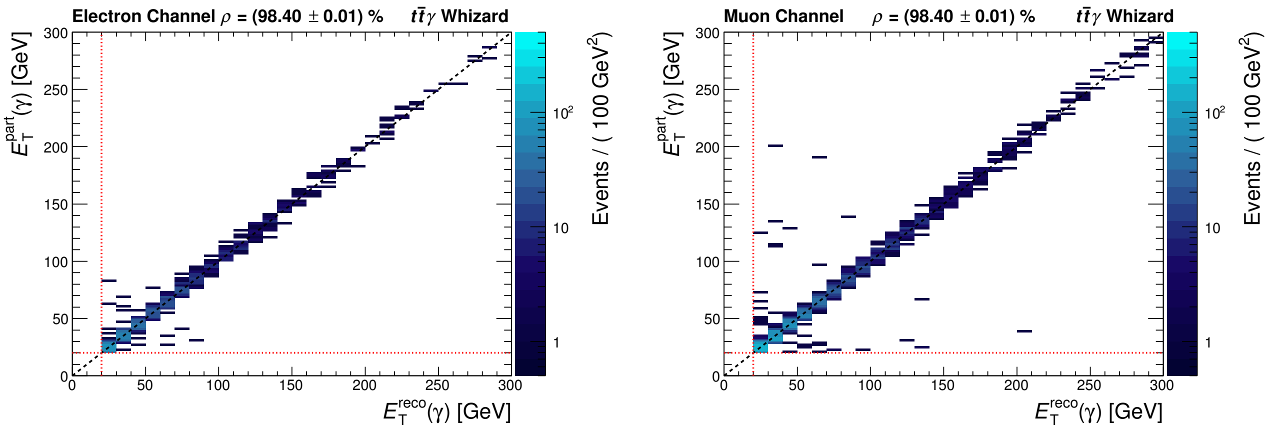

Figure 4.7: Correlation histogram between reconstructed photons and particle level photons for the $p_T(\gamma)$ distribution. The dotted vertical line shows the reconstruction level cut, while the dotted horizontal line shows the cut at particle level. Distributions for the electron (muon) channel are shown on the left (right).

Firstly, the cuts imposed by this method are applied at parton level and they should be translated into cuts applied on hadrons, since they are only observable. The particle level definition would be more dependent upon the simulation of hadronisation and upon the parton-showering programs. Therefore, the result will retain a model dependency, which is to be avoided.

Secondly, a track- (or calorimetric-) isolation cut on the photon identification at the reconstruction level would eliminate the discrimination power between hadrons and photons. The discrimination power originates from the different shapes of p_T^{iso} for hadrons and for photons. The p_T^{iso} distribution for hadrons is of wider shape, as they are accompanied with more intense hadronic activity. Moreover, a residual amount of hadrons mis-identified as photons would still leak into the photon definition (in the regions below the isolation cut). The likelihood discrimination measures such leakage using a clear definition (with the templates) of what a hadron and a photon are respectively across the full $p_T^{iso}(\gamma)$ range. In terms, the determination of the amount of hadrons within the photon definition would need to be estimated by a cut-based approach. This approach has been tested, see App. D.5, and its precision has been outperformed, in terms of uncertainty on the cross section, by the likelihood method. Furthermore, the template-based approach gives a clear definition of the photon at an observable level and the equivalence with respect to a photon definition in a reduced isolation range has been demonstrated in, see Sec. D.3.

Thirdly, the E_T^{miss} is defined using also the photon energy, therefore the E_T^{miss} would need to be redefined at both reconstruction and particle level. A model-independent definition of the neutrino at particle level is difficult to achieve as neutrinos escape detection, see Sec. 4.2.4.

In order to further investigate the relation between the photon definition used here and the template approach, the track isolation distribution is re-built at particle level. The $p_T^{iso}(\gamma)$ distribution is defined as the scalar sum of all stable particle momenta with $p_T > 1$ GeV within a cone of $R = 0.2$ with respect to the photon. Figure 4.8 shows a comparison between the particle-level defined isolation and the isolation defined for reconstructed photons on the signal samples. It can be seen that the agreement is good.

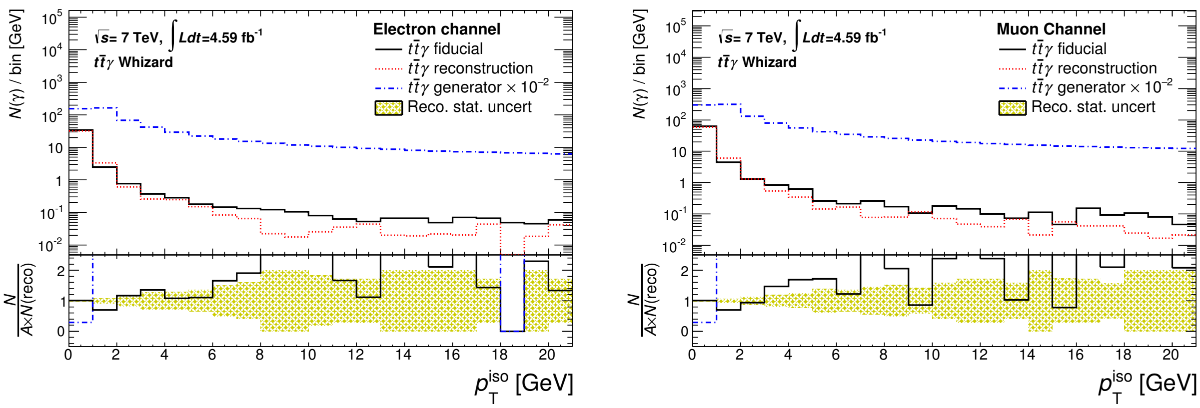

Figure 4.8: Comparison between particle level, labelled "fiducial" and drawn with continuos line, and reconstruction level objects for the photon pseudorapidity. For each distribution, the ratio with respect to the reconstructed distribution times the acceptance is drawn on the bottom pad. The plot on the left (right) shows the $p_{\mathrm{T}}^{\mathrm{iso}}(\gamma)$ in the electron (muon) channel

4.2.4 Neutrinos

Neutrinos are not included in the fiducial phase-space definition. Nonetheless they are defined for comparison reasons. This definition retains a model dependency, as neutrinos are not directly measured in the detector. Furthermore, depending upon the definition at particle level of the neutrino and that of a photon the $E_{\mathrm{T}}^{\mathrm{miss}}$ at reconstruction level needs to be redefined. Two definitions are compared:

1. The particle level $\boldsymbol{E}_{\mathrm{T}}^{\mathrm{miss,truth}}$ is defined as the vectorial sum of all neutrinos (defined by the PDGID) not originated from hadron decays. The $E_{\mathrm{T}}^{\mathrm{miss,truth}}$ quantity is the magnitude of $\boldsymbol{E}_{\mathrm{T}}^{\mathrm{miss,truth}}$.

2. The particle level $E_{\mathrm{T,x}}^{\mathrm{miss,truth}}$ and $E_{\mathrm{T,y}}^{\mathrm{miss,truth}}$ are defined as the vectorial sum of all p_x and p_y components of non interacting particles. The $E_{\mathrm{T}}^{\mathrm{miss,truth}}$ is as defined by Eq. 3.5:

$$E_{\mathrm{T}}^{\mathrm{miss,truth}} = \sqrt{(\boldsymbol{E}_{\mathrm{T,x}}^{\mathrm{miss,\ truth}})^2 + (\boldsymbol{E}_{\mathrm{T,y}}^{\mathrm{miss,truth}})^2} \tag{4.6}$$

Figure 4.9 compares the two definitions and `WHIZARD` and `MadGraph` generators. In what follows the second definition was used as default.

4.2.5 Selection requirements

In this section the selection requirements defining the fiducial phase-space are reviewed and motivated. The cuts imposed at this level bare a close correspondence with the cuts imposed at detector level. The selection cuts aim at a common phase-space in the two channels.

Decay channel:

Only events from $t\bar{t}$ decays in the single-electron or single-muon channels are considered. Events from $W \to \tau$ decays and events where both W-bosons decay leptonically are not considered in the phase-space.

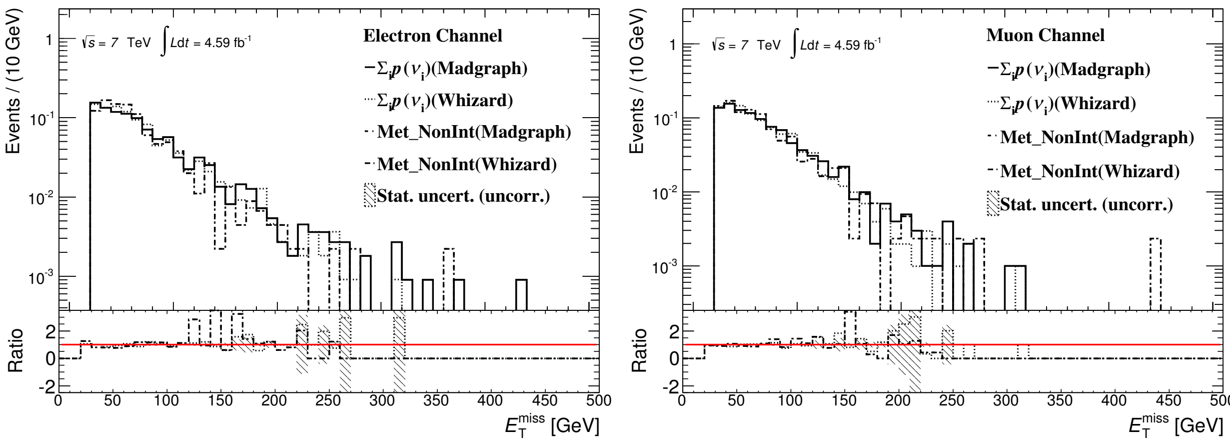

Figure 4.9: Comparisons for different definitions of the particle level $E_{\mathrm{T}}^{\mathrm{miss}}$. The plot on the left (right) shows the distribution for the electron (muon) channel. Both definitions (see text) are computed for both `WHIZARD` and `MadGraph`. The entries labelled $\sum_i p_{\mathrm{T}}(\nu_i)$ and "Met_NonInt" correspond to the first and second definitions respectively. On the bottom of each plot, the ratio between each distribution and $\sum_i p_{\mathrm{T}}(\nu_i)$ (`MadGraph`) is shown; the band corresponds to the uncorrelated portion of the statistical uncertainty.

Angular Separations:

Particles are requested to be isolated in the $\eta - \varphi$ plane. To achieve this angular separations between particles are requested:

(i) electron-jet: the jet with $\Delta R(e, j) \leq 0.2$ is removed from the event;

(ii) jet-photon: the jet with $\Delta R(j, \gamma) \leq 0.1$ is removed from the event;

(iii) muon-jet: the muon with $\Delta R(\mu, j) \leq 0.4$ is removed from the event.

Lepton cuts:

Exactly one good electron (muon) is required in the single-electron (muon) channel. No other good muon (electron) can be present in the event.

Jet cuts:

At least four good jets have to be selected among which at least one should be a b-jet.

Photon cuts:

Events with $N(\gamma) < 1$ are rejected. Additionally the event is dropped if any photon has a $\Delta R(j, \gamma) < 0.5$ and the photon is removed from the collection if $\Delta R(\ell, \gamma) < 0.7$.

The effects of the angular cuts are shown in Fig. 4.10. The distributions on the top show the angular separation between the photon and the the highest-p_{T} jet in the event (j^{lead}), while the distributions on the bottom show the angular separation between the photon and the lepton. A good agreement between particle- and reconstruction- level is visible.

Motivated by a common phase-space for electrons and muons, and willing to decrease model dependencies (e.g. in the definition of the transverse missing energy) the cuts on the $E_{\mathrm{T}}^{\mathrm{miss}}$, the $m_{\mathrm{T}}(W)$, and the $m(e, \gamma)$ $Z-$veto are not included in the Fiducial Region (FR). Nonetheless, a

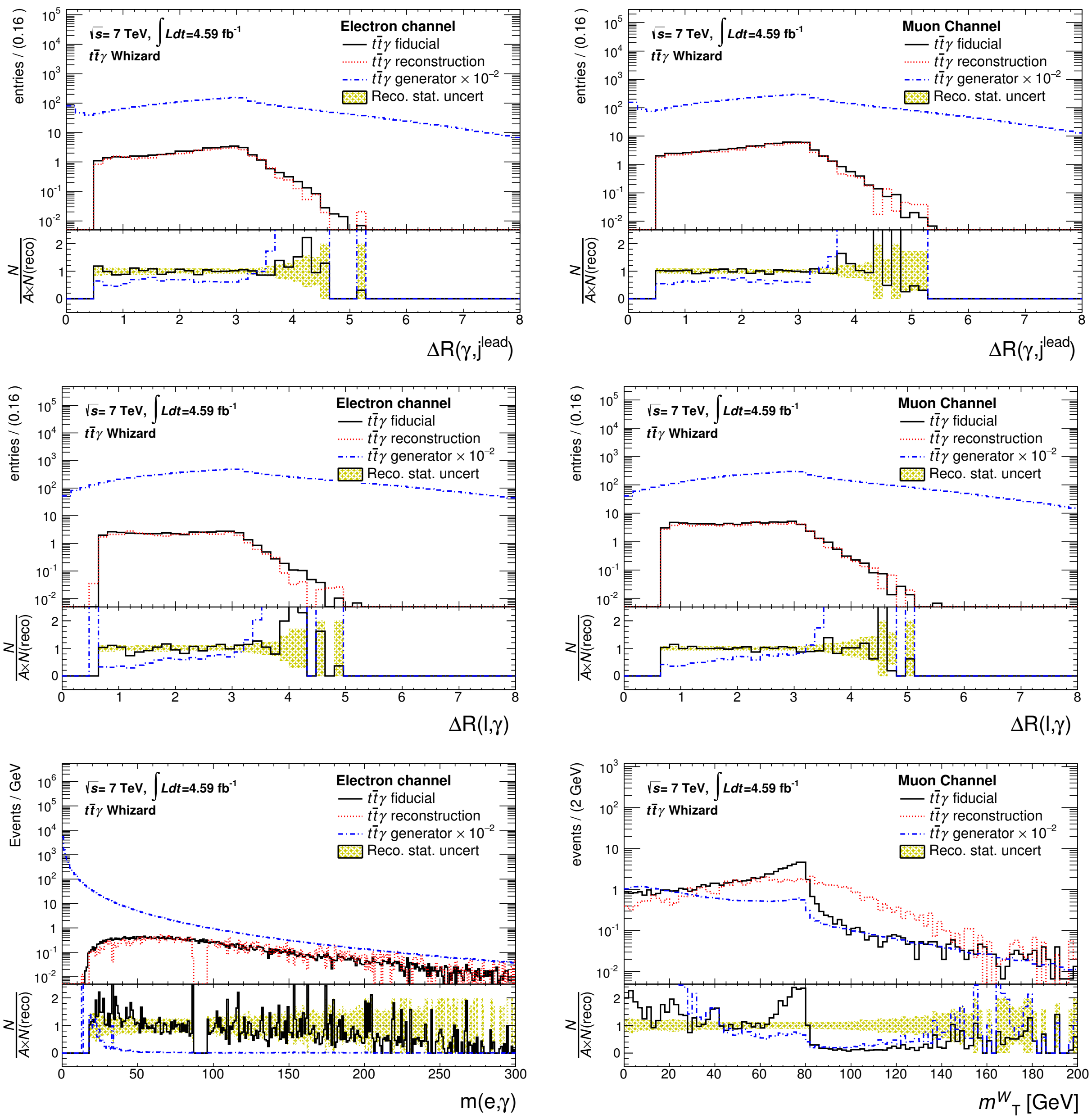

Figure 4.10: Particle- to reconstruction- level comparisons for the $\Delta R(\gamma, j^{\text{lead}})$ (top), the $\Delta R(\gamma, \ell)$ (middle), the $m(e, \gamma)$ and the $m_{\mathrm{T}}(W)$ (bottom). Distributions on the left (right) are for the electron (muon) channel. The dotted line indicates the reconstruction level quantities, while the continuous lines is for the particle level quantity. For comparisons the level of extrapolation to the generator phase-space can be seen with the dashed lines. For each distribution, the ratio with respect to the reconstructed distribution times the acceptance is drawn on the bottom pad. The plots on the right show distributions for the electron channel, while the distributions on the right show plots for the muon channel.

reasonable agreement, as shown in Fig. 4.10 is observed between particle and reconstructed level for this quantities. Additional comparisons can be found in App. C.

4.2.6 Summary

Using quantities which are observable and which are not dependent upon the choice of a given simulation program, the particles that underpin the $t\bar{t}\gamma$ cross section measurement have been defined. A set of phase-space defining cuts has been applied to these definitions. These have been chosen to be as close as possible to the ones applied on data, yielding a phase-space within the detector acceptance.

Table 4.1 summarises the particle- to reconstruction- level correlations for the kinematic properties of leptons, jets and photons. The correlations are extracted by applying all phase-space requirements. It can be seen that the correlation is excellent and that it is independent of the simulation programs.

Variable	**Simulation program**			
	`WHIZARD`		`MadGraph`	
	Electron channel [%]	Muon channel [%]	Electron channel [%]	Muon channel [%]
$p_{\mathrm{T}}(\ell)$	99.63 ± 0.01	100.00 ± 0.01	99.69 ± 0.01	100.00 ± 0.01
$\lvert\eta(\ell)\rvert$	100.00 ± 0.01	96.7 ± 0.02	100.00 ± 0.01	96.25 ± 0.04
$p_{\mathrm{T}}(\gamma)$	98.40 ± 0.01	98.49 ± 0.01	99.46 ± 0.01	98.81 ± 0.01
$\lvert\eta(\gamma)\rvert$	98.49 ± 0.01	99.63 ± 0.01	98.81 ± 0.01	99.69 ± 0.01
$p_{\mathrm{T}}(j^{\mathrm{lead}})$	96.70 ± 0.02	87.39 ± 0.30	96.25 ± 0.03	86.34 ± 0.35
$\lvert\eta(j^{\mathrm{lead}})\rvert$	87.39 ± 0.30	77.07 ± 0.99	86.34 ± 0.35	77.08 ± 0.99

Table 4.1: Particle-to-reconstruction correlations factors estimated with `WHIZARD` and `MadGraph`. Values are shown separately for the electron channel and muon channel. Uncertainties are statistical only.

4.3 Categorisation of events and efficiencies

The particle definition and selection criteria defined in Sec. 4.2 are applied to the `MadGraph` and `WHIZARD` simulations. The acceptance factor of Eq. 4.4 is evaluated as:

$$A = \frac{N_{\mathrm{Part}}(\mathrm{cuts})}{N_{\mathrm{Gen}}(\mathrm{all})} \tag{4.7}$$

where $N_{\mathrm{Part}}(\mathrm{cuts})$ is the number of events generated inside the FR and $N_{\mathrm{Gen}}(\mathrm{all})$ is the total number of events generated in the single-electron and -muon channels respectively. A is found to be about 8% for `WHIZARD` and 17% for `MadGraph` as shown in Tab. 4.2. The larger acceptance for `MadGraph` is explained by the higher generator-level p_{T}-requirement for leptons, jets and photons of 15 GeV. For the $\sigma_{t\bar{t}\gamma}^{\mathrm{fid}}$ extraction A is set to be equal to one.

The efficiency with respect to simulations is calculated by filling a 2×2 matrix $(P_{\mathrm{mig}})_{i,j}$ (so-called migration matrix), which categorises events based on the fulfilment (or not) of the particle

Simulation	Acceptance	
	Electron channel	**Muon channel**
`WHIZARD`	$(8.09 \pm 0.08)\%$	$(7.81 \pm 0.08)\%$
`MadGraph`	$(17.3 \pm 0.14)\%$	$(16.6 \pm 0.13)\%$

Table 4.2: Acceptances with respect to the volume defined in Sec. 4.2 for the electron channel (left column) and and the muon channel (right column). Only statistical uncertainties are shown.

definition and on the fulfilment (or not) of the reconstruction cuts. The calculation is made in the range $E_{\mathrm{T}}(\gamma) > 20$ GeV. The migration matrix for `WHIZARD` is found to be

$$P_{\mathrm{mig}} = \left(\begin{array}{c|cc} & \text{Pass Reco} & \text{Fail Reco} \\ \hline \text{Pass Particle} & 0.25\%(e)\ 0.45\%(\mu) & 1.84\%(e)\ 1.55\%(\mu) \\ \text{Fail Particle} & 0.13\%(e)\ 0.24\%(\mu) & 97.78\%(e)\ 97.78\%(\mu) \end{array}\right) \tag{4.8}$$

equivalently for `MadGraph` the matrix reads

$$P_{\mathrm{mig}} = \left(\begin{array}{c|cc} & \text{Pass Reco} & \text{Fail Reco} \\ \hline \text{Pass Particle} & 0.56\%(e)\ 1.0\%(\mu) & 3.87\%(e)\ 3.28\%(\mu) \\ \text{Fail Particle} & 0.26\%(e)\ 0.48\%(\mu) & 95.32\%(e)\ 95.16\%(\mu) \end{array}\right) \tag{4.9}$$

Matrices are normalised to the total number of generated events. They are also calculated in exclusive sets based upon the photon transverse energy, and they can be found in App. C.5. The tight FR and reconstruction cuts induce that more than 95% of the `MadGraph` events and more than 97% of `WHIZARD` the events are not generated within the FR, nor are reconstructed. The off-diagonal items denote the inward and outward event migrations. They include contributions from $t\bar{t}$ decays in the dilepton channel, with both W-bosons decaying into a lepton (e, μ, τ) and in the single-τ channel ($W \to \bar{\tau}\nu_{\tau}$). These contribution are from events that are not part of the FR, but reconstructed as such. The off-diagonal asymmetry can be explained by the 5 GeV extrapolation in transverse momentum for electrons and the non application of the $E_{\mathrm{T}}^{\mathrm{miss}}, m_{\mathrm{T}}(W)$ and the $m(e,\gamma)Z -$ veto cuts at particle-level. Consequently, a larger portion of events passing particle-level cuts fail reconstruction cuts. The addition of those requirements, while keeping the same $p_{\mathrm{T}}(\ell)$ cut for electrons and muons, reduces the asymmetry to about 1.3 % for `WHIZARD` and to about 2.7 % for `MadGraph`. Nonetheless, these cuts are not applied for the reasons explained in Sec. 4.2.5. The efficiency correction factor C is defined based on the migration matrix Eq. 4.8 and Eq. 4.9 as:

$$C = \frac{N_{\mathrm{Reco}}(\mathrm{cuts})}{N_{\mathrm{Part}}(\mathrm{cuts})} \tag{4.10}$$

where N_{Reco} denotes the number of events passing reconstruction cuts, which includes event migrations. It corresponds to the addition of first column items of the migration matrix. N_{Part} denotes the total number of events passing particle level cuts and it corresponds to the addition of the first line items of the migration matrix.

Efficiencies are calculated with a 2.1% and 2.9% statistical accuracy for `MadGraph` and `WHIZARD` respectively and they read close to 18% for the electron channel and 34% for the muon channel.

Exact estimates and uncertainties in the range $E_\mathrm{T}(\gamma) =]20\ \mathrm{GeV}, \infty[$ are summarised in Tab. 4.3.
Figure 4.11 shows the correction factor C as evaluated in exclusive $p_\mathrm{T}(\gamma)$-bins. The efficiencies

	Efficiency	
Generator	**Electron channel**	**Muon channel**
`WHIZARD`	$(17.8 \pm 0.5) \times 10^{-2}$	$(34.3 \pm 1.0) \times 10^{-2}$
`MadGraph`	$(18.5 \pm 0.4) \times 10^{-2}$	$(34.6 \pm 0.7) \times 10^{-2}$

Table 4.3: Efficiencies for `WHIZARD` and `MadGraph` generators.

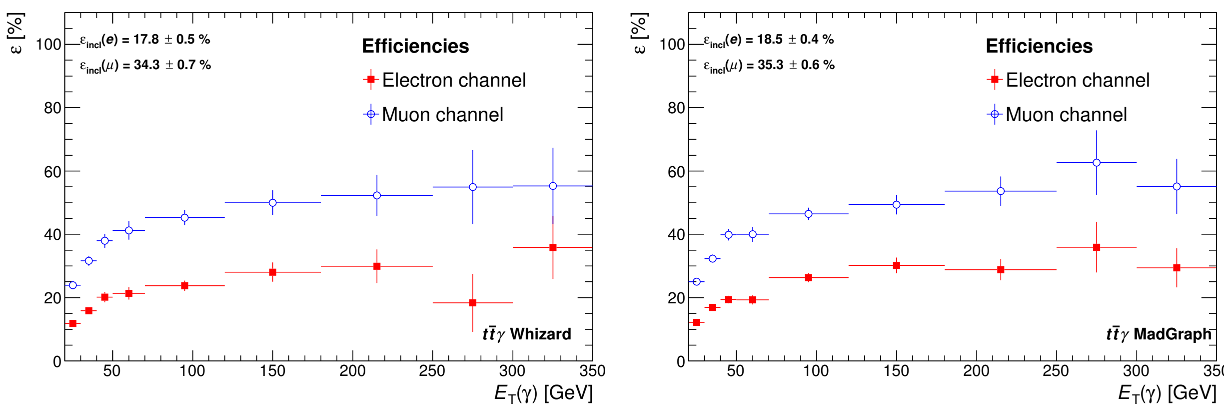

Figure 4.11: Efficiency correction factor evaluated as a function of $p_\mathrm{T}(\gamma)$ from the `WHIZARD` (left) and `MadGraph` (right) samples respectively. Bin-by-bin migration effects are included in the calculation. The uncertainties are statistical only.

obtained from the two simulation programs are in excellent agreement.

4.4 Next-to-leading order theoretical prediction

The $t\bar{t}\gamma$ cross section result is compared to that of the Next-to-Leading-Order (NLO) calculation in the narrow-width approximation [56], see Sec. 1.4.2.

This calculation is based on the method of generalised D-dimensional unitarity extended to massive particles and on the dipole formalism which are used, respectively, to calculate one-loop virtual amplitudes and real emission corrections. Top quarks are treated in the narrow-width approximation with all spin correlations retained. The hadronic decays of W-bosons are considered into two families of light quarks, always treated as massless. The W-bosons are considered in their mass-shells and no Quantum Chromodynamics (QCD) radiative corrections to the hadronic decays are considered. The strong coupling constant is evaluated using one- and two-loop running with five massless flavours.

Because of the treatment of top quarks as unstable particles, this calculation is less dependent on the kinematics of the phase-space defining it, see Fig. 4.12. In particular, the k-factor is considered to be stable with respect to the photon transverse momentum. Whilst the original calculation ($pp \to t\bar{t}\gamma \to b\mu^+\nu_\mu\bar{b}jj\gamma$) was performed at a centre-of-mass energy ($\sqrt{s}$) of 14 TeV, a dedicated prediction [54] at $\sqrt{s} = 7$ TeV has been calculated.

The phase-space is defined by a single high-p_{T} muon, at least four jets (j) and a neutrino with large momentum. Specifically, the particles are subject to the following definition:

- The muon (μ) is required to have $p_{\mathrm{T}}(\mu) > 20$ GeV and rapidity (y) $|y(\mu)| < 2.5$.
- Jets are clustered with the anti-k_{T} [103] algorithm with radius parameter $R = 0.4$, and they are required to have $p_{\mathrm{T}}(j) > 25$ GeV and $|y| < 2.5$
- The photon is constructed using the *infra*-red safe *Frixione* prescription [122] with radius parameter of $R = 0.5$. This method guarantees photon isolation from near-by hadronic activity. A good photon is required to have $p_{\mathrm{T}}(\gamma) > 15$ GeV and $y < 2.37$.
- A good neutrino is required to have $p_{\mathrm{T}}(\nu) > 25$ GeV.
- A b-jet is defined as a jet that contains b-quarks from top quark decays in the clusterisation of the jet.

Events are selected applying the following selection criteria:

- The event must contain only one good muon and only one good neutrino.
- The event has to contain at least four good jets, at least two of them must be b-jets.
- Any pair of i and j jets needs to be separated by $\Delta R(j_i, j_j) > 0.4$.
- The muon is required to have an angular separation with any good jet of $\Delta R(j, \mu) > 0.4$.
- The W transverse mass, defined as $m_{\mathrm{T}}(W) = \sqrt{2p_{\mathrm{T}}(\nu) \cdot p_{\mathrm{T}}(\mu)(1 - \cos\Delta\phi)}$, must fulfil the condition: $p_{\mathrm{T}}(\nu) + m_{\mathrm{T}}(W) > 60$ GeV.
- The final-state photon is required to be separated with the muon by $\Delta R(\gamma, \mu) < 0.4$ and with any jet by $\Delta R(\gamma, j) < 0.5$

For the renormalisation and factorisation scales $\mu_{\mathrm{R}} = \mu_{\mathrm{F}} = \mu = m_t$. The calculated Leading-Order (LO) and NLO cross sections are:

$$\sigma^{\mathrm{LO}}_{t\bar{t}\gamma} = 14.7 \pm 0.1\ (\mathrm{stat})^{+5.8}_{-3.8}\ (\mathrm{syst})\ \mathrm{fb} \tag{4.11}$$

and

$$\sigma^{\mathrm{NLO}}_{t\bar{t}\gamma} = 24.5 \pm 0.1\ (\mathrm{stat})^{+5.6}_{-4.5}\ (\mathrm{syst})\ \mathrm{fb} \tag{4.12}$$

The upper- and lower- bounds correspond to scale variations by a factor of two around the central value $\mu = m_t$. The quark-gluon annihilation, appearing only at NLO, is assumed to be at the origin of this scale dependence [56]. The large value of the k-factor is speculated to be caused by additional radiation originated by high-p_{T} jets [56]. The Parton Density Function (PDF) set used for the LO (NLO) calculation is the MSTW2008 [24–26]. α_{s} was evaluated using a two-loop running from $\alpha_{\mathrm{s}}(m_Z)$. The top has a mass of $m_t = 172$ GeV and a decay width of $\Gamma_t = 1.3237$ GeV. The fine structure constant used in all cases is $\alpha_{\mathrm{QED}} = 1/137$.

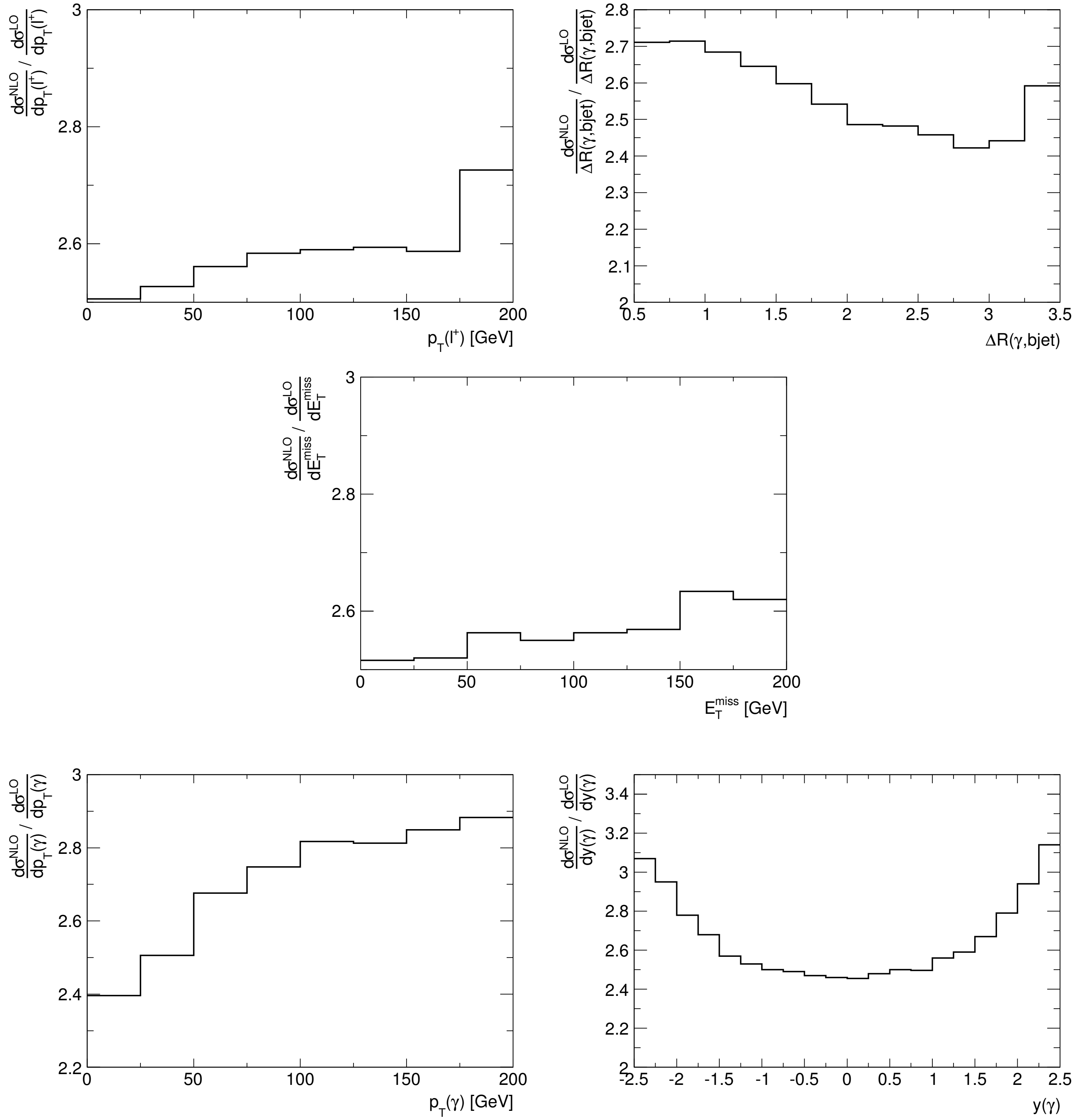

Figure 4.12: k-factor $\sigma^{\mathrm{NLO}}_{t\bar{t}\gamma}/\sigma^{\mathrm{LO}}_{t\bar{t}\gamma}$, with $\mu_{\mathrm{R}} = 2m_t$ and $\mu_{\mathrm{F}} = \sqrt{\hat{s}}$, as a function of: the lepton p_{T} on the upper left frame, the $\Delta R(\gamma, b\text{-jet})$ on the upper right frame, the of missing transverse momentum in the middle frame, the $p_{\mathrm{T}}(\gamma)$ in the bottom left frame and the$y(\gamma)$ in the lower right frame [54] for pp collisions at $\sqrt{s} = 7$ TeV.

The authors of this result provided also a dedicated calculation with $\mu_{\mathrm{R}} = 2m_t$ and $\mu_{\mathrm{F}} = \sqrt{\hat{s}}$ with all other settings kept as above, of which the results can be seen in. The results are:

$$\sigma^{\mathrm{LO}}_{t\bar{t}\gamma} = 10.9 \pm 0.1\ (\mathrm{stat})^{+4.3}_{-2.8}\ (\mathrm{syst})\ \mathrm{fb} \tag{4.13}$$

and

$$\sigma^{\mathrm{NLO}}_{t\bar{t}\gamma} = 27.5 \pm 0.1\ (\mathrm{stat})^{+6.3}_{-5.1}\ (\mathrm{syst})\ \mathrm{fb} \tag{4.14}$$

For the calculation performed with $\mu_{\mathrm{R}} = \mu_{\mathrm{F}} = m_t$ and for the calculation performed with $\mu_{\mathrm{R}} = 2m_t$ and $\mu_{\mathrm{F}} = \sqrt{\hat{s}}$ the corresponding k-factor are 1.67 and 2.55 respectively.

4.4.1 Comparison with the theoretical phase-space

The LO theoretical calculation has been compared with that obtained with the `WHIZARD` and `MadGraph` simulations. The same phase-space cuts as used in the $\sqrt{s} = 7$ TeV theory calculation have been applied to the generated event four-vectors. However, the theoretical calculation was originally performed in the μ^+ channel, consequently only positive muons are selected for this comparison. All the cuts are made as consistent as possible with the theoretical calculation [56]:

Muons Muons are required to have $p_{\mathrm{T}}(\mu) > 20$ GeV and $|\eta(\mu)| < 2.5$. The event must contain a single-muon fulfilling these requirements.

Jets At least four jets, each constructed with the anti-k_{T} algorithm, with radius parameter $R = 0.4$, and each required to have $p_{\mathrm{T}}(j) > 25$ GeV and $|\eta(j)| < 2.5$.

Photons Photons are required to have $E_{\mathrm{T}}(\gamma) > 15$ GeV and $|\eta(\gamma)| < 1.37$ or $1.52 < |\eta(\gamma)| < 2.37$.

Missing transverse energy definition. The magnitude of the four-vector sum of all neutrinos in the event ($E_{\mathrm{T}}^{\mathrm{miss}}$) is required to be $E_{\mathrm{T}}^{\mathrm{miss}} > 25$ GeV.

W **transverse mass.** A W transverse mass and $E_{\mathrm{T}}^{\mathrm{miss}}$ requirement are imposed: $E_{\mathrm{T}}^{\mathrm{miss}} + m_{\mathrm{T}}(W) > 60$ GeV. The $m_{\mathrm{T}}(W)$ is built from the lepton and from the above defined $E_{\mathrm{T}}^{\mathrm{miss}}$.

Angular separations. Any pair of jets (i,j) is required to have $\Delta R(i,j) > 0.4$ and each jet is required to have $\Delta R(j,\mu) > 0.4$. The photon is separated from the lepton with $\Delta R(\gamma,\mu) > 0.4$. Any jet is separated from the photons with $\Delta R(\gamma,j) > 0.5$.

The LO cross section obtained with `MadGraph` or `WHIZARD` after applying the theory cuts $\sigma^{\mathrm{LO,\,cuts}}_{t\bar{t}\gamma}$ is:

$$\sigma^{\mathrm{LO,\,cuts}}_{t\bar{t}\gamma} = \left(\frac{N^{\mathrm{gen,\,cuts}}}{N^{\mathrm{gen,\,all}}}\right) \times \sigma^{\mathrm{LO}}_{t\bar{t}\gamma} \tag{4.15}$$

where: $N^{\mathrm{gen,\,cuts}}$ is the total number of events at generator level after applying the phase-space cuts used in the theoretical calculation. $N^{\mathrm{gen,\,all}}$ is the total number of events generated in the single-positive-muon channel, $\sigma^{\mathrm{LO}}_{t\bar{t}\gamma}$ fb is the LO single-lepton cross section of the generated $t\bar{t}\gamma$ simulation (`MadGraph` or `WHIZARD`) sample.

A reasonable agreement between theory and the two generators is obtained, as shown on Tab. 4.4.

Sample	$\sigma_{t\bar{t}\gamma}^{e,\mathrm{LO}}$ [fb]	$\sigma_{t\bar{t}\gamma}^{\mu,\mathrm{LO}}$ [fb]	$\sigma_{t\bar{t}\gamma}^{\mathrm{LO}}$ **Theory**	μ_{R}	μ_{F}
`WHIZARD`	8.2 ± 0.5 (stat)	9.2 ± 0.6 (stat)	10.9 ± 0.1	$2m_t$	$\sqrt{\hat{s}}$
`MadGraph`	14.7 ± 0.6 (stat)	16.3 ± 0.6 (stat)	14.8 ± 0.4	m_{top}	m_{top}

Table 4.4: Leading order cross sections as obtained for `WHIZARD` and `MadGraph` in the theoretical phase-space. Numbers are based on samples of 2.5×10^4 events. A reasonable agreement is observed.

4.5 Next-to-leading order prediction in the fiducial region

The NLO theoretical prediction for the $t\bar{t}\gamma$ production cross section in the fiducial region is obtained by applying the k-factor [56] of 2.53 for `WHIZARD` and 1.67 for `MadGraph` to the fiducial leading-order cross section

$$\sigma_{t\bar{t}\gamma,\,\mathrm{fid}}^{NLO} = \bar{k} \times \sigma_{t\bar{t}\gamma}^{\mathrm{LO}} \times \frac{N^{\text{gen, fid}}}{N^{\text{gen, all}}} \tag{4.16}$$

where the $\sigma_{t\bar{t}\gamma}^{\mathrm{LO}}$ is the generator cross section. $N^{\text{gen, all}}$ is the total number of generated events in the single-electron (muon) channels and $N^{\text{gen, fid}}$ is the total number of events at generator level (no event selection) inside the fiducial region, $\bar{k}$ is an average k-factor obtained after weighting the binned k-factor with the E_{T}-spectrum of the photons at particle level

$$\bar{k} = \frac{\sum_i \left[k_i \times N_i^{\text{gen, fid}}\right]}{\sum_i N_i^{\text{gen, fid}}} = \begin{cases} 2.53 \pm 0.45 & (\texttt{WHIZARD}) \\ 1.67 \pm 0.30 & (\texttt{MadGraph}) \end{cases} \tag{4.17}$$

where k_i is the k-factor in the i-th E_{T}-bin and N_i^{fid} is the number of photons that passed the fiducial requirements in the i-th p_{T}-bin. The uncertainty in the k-factor above is obtained by scale variations by a factor of two around the central value used for the NLO calculation, m_t. The systematic uncertainty due to m_t is estimated using `MadGraph` and is found to be $\pm 5\%$, which is negligible compared to the one obtained by scale variations. However the fluctuations of the k-factor with respect to the γ transverse energy are small with respect to the twenty percent uncertainty from the scale variations. The NLO theoretical cross sections are derived for `WHIZARD` and `MadGraph` in the single-muon channel as a function of photon transverse energy bins and can bee seen on Fig. 4.13.

All predictions are in agreement with each other across the entire $E_{\mathrm{T}}(\gamma)$ range. Table 4.5 shows the inclusive ($E_{\mathrm{T}}(\gamma) > 20$ GeV) cross sections as estimated from the two simulation programs for the electron and muon channel separately, and it can be seen that estimates agree between channels within statistical uncertainties. Therefore, the cross section with respect to which the measurement

Sample	$\sigma_{t\bar{t}\gamma}^{e,\mathrm{fid}}$ [fb]	$\sigma_{t\bar{t}\gamma}^{\mu,\mathrm{fid}}$ [fb]
`WHIZARD`	50.7 ± 0.5 (stat) $\pm$ 10.1 (theor)	48.4 ± 0.5 (stat) 9.7 (theor)
`MadGraph`	49.3 ± 0.4 (stat) $\pm$ 9.9 (theor)	47.2 ± 0.4 (stat) 9.4 (theor)

Table 4.5: NLO cross sections in the FR as predicted by `WHIZARD` and `MadGraph` generators. All estimates are in agreement within statistical uncertainties

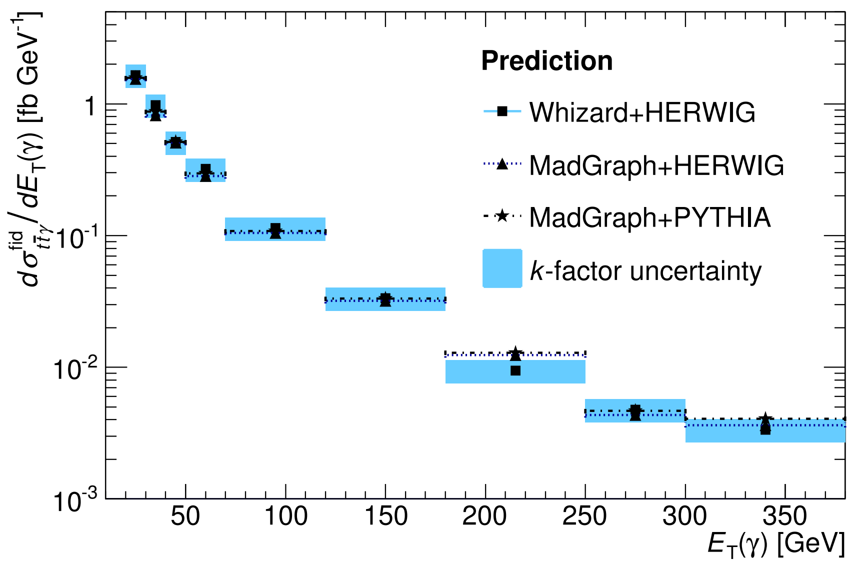

Figure 4.13: Theoretical prediction in bins of photon transverse energy evaluated with the `WHIZARD` (interfaced to `HERWIG`) and `MadGraph` (interfaced to both `PYTHIA` and `HERWIG`) LO generators and normalised to the NLO theoretical prediction. Errors include the k-factor uncertainty and the statistical uncertainty for each sample.

of the inclusive cross section is compared reads:

$$\sigma^{\texttt{WHIZARD}}_{t\bar{t}\gamma} = 48.4 \pm 0.5 \text{ (stat) } \pm 9.7 \text{ (theor) fb} \tag{4.18}$$

for the `WHIZARD` generator and

$$\sigma^{\texttt{MadGraph}}_{t\bar{t}\gamma} = 47.2 \pm 0.4 \text{ (stat)} \pm 9.4 \text{ (theor) fb} \tag{4.19}$$

for the `MadGraph` generator.

CHAPTER 5

Statistical model

The aim of the analysis presented in this thesis is the experimental determination of the $t\bar{t}\gamma$ cross section, as defined in Chap. 4. This value is intrinsically defined as the limiting frequency of the increasing number of observations. Therefore, because of the infinite number of observations needed to access this definition, the true value remains inaccessible. The measurement is defined as the inference made on the true value of $\sigma_{t\bar{t}\gamma}$ based upon a limited number of observations.

The inference must be characterised by a single value of $\sigma_{t\bar{t}\gamma}$ being as close as possible to the truth, but also by a range of values which contains the true value with a fixed, and arbitrarily-defined, probability. This range is referred to as a confidence interval, or most commonly as the error. The probability is, typically, chosen to be 0.68 and this property is defined as *coverage*.

This chapter defines the methods used for making the inference on the $t\bar{t}\gamma$ cross section from the observed candidate data.

At first in Sec. 5.1, the choice of this function of the data (likelihood *estimator*) is motivated. It is then followed by a detailed description (Sec. 5.2). Because data are distributed according to the track-isolation of the photon variable ($p_{\mathrm{T}}^{\mathrm{iso}}$), defined in Sec. 3.8, the likelihood *estimator* needs a parametrisation of the probability density functions modelling both the signal and the background contributions. In order to avoid a model (or simulation-induced) dependency, these probability density functions are determined from data in the form of template functions, or simply templates. Sections 5.3 and 5.4 explain the determination of the templates modelling true photons (also called prompt-photons) and the hadrons (or hadron decay products) misidentified as photons. The former defines ultimately what a photon is considered to be at the detector level. The latter defines what the response for a hadron reconstructed as a photon is.

The statistical uncertainty decreases with the increase of the number of observations, however, the modelling of the signal and of the background depends on variables of which no information is found within the $p_{\mathrm{T}}^{\mathrm{iso}}$ distribution. These variables are determined by auxiliary measurements at a certain confidence level and, therefore, their uncertainty needs to be included into the final estimation. The added uncertainty originated from the inclusion of those variables cannot increase with the increase of the number of observations in $p_{\mathrm{T}}^{\mathrm{iso}}$. They are defined as being systematic biases of the measurement, or most commonly, systematic uncertainties. Whilst the measurements of these uncertainties are explained in Chap. 7, the parameterised inclusion into the estimator of $\sigma_{t\bar{t}\gamma}$

is discussed in Sec. 5.5.

The chapter is concluded with Sec. 5.6, where the final *estimator* function is summarised. The properties of the estimator are thoroughly validated in App. D.2.

5.1 *Estimator* choice

In order to perform the inference on the true value of the $\sigma_{t\bar{t}\gamma}$ cross section, a function of the data, returning both the single value and the confidence interval, must be defined. This function is commonly called an *estimator* and its output an *estimate*. The choice of the *estimator* is not unique, but its response, *i.e.* its returned *information*, is chosen to verify some conditions. The precision of the *estimate* must increase with the number of observations (so-called statistical uncertainty) and it must be conditional with respect to what is being extracted. The conditionality means that irrelevant information of the data, with respect to the $t\bar{t}\gamma$ cross section, should not increase the precision of the *estimate* [123].

The construction of the confidence interval must be independent on the choice of the *estimator*, which is dependent on its parameterisation. An unique construction for a one parameter problem [124] can be generalised to n parameters under some conditions [125]. Whichever way the confidence interval is constructed, the reproducibility of the measurement is guaranteed when *coverage* exits.

The *estimator* chosen for this measurement is the profile likelihood ratio which is based upon the widely used maximum likelihood method. For a set of N independent observations of a variable (x) $\boldsymbol{x} = x_1 \dots x_N$ distributed according to a probability density function (F) parametrised by a common parameter set $\boldsymbol{\xi}$ ($F = f(x_i|\boldsymbol{\xi})^1$) the likelihood ($L$) is defined based upon the joint probability of the observations

$$L = L(\boldsymbol{x}|\xi) = \prod_{i=1}^{N} f(x_i|\xi) \tag{5.1}$$

and it is considered to be a function of the data. It was shown [126,127] that (under some regularity conditions) the solution for $\frac{d}{d\boldsymbol{\xi}} \ln(L) = 0$ corresponds to the maximal amount of information that can be extracted from observations.

The motivation for this choice is based upon the properties of this function. Firstly, the maximum likelihood method is proven to converge asymptotically, *i.e.* with increasing number of observations, to the true value of $\sigma_{t\bar{t}\gamma}$ [128]. Secondly, the maximum is extracted by calculating the full n-dimensional derivative $\frac{d}{d\boldsymbol{\xi}} \ln(L) = 0$ for n parameters needed to be estimated. The convergence occurs, typically, as $1/N$, but it can occur even faster. With increasing N, L is Gaussian distributed and has a parabolic shape, and it was shown that the values of the *estimate*s contained in the range $-\frac{1}{2} < \log L < +\frac{1}{2}$ guarantee coverage [123]. Thirdly, the distribution of its *estimates* is found to be invariant under transformation of an arbitrarily defined function [123], guarantying the independence of the *estimates* from the choice of the *estimator*. Finally, this definition allows for estimation from simultaneous observations (for example different $t\bar{t}\gamma$ decay channels) characterised by a different probability density function (pdf).

The analytical solution of $\frac{d}{d\boldsymbol{\xi}} \ln(L) = 0$ increases in complexity with the increase of n (and on the parametrisation of L) and it is not always achievable.

[1] As pointed out by Feldman and Cousins [125] the pedantic and usual parametrisation of a pdf is labelled by $f(x_i;\boldsymbol{\xi})$ and the labelling $f(x_i|\boldsymbol{\xi})$ identifies the conditional probability of x_i given $\boldsymbol{\xi}$. However, for consistency, $f(x_i|\boldsymbol{\xi})$ identifies here both meanings and the differentiation is given by the context.

The likelihood ratio is defined [125] as the ratio of the unconditional likelihood for $\boldsymbol{\xi}$ to the conditional likelihood of the *estimate* $\hat{\boldsymbol{\xi}}$:

$$\lambda(\boldsymbol{x}|\hat{\boldsymbol{\xi}}) = \frac{L(\boldsymbol{x}|\boldsymbol{\xi})}{L(\boldsymbol{x}|\hat{\boldsymbol{\xi}})} \tag{5.2}$$

The likelihood ratio provides a n-dimensional generalised method for determining the confidence interval upon one parameter with conditional estimation of the remainders. The estimation of parameters irrelevant to the measurement (must) conserve the conditionality principle. This method was proven to guarantee coverage [125]. The profile likelihood ratio method [129] was chosen because of its asymptotic properties, it distributes as a χ^2 probability density function with increasing number of observations N [130]. The known distribution of the likelihood method allows for an analytical integration over the parameters phase-space for the calculation of the interval of the measurement and for the calculation of the exclusion interval, when assuming that $\sigma_{t\bar{t}\gamma} = 0$ [131]. Moreover, this method guarantees the asymptotic coverage even for non parabolic shapes of the likelihood ratio.

5.2 Likelihood description

In this section, the exact definition of likelihood used in the analysis is explained. The description is generalised to the case of an inclusive cross section measurement, where the acceptance term is included in the cross section definition. The formalism below remains valid in the case of the measurement of the cross section in a fiducial region, as the acceptance term is set to unity without additional changes to the likelihood.

From the cross section definition given in Eq. 4.4 the number of signal events for the $t\bar{t}\gamma$ production process is $N_s = N - N_b$, where N and N_b are respectively the number of observed data events and estimated background events. The extended Poisson likelihood functional, representing the probability to observe N independent data events given an expectation of (N_s+N_b) in a specific range of $p_{\mathrm{T}}^{\mathrm{iso}}$ is

$$L\left(p_{\mathrm{T}}^{\mathrm{iso}} \,|\, N_s, N_b\right) = \underbrace{\frac{(N_s+N_b)^N}{N!} e^{-(N_s+N_b)}}_{\text{Poisson expectation}} \times P_{\mathrm{lum}}(\mathcal{L} \,|\, \hat{\mathcal{L}}) \times P_{\mathrm{eff}}(\varepsilon \,|\, \hat{\varepsilon}) \times \prod_{i=1}^{n} P_{\mathrm{Bck}}(b_i \,|\, \hat{b}_i) \tag{5.3}$$

where $\varepsilon = A \cdot C$ is the combined signal **efficiency** and **acceptance** and $\mathcal{L} = \int L_{\mathrm{Lumi}} dt$ is the integrated **luminosity**. Generally speaking, for a given variable x, $P(x|\hat{x})$ is the probability of x given $\hat{x}$, where $\hat{x}$ denotes the (unconditional) maximum *estimate* of x. Consequently,

- $P_{\mathrm{lum}}(\mathcal{L} \,|\, \hat{\mathcal{L}})$ describes the uncertainty on the luminosity.
- $P_{\mathrm{eff}}(\varepsilon \,|\, \hat{\varepsilon})$ describes the different systematic uncertainties, affecting the efficiency.
- $P_{\mathrm{bck}}(b_i \,|\, \hat{b}_i)$ describes the uncertainty over the i-th background b_i.

The modelling of the signal and the different backgrounds can be expressed as:

$$\begin{aligned} P(p_{\mathrm{T}}^{\mathrm{iso}} \,|\, N_s + N_b) &= P_s(p_{\mathrm{T}}^{\mathrm{iso}} \,|\, N_s + N_b) + P_b(p_{\mathrm{T}}^{\mathrm{iso}} \,|\, N_s + N_b) \\ &= \underbrace{\left(\frac{N_s}{N_s+N_b}\right) F_s(p_{\mathrm{T}}^{\mathrm{iso}} \,|\, N_s)}_{\text{Signal}} + \underbrace{\left(\frac{N_b}{N_s+N_b}\right) \sum_{i=1}^{n} F_b^i(p_{\mathrm{T}}^{\mathrm{iso}} \,|\, N_b^i)}_{\text{Backgrounds}} \end{aligned} \tag{5.4}$$

where $F_s(p_{\mathrm{T}}^{\mathrm{iso}} \mid N_s)$ and $F_b^i(p_{\mathrm{T}}^{\mathrm{iso}} \mid N_b^i)$ are pdf for the signal and the i-th background respectively. The terms $N_s/(N_s+N_b)$ and $N_b/(N_s+N_b)$ are just normalisation terms for the probability functions, with $N_b = \sum_i N_b^i$. The terms $F_s(p_{\mathrm{T}}^{\mathrm{iso}} \mid N_s)$ and $F_b^i(p_{\mathrm{T}}^{\mathrm{iso}} \mid N_b^i)$ define respectively what a (prompt) photon and a background photon are. They are based upon binned normalised track-isolation distributions (templates) derived from data and simulations. A template $T(p_{\mathrm{T}}^{\mathrm{iso}}|x)$ is related to its corresponding pdf by

$$T = \int_V dp_{\mathrm{T}}^{\mathrm{iso}} F(p_{\mathrm{T}}^{\mathrm{iso}}|x) \tag{5.5}$$

in any defined $p_{\mathrm{T}}^{\mathrm{iso}}$ range (bin) V.

The background processes to the $t\bar{t}\gamma$ production cross section are of three types: (i) background process to $t\bar{t}$ production with an additional photon, (ii) electrons misidentified as photons and (iii) hadrons, or hadron decay products, misidentified as photons.

Photons from the $t\bar{t}\gamma$ process, photons from background processes with and additional photon and electrons faking a photon are indistinguishable prompt-like objects and they share the same pdf. Therefore it is required to distinguish between two types of templates that need to be determined: the prompt-photon template (for all prompt-like objects) and the hadrons misidentified as photons template (or *hadron-fake* template for short). These two templates will provide a discrimination between signal and background through their shape differences. As it can be seen in Fig. 5.1, hadrons misidentified as photons or hadron-decay products have, typically, wide isolation distribution, because their showers developed in the electro magnetic calorimeter are accompanied with intense hadron activity. Photons and electrons have a narrower isolation distribution.

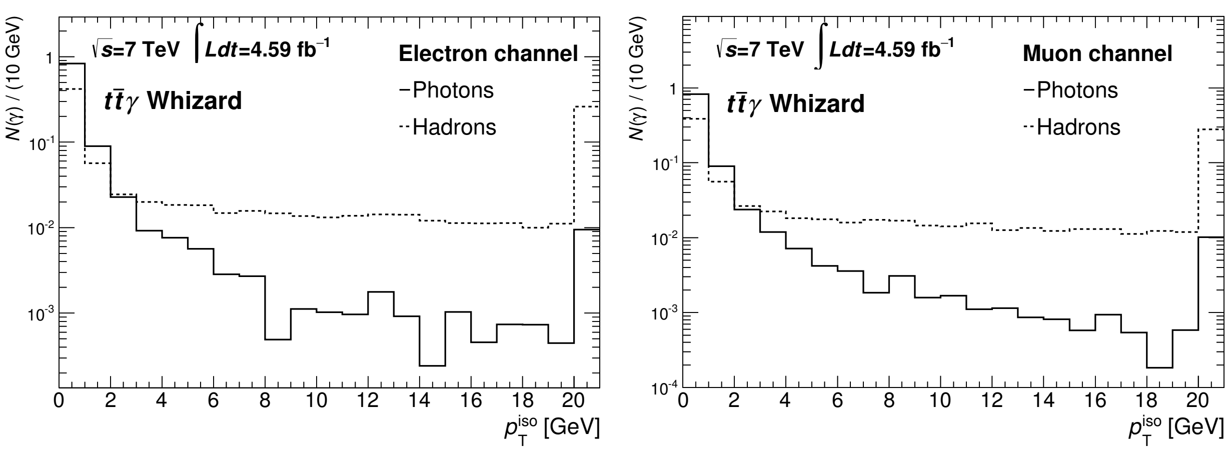

Figure 5.1: Comparison of the $p_{\mathrm{T}}^{\mathrm{iso}}(\gamma)$ distribution, as reconstructed from simulations, for photons (continuous line) and hadrons (dotted line). Distributions for the electron (muon) channel are shown on the left (right) and they are normalised to their area. The last bin contains any overflow.

The derivation of the template describing prompt-like objects is described in Sec. 5.3 while the template describing hadrons (or hadron decay products) misidentified as photons is described in Sec. 5.4. The estimation of the number of background events originating from $t\bar{t}$ background processes with an additional photon and the number of events with an electron faking a photon are described in Chapter 6.

5.3 Prompt-photon template

The template for prompt-like objects is determined from data. A Control Region (CR) enhancing candidate events from $Z(\rightarrow e^+e^-)$ decays is defined using the following selection criteria:

- A single electron trigger must have been fired.
- A good vertex with at least four associated tracks must have been reconstructed.
- The event must contain at least two electrons with opposite charge and they should match tight criteria on the shower-shapes.
- The electron with highest transverse energy must have $E_{\mathrm{T}}(e) > 25$ GeV and it has to be matched to the trigger object.
- The second E_{T}-ordered electron must have $E_{\mathrm{T}}(e) > 20$ GeV, not lie in the crack-region $(1.37 < |\eta(e)| < 1.52)$.
- The invariant mass of the electron-positron pair (e^-, e^+) must be $66 \leq m(e^-, e^+) < 106$ GeV.

The $p_{\mathrm{T}}^{\mathrm{iso}}$ distribution is considered only for the sub-leading electron. This avoids trigger-induced biases. The resulting $p_{\mathrm{T}}^{\mathrm{iso}}(e)$ distributions are shown in Fig. 5.2 in different regions of pseudorapidity and transverse energy. The dependence in $E_{\mathrm{T}}(e)$ and $\eta(e)$ spectra is assumed to be negligible. Typically, 96% of all candidate events are distributed in the first two isolation bins.

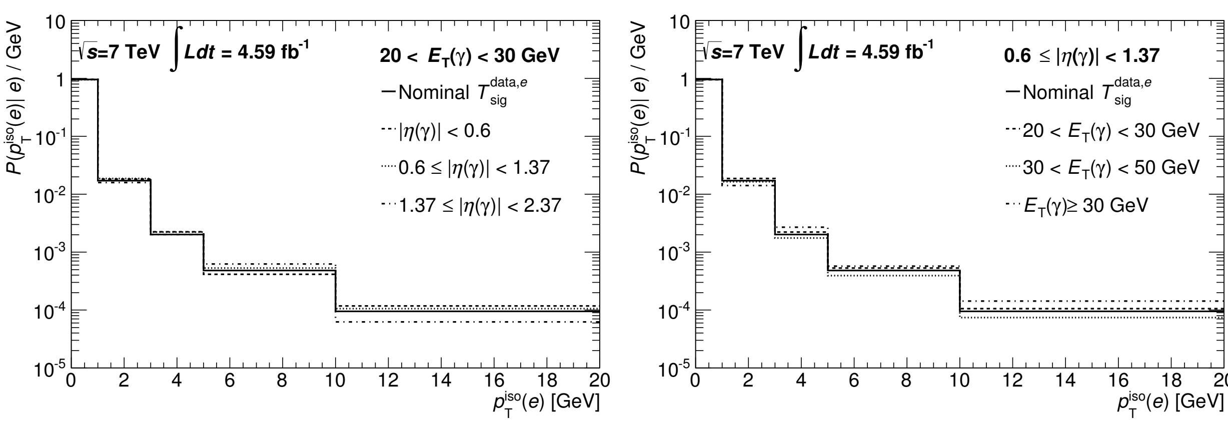

Figure 5.2: $p_{\mathrm{T}}^{\mathrm{iso}}(e)$ distributions as obtained from data $Z(\rightarrow e^+e^-)$ selection in bins of of $|\eta(e)|$ (left) and $p_{\mathrm{T}}(e)$ (right). Based on inputs derived elsewhere [86]. The distributions show the probability $P(p_{\mathrm{T}}^{\mathrm{iso}}|e)$ of observing an electron from $Z(\rightarrow e^+e^-)$ decays in a given $p_{\mathrm{T}}^{\mathrm{iso}}$ bin per GeV. The last bin contains any overflows.

Whilst the dependence on the kinematic is found to be rather small, a comparison of electrons to simulated photons from $t\bar{t}\gamma$ decays (see Fig. 5.3) shows some discrepancies. However, simulated $Z(\rightarrow e^+e^-)$ decays (with PYTHIA) are in agreement with data in $p_{\mathrm{T}}^{\mathrm{iso}}(e)$. This indicates that the differences are due to the extrapolation from electrons to photons.

The differences between electrons and photons (in $p_{\mathrm{T}}^{\mathrm{iso}}$) are a bit larger for $0.6 < |\eta(e)| < 1.81$, and in general smaller for $1.81 < |\eta(e)| < 2.37$. Furthermore, $(t\bar{t}\gamma)$ photons are less isolated with increasing transverse energy, collinear photon emissions are supposed to dominate this region.

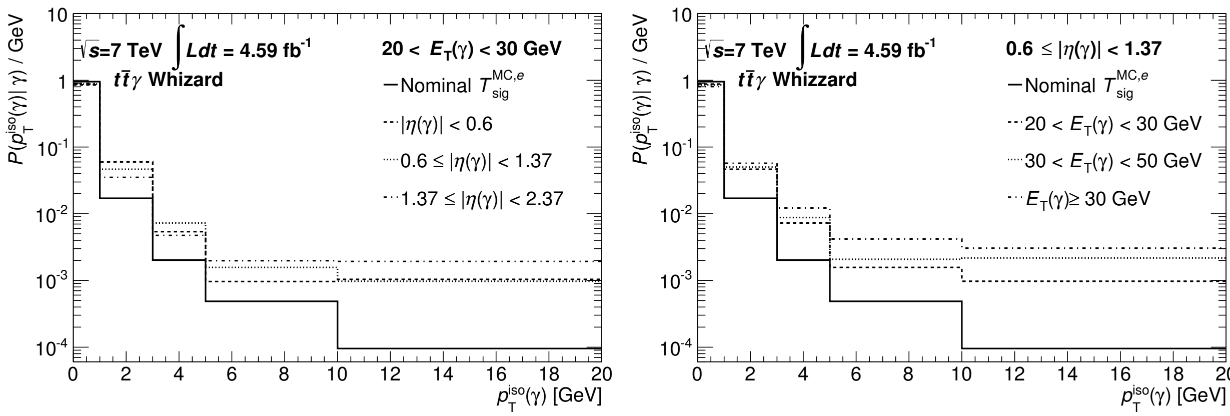

Figure 5.3: $p_{\mathrm{T}}^{\mathrm{iso}}(\gamma)$ distributions from WHIZARD simulations in bins of $|\eta(\gamma)|$ (left) and $p_{\mathrm{T}}(\gamma)$ (right). This plot was based on inputs derived elsewhere [86]. The distributions show the probability $P(p_{\mathrm{T}}^{\mathrm{iso}}|\gamma)$ of observing a photon in a given $p_{\mathrm{T}}^{\mathrm{iso}}$bin per GeV. The last bin contains any overflow.

Overall, photons (from $t\bar{t}\gamma$ decays) are less isolated than electrons (from $Z(\rightarrow e^+e^-)$). The difference can be explained due to the different jet multiplicities involved in those decays. Because the ($t\bar{t}\gamma$) photons are surrounded by large hadronic activity because of the at least four jets in the final state, a last selection requirement for at least four high-p_{T} jets in the event of Z-decays is required.

In order to obtain the final prompt-photon template, the electron $p_{\mathrm{T}}^{\mathrm{iso}}(e)$ distribution in $Z(\rightarrow e^+e^-)$ candidate data events is corrected using weights (w_i) on templates obtained from $Z(\rightarrow e^+e^-)$ ($T_{\mathrm{sig},i}^{\mathrm{MC},e}$) and $t\bar{t}\gamma$ ($T_{\mathrm{sig},i}^{\mathrm{MC},\gamma}$) simulations in twelve $E_{\mathrm{T}} \times \eta$ bins (indexed by i):

$$T_{\mathrm{sig}}^{\mathrm{data}} = T_{\mathrm{sig}}^{\mathrm{data},e} + \sum_{i=E_{\mathrm{T}},\eta \text{ bins}} w_i \left(T_{\mathrm{sig},i}^{\mathrm{MC},\gamma} - T_{\mathrm{sig},i}^{\mathrm{MC},e} \right). \tag{5.6}$$

The three E_{T} bins are defined as 20 GeV $\leq E_{\mathrm{T}} <$ 30 GeV, 30 GeV $\leq E_{\mathrm{T}} <$ 50 GeV and $E_{\mathrm{T}} \geq$ 50 GeV. The four η bins are defined as $|\eta| < 0.6$, $0.6 \leq |\eta| < 1.37$, $1.52 \leq |\eta| < 1.81$ and $1.81 \leq |\eta| < 2.37$. The relative weight for each bin i is calculated from the photon E_{T} and η spectra of the $t\bar{t}\gamma$ simulations. The final templates are shown in Fig. 5.4.

5.4 Template for hadrons misidentified as photons

The template for hadrons, or hadron decay products, misidentified as photons is derived, as for the prompt-photon template, from a CR in data. The CR is characterised by selection requirements meant to enrich the amount of hadrons. As explained in Sec. 3.5.4, the photon identification is based upon the application of rectangular cuts on the shower-shapes variables (in both the Electromagnetic Calorimeter (ECAL) and Hadronic Calorimeter (HCAL)), and upon of the information recorded by the finely η-segmented first layer of the ECAL (see Sec. 2.4.2). Hadron activity in the calorimeters is characterised by a broad electromagnetic shower profile. The application of those cuts discriminates the bulk of hadrons, and hadron decay products, against the photons. Therefore, the enrichment of hadron candidates in this CR is obtained by inverting the tight photon criteria, *i.e.* by requesting the photon candidate to fail a portion of those cuts. The following section explains in more details how this is achieved.

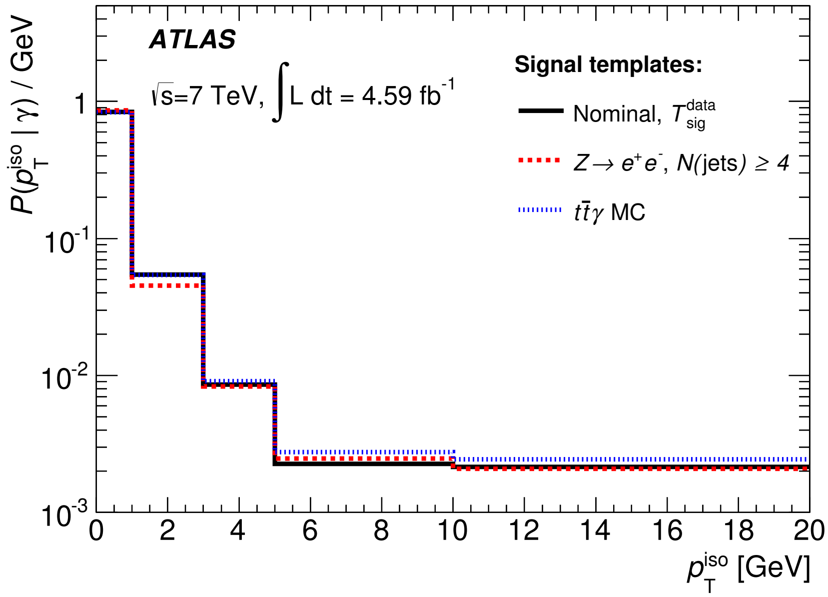

Figure 5.4: Comparison of the nominal prompt-photon track-isolation template with the template obtained from data using a $Z(\to e^+e^-)+\geq 4$ jets selection, and with the template obtained from $t\bar{t}\gamma$ simulation. The final prompt-photon template is denoted "Nominal, $T_{\rm sig}^{\rm data}$". The distributions show the probability $P(p_{\rm T}^{\rm iso}|\gamma)$ of observing a photon in a given $p_{\rm T}^{\rm iso}$ bin per GeV. The last bin contains any overflow. [132].

5.4.1 Definition of the hadron-enriched selection

A (*tight*) photon candidate is requested to fulfil all the requirements on the variables $F_{\rm side}$, $w_{\rm s,3}$, ΔE, $E_{\rm ratio}$ and $w_{s_{\rm tot}}$ (see Sec. 3.5.4). A side-band criterion to define a hadron-enriched CR would be to request the failure of at least one of those requirements, as long as they are uncorrelated (or weekly correlated). This is the case for all above variables with the exception of the total front lateral shower width ($w_{s_{\rm tot}}$), which is correlated with the track- and calorimetric- isolation distributions of photons. Therefore, any of the cuts on $F_{\rm side}$, $w_{\rm s,3}$, ΔE and $E_{\rm ratio}$ is requested to fail. This criterion is applied on candidate events events that are selected from the `JetTauEtmiss` stream with the following added requirements:

- No specific trigger is required and no matching to any trigger object is performed.
- The event must have a good primary vertex with at least six reconstructed tracks pointing to it.
- The event must contain either five jets with $p_{\rm T}(j) > 20$ GeV, or two jets with $p_{\rm T}(j) > 40$ GeV and two jets with $p_{\rm T}(j) > 20$ GeV.
- The event must contain at least a photon (failing at least one of the identification criteria listed previouselly) with $E_{\rm T}(\gamma) > 20$ GeV and $|\eta| < 2.37$.

Figure 5.5 shows the $p_{\rm T}^{\rm iso}(\gamma)$ distribution of the selected candidate events in gaps of pseudorapidity and transverse energy. Three η regions are defined $|\eta(\gamma)| \leq 0.6$, $0.6 < |\eta(\gamma)| \leq 1.37$ and

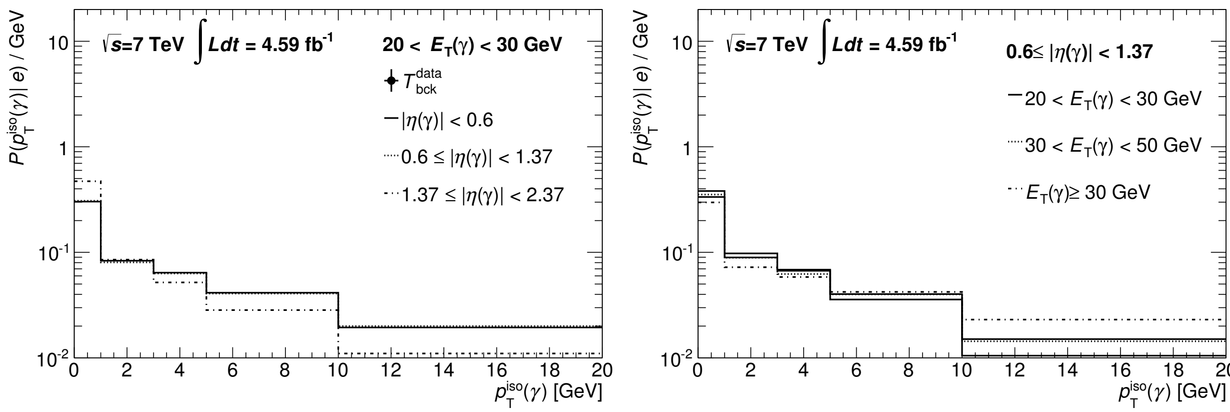

Figure 5.5: Photon track isolation from data in the CR enriched with hadron fakes in bin of $|\eta(\gamma)|$ (left) and $E_{\mathrm{T}}(\gamma)$ (right). [86]. The distributions show the probability $P(p_{\mathrm{T}}^{\mathrm{iso}}|\gamma)$ of observing a photon in a given $p_{\mathrm{T}}^{\mathrm{iso}}(\gamma)$ bin per GeV. The last bin contains any overflow.

$1.37 < \eta(\gamma) \leq 2.37$. The three E_{T} regions are defined as $20 < E_{\mathrm{T}}(\gamma) < 30$ GeV, $30 \leq E_{\mathrm{T}}(\gamma) < 50$ GeV and $E_{\mathrm{T}}(\gamma) > 50$ GeV. A small, but non negligible, dependance on the transverse energy can be identified from the distribution shown on Fig. 5.5 right: the isolation tends to degrade with increasing transverse energy. Indeed, the probability of hadron emission form jet fragmentation increases with the transverse momentum. These hadrons can be emitted with sufficient energy, and at sufficiently large angles, with respect to the jet that they can degrade the track-isolation distribution.

5.4.2 Template derivation

Because of the E_{T}- and η-dependency of the photon isolation, the final template is expressed as a function of those variables. Therefore, extrapolation weights from the CR to the $t\bar{t}\gamma$ selection have to be determined for both kinematic variables of the photon. These weights (w) are obtained from the E_{T}- and η-spectra of the photons falling at least one of the shower-shape cuts under the $t\bar{t}\gamma$ selection criteria.

The η-independent template $T_{\mathrm{bck}}^{\mathrm{data}}(I_\eta)$ in the η-range I_η is obtained from

$$T_{\mathrm{bck}}^{\mathrm{data}}(I_\eta, E_{\mathrm{T}}) = \frac{1}{\mathcal{N}_\eta} \int_{I_\eta} d\eta \; w(\eta) \; T_{\mathrm{bck}}^{\mathrm{CR}}(\eta, E_{\mathrm{T}}) \tag{5.7}$$

where the weights $w(\eta)$ are determined based on the fraction of events in any given η bin over the total number of events passing this selection requirements ($w(\eta) = \frac{N(\eta)}{N_{\mathrm{candidates}}}$), $\mathcal{N}$ is a normalisation pre-factor and $T_{\mathrm{bck}}^{\mathrm{CR}}(\eta, p_{\mathrm{T}})$ is the normalised track-isolation distribution of candidate events in the CR. Values of $w(\eta)$ are shown in Fig. 5.6 (left).

The E_{T}-dependency is treated in the same manner. The E_{T}-independent template across a range $I_{E_{\mathrm{T}}}$ of $E_{\mathrm{T}}(\gamma)$ is derived by reweighing the E_{T}-dependent templates obtained in the CR ($T_{\mathrm{bck}}^{\mathrm{CR}}(\eta, E_{\mathrm{T}})$ ranges

$$T_{\mathrm{bck}}^{\mathrm{data}}(I_{E_{\mathrm{T}}}, \eta) = \frac{1}{\mathcal{N}_{p_{\mathrm{T}}}} \int_{I_{E_{\mathrm{T}}}} dp_{\mathrm{T}} \; w(E_{\mathrm{T}}) \; T_{\mathrm{bck}}^{\mathrm{CR}}(\eta, E_{\mathrm{T}}) \tag{5.8}$$

where the weighting factors $w(E_\mathrm{T})$ are extracted from the E_T-spectrum of *hadron-fakes* in the $t\bar{t}\gamma$ selection on data. Specifically, the data spectrum is described by a Poisson pdf. In practice the Poisson distribution is approximated by an exponential function ($f_w^\mathrm{A}(E_\mathrm{T})$) and its parameters are extracted from a best fit on data:

$$f_w^\mathrm{A}(E_\mathrm{T}) = e^{-\tau E_\mathrm{T}} \tag{5.9}$$

where τ indicates the spectrum's slope. Accidental background events may distort the spectrum shape, especially at high-E_T. A second fitting function is also introduced $f_w^\mathrm{B}(E_\mathrm{T})$:

$$f_w^\mathrm{B}(E_\mathrm{T}) = e^{-\tau E_\mathrm{T}} + C \tag{5.10}$$

with C being a constant factor parametrising accidental events. Figure 5.6 (right) shows the estimation's result using both functions. It can be seen that the addition of the constant term does not bias significantly the slope. The E_T-dependent weight ($w(E_\mathrm{T})$) itself is obtained in the

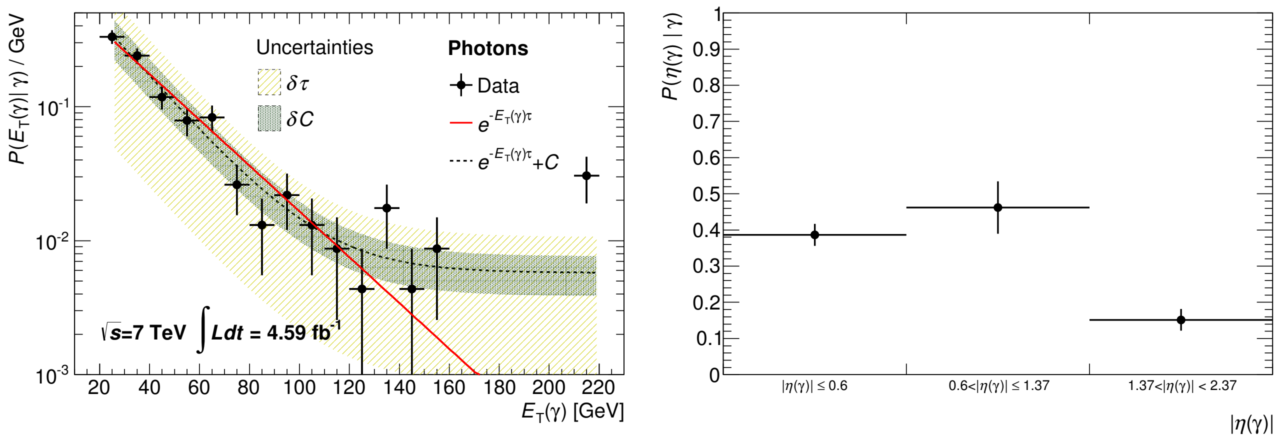

Figure 5.6: Left: The photon E_T spectrum in data with the nominal photon shower-shapes requirements replaced by the CR shower-shapes requirements [86]. The continuous (dashed) line represents the fit with an exponential (exponential plus accidental background) pdf. The hatched (dotted) filled area shows the statistical uncertainty as estimated from the fit for the τ (C) parameter. The distribution shows the probability $P(E_\mathrm{T}(e)|\gamma)$ of observing a photon in a given $E_\mathrm{T}(\gamma)$ bin per GeV. The last bin contains any overflow and it is not included in the fit. Right: probability distribution of weights $w(\eta)$, in three pseudo rapidity bins, used for deriving the η-independent template [86].

ranges of $E_\mathrm{T}(\gamma)$ as:

$$w(E_\mathrm{T}) = \frac{1}{\mathcal{C}} \int_{I_{E_\mathrm{T}}} dE_\mathrm{T}\; f_w^{i=\mathrm{A,B}}(E_\mathrm{T}) \tag{5.11}$$

with $\mathcal{C} = \int_0^\infty dE_\mathrm{T}\; f_w^{i=\mathrm{A,B}}$ being a normalisation constant and I_{E_T} the bin ranges. The weights as a function of the $E_\mathrm{T}(\gamma)$ bins used in this measurement are summarised in Tab. 5.1.

The final *hadron-fake* template $T_\mathrm{bkg}^\text{data, nom}$ is build from both the E_T-and η- dependent templates in the CR $(T_\mathrm{bck}^\mathrm{CR}(E_\mathrm{T},\eta))$

$$T_\mathrm{bkg}^\text{data, nom} \equiv T_\mathrm{bkg}^\text{data, nom}(I_{E_\mathrm{T}}) = \frac{1}{\mathcal{N}} \int_{I_\eta} d\eta \int_{I_{E_\mathrm{T}}} dE_\mathrm{T}\; T_\mathrm{bck}^\mathrm{CR}(E_\mathrm{T},\eta) = \frac{1}{\mathcal{N}} \left[T_\mathrm{bck}^\mathrm{data}(\eta) \oplus T_\mathrm{bck}^\mathrm{data}(E_\mathrm{T})\right] \tag{5.12}$$

$I_{E_{\rm T}}$[GeV]	$dw^{\rm A}/dE_{\rm T}$[GeV^{-1}]	$dw^{\rm B}/dE_{\rm T}$[GeV^{-1}]	δw[GeV^{-1}]
$20 < E_{\rm T}(\gamma) < 30$	3.18	3.49	± 0.50
$30 \leq E_{\rm T}(\gamma) < 40$	2.14	2.17	± 0.18
$40 \leq E_{\rm T}(\gamma) < 50$	1.45	1.36	± 0.10
$50 \leq E_{\rm T}(\gamma) < 70$	1.64	1.41	± 0.20
$70 \leq E_{\rm T}(\gamma) < 120$	1.18	1.01	± 0.22
$120 \leq E_{\rm T}(\gamma) < 180$	0.17	0.41	± 0.13
$180 \leq E_{\rm T}(\gamma) < 250$	0.02	0.41	± 0.17
$250 \leq E_{\rm T}(\gamma) < 300$	10^{-3}	0.29	± 0.14
$E_{\rm T}(\gamma) \geq 300$	$< 10^{-3}$	0.46	± 0.20

Table 5.1: Differential weights used in Eq. 5.8 for the determination of $E_{\rm T}$-independent templates in each $E_{\rm T}$-bin $I_{E_{\rm T}}$. The column labelled $dw^{\rm A}/dE_{\rm T}$ shows the weights obtained with $f_w^{\rm A}(E_{\rm T})$, while the column labelled $f_w^{\rm B}(E_{\rm T})$ shows the weights obtained with $f_w^{\rm B}(E_{\rm T})$. The column labelled δw shows the uncertainty as estimated from the fit.

with $\mathcal{N}$ being normalisation factor. It is considered to be $E_{\rm T}$- and η- independent in the entire ranges $I_{E_{\rm T}}$ and I_η.

For the extraction of the $\sigma_{t\bar{t}\gamma}$ spectrum in $E_{\rm T}(\gamma)$ bins, the *hadron-fake* template has to retain its $E_{\rm T}(\gamma)$ dependency, this is achieved within the likelihood modelling, as explained in Sec. 5.5.1. However, the effect on the cross section of the $E_{\rm T}$-dependency is found to be less than one percent.

5.4.3 Prompt-photon contamination

The templates determined in Sec. 5.4.2 are based on the requirement that at least one, but not all, shower-shape variable fails the tight identification criterion, therefore (prompt-) photons may leak into the hadron-enriched CR. This eventual leakage (referred here also as the prompt-photon contaminant) causes the definition of the pdf for the *hadron-fakes* to be, eventually, biased. Therefore, the probability of a photon to be identified as a hadron or a hadron decay product needs to be estimated. This section explains the method used for extracting this probability from data and the method used for correcting the templates obtained in Eq. 5.12 for this leakage.

In order to extract the prompt-photon contamination in the *hadron-fake* template, a simple extended likelihood function L_f is maximised:

$$L_f = \frac{n_{\rm tot}^{N_{\rm f}} e^{n_{\rm tot}}}{N_{\rm f}!} \times n_{\rm tot} \times \left[\left(1 - f\,\hat{\theta}\right) T_{jj}^{\rm MC} + f\,\hat{\theta}\, T_{\rm sig}^{\rm data,\gamma}\right] \times \frac{1}{\sqrt{2\pi\sigma_\theta^2}} \exp\left[-\frac{(\theta-\hat{\theta})^2}{2\sigma_\theta^2}\right] \tag{5.13}$$

where $N_{\rm f}$ is the total number of events observed in data within the *hadron-fake* background control region, f is the fraction of prompt-photons leaking into this region, $T_{jj}^{\rm MC}$ is a simulation-based background template modelling the probability of true *hadron-fakes* (*i.e.* without photon contamination) and $T_{\rm sig}^{\rm data,\gamma}$ is the signal template of Eq. 5.6. The parameter $\hat{\theta}$ represents the added uncertainty on f and it is considered to be a *nuisance* to the determination of f, the latter being distributed according to a Gaussian pdf of mean $\theta = 1$ and width σ_θ.

Simulation-based templates

Dijet (j, j') ensembles generated with `PYTHIA` at different $E_{\mathrm{T}}(j)$ jet thresholds have been used (see table 5.2). These simulations are based on the Leading-Order (LO) perturbative QCD matrix elements for the $pp \to jj'$ hard sub-processes, with initial- and final- state radiation included with a p_{T}-ordered parton showering algorithm calculated in a leading-logarithmic approximation. The generated samples use an underlying event model for multiple parton interactions and the Lund string model for hadronisation [133]. `PYTHIA` LO jet samples have been used in previous ATLAS analyses, *e.g.* for studies on multi-jet production with up to six jets in the final state [134].

Description	**FE $\times$ σ [nb]**
`PYTHIA` JF17 filtered dijet, $E_{\mathrm{T}}(j) > 17$ GeV	1.4×10^{6}
`PYTHIA` JF35 filtered dijet, $E_{\mathrm{T}}(j) > 35$ GeV	6.4×10^{4}
`PYTHIA` JF70 filtered dijet, $E_{\mathrm{T}}(j) > 70$ GeV	3.7×10^{3}

Table 5.2: `PYTHIA` jet samples used to extract the simulation-based background templates $T^{\mathrm{MC}}_{j\gamma}$ and T^{MC}_{jj}. Dijet events are selected before detector simulation, the corresponding Filter Efficiency (FE) multiplied by the matrix element cross section is shown.

The following procedure has been followed:

- At first, the same selection as used for the data-based extraction of the *hadron-fake* templates is applied, see Sec. 5.4.1.
- Then, two different track-isolation templates, $T^{\mathrm{MC}}_{j\gamma}$ and T^{MC}_{jj}, are obtained according to the following additional selections:
  - **Jet-photon selection $T^{\mathbf{MC}}_{j\gamma}$**: events are required to have a photon candidate passing the tight identification criteria excepting for one of the four strip variables F_{side}, $w_{\mathrm{s},3}$, ΔE, E_{ratio}.
  - **Jet-jet selection $T^{\mathbf{MC}}_{jj}$**: information from the High Energy Monte Carlo Record (HepMC) [120] is used directly to discard events containing photons.

Therefore, the $T^{\mathrm{MC}}_{j\gamma}$ and T^{MC}_{jj} templates represent the probability, obtained from simulations, of *hadron-fakes* with and without the prompt-photon contamination respectively (*i.e.*, $T^{\mathrm{MC}}_{j\gamma}$ should be comparable to the nominal data-based template as the contamination in the control region is unknown in data; T^{MC}_{jj} corresponds to an ideal non-contaminated *hadron-fake* template).

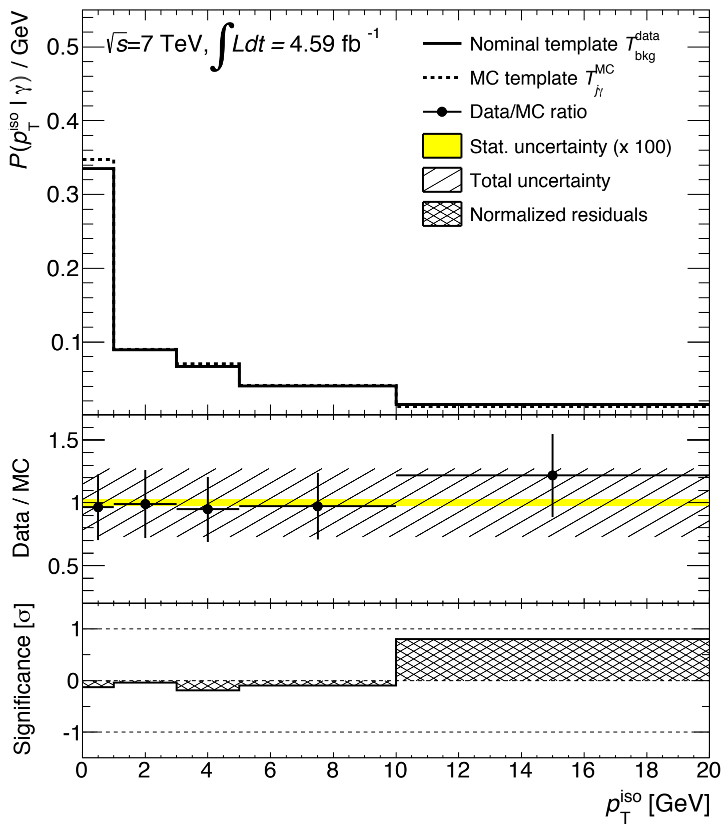

Figure 5.7: Comparison of the data-driven $T_{\rm bkg}^{\rm data,\ nom}$ and MC-based $T_{j\gamma}^{\rm MC}$ background templates (top), ratio of the two templates (middle) and normalised residuals (bottom). In the middle plot, considering the statistical uncertainty only, the two templates disagree. Including an uncertainty of 27% (obtained from a χ^2 test-statistic using pseudo-experiments), and as indicated by the dashed area, an agreement is reached. The maximal deviation of the normalised residuals (bottom) is below 1σ.

Determination of σ_θ

Without accounting for systematic uncertainties, the nominal data-based $T_{\mathrm{bkg}}^{\mathrm{data,\ nom}}$ and the simulation-based $T_{j\gamma}^{\mathrm{MC}}$ background templates do not agree (the statistical uncertainty $\mathcal{O}(10^{-4})$ is negligible in both cases). These two templates are shown in the upper plot of Fig. 5.7. The maximum difference is found to be about 18% at the last $p_{\mathrm{T}}^{\mathrm{iso}}$ bin.

In order to account for this simulation-to-data discrepancy, an uncertainty to the simulation-based template is extracted from a χ^2 test-statistic using pseudo-experiments. The amount of uncertainty on the overall normalisation, *i.e.* over the total number of events, is randomised and the χ^2 between the $T_{\mathrm{bkg}}^{\mathrm{data,\ nom}}$ and $T_{j\gamma}^{\mathrm{MC}}$ templates is calculated. As shown in Fig. 5.8, the p-value reaches a plateau (p-value > 0.95) at a value of 27% uncertainty. After inclusion of this additional uncertainty, both templates agree within 1σ.

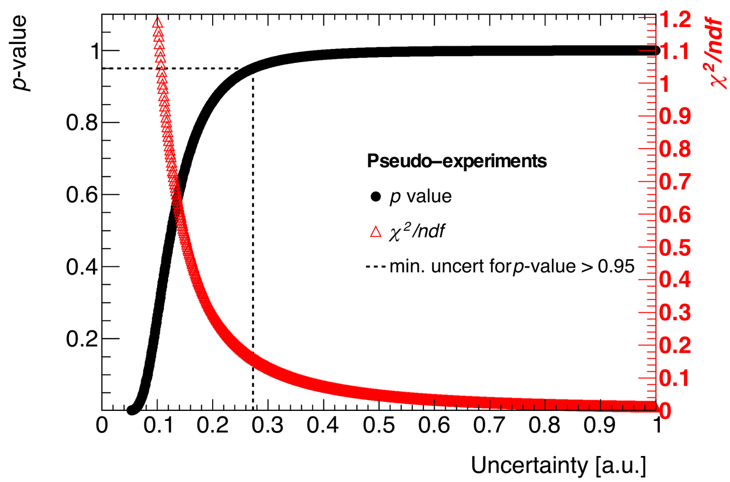

Figure 5.8: χ^2/ndf and p-value of the $T_{\mathrm{bkg}}^{\mathrm{data,\ nom}}$ and $T_{j\gamma}^{\mathrm{MC}}$ templates as a function of the background uncertainty as obtained from pseudo-experiments. The dashed lines indicates the minimal value for which the p-value > 0.95.

Extraction of the fraction f

The likelihood function L_f of Eq. 5.13 is used to fit the data in the *hadron-fake* control region to extract the amount of signal (true prompt-photons) leaking into the background template. The uncertainty on the nuisance parameter $\hat{\theta}$, σ_θ, is taken as the 27% uncertainty to the simulation-based template as explained previously. The fraction of prompt-photon contamination f is derived from the minimisation of L_f (eq. 5.13).

Upper and lower limits to f are extracted at a 68.3% Confidence Level (CL) by constructing the confidence belt with the *Feldman-Cousins* technique [125] using pseudo-experiments. The profile likelihood ratio is chosen as the ordering principle for the construction. Fig. 5.9 shows such interval on a set of 10^5 pseudo-experiments. The result of the fit is shown in Fig. 5.10 from which f is found to be:

$$f = \left(6.1^{+1.7}_{-0.9}(\mathrm{syst})\right) \times 10^{-2}. \tag{5.14}$$

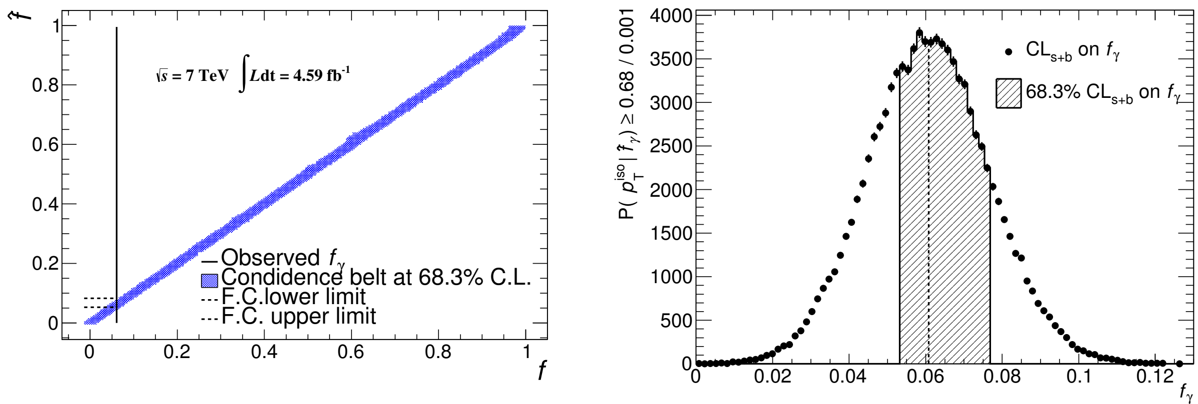

Figure 5.9: Extraction of the upper and lower limits on the fraction f. The Feldman Cousins (F.C.) confidence belt, as obtained from pseudo-experiments, is shown on the left. The horizontal line (observed f) corresponds to the maximum of the likelihood evaluated on data, while the dotted horizontal lines correspond to the upper and lower limits of the 68.3% Confidence Level (CL). The distribution of the *estimates* of f is shown on the right. The points represent the estimated values of f using pseudo-experiments; the dashed area corresponds to the interval covering a 68.3% CL. The dotted line represents the best fit value of f.

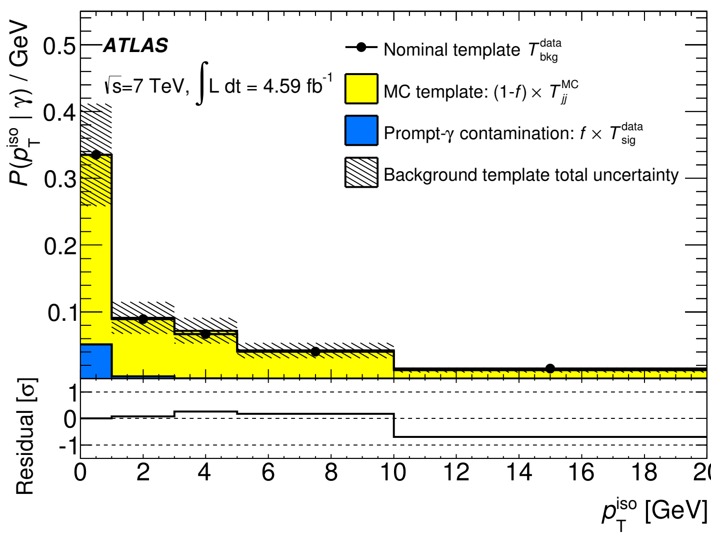

Figure 5.10: Track-isolation background template distribution after maximisation of the likelihood L_f defined in Eq. 5.13 (top) and normalised residuals (bottom). The markers correspond to the nominal hadron background template. The stacked filled histograms represent the fraction of prompt photons in the hadron-fake control region (obtained as $f \times T_{\text{sig}}^{\text{data}}$) and the fraction of hadron-fakes (obtained from the simulation-based template as $(1-f) \times T_{jj}^{\text{MC}}$) as given by the fit. The normalised residuals, shown in the bottom plot, are defined as the difference between the "Nominal template" and the sum of $(1-f) \times T_{jj}^{\text{MC}}$ and $f \times T_{\text{sig}}^{\text{data}}$, divided by the total uncertainty σ_θ. The last bin contains any overflow [132].

5.5 Modelling of uncertainties

In this section the inclusion of systematic uncertainties in the likelihood is discussed. For a correct parametrisation in the likelihood the deduced confidence interval on $\sigma_{t\bar{t}\gamma}$ must decrease in size with the increase of the number of observations. However, it also must increase in size with the increase of the systematic component of the uncertainty. This component must be broken-down into individual parameters for each individual uncertainty source. Specific parameters modelling the template shapes or affecting only a background contribution are labelled by α, while the remainder (generic) parameters modelling efficiency changes are labelled by the θ. These parameters are of no interest to the final measurement, but their *estimates* need, however, to be determined. For this reason they are so-called nuisance parameters (or simply nuisances). In fact, their value and uncertainty are truly determined by separate estimations (so-called auxiliary measurements) thoroughly detailed in Chap. 7. No real information is, usually, contained within the data used extract the $\sigma_{t\bar{t}\gamma}$. Therefore, their determination trough the likelihood should not decrease the confidence level on the cross section.

Let the uncertainty on the integrated luminosity ($\mathcal{L}$) be an example. In $p_{\mathrm{T}}^{\mathrm{iso}}$ there is no information about the value of the luminosity, however the cross section depends upon it. The value of, and uncertainty on, the luminosity are estimated through Van der Meer scans in dedicated Large Hadron Collider (LHC) runs. This is a typical example of an auxiliary measurement. While it is clear that the result of this measurement should be included in the likelihood as the luminosity affects the cross section, it is also clear that changes in the $t\bar{t}\gamma$ selection should not affect the value of $\mathcal{L}$ nor its error.

Being properly strict, from the *frequentist* point of view the observations, upon which these parameters are truly determined, should be added to the portion of data used for the inference on the cross section. However, given the sheer number of the parameters and corresponding observations the inclusion of the auxiliary data is in practice almost impossible. Approximations are used istead. The incorporation in the likelihood modelling is two-fold.

1. An interpolation of each θ (α) must be made to the cross section (and to each N_{b^i}). This interpolation must be calibrated such as any unit change of the *estimate* $\hat{\theta}$ ($\hat{\alpha}$) corresponds to the desired shift of $\sigma_{t\bar{t}\gamma}$ (N_{b^i}).

2. An assumption must be made on each pdf modelling each nuisance parameter. These pdf are included into the likelihood, making use of its properties, as multiplicative terms (see Eq. 5.3).

The choice of the pdf modelling is motivated in Sec. 5.5.3. The description of the interpolation is split into the simpler case where no correlation between parameters is introduced (Sec. 5.5.4), and to a more general case where (some) parameters are allowed to be correlated to each other (see Sec. 5.5.5).

5.5.1 Template modelling in the likelihood

Nuisance parameters can also model the shape of the template distributions. ATLAS analyses typically use algorithms to define parametric functions of the templates with respect to the variation [135]. The parametrisation is often referred to as *morphing*. Several techniques exist with varying complexity. In the analysis presented in this thesis, an *ad hoc* technique is developed.

It is based on the assumption that any template T can be expressed as a perturbative expansion:

$$T(p_{\mathrm{T}}^{\mathrm{iso}}|\alpha) = T_0\left(p_{\mathrm{T}}^{\mathrm{iso}}\right) + \sum_{i=1}^{\infty} \frac{\alpha^i}{\mathcal{C}_i}\left[T_0(p_{\mathrm{T}}^{\mathrm{iso}}) - T_i(p_{\mathrm{T}}^{\mathrm{iso}})\right] \tag{5.15}$$

with $T_i(p_{\mathrm{T}}^{\mathrm{iso}})$ being the systematic correction in the order i and α characterising the strength of this correction. As usual, $\mathcal{C}_i$ are a normalisation coefficients.

Assuming small corrections, $T(p_{\mathrm{T}}^{\mathrm{iso}}|\alpha)$ is approximated linearly by:

$$T(p_{\mathrm{T}}^{\mathrm{iso}}|\alpha) \simeq \frac{1}{\mathcal{C}}\left[(1-\alpha)T^{\mathrm{nom}}\left(p_{\mathrm{T}}^{\mathrm{iso}}|\alpha\right) + \alpha\ \pi(\alpha)\ T^{\mathrm{corr.}}(p_{\mathrm{T}}^{\mathrm{iso}}|\alpha)\right] \tag{5.16}$$

where $T^{\mathrm{corr.}}$ indicates a template with a systematic variation, α is a parameter which is allowed to float and sizes the strength of the correction. The term $\pi(\alpha)$ acts as a response function, normalising unit changes of α to template variations, such as α is centred around zero. $\mathcal{C}$ is a global normalisation constant.

The approximation of small corrections remains valid as long as the deviations of the *estimate* of α are small with respect to its (nominal) input value (zero). These variations are constrained by a pdf, the variance of which corresponds to the measured uncertainty on α. Section 5.5 motivates the choice of such pdf. The examination of the *post*-fit pull (normalised differences with respect to the input) on α gives the size of the correction. As long as the pull is consistent with zero (and variance one), then the small corrections approximation remains valid. Extensive tests are shown in parallel with the results on the cross section, in Sec. 8.2.

This correction is applied in order to model the $E_{\mathrm{T}}(\gamma)$ dependence of the templates, as well as the extrapolation from electrons to photons (for the signal template only). Figure 5.11 shows the two-dimensional probability for the signal template as a function of the correction α and $p_{\mathrm{T}}^{\mathrm{iso}}$. Similarly the $E_{\mathrm{T}}(\gamma)$ dependence in the *morphing* parameter is shown in Fig. 5.12. For the $E_{\mathrm{T}}(\gamma)$ dependence two interpolations are made, modelling upwards ($\alpha_{E_{\mathrm{T}}}^{\mathrm{up}}$) and downwards ($\alpha_{E_{\mathrm{T}}}^{\mathrm{down}}$) variations of the photon E_{T} with respect to the nominal template.

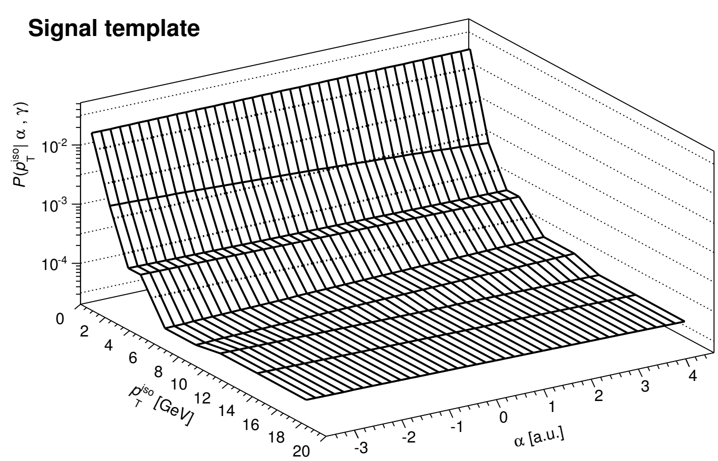

Figure 5.11: Parametrisation of $T_{\mathrm{sig}}^{\mathrm{data}}$ as a function of α and $p_{\mathrm{T}}^{\mathrm{iso}}$, modelling the electron to photon extrapolation

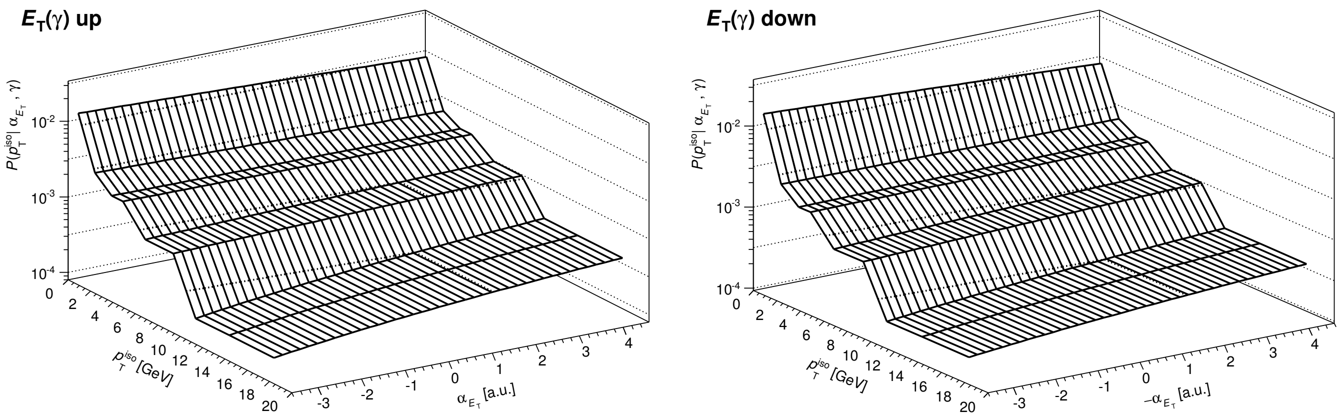

Figure 5.12: Parametrisation of $T_{\mathrm{bkg}}^{\mathrm{data,\ nom}}$ as a function α and $p_{\mathrm{T}}^{\mathrm{iso}}$, modelling the $E_{\mathrm{T}}(\gamma)$ dependence. Upwards (downwards) variations with respect to the E_{T}-independent $T_{\mathrm{bkg}}^{\mathrm{data,\ nom}}$ are shown on the left (right).

In the differential measurement each nominal template is calibrated to its corresponding $E_{\mathrm{T}}(\gamma)$ weight, see Tab. 5.1 by shifting the nominal value of parameter $\alpha_{E_{\mathrm{T}}(\gamma)}^{\mathrm{down,up}}$ accordingly. In the inclusive measurement the no E_{T}-dependence of the templates was used, and the corresponding uncertainty was found to be small.

5.5.2 Modelling of the prompt-photon contamination in the *hadron-fake* template

The *hadron-fake* template describes the binned probability of a jet being mis-reconstructed as a photon. While the nominal fake background template is extracted using a data-based procedure, the residual contamination of true prompt-photons inside the template is extracted by combining data and simulation-based templates. In order to avoid a binned simulation-dependency in the nominal likelihood fit (used to compute the cross section), the fact that the prompt-photons are distributed according to the signal template $T_{\mathrm{sig}}^{\mathrm{data},\gamma}$ is used. The corrected fake template $T_{\mathrm{bkg}}^{\mathrm{corr}}$, taking into account the prompt-photon contamination, can thus be parametrised as

$$T_{\mathrm{bkg}}^{\mathrm{corr}}(p_{\mathrm{T}}^{\mathrm{iso}} \mid N_b^{\mathrm{fake}}) = \left(\frac{1}{1-\alpha_{\mathrm{fake}}\cdot f}\right)\left[T_{\mathrm{bkg}}^{\mathrm{data,\ nom}}(p_{\mathrm{T}}^{\mathrm{iso}} \mid N_b^{\mathrm{fake}}) - \alpha_{\mathrm{fake}}\cdot f \times T_{\mathrm{sig}}^{\mathrm{data},\gamma}(p_{\mathrm{T}}^{\mathrm{iso}} \mid N_b^{\mathrm{fake}})\right] \tag{5.17}$$

where N_b^{fake} is the number of *hadron-fakes*, $T_{\mathrm{bkg}}^{\mathrm{data,\ nom}}$ is the data-based nominal (*i.e.* uncorrected) background template, f is the prompt-photon contamination and α_{fake} is a scale-factor modelling the strength of the correction. In the case of no correction being applied $\alpha_{\mathrm{fake}} = 0$ and hence $T_{\mathrm{bkg}}^{\mathrm{corr}} \equiv T_{\mathrm{bkg}}^{\mathrm{data,\ nom}}$. As usual, the term $1/(1-\alpha_{\mathrm{fake}}\cdot f)$ is just a normalisation factor.
Figure 5.13 shows the effect of different strength factors in the *hadron-fake* background template. The case $\alpha_{\mathrm{fake}} = 0$ corresponds to not applying any correction (*i.e.* using the nominal, contaminated, background template $T_{\mathrm{bkg}}^{\mathrm{data,\ nom}}$), while $\alpha_{\mathrm{fake}} = 1$ corresponds to the usage of the corrected template $T_{\mathrm{bkg}}^{\mathrm{corr}}$.

Because of the partial model dependency of f, the strength factor α is let free to float and is determined by the data in the likelihood fit. This strength factor is treated as a nuisance parameter

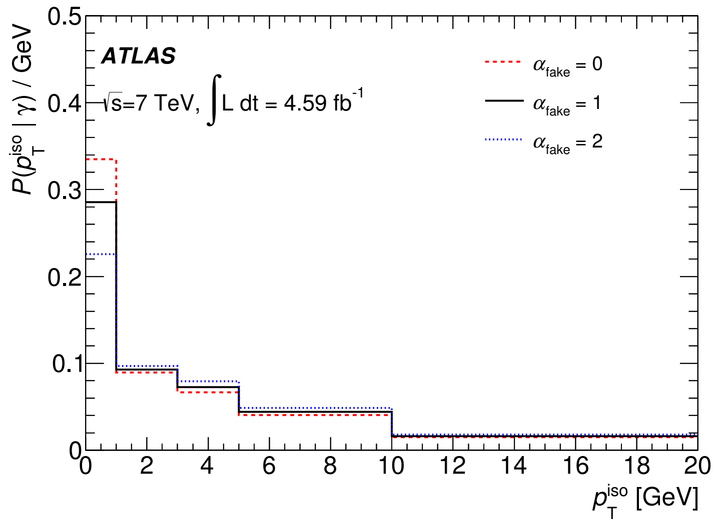

Figure 5.13: Modeling of the *hadron-fake* template as a function of the fraction of true photons in the background control region. The strength factor α_{fake} is varied from $\alpha_{\text{fake}} = 0$ to $\alpha_{\text{fake}} = 2$. The nominal value corresponds to $\alpha_{\text{fake}} = 1$ (corresponding to the corrected data-driven template $T_{\text{bkg}}^{\text{corr}}$), while the templates for $\alpha_{\text{fake}} = 0$ and $\alpha_{\text{fake}} = 2$ correspond respectively to the $\pm 1\,\sigma$ variation of f.

and, as described in section Sec. 5.5.4, it is constrained by a Gaussian pdf which's width is set to 27% corresponding to the maximum uncertainty estimated on f (see Eq. 5.14).

5.5.3 Choice of probability density functions

The choice of the pdf with which the nuisance parameters distribute is typically the normal distribution $\mathcal{N}$:

$$\mathcal{N}(x|\,\hat{x},\,\sigma_x) = \frac{1}{\sqrt{2\pi\sigma_x^2}} \exp\left[-\frac{(x-\hat{x})^2}{2\sigma_x^2}\right] \tag{5.18}$$

upon an observable x with mean $\hat{x}$ and variance σ_x. This is motivated by the central limit theorem [136], according which the *estimator* of the mean, of any well defined pdf (with fixed variance), is normally distributed.

Re-using the example of the integrated luminosity, if the measurement was to be repeated with several Van Der Meer scans, then the results would distribute according to the normal distribution.

Moreover, the majority of nuisance parameters are considered to have a well defined pdf, so $\mathcal{N}$ is a correct approximation. For a small fraction of systematic components this is not obvious. For example, the parametrisation with a normal distribution of systematic uncertainties evaluated from two disconnected variations, such as the choice of the Monte Carlo (MC) generator or the choice of parton shower program, see Sec. 7.1.

The argument in this case is the fact that, because these sources are calculated from the two point variation of a large number of different type parameters varied simultaneously, which may share very different distributions, in some cases their pdf is not clearly defined or are unphysical. This mis-modelling can be resolved by the definition of a pdf which is continuous with a flat top and rapidly falling to zero for values close to its variance

$$\mathcal{B}(x|\ \hat{x},\ \sigma_x) = \frac{1}{2}\left\{\tanh\left[\left(\frac{x-\hat{x}}{\sqrt{\sigma_x}}\right)^{-2}\right] - \tanh\left[-\left(\frac{x-\hat{x}}{\sqrt{\sigma}}\right)^{-2}\right]\right\}. \tag{5.19}$$

The variance σ_x of $\mathcal{B}(x|\hat{x}, \sigma_x)$ corresponds to the estimated uncertainty on the nuisance parameter x, associated to a two-point systematic variation. It is approximatively constant for (small) variations of x, therefore independent of the unphysical meaning of x. A comparison of $\mathcal{B}(x|\hat{x}, \sigma_x)$ with $\mathcal{N}(x|\hat{x}, \sigma_x)$ with respect to an equally increasing variance is shown in Fig. 5.14. It can be seen that compared to the normal distribution, $\mathcal{B}(x|\hat{x}, \sigma_x)$ is has a near-to-constant probability value for ranges of $x \leq \sigma$.

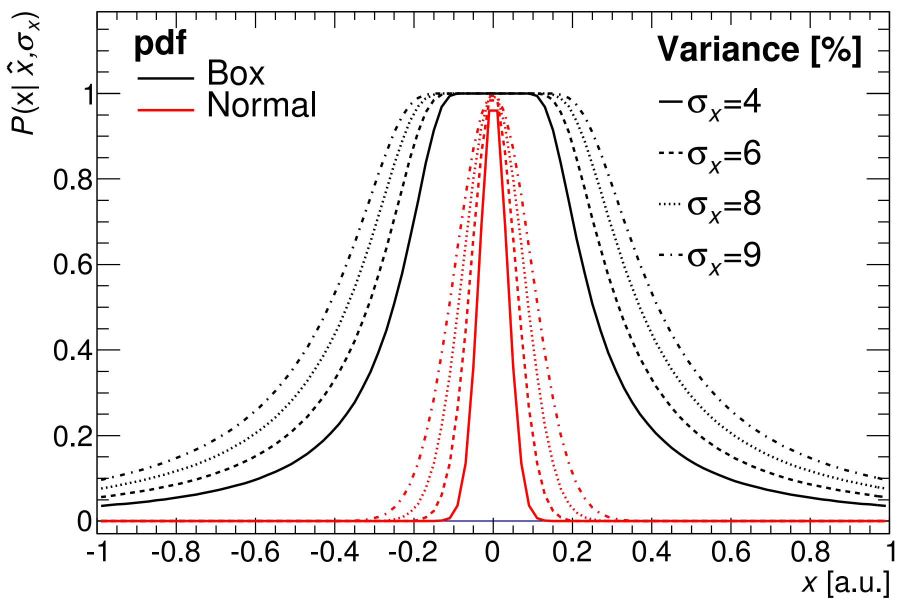

Figure 5.14: Comparison with increasing variance of the normal distribution and the square distribution. The black lines labelled by "Box pdf" correspond to $\mathcal{B}(x|\hat{x}, \sigma_x)$ and the red lines labelled by "Normal pdf" correspond to $\mathcal{N}(x|\hat{x}, \sigma_x)$.

In a first moment, the $\mathcal{B}(x|\hat{x}, \sigma_x)$ pdf was included into the likelihood to be associated with nuisance parameters modelling systematic uncertainties estimated from variable variations of which the true physical distribution is unknown (specifically the signal modelling systematic uncertainties: MC generator choice, parton shower, etc. . . , see Sec. 7.1). However, as with either $\mathcal{B}(x|\hat{x}, \sigma_x)$ or $\mathcal{N}(x|\hat{x}, \sigma_x)$ modelling in the likelihood similar uncertainties on x and on the cross section were observed it was, finally, chosen to model all uncertainties by Gaussian pdf, as it eases the reproducibility (or future combination with other measurements) of the result.

5.5.4 Modelling of uncorrelated uncertainties

As explained in the previous section, every systematic uncertainty is associated to an independent nuisance parameter θ_i which is distributed according to a normal distribution as:

$$P_i^{\mathrm{Sys}}(\theta_i \,|\, \hat{\theta}_i) = \mathcal{N}(\theta_i | \, \hat{\theta}_i, \, \sigma_{\theta_i}) = \frac{1}{\sqrt{2\pi\sigma_{\theta_i}^2}} \exp\left[-\frac{(\theta_i - \hat{\theta}_i)^2}{2\sigma_{\theta_i}^2} \right] \tag{5.20}$$

where $\hat{\theta}_i$ is the unconditional best fit and σ_{θ_i} is its associated uncertainty. By denoting $\boldsymbol{\theta} = \{\theta_0, \ldots, \theta_{\mathrm{Sys}}\}$ the vector of all nuisance parameters, the effect of each systematic in the cross section measurement is taken into account by promoting the efficiency to be a function of the nuisance parameters:

$$\varepsilon \times \sigma_{t\bar{t}\gamma} \quad \to \quad \varepsilon(\boldsymbol{\theta}) \times \sigma_{t\bar{t}\gamma}. \tag{5.21}$$

Similarly, the uncertainty on the number of background events N_b^i is modelled with a Gaussian pdf:

$$P_i^{\mathrm{Bck}}(b_i \,|\, \hat{b}_i) = \mathcal{N}(N_{b_i} | \hat{N}_{b_i}, \, \sigma_{b_i}) = \frac{1}{\sqrt{2\pi\sigma_{b_i}}} \exp\left(\frac{N_{b_i} - \hat{N}_{b_i}}{\sigma_{b_i}} \right)^2 \tag{5.22}$$

The mean $\hat{N}_{b_i}$ and width σ_{b_i} of each Gaussian probability function correspond respectively to the prediction and to the uncertainty estimated for the corresponding background component. For both the combined efficiency ε and the integrated luminosity $\mathcal{L} = \int L_{\mathrm{Lumi}} dt$, also Gaussian pdf are used to model the uncertainty on the corresponding parameter, so that:

$$P_{\mathrm{eff}}(\varepsilon|\hat{\varepsilon}) = \mathcal{N}(\varepsilon|\hat{\varepsilon}, \sigma_\varepsilon) = \frac{1}{\sqrt{2\pi\sigma_\varepsilon}} \exp\left(\frac{\varepsilon - \hat{\varepsilon}}{\sigma_\varepsilon} \right)^2 \quad , \quad P_{\mathrm{lum}}(\mathcal{L} \,|\, \hat{\mathcal{L}}) = \frac{1}{\sqrt{2\pi\sigma_{\mathcal{L}}}} \exp\left(\frac{\mathcal{L} - \hat{\mathcal{L}}}{\sigma_{\mathcal{L}}} \right)^2 \tag{5.23}$$

The effect of the different systematic uncertainties in the fit is to widen the likelihood according to the Gaussian pdf describing each systematic source irrespectively of the number of observations N. Considering a different combined efficiency $\varepsilon^\ell = (A \cdot C)_\ell$ for each lepton channel ℓ, the optimal interpolation to each parameter (and consequently to $\sigma_{t\bar{t}\gamma}$) is chosen to be:

$$\varepsilon^\ell \times \sigma_{t\bar{t}\gamma} \quad \to \quad \varepsilon^\ell(\boldsymbol{\theta}^\ell) \times \sigma_{t\bar{t}\gamma} = \varepsilon^\ell \times \prod_{i=1}^{N_{\mathrm{Sys.}}} \theta_i^\ell \times \sigma_{t\bar{t}\gamma} \tag{5.24}$$

where $\boldsymbol{\theta}^\ell = \{\theta_1, \, \ldots, \, \theta_{N_{\mathrm{Sys.}}}\}_\ell$ denotes the vector of systematic nuisances over the channel ℓ. All nuisance parameters, and corresponding pdf, are set such as $\hat{\theta}_i^\ell$ distribute around one.

In a similar way, each background N_{b_i} parameter is subject to the penalty term:

$$N_{b_i} \quad \to \quad \varepsilon(\boldsymbol{\alpha}_i) \times N_{b_i} = \varepsilon_i \times \prod_{i=1}^{N_{\mathrm{Bck\text{-}sys.}}} \alpha_i \times N_{b_i} \tag{5.25}$$

where $\boldsymbol{\alpha} = \{\alpha_1, \ldots, \alpha_{N_{\mathrm{Bck.\ sys.}}}\}$ denotes the vector of systematic nuisances contributing to the parameter N_{b_i} and ε_i acts as an effective efficiency fixed to unity. For each nuisance, the distance with respect to unity represents the amount of constraint added to the likelihood. The cumulative pdf over all the systematics then becomes:

$$P^{\text{Sys.}}_{\text{Eff}}(\boldsymbol{\theta}\,|\,\hat{\boldsymbol{\theta}}) = \prod_{i=1}^{N_{\text{Sys.}}} P^{\text{Sys.}}_{i}(\theta_i\,|\,\hat{\theta}_i) = \prod_{i=1}^{N_{\text{Sys.}}} \frac{1}{\sqrt{2\pi\sigma^2_{\theta_i}}} \exp\left[-\frac{(\theta_i-\hat{\theta}_i)^2}{2\sigma^2_{\theta_i}}\right] \tag{5.26}$$

The cumulative pdf over all background uncertainties is:

$$P^{\text{Sys.}}_{\text{Bck.}}(\boldsymbol{\alpha}\,|\,\hat{\boldsymbol{\alpha}}) = \prod_{i=1}^{N_{\text{Bck-sys.}}} P_{b_i}(\alpha_i\,|\,\hat{\alpha}_i) = \prod_{i=1}^{N_{\text{Bck-sys.}}} \frac{1}{\sqrt{2\pi\sigma^2_{\alpha_i}}} \exp\left[-\frac{(\alpha_i-\hat{\alpha}_i)^2}{2\sigma^2_{\alpha_i}}\right] \tag{5.27}$$

In the likelihood, the efficiency ε, the luminosity $\mathcal{L}$ and the number of events for each background contribution N_{b_i}, are fixed parameters of the fit, while the corresponding systematic nuisance parameters, $\hat{\boldsymbol{\theta}}$ and $\hat{\boldsymbol{\alpha}}$, are left free to float.

5.5.5 Treatment of correlated uncertainties

Some systematic uncertainties are correlated either across the electron and muon channels, or with respect to the signal and background modelling components. The uncertainties were determined by two independent simulated data ensembles for the electron and muon channel respectively. This information is incorporated in the likelihood by means of a response function $\pi^{\ell}(\hat{\theta}_i, \sigma^1_i, \ldots, \sigma^{N_{\text{channels}}}_i)$ which models the correct efficiency (acceptance) $\varepsilon(\hat{\boldsymbol{\theta}}_{\ell})$ change for each channel ℓ per unit change of $\hat{\theta}_i$. In particular, $\pi^{\ell}(\hat{\theta}_i, \sigma^1_i, \ldots, \sigma^{N_{\text{channels}}}_i)$ is defined as follows:

$$\pi^{\ell}(\hat{\theta}_i, \sigma^1_i, \ldots, \sigma^{N_{\text{channels}}}_i) = \hat{\theta}_i\left[1-\frac{1}{2}\left(\sigma^{\ell}_i - \frac{1}{N_{\text{channels}}}\sum_{k=1}^{N_{\text{channels}}}\sigma^k_i\right)\right] \tag{5.28}$$

which is included in the likelihood as a multiplicative term on ν^{ℓ}_j:

$$\begin{aligned}\nu^{\ell}_j = \nu^{\ell}_j(\sigma_{t\bar{t}\gamma}, \varepsilon(\boldsymbol{\theta}), \mathcal{L}, N_{b_1}(\boldsymbol{\alpha_1}), .., N_{b_n}(\boldsymbol{\alpha_n})) = \\ \varepsilon(\pi^{\ell}(\boldsymbol{\theta}))\mathcal{L}\sigma_{t\bar{t}\gamma}\int_{V_j} dp^{\text{iso}}_{\text{T}} F^j_S(p^{\text{iso}}_{\text{T}}|\sigma_{t\bar{t}\gamma}) + \sum_{i=1}^{n} N_{b_i}(\boldsymbol{\alpha}_i)\int_{V_j} dp^{\text{iso}}_{\text{T}} F^j_{b^i}(p^{\text{iso}}_{\text{T}}|N_{b_i}(\boldsymbol{\alpha}_i)).\end{aligned} \tag{5.29}$$

V_j denoting the range of a $p^{\text{iso}}_{\text{T}}$ bin, and with:

$$\varepsilon(\pi(\hat{\boldsymbol{\theta}}))^{\ell} = \varepsilon^{\ell}\prod_{i=1}^{N_{\text{Sys.}}} \pi^{\ell}_i(\hat{\theta}_i, \sigma^{e\text{ chan.}}_i, \sigma^{\mu\text{ chan.}}_i) \qquad , \qquad N_{b_i}(\boldsymbol{\alpha}_b) = \prod_{i=0}^{N^b_{\text{Bck-sys}}} \alpha_i N_b \tag{5.30}$$

where $\boldsymbol{\alpha}_b = (\theta_k, \ldots, \alpha_{N^b_{\text{Bck. systs.}}})$ includes all nuisances (θ_i and α_i) to be applied on the background b. In the practice this correction is small, as the majority of the electron channel uncertainties are close to the ones of the muon channel.

5.6 Full likelihood and likelihood ratio

Given the definition of the cross section in terms of N_s, ε and $\mathcal{L}$

$$\sigma_{t\bar{t}\gamma} = \frac{N_s}{\varepsilon \cdot \mathcal{L}}, \tag{5.31}$$

and taking into account the pdf modelling the different parameters, the expanded form of the likelihood (Eq. 5.3) used to fit N_{bins} for an expectation of N_j events in each bin j and for reads:

$$L_{\text{tot}}\left(p_{\text{T}}^{\text{iso}} \,|\, \sigma_{t\bar{t}\gamma},\, \varepsilon(\boldsymbol{\theta}), \mathcal{L},\, N_{b_1}(\boldsymbol{\alpha_1}), .., N_{b_n}(\boldsymbol{\alpha_n})\right) = \underbrace{\prod_{\ell=1}^{N_{\text{channels}}} \left[\prod_{j=1}^{N_{\text{bins}}^{\ell}} \frac{\nu_j^{N_j}}{N_j!} \cdot e^{\nu_j}\right]}_{\text{Poisson expectation}} \times \underbrace{\prod_{l=1}^{N_{\text{Bkg Sys.}}} \mathcal{N}(\alpha_l|\hat{\alpha}_l, \sigma_{\alpha_l})}_{\text{Background uncertainties}} \times \underbrace{\prod_{k=1}^{N_{\text{Sys.}}} \mathcal{N}(\theta_k|\hat{\theta}_k, \sigma_{\theta_k})}_{\text{Efficiency/acceptance uncertainties}} \times \underbrace{\mathcal{N}(\mathcal{L}|\hat{\mathcal{L}}, \sigma_{\mathcal{L}})}_{\text{Luminosity uncertainty}} \tag{5.32}$$

where ν_j is defined as:

$$\nu_j = \nu_j(\sigma_{t\bar{t}\gamma}, \varepsilon(\boldsymbol{\theta}), \mathcal{L}, N_{b_1}(\boldsymbol{\alpha_1}), .., N_{b_n}(\boldsymbol{\alpha_n})) = \varepsilon(\pi(\boldsymbol{\theta}))\mathcal{L}\sigma_{t\bar{t}\gamma} \int_{V_j} dp_{\text{T}}^{\text{iso}} F_S^j(p_{\text{T}}^{\text{iso}}|\sigma_{t\bar{t}\gamma}) + \sum_{i=1}^{n} N_{b_i}(\boldsymbol{\alpha}_i) \int_{V_j} dp_{\text{T}}^{\text{iso}} F_{b^i}^j(p_{\text{T}}^{\text{iso}}|N_{b_i}(\boldsymbol{\alpha}_i)). \tag{5.33}$$

$\mathcal{N}(x|\hat{x}, \sigma_x)$ denotes the normal pdf modelling the x nuisance parameter (according to Eq. 5.23, Eq. 5.26 and Eq. 5.27).

Finally, a profile likelihood ratio λ_s is built from Eq. 5.32 by considering the cross section as the parameter of interest with respect to N_b, ε and $\mathcal{L}$, that are considered as nuisance parameters:

$$\lambda_s(p_{\text{T}}^{\text{iso}} \,|\, \sigma_{t\bar{t}\gamma}) = \frac{L(p_{\text{T}}^{\text{iso}} \,|\, \sigma_{t\bar{t}\gamma}, \hat{\hat{N}}_b, \hat{\hat{\varepsilon}}(\boldsymbol{\theta}), \hat{\hat{\mathcal{L}}})}{L(p_{\text{T}}^{\text{iso}} \,|\, \hat{\sigma}_{t\bar{t}\gamma},\, \hat{N}_b,\, \hat{\varepsilon}(\boldsymbol{\theta}),\, \hat{\mathcal{L}})} \tag{5.34}$$

where, for a given parameter x ($x \equiv N_b$, ε, $\mathcal{L}$), the numerator denotes the **conditional likelihood** *estimator* of x, (*i.e.*, $\hat{\hat{x}}$ is the value of x that maximises the likelihood function for a given $\sigma_{t\bar{t}\gamma}$), and the denominator denotes the **maximised (unconditional) likelihood** *estimator*. The effect of the nuisance parameters is to broaden the profile likelihood ratio, which is a function of $\sigma_{t\bar{t}\gamma}$, reflecting the loss of information originated from the inclusion of systematic uncertainties. The maximisation of the Eq. 5.34 is performed with the `MINOS` technique [129, 137, 138] implemented within the `RooFit/RooStats` [139, 140] framework of `ROOT` [84]. This framework is also used to extract the upper and lower limits of the confidence interval to the cross section within a 68% confidence level interval. Two maximisation (fitting) methods have then been developed:

- The **unconstrained** fit method, in which all nuisance parameters are fixed to their maximum likelihood *estimate*. Only the $\sigma_{t\bar{t}\gamma}$ and the number of *hadron-fakes* are allowed to float. The output of this fit corresponds to the **statistical** uncertainty.
- In the **constrained** fit method, where all (nuisance) parameters are allowed to vary. This fit yields the **total** uncertainty on the cross section.

CHAPTER 6

Background processes to $t\bar{t}\gamma$

The likelihood fit method, described in Chap. 5, is able to discriminate between hadrons, or hadron decay products, and photons. However W- and Z-bosons production and the top electroweak production may also feature final states with a single lepton, jets, large transverse missing energy and high-E_{T} photons. Final states from these processes constitute a background to a $t\bar{t}\gamma$ cross section measurement. When applying the $t\bar{t}\gamma$ section criteria, the contribution from these background processes is largely reduced. However, a residual amount of background events passes the $t\bar{t}\gamma$ selection criteria, see Fig. 6.1.

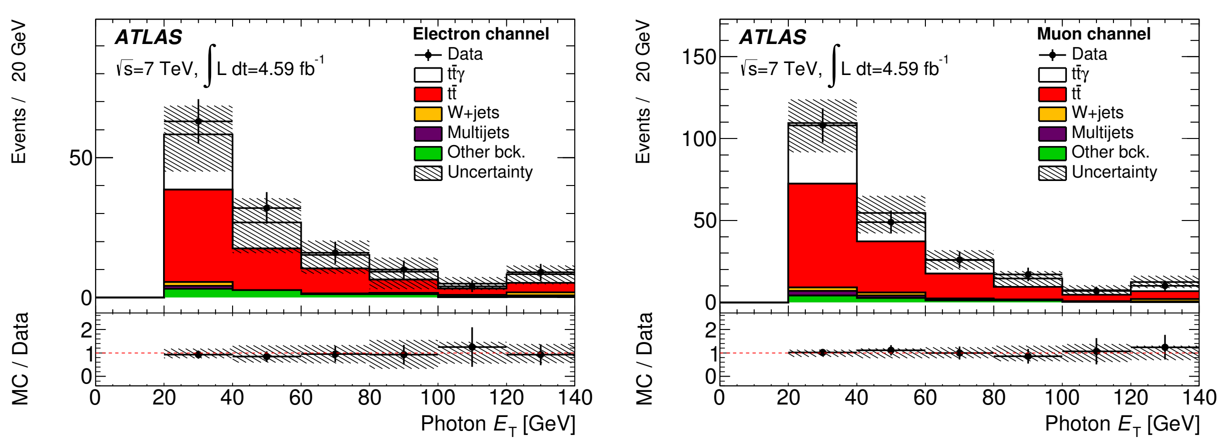

Figure 6.1: The photon transverse energy from event candidates in data is compared to simulation. The plot on the left (right) shows the distribution obtained in the electron (muon) channel. The last bin contains any overflow. The entry labelled "Other backgrounds" includes events from Z plus jets, single top and diboson production.

Moreover, electrons and photon candidates share a similar detector response. They develop electromagnetic showers in the calorimeters with very similar shower shapes. Generally speaking, electrons can be distinguished from photons using tracking information. Photons that enter the electromagnetic calorimeter without being converted to e^+e^- pairs (unconverted photons) do not have associated tracks in the direction of their calorimeter clusters. Tracks of electron-positron pairs, produced by photons before interacting with the calorimeter (converted photons), are associated to a vertex which is displaced with respect to that of the hard scatter. The identification of the $\gamma \to e^+e^-$ vertex allows to discriminate between electron and photon candidates. However, electrons with misidentified tracks are reconstructed as photons. Also, any jet activity, close to the electron, may be reconstructed as tracks in the direction of the electromagnetic clusters, misidentifying the electron as a converted photon.

Therefore, background processes with additional photon radiation and the amount of electrons misidentified as photons need to be quantified. In order to reduce the cross section's model dependency, the estimation of the leading backgrounds is based on data. For the processes with relatively small production rate (single top, diboson and Z-boson production) the estimation is based upon simulations.

In this chapter the description of the photon background estimation is presented based upon the final estimation background rate. At first, in Sec. 6.1, the number of electrons misidentified as photons is determined. Section 6.2 and Sec. 6.3 describe the procedure used for the determination of W plus jets plus photon production and multijet plus photon production. Section 6.4 shows the residual, simulation based, estimation of photons from single top, diboson and Z plus jet production. A summary is finally given in Sec. 6.5.

6.1 Electrons misidentified as photons

Events with one electron being reconstructed as a photon constitute the most important background to $t\bar{t}\gamma$ events after the misidentification of hadrons, or hadron decay products, as photons. These events are mainly dominated by $t\bar{t}$ and Z decays. The method used is based upon the determination of a Control Region (CR) in data on which electron-to-photon misidentification rates are applied.

6.1.1 Fake rate determination

The rate of electrons faking a photon is determined from $Z(\to e^+e^-)$ decays in data. In fact, events with electron-positron pairs selected around the Z mass window are dominated by true electrons. Electrons from $Z(\to e^+e^-)$ decays can emit hight-E_T photons while traversing the detector. These photons are typically back-to-back with respect to the non-radiating electron.

Therefore, in events with an electron being misidentified as a photon (*fake photon*, or simply *fake*), the resulting invariant mass $m(e,\gamma)$ is close to the Z-boson mass peak. These events can be used in order to estimate the $e \to \gamma$ fake rate ($f.r.(e \to \gamma)$).

By applying two distinct selection criteria for $Z(\to e^+e^-)$ and $Z(\to e\gamma)$ decays, the fraction of candidate events of the latter to the former can be used for determining the $f.r.(e \to \gamma)$. The method is referred to as *tag and probe*. The electron with highest-E_T, in both cases, is used for trigger matching (tag), while the second e/γ object (electron or photon) is used to calculate the invariant mass with the tag (this e/γ object is referred-to as the probe). Considering the combined trigger, reconstruction and identification efficiency for the tag (ε_tag) and the probe ($\varepsilon_\mathrm{probe}$), the number of electron-positron pairs truly originating from Z-boson decays $N^\mathrm{true}_{Z(\to e^+e^-)}$ relates to the number of observed $Z(\rightarrow e^+e^-)$ candidate events $N_{Z(\rightarrow e^+e^-)}$ by:

$$N_{Z(\rightarrow e^+e^-)} = N^{\text{true}}_{Z(\rightarrow e^+e^-)} \cdot \varepsilon_{\text{tag}} \cdot \varepsilon_{\text{probe}} \tag{6.1}$$

and, with $N_{Z(\rightarrow e\gamma)}$ being the number of $Z(\rightarrow e\gamma)$ candidate events:

$$N_{Z(\rightarrow e\gamma)} = N^{\text{true}}_{Z(\rightarrow e^+e^-)} \cdot \varepsilon_{\text{tag}} \cdot f.r.(e \rightarrow \gamma) \tag{6.2}$$

Therefore, the $f.r.(e \rightarrow \gamma)$ can be simply expressed as:

$$f.r.(e \rightarrow \gamma) = \varepsilon_{\text{probe}} \cdot \frac{N_{Z(\rightarrow e\gamma)}}{N_{Z(\rightarrow e^+e^-)}} \tag{6.3}$$

6.1.2 Event selection

Electron and photon candidates, used for the determination of the $f.r.(e \rightarrow \gamma)$, follow the definition detailed in Sec. 3.5.2 and Sec. 3.5.4 respectively. Overlapping definitions of defined objects are avoided using the method described in Sec. 3.6. The $Z(\rightarrow e^+e^-)$ and $Z(\rightarrow e\gamma)$ events are selected by requiring the following cuts.

- The tag electron in the event is required to fulfil the tight identification criteria and it is require to have $E_{\text{T}}(e) > 25$ GeV and to be matched to the single electron trigger object (see table 3.1). The calorimetric (E_{T}^{20}) and track (p_{T}^{30}) isolation cuts applied are the same as for the $t\bar{t}$ event selection.
- In the $Z(\rightarrow e^+e^-)$ event selection, exactly two back-to-back electrons with $\Delta\varphi(e^-, +e^+) > 150°$ and opposite charge are required.
- In the $Z(\rightarrow e\gamma)$ event selection, the photon and electron must be back to back with $\Delta\varphi(e, \gamma) > 150°$.
- The invariant masses $m(e^-, e^+)$ and $m(e, \gamma)$, for the $Z(\rightarrow e^+e^-)$ and $Z(\rightarrow e\gamma)$ event selections respectively, are required to be within 50 GeV around $m_Z = 91$ GeV.
- In both $Z(\rightarrow e^+e^-)$ and $Z(\rightarrow e\gamma)$ selections a veto for muons with $p_{\text{T}}(\mu) > 20$ GeV is applied.

The reconstructed invariant masses $m(e^-, e^+)$ and $m(e, \gamma)$ for the $Z(\rightarrow e^+e^-)$ and $Z(\rightarrow e\gamma)$ event selections are compared in Fig. 6.2 (left), while the angular separations in φ between the tag and the probe are shown in Fig. 6.2 (right). The small displacement of $m(e, \gamma)$ with respect to $m(e^-, e^+)$ indicates that, indeed, the probe is a high-E_{T} photon carrying most of the electron's energy. Moreover, the close similarity of the angular separations in φ of the reconstructed objects from the $Z(\rightarrow e^+e^-)$ and $Z(\rightarrow e\gamma)$ event selections, peaking at $\Delta\varphi \simeq \pi$, shows that both the electron-positron and electron-photon objects are indeed, mostly back-to-back.

6.1.3 Extraction of $f.r.(e \rightarrow \gamma)$.

Although the candidate events selected by the requirements of Sec. 6.1.2 are dominated by real Z decays (signal) events, a residual contamination from non $Z(\rightarrow e^+e^-)$ decays can leak into this selection. In fact, hadrons from jet fragmentation can be misidentified as electrons or photons and

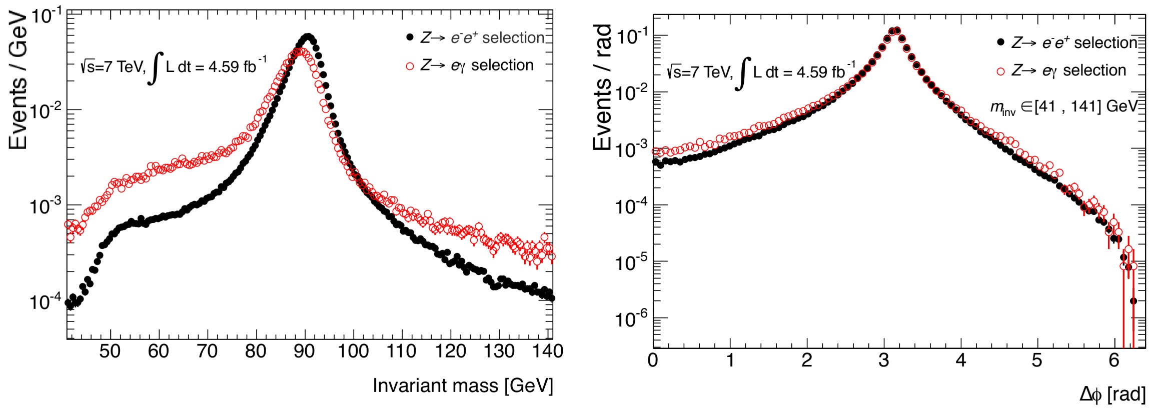

Figure 6.2: Distributions of the invariant mass (left) and angular separation (right) for the $Z \to ee$ and $Z \to e\gamma$ event selections in the invariant mass range $[41, 141]$ GeV [86]. Distributions are normalised to their area.

contaminate the $Z(\to e^+e^-)$ and $Z(\to e\gamma)$ selections. The invariant mass of hadrons misidentified as e/γ objects is broader and does not have a resonant peak around m_Z. This difference in shape is used by a fit-based approach in order to extract the number of events for $N_{Z(\to e^+e^-)}$ and $N_{Z(\to e\gamma)}$.

The invariant mass spectrum for signal $N_{Z(\to e^+e^-)}$ (and $N_{Z(\to e\gamma)}$) events is assumed to be well described by a Crystal Ball [141, 142] probability density function (pdf) (F_{CB}), while the broader invariant mass of misidentified hadrons as leptons N_{had} is described by a Gaussian pdf ($\mathcal{N}_{\text{had}}$). Therefore, the invariant mass distribution approximating the total candidate events $N^{\text{tot}}_{Z(\to e^+e^-)}$ ($N^{\text{tot}}_{Z(\to e\gamma)}$) is :

$$N_k^{\text{tot}} = N_k \cdot F_{\text{CB}} + N_{\text{had}} \cdot \mathcal{N}_{\text{had}} \tag{6.4}$$

with $k = Z(\to e^+e^-),\ Z(\to e\gamma)$. A fit of N_k^{tot} on data extracts N_k and N_{had}. The $f.r.(e \to \gamma)$ are derived in bins of E_{T} and η *post*-fit using Eq. 6.3. Figure 6.3 shows the determined $f.r.(e \to \gamma)$.

Systematic uncertainties

Both modelling of N_k^{tot} and fit range are varied in order to extract systematics uncertainties to the binned fake rates. Specifically, any combination of the ranges $60 < m < 120$ GeV, $70 < m < 110$ GeV and $80 < m < 100$ GeV with fit functions comprising a Crystal Ball (signal only) and Crystal Ball (signal) plus a second order polynomial (background) were implemented in order to extract systematic uncertainties. The larger variation was taken as systematic uncertainty, corresponding to 10% on the $f.r.(e \to \gamma)$, and was conservatively considered to be constant across the entire E_{T} and η range.

The dependancy upon the number of pile-up interactions is estimated by evaluating the $f.r.(e \to \gamma)$ as a function of the mean number of interactions [86].

The bias induced by the selection of the E_{T}-leading electron was found to be less than a few percent on the $f.r.(e \to \gamma)$, and therefore negligible [86]. The difference was evaluated by requiring that the E_{T} of the tag should be higher than the photon's energy in the transverse plane.

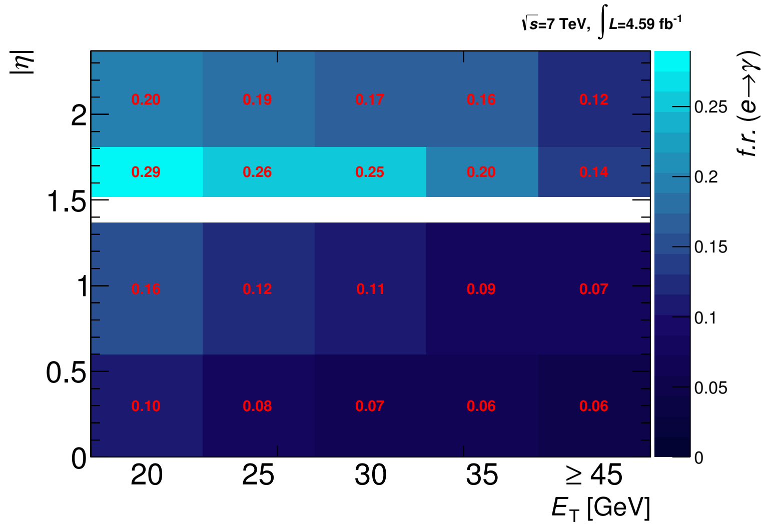

Figure 6.3: The $e \rightarrow \gamma$ fakes rates as a function of η and E_{T} of the e/γ object. Based on collaborative inputs [86]. The empty area of the histogram corresponds to the calorimeter crack-region ($1.37 < |\eta(e)| < 1.52$), in which reconstructed electrons and photons are discareted.

6.1.4 Control Region definition

The special selection defining the CR used for determining electrons misidentified as photons is explained in this section. The CR is characterised by the requirement of an additional electron fulfilling all the photon requirements. The nominal $t\bar{t}$ selection requirements are imposed with, specifically, the following additional criteria.

- The appropriate lepton trigger must have fired, see Sec. 3.6.
- The event must contain at least four good jets (j) with $p_{\mathrm{T}}(j) > 25$ GeV of which at least one must be tagged as a b-jet.
- The event must contain at least one good electron (muon) with $E_{\mathrm{T}}(e) > 25$ (20) GeV matched to the trigger object. A second good electron with $E_{\mathrm{T}}(e) > 20$ GeV must be present in the event. In events with two (or more) electrons with $E_{\mathrm{T}}(e) > 25$ GeV, either of those electrons can be faking a photon. These events are treated twice in the selection each time identifying one as the electron and one as the electron faking a photon (labelled in this section as *fake*). The fake must fulfil the following requirements:
  - $E_{\mathrm{T}}(f) > 20$ GeV, $1.52 < |\eta(f)| < 2.37$ and $|\eta(f)| < 1.37$;
  - $\Delta R(j, f) > 0.5$, $\Delta R(l, f) > 0.7$;
  - for the electron channel the $m(e, f)$ must be outside a 5 GeV window around $m_Z =$ 91 GeV.

Events are categorised into the ee channel and μe channel. The former corresponds to the $t\bar{t}$ electron channel with an additional fake, while the latter corresponds to the $t\bar{t}$ muon channel with and additional fake. Totals of 325 electron and 467 muon events pass the above event selection.

Reconstructed events are reweighted according to the $f.r.(e \to \gamma)$ as a function of η and E_{T}, shown in Fig. 6.3. The event weight ($w_{f.r.(e\to\gamma)}$) is obtained by summing the weights of each fake candidate f_i

$$w_{f.r.(e\to\gamma)} = \sum_{i=1}^{N_{\text{e-fakes}}} f.r.(e \to \gamma)\,[E_{\mathrm{T}}(f_i), \eta(f_i)] \tag{6.5}$$

over all fake candidates ($N_{e\text{-fakes}}$), any electron with $E_{\mathrm{T}}(e) > 25$ GeV is considered to be a fake. This procedure avoids any selection bias upon the fake identification. The number of events with an electron faking a photon, after reweighing, are found to be 29 and 42 for the electron and muon channels respectively. Table 6.1 compares the estimated $e \to \gamma$ background to the expectations from simulations.

Contribution	ee **channel [events]**	μe **channel [events]**
$t\bar{t}$	17.15 ± 0.19 (stat) ± 4.67 (sys)	31.07 ± 0.27 (stat) ± 6.72 (syst)
$t\bar{t}\gamma$	0.38 ± 0.03 (stat) ± 1.13 (sys)	0.69 ± 0.04 (stat) ± 1.70 (sys)
$Z+$jets	2.14 ± 0.22 (stat) ± 1.91 (sys)	0.12 ± 0.04 (stat) ± 4.10 (syst)
$W+$jets	< 0.06 (stat⊕sys)	< 0.01 (stat⊕sys)
Multijets	2.52 ± 0.11 (stat)	0.26 ± 0.01(stat)
Dibosons	0.09 ± 0.02 (stat) ± 0.03 (sys)	0.06 ± 0.02 (stat) ± 0.08 (sys)
Single top	0.44 ± 0.05 (stat) ± 0.10 (sys)	0.89 ± 0.07 (stat) ± 0.21 (sys)
Total Expected	22.78 ± 0.32 (stat) ± 5.17 (sys)	33.09 ± 0.28 (stat) ± 8.06 (syst)
Data	29.40 ± 1.55 (stat) ± 2.7 (sys)	41.46 ± 1.92 (stat) ± 4.20 (sys)

Table 6.1: Estimated number of events with an electron misidentified as a photon. Systematic uncertainties correspond to those detailed on table 6.2. A 10% uncertainty is assigned to data candidates corresponding to the uncertainties on the fake rates obtained in Sec. 6.1.1. The expectation was obtained at reconstruction level using the same selection and reweighting as for Data.

The data-to-simulation comparison (see Fig. 6.4), after event selection and reweighting, shows a reasonable agreement when systematic uncertainties (comprising the jet, lepton and missing transverse energy modelling) are considered. A detailed description on each component can be found in Chap. 7.

On the $t\bar{t}$ sample uncertainties are found to be of the order of 21% and are mainly driven by the jet energy scale (14%). The knowledge on $t\bar{t}$, $t\bar{t}\gamma$ and Single top is limited by the systematic uncertainties, while the estimation for $Z+$jets, $Z+$jetsand dibosons is limited by the size of data. Table 6.2 shows the full breakdown for each simulated sample.

	Uncertainty ee channel [%]					
Source	W**+jets**	Z**+jets**	**Dibosons**	**Single top**	$t\bar{t}$	$t\bar{t}\gamma$
Jet energy scale	< 0.01	29.30	22.09	16.49	16.17	21.71
Jet energy resolution	< 0.01	79.64	26.26	13.92	3.96	6.19
Jet reconstruction efficiency	< 0.01	0.97	< 0.01	3.90	0.14	0.00
Electron energy scale	< 0.01	7.30	< 0.01	<0.01	0.30	2.95
Electron energy resolution	< 0.01	5.18	10.73	5.67	0.39	2.52
Cell-out and soft terms	< 0.01	6.045	<0.01	<0.01	0.15	2.05
Pile-up	< 0.01	4.49	< 0.01	0.00	0.14	0.06
Total	0.03	89.41	38.22	22.56	21.40	29.62
	Uncertainty μe channel [%]					
Source	W**+jets**	Z**+jets**	**Dibosons**	**Single top**	$t\bar{t}$	$t\bar{t}\gamma$
Jet energy scale	< 0.01	6.03	0.63	36.30	16.54	19.28
Jet Energy resolution	< 0.01	3.46	82.80	8.28	2.35	7.01
Jet reconstruction efficiency	< 0.01	< 0.01	< 0.01	< 0.01	0.06	0.23
Muon momentum resoultion	< 0.01	< 0.01	< 0.01	0.80	0.14	< 0.01
Muon momentum scale	< 0.01	< 0.01	< 0.01	< 0.01	0.00	< 0.01
Cell-out and soft terms	< 0.01	< 0.01	< 0.01	0.00	0.13	0.54
Cell Out Down	< 0.01	< 0.01	< 0.01	0.00	0.14	0.43
Pile-up	< 0.01	< 0.01	< 0.01	0.02	0.09	0.67
Total	0.03	34.13	137.05	23.03	21.64	24.78

Table 6.2: Summary of systematic uncertainties for the ee (μe) channel are shown on the top (bottom).

The $f.r.(e \to \gamma)$ is estimated with a systematic uncertainty of 10% (see Sec. 6.1.1) consequently the estimated event yield in the electron and muon channels is 29.4 ± 1.6 (stat) ± 2.9 (sys) and 41.5 ± 1.9 (stat) ± 4.2 (syst) events respectively. This estimation is compatible with the expectation of 22.78 ± 0.32 (stat) ± 5.17 (syst) events for the electron channel and 33.09 ± 0.28 (stat) ± 8.06 (syst) events for the muon channel. The difference in the yielded number of events from simulation and data is associated with the mismodelling of the jet multiplicites by `MC@NLO` see Fig. 6.5. This is a known feature allready observed by ATLAS with the measurement of the $t\bar{t}$ cross section as a function of jet multiplicity [118]. In fact, as the `MC@NLO` simulation underestimates the number of jets in the event, the probability of an electron being identified as a photon (due to mis-matched jet tracks being associated to calorimeter clusters) decreases. Thus, the overall simulation-based determination of electrons faking photons is underestimated. This further motivates the choice of a background estimation derived from data.

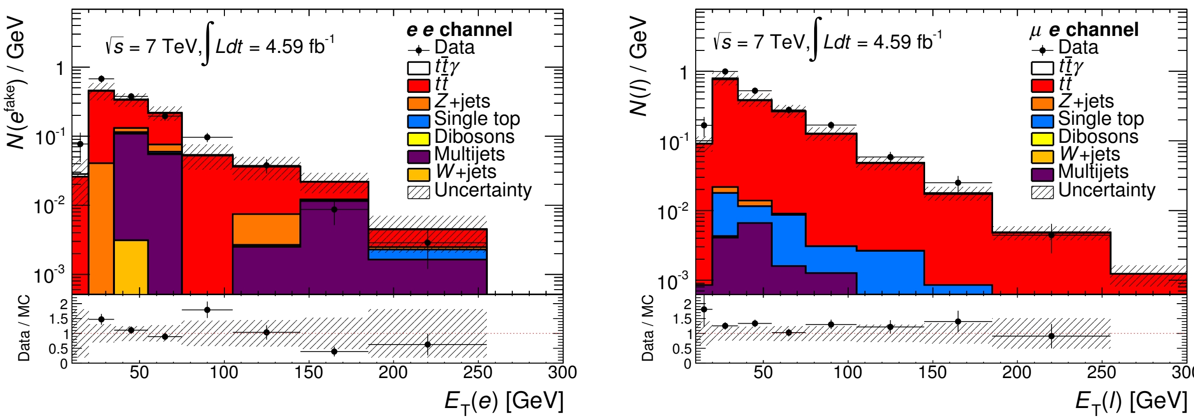

Figure 6.4: Transverse energy of the electron faking a photon candidate. The plot on the left (right) shows event candidates in the ee (μe) channel. The band includes the simulation-based statistical uncertainty from all samples, as well as detector uncertainties (see main text) applied on the $t\bar{t}$ sample. The agreement is significantly better when detector uncertainties on the other simulation samples are added. The last bin contains any overflow.

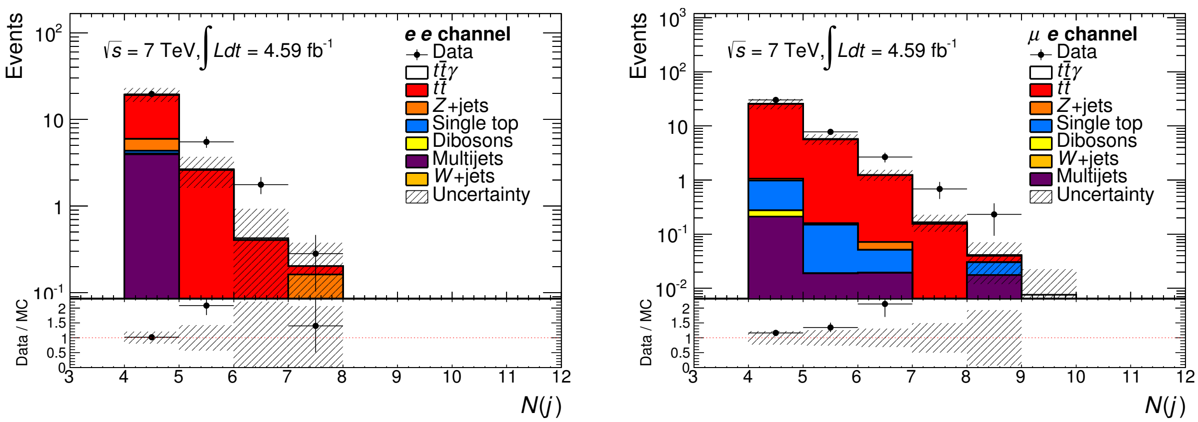

Figure 6.5: The jet multiplicity distribution is shown. The plot on the left (right) shows event candidates in the ee (μe) channel. The band includes the simulation-based statistical uncertainty from all samples, as well as detector uncertainties (see main text) applied on the $t\bar{t}$ sample. Both distributions illustrate the underestimation of the MC@NLO simulation program (labelled as $t\bar{t}$) with increasing jet multiplicities in the event.

6.1.5 Closure

In order to estimate the bias of the method a *closure* test is performed. The simulation-based estimates at reconstruction level, shown in Tab. 6.1 (which are obtained by using the method described above), are compared to the estimates obtained by applying data-to-simulation Scale Factors (SF) on the $f.r.(e \to \gamma)$.

$$\mathrm{SF} = \frac{f.r.(e \to \gamma)}{f.r.(e \to \gamma)^{\mathrm{MC}}} = \frac{(N_{Z(\to e\gamma)}/N_{Z(\to e^+e^-)})\big|_{\mathrm{Data}}}{(N_{Z(\to e\gamma)}/N_{Z(\to e^+e^-)})\big|_{\mathrm{MC}}} \tag{6.6}$$

with $f.r.(e \to \gamma)^{\mathrm{MC}}$ being the fake rates as determined from simulation. The extracted SF are shown in Fig. 6.6 and they were found to be close to one across all η and E_{T} ranges.

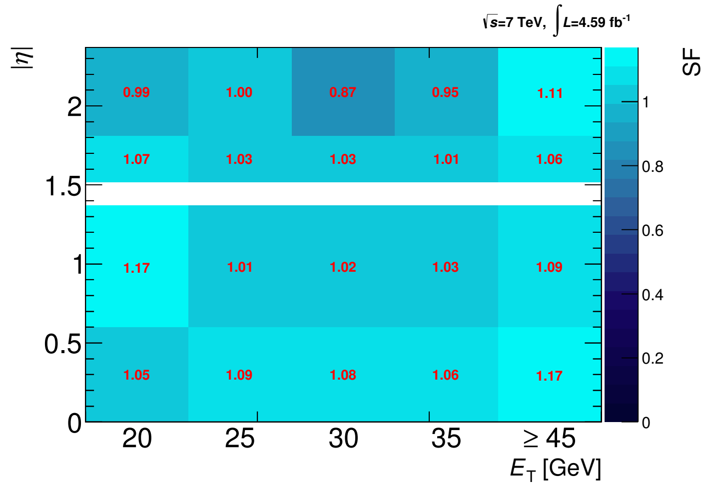

Figure 6.6: The $e \to \gamma$ SF in η and E_{T} bins [86]. The empty area of the histogram corresponds to the calorimeter crack-region ($1.37 < |\eta(e)| < 1.52$), in which reconstructed electrons and photons are discarted.

The SF are obtained from data-to-simulations comparisons of $Z(\to e^+e^-)$ and $Z(\to e\gamma)$ decays. They are applied to events passing the full $t\bar{t}\gamma$ event selection, for which an electron is reconstructed as a photon. The matching of true electrons to objects being reconstructed as photons is performed using the `MCTruthClassifier` tool [143]. The same simulation samples used for the obtention of Tab. 6.1 are used in this case.

	Estimates [events]			
Contribution	**MC** ee	**DD** ee	**MC** μe	**DD** μe
$t\bar{t}$	18.6 ± 0.9	17.2 ± 0.2 (stat) ± 4.7 (syst)	30.1 ± 1.1	31.1 ± 0.3 (stat) ± 6.7 (syst)
$t\bar{t}\gamma$	0.2 ± 0.1	0.4 ± 0.1 (stat) ± 1.1 (syst)	0.5 ± 0.1	0.7 ± 0.1 (stat) ± 1.7 (syst)
Z+jets	2.6 ± 1.0	2.1 ± 0.2 (stat) ± 1.9 (syst)	0.1 ± 0.1	0.1 ± 0.1 (stat) ± 4.1 (syst)
W+ jets	< 0.1	< 0.1	< 0.1	< 0.1
Dibosons	< 0.1	< 0.1	< 0.1	< 0.1
Single top	0.6 ± 0.3	0.4 ± 0.1 (stat) ± 0.1 (syst)	0.1 ± 0.3	0.9 ± 0.1 (stat) ± 0.2 (syst)
Total	22.1 ± 1.4	20.3 ± 3.0 (stat) ± 5.2 (syst)	31.7 ± 1.2	32.3 ± 2.9 (stat) ± 8.1

Table 6.3: Estimates of number of events with electrons faking photons obtained from simulation for events passing the full $t\bar{t}\gamma$ selection and of which the reconstructed photon is matched, at truth level, to an electron (columns labelled “MC”). Events are weighted by the corresponding SF. Uncertainties are statistical only. Estimates obtained with the data based method on simulation are shown for comparison (columns labeled "DD").

Estimates are summarised in Tab. 6.3 and are found to be consistent within uncertainties with those of Tab. 6.1. The statistical uncertainties for both methods are uncorrelated because of the two different selections; systematic uncertainties, because of correlations, are applied only to data based method.

The differences yielded by the comparison of both methods are found to be less than two events for the electron channel and less than one event for the muon channel, smaller than total uncertainty on the fake rates (of the order of 10%).

6.2 W plus jets production in association with a photon

Production of W-bosons plus jets in association with at least a high-E_{T} final sate photon is the third most important background source to the $t\bar{t}\gamma$ production cross section measurement. This section reviews the method, based on data, used to estimate the number of $W\gamma+$jets events. The principle is based upon the definition, at first, of a phase-space, referred to as a CR, which enriches events from W production. The number of $W\gamma+$jets events ($N_{CR}^{W\gamma,\mathrm{Data}}$) is extracted from data by using the template fit method defined in Chap. 5. Then, an extrapolation is made, using simulation information, to the phase-space where the $t\bar{t}\gamma$ measurement is performed, also referred in the following as the Signal Region (SR). Thus, the number of background events from $W\gamma+$jets production ($N_{\mathrm{SR}}^{W\gamma,\mathrm{Data}}$) is extracted:

$$N_{\mathrm{SR}}^{W\gamma,\mathrm{Data}} = N_{\mathrm{CR}}^{W\gamma,\mathrm{Data}} \cdot \left(\frac{N_{SR}^{W\gamma,\mathrm{MC}}}{N_{CR}^{W\gamma,\mathrm{MC}}}\right) \tag{6.7}$$

with $N_{SR}^{W\gamma,\mathrm{MC}}$ and $N_{SR}^{W\gamma,\mathrm{MC}}$ being the number of $W\gamma+$jets events in the the SR and CR respectively, as estimated from simulation.

The validity of this method relies on the fact that the same Monte Carlo (MC) generator is used to simulate ensembles of events for the SR and the CR; these two sets are statistically independent. The model dependency is removed through the ratio $N_{SR}^{W\gamma,\mathrm{MC}}/N_{CR}^{W\gamma,\mathrm{MC}}$ which cancels out the simulated Matrix-Element (ME) dependency and leaves only an acceptance dependency. The shape of the photon's track-isolation remains simulation independent as it is defined via the templates (see Sec. 5.3).

6.2.1 Phase-space definition

In this section the phase-space and selection requirements which define the CR are detailed. The same object definition used for the $t\bar{t}\gamma$ selection criteria is used here and only a few cuts are reversed. Specifically, each event must fulfil the following criteria.

- The number of good jets requirement is inverted from at least four (for the $t\bar{t}\gamma$ selection) to at most three.
- The same b-tagging algorithm (*MV1*), used in the $t\bar{t}\gamma$ selection, is used here to request a b-tagging veto in the event.
- The event must, of course, contain at least a photon matching the tight definition criteria and being separated from the other objects as discussed in Sec. 3.6.
- In the electron channel, the event inside the range $m_Z - 15$ GeV $\leq m(e,\gamma) \leq m_Z + 15$ GeV is excluded, in order to suppress radiation from Z decay products, where $m_Z = 91$ GeV.

$W\gamma+$jets events are simulated with both the SHERPA and ALPGEN MC generators, see Sec. 3.4. Totals of 2910 and 6181 candidate events are selected for the electron and muon channels respectively, including $W\gamma$+jets events and background contributions. Out of these numbers, simulations predict 1027 and 3090 events to be from $W\gamma+$jets in the electron and muon channels respectively. Reconstruction level observables for simulations and data are in good agreement for the photon's kinematic distributions (see Fig. 6.7) as well as for other reconstructed objects (see Fig. 6.8).

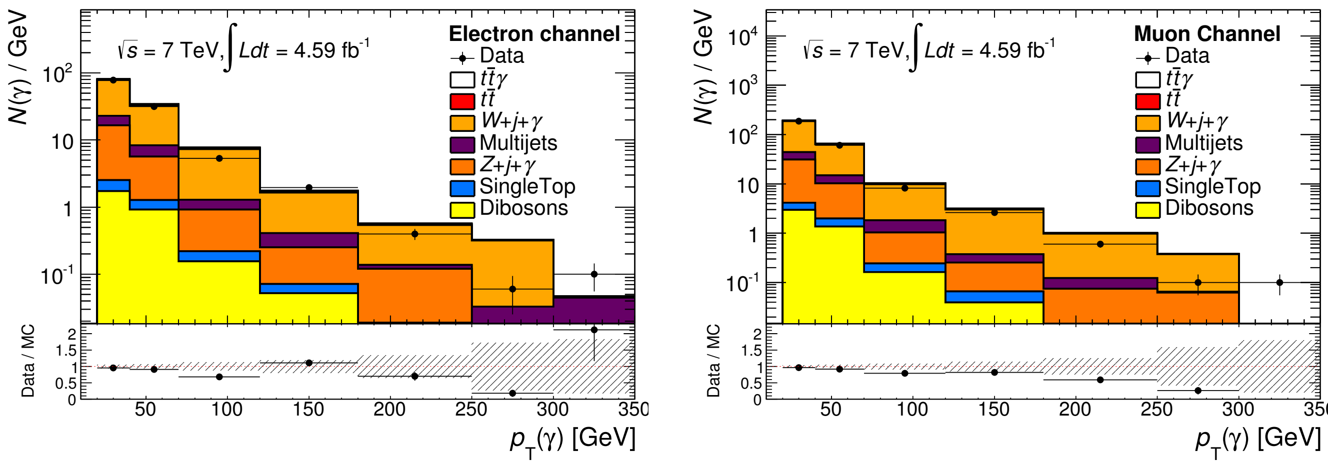

Figure 6.7: Data-to-simulation comparisons for the photon $p_{\mathrm{T}}(\gamma)$ in the $W\gamma+$jets control region for the electron (lef) nad the muon (right) channels. The filled band corresponds to the quadrature sum of statistical uncertainties of the simulated samples and of the multijet background. The last bin contains any overflow.

An overall normalisation correction is applied on simulations for $W\gamma+$jets. It is motivated by the fact that the $W+$jets production is charge asymmetric in pp colliders, *i.e.* the production of $W^{+}+$jets is significantly higher than that of $W^{-}+$jets, as the u-quark density in the proton is larger than the d-quark one [144]. The correction exploits the fact that the theory predicts with higher precision the ratio $\left(\mathcal{R}^{W}=\frac{\sigma^{W^{+}+\mathrm{jets}}}{\sigma^{W^{-}+\mathrm{jets}}}\right)$ of the $W^{+}+$jets to $W^{-}+$jets production cross sections ($\mathcal{R}^{W}=1.429\pm0.013$, next-to-next-to-next-leading order calculation [24, 145]) than the total $W+$jets cross section [145, 146]. Data in the CR are split into two subsets based on the reconstructed lepton's charge each containing $N_{\mathrm{CR}}^{W\gamma,\mathrm{Data}+}$ and $N_{\mathrm{CR}}^{W\gamma,\mathrm{Data}-}$ events for positive and negative charged leptons respectively [1]. Therefore, the normalisation correction factor for the $W\gamma+$jets simulation samples ($\varepsilon^{\mathrm{c}}_{W\gamma}$) can be obtained as:

$$\varepsilon^{\mathrm{c}}_{W\gamma}=\frac{\mathcal{R}^{W}+1}{\mathcal{R}^{W}-1}\times\frac{N_{\mathrm{CR}}^{W\gamma,\mathrm{Data}+}-N_{\mathrm{CR}}^{W\gamma,\mathrm{Data}-}}{N_{\mathrm{CR}}^{W\gamma,\mathrm{Data}+}+N_{\mathrm{CR}}^{W\gamma,\mathrm{Data}-}} \tag{6.8}$$

The correction holds as long as the charge asymmetry for background processes to $W+$jets production is negligible, which is the case for the processes considered here.

Both the CR and the SR use b-tagging algorithms in their definition. The selection efficiency on the simulated samples is dependent upon the heavy flavour content.

[1]The rate of the wrong lepton charge assignment is negligible [112, 147].

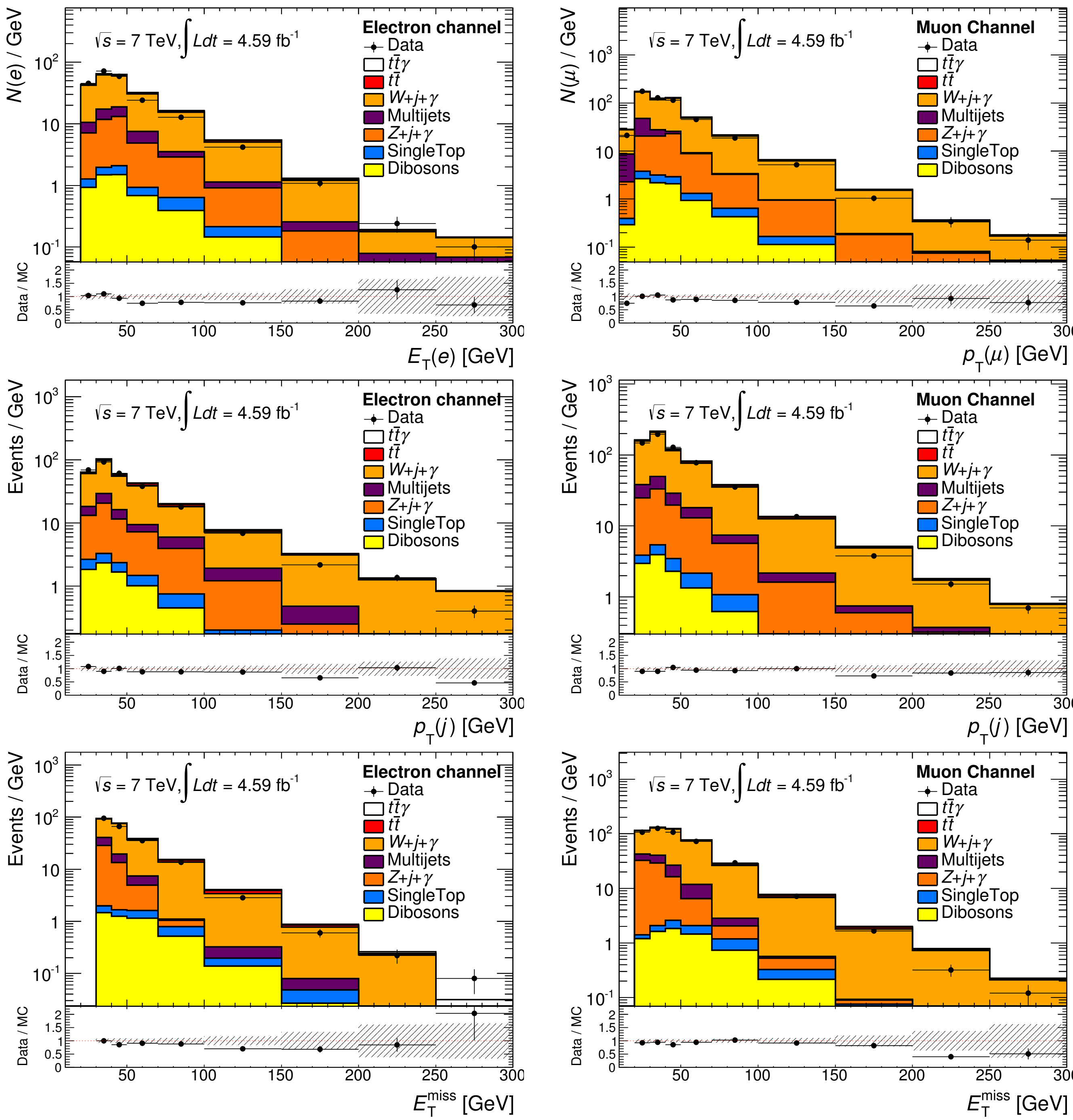

Figure 6.8: Data-to-simulation comparisons for the transverse energy of the electron ($E_{\mathrm{T}}(e)$), the transverse momentum of the muon ($p_{\mathrm{T}}(\mu)$), the jet's trasnverse momentum ($p_{\mathrm{T}}(j)$) and the magnitude of the missing energy in the transverse plane ($E_{\mathrm{T}}^{\mathrm{miss}}$). The left-hand side distributions are in the electron channel while the right-hand side distributions are in the muon channel. The filled band corresponds to the quadrature sum of statistical uncertainties of the simulated samples and of the multijet background. The last bin contains any overflow.

Therefore, a residual model dependency upon the extrapolation from CR to SR persists, see Tab. 6.4. The relative flavour content for $W+c(c)$, $W+b\bar{b}$ and W+light quarks have been determined from data and a correction factor has been applied on $W\gamma$ + jets simulations [148, 149].

Due to the different jet multiplicities for the SR ($N(j) \geq 4$) and for the CR ($N(j) < 4$), the independence of the extrapolation on the number of jets has to be ensured. Equation 6.7 has been computed before extracting of the number of events with prompt-photons. The results of the extrapolation, shown in Tab. 6.4, are independent when considering the systematic uncertainties of the method.

	Electron channel [events]		**Muon channel** [events]	
Jet multiplicity	`SHERPA`	`ALPGEN`	`SHERPA`	`ALPGEN`
$N(j) = 1$	13.55 ± 0.31	7.02 ± 0.16	9.6 ± 0.15	7.17 ± 0.11
$N(j) = 2$	21.17 ± 0.78	8.17 ± 0.30	11.00 ± 0.29	7.49 ± 0.20
$N(j) = 3$	16.67 ± 1.12	10.90 ± 0.73	11.42 ± 0.60	8.88 ± 0.47
$N(j) < 4$	15.13	7.48	10.01	7.33

Table 6.4: Simulation-based extrapolations of W + jets candidates to the signal region as a function of the jet multiplicity before extraction of the number of events with prompt-photons. The estimates have been obtained by applying the $\varepsilon^{c}_{W\gamma}$ correction factor of Eq. 6.8. Numbers are shown before correcting for the relative flavour content in simulations (`SHERPA` or `ALPGEN`), thus enhancing the differences between `SHERPA` and `ALPGEN`. The uncertainties are statistical only and are determined from the size of data in the Control Region. The small dependency on the jet multiplicity is negligible when considering the systematic uncertainties of the method, which are about 27% for the electron channel and 23% for the muon channel.

6.2.2 Extraction of $W\gamma$ + jets events

The final number of $W\gamma$ + jets events within the CR is extracted using the profile likelihood fit method on the track isolation ($p_{\mathrm{T}}^{\mathrm{iso}}$) as described in details in Chap. 5. A simplified statistical model has been used, where no systematic uncertainties have been included into the likelihood and the fit is performed independently for the electron channel and the muon channel. The results are obtained in bins of photon transverse energy as well as in the inclusive $E_{\mathrm{T}}(\gamma)$-range. Results obtained by the former are used as inputs to the determination of the differential cross section, while the results of the latter are used as inputs for the inclusive cross section. This splitting is motivated by the correlation of systematic uncertainties across the entire $E_{\mathrm{T}}(\gamma)$-range which are different from the uncertainties when computing the measurement in a specific $E_{\mathrm{T}}(\gamma)$ bin.

As the correction for the relative flavour content for the $W\gamma$ + jets simulation samples is determined from a control sample defined with at least two jets, the CR subset with $N(j) = 1$ is excluded.

As discussed in Sec. 5.3, prompt-photons from any processes are assumed to be distributed according to the “signal template". Hadrons, or hadron decay products misidentified as photons (*hadron fakes*) are distributed according to the pdf discussed in Sec. 5.4. For both types of templates the dependency in photon transverse energy has been accounted for.

Contributions from processes other than $W\gamma$ + jets, passing the CR event selection criteria, may also feature a final state photon. Therefore they constitute a background and they need to be subtracted from data before extrapolating to the SR . These processes are the single top production, the diboson production, and the $Z +$ jets production. Multijet events with additional radiation are also considered.

Simulations determine the number of events with photon candidates (prompt-photons plus *hadron-fakes*) for all of these background contributions[2]. However, the prompt-photon contribution, for each process, is extracted using the template fit method (within the CR) on the simulated sets. This preserves the model independency of the photon definition. The cross section uncertainty on each simulated background sample is taken into account as an uncertainty on the final $W\gamma +$ jets yield.

Table 6.5 summarises the breakdown of contributions as estimated from the fit (in the range $E_{\mathrm{T}}(\gamma) > 20$ GeV) for electron $(e)/\gamma$ objects and for *hadron-fakes*. For comparison, the purity, defined as the fraction of events with e/γ to the total, is also shown. From the fit on data a total of 775 and 1401 events with are extracted for the electron and muon channels respectively. The fit result for photons candidates with $E_{\mathrm{T}}(\gamma) > 20$ GeV is shown in Fig. 6.9.

Component	e/γ **[events]**	***hadron-fakes*[events]**	**Purity [%]**	**Total [events]**
		Electron channel		
Data	775^{+34}_{-32}	158 ± 19	83	936
Single top	3^{+3}_{-2}	3 ± 2	50	6
Dibosons	6 ± 3	3.12 ± 2	67	9.469
$Z +$ jets	142^{+15}_{-13}	32 ± 8	81	175
Multijets	59^{+10}_{-9}	25 ± 7	70	84
$t\bar{t}\gamma$ induced and $t\bar{t}_{e\rightarrow\gamma}$	35^{+6}_{-10}	13 ± 15	73	48
$W +$ jets	163^{+18}_{-17}	129 ± 14	56	292
		Muon channel		
Data	1401^{+45}_{-44}	337 ± 27	80	1739
Dibosons	1^{+5}_{-4}	8 ± 3	60	19
Single top	10 ± 4	4 ± 3	74	13
$Z +$ jets	148^{+15}_{-14}	41 ± 9	78	190
Multijets	90^{+12}_{-11}	25 ± 7	79	115
$t\bar{t}\gamma$ induced and $t\bar{t}_{e\rightarrow\gamma}$	74^{+10}_{-15}	30 ± 9	71	105
$W +$ jets	349^{+26}_{-25}	287 ± 21	55	638

Table 6.5: Fit results showing the extracted number of events with e/γ objects and the number of hadron fakes for each background component. For "closure" purposes the expected contribution of $W\gamma +$ jets as estimated from simulations is also shown. The purity is defined as the fraction of events with e/γ with respect to the total.

[2]The multijet background is determined from data, as explained in Sec. 6.3.

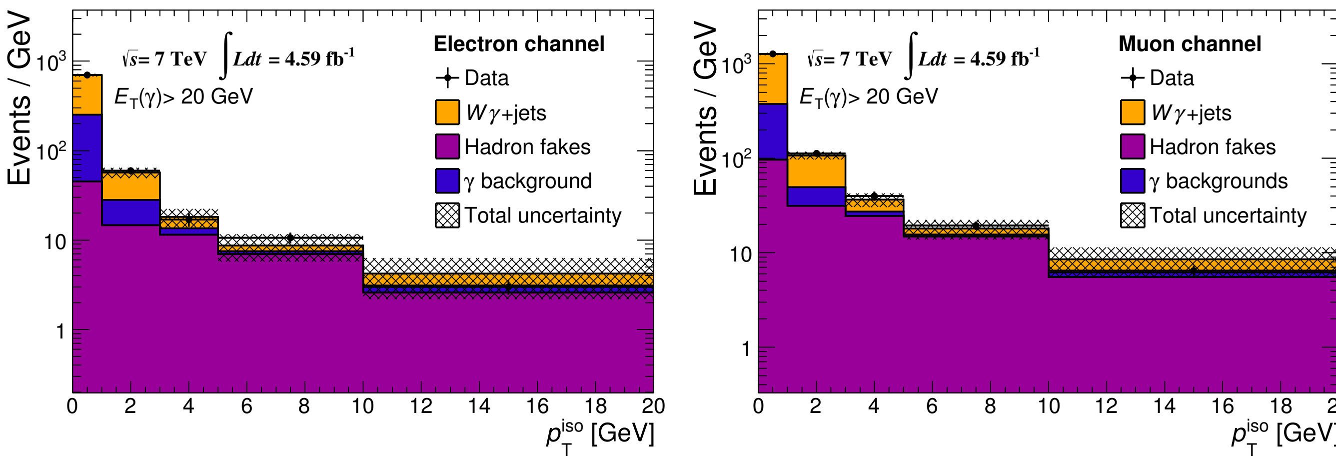

Figure 6.9: Result of the track isolation fit for extracting prompt-photons in the $W\gamma+$jets control region. The result shown here was performed in the entire $E_{\rm T}(\gamma) > 20$ GeV range. The result for the electron channel is shown on the left, while the result for the muon channel is shown on the right

Moreover, $t\bar{t}$ events may leak into the CR and this signal-induced background needs to be determined. It is constituted by $t\bar{t}\gamma$ events and $t\bar{t}$ events with electrons being misidentified as photons [3]. The size and uncertainty of this background is correlated with the measurement of the $t\bar{t}\gamma$ cross section, however it was found to be negligibly small. Specifically, the contribution from both processes ($t\bar{t}\gamma$ and $t\bar{t}_{e\to\gamma}$) is of the order of 1% and 2% for the electron and muon channels respectively. Because of the high b-tagging identification efficiency, the $t\bar{t}\gamma$ contribution is less than 30% of this estimation. The $t\bar{t}\gamma$ cross section component of the uncertainty on those numbers is small (20%) compered to the statistical component (50%).

The contribution of electrons misidentified as photons from $W+$jets production in the SR is estimated using the $e \to \gamma$ misidentification rates, which were calculated in Sec. 6.1.3. It is found to be of 0.06 ± 0.06 events in the electron channel and < 0.01 events in the muon channel.

After subtraction of the e/γ backgrounds and extrapolation to the signal region the total amount of $W\gamma+$jets events contributing to the measurement of the $t\bar{t}\gamma$ cross section is 6.3 ± 0.3 (stat.) $\pm\, 1.8$ (syst) for the electron channel and $7.4^{+0.5}_{-0.4}$ (stat) $\pm\, 4.3$ (syst) in the muon channel.

Systematic uncertainties

The total amount of systematic uncertainty in the estimation of the $W\gamma+$jets background is of about 28% for the electron channel and 58% in the muon channel. These uncertainties were estimated from the differences with respect to the jet multiplicities, the differences induced by the difference in heavy flavour composition in the `SHERPA` and `ALPGEN` simulations and the overall normalisation of the $W\gamma+$jets samples in the control region.

[3] Essentially from the $t\bar{t}$ dilepton-mode.

6.2.3 Differences in the electron and muon channels

The $W\gamma+$jets cross sections are identical for both the electron and muon channels, however the event selection in the CR yields 2910 and and 6181 events in the electron and muon channels respectively. The reason behind the near to double event selection efficiency in the muon channel can be explained by the acceptance difference between the two channels. The minimum $p_{\mathrm{T}}(\mu)$ cut for muons is at 20 GeV to be compared with the $E_{\mathrm{T}}(e) > 25$ GeV for electrons. An invariant mass cut of $|\Delta m(e,\gamma)| < 15$ GeV is added in the electron channel, suppressing $Z(\to e^{+}e^{-})$ decays, but no $|\Delta m(\mu,\gamma)|$ cut is imposed in the muon channel.

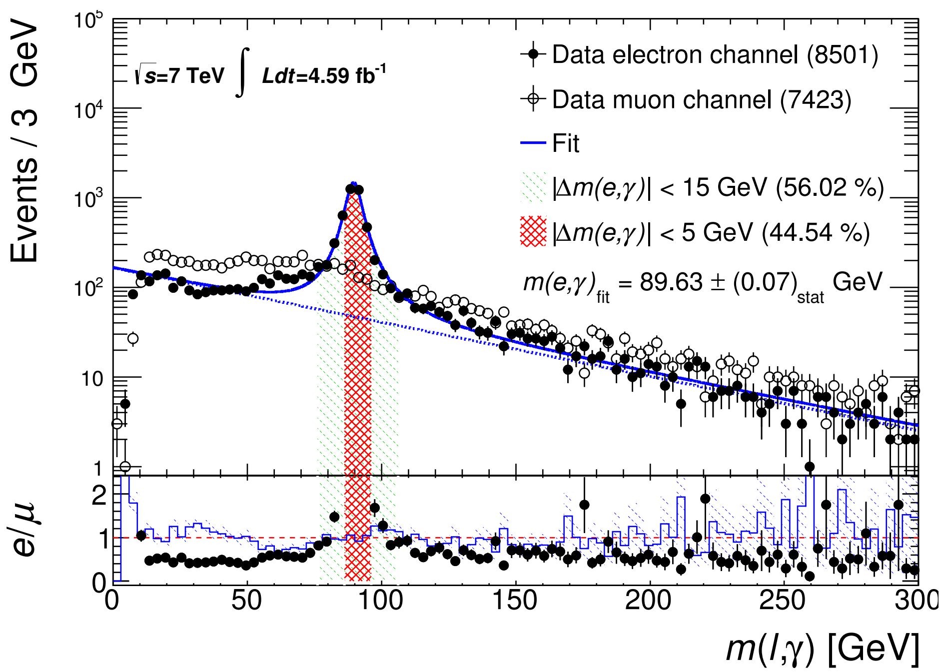

Figure 6.10: Invariant mass between the reconstructed lepton and photon. Filled dots correspond to the electron channel while open markers correspond to the muon channel. The invariant mass, for the electron represented by a continuous line, is fitted to data by a Breit-Wigner with an exponential background. The dotted line represents the fit on data considering only the falling exponential (background component). The two dashed areas compare the estimation of the relative integral of data excluded when applying a Δm cut of 15 GeV and of 5 GeV. On the bottom plot, the fraction of data in the electron channel to the muon channel is labelled by filled markers. The continuous line shows the data to fit ratio, the filled area shows the statistical uncertainty.

The effect of the invariant mass between the electron and the photon, $m(e,\gamma)$ has been evaluated by running the full $W\gamma+$jets selection on data without including the latter cut. Figure 6.10 shows the reconstructed invariant mass between the photon and the lepton for the electron and muon channel respectively. The data in the electron channel have been fitted with a Breit-Wigner pdf added to a slowing falling exponential. Although the choice of fitting function might not entirely describe the data, it is considered to be accurate enough for the purpose of this study.

The increase of the $\Delta m(e,\gamma)$ cut from a 5 GeV window around the Z-boson mass to a 15 GeV window corresponds to a relative decrease in the selection efficiency of roughly 12%. The difference in yields of roughly 990 events between electron and muon channels before applying any $\Delta m(e,\gamma)$

cut can be explained by the lower minimum p_{T}-requirement for muons. Figure 6.11 shows the two-dimensional distribution of the photon transverse energy with respect to the invariant mass of the reconstructed lepton-photon object. The excess of events due to Z-boson decays is clearly evident in the electron channel. Figure 6.12 shows the two-dimensional distribution of the transverse energy (momentum) required for electrons (muons) with respect to the lepton-photon invariant mass.

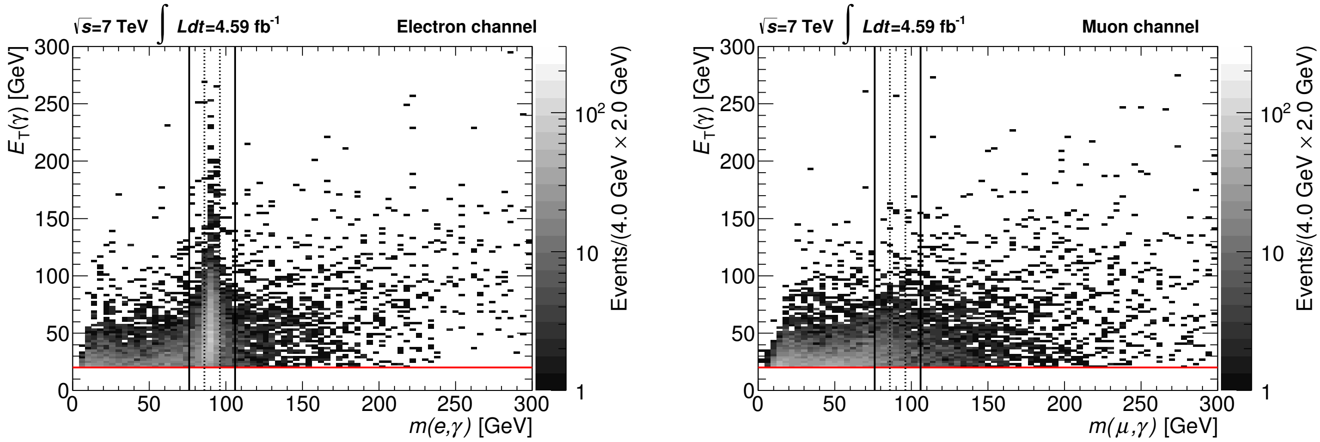

Figure 6.11: The photon transverse energy (on the Y axis) against the invariant mass of the reconstructed lepton-photon (on the X axis) are shown for the electron channel on the left and for the muon channel on the right. The invariant mass cut around the Z-boson mass is not applied. The continuous vertical lines indicate the invariant mass window of ± 15 GeV around the Z-peak, while the dotted vertical lines indicate the ± 5 GeV window. The horizontal line indicates minimum photon $E_{\mathrm{T}}(\gamma)$ cut applied to the selection.

6.3 Multijet production with additional photons

The multijet background is mainly composed of events with jets misidentified as *tight* leptons, jets with associated photon production and photons resulting from jet fragmentation. This background is estimated using a control sample in data. This control sample is characterised by relaxed identification and isolation criteria imposed on the lepton. This method is referred to as the *matrix method* [150]. A two step approach is used: firstly, the control sample with relaxed identification criteria on the leptons, is determined; secondly, the amount of prompt-photons within this sample is determined. The following sections explain in more details the two steps.

6.3.1 Definition of the control sample

For simplicity, isolated leptons are called real leptons, and jets misidentified as leptons, or non-isolated leptons that pass the identification and isolation criteria, are called *fake leptons*. A control sample based on the $t\bar{t}$ selection requirements is defined on data. The difference with respect to the nominal selection is that the lepton identification criteria, defined in Sec. 3.5, are replaced with relaxed requirements. The rectangular cuts on the shower shapes defining the electron are widened, and the isolation requirement for both electron and muons is discarded. This event selection is

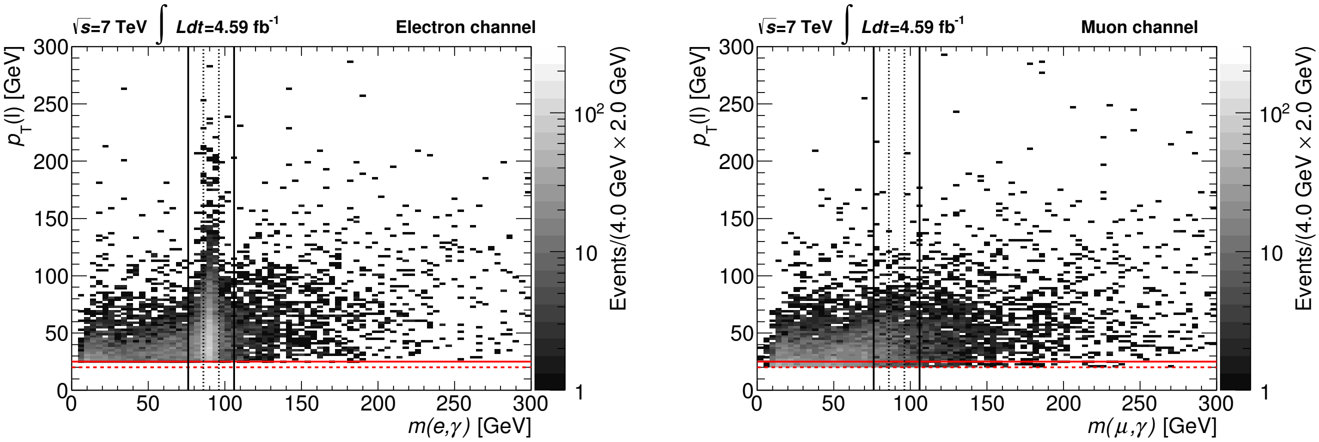

Figure 6.12: The electron (muon) transverse energy (momentum) against the invariant mass of the reconstructed electron- (muon-) photon is shown for the electron (muon) channel on the left (right). The invariant mass cut around the Z-boson mass is not applied. The continuous vertical lines indicate the invariant mass window of ± 15 GeV around the Z-peak, while the dotted vertical lines indicate the ± 5 GeV window. For each plot, the horizontal continuous line indicates the minimum electron-E_{T} cut (20 GeV) applied to the selection, while the horizontal dotted line indicates the minimum muon-p_{T}requirement (25 GeV).

called *loose* selection and contains N^{loose} events. The corresponding lepton's definition is refereed to as a *loose* lepton. The nominal selection requirements defines a second sample as being *tight* and containing N^{tight} events. The method makes the assumption that the total number of events in either samples is linear with respect to the number of real and fake leptons. The linearity for the loose sample can be expressed as:

$$N^{\mathrm{loose}} = N^{\mathrm{loose}}_{\mathrm{real}} + N^{\mathrm{loose}}_{\mathrm{fake}} \tag{6.9}$$

with $N^{\mathrm{loose}}_{\mathrm{real}}$ and $N^{\mathrm{loose}}_{\mathrm{fake}}$ being the number of events within the samples using the loose and tight lepton definitions respectively. Considering the probability for a real loose lepton to be identified as tight (f_{real}) and the probability for a fake loose lepton to be identified as a tight fake lepton ($\hat{f}_{\mathrm{fake}}$), the linearity in the tight sample can be expressed as:

$$N^{\mathrm{tight}} = N^{\mathrm{tight}}_{\mathrm{real}} + N^{\mathrm{tight}}_{\mathrm{fake}} = f_{\mathrm{real}} N^{\mathrm{loose}}_{\mathrm{real}} + \hat{f}_{\mathrm{fake}} N^{\mathrm{loose}}_{\mathrm{fake}} \tag{6.10}$$

From Eq. 6.9 and Eq. 6.10 it follows that the number of fake leptons passing the tight selection ($N^{\mathrm{tight}}_{\mathrm{fake}}$) is:

$$N^{\mathrm{tight}}_{\mathrm{fake}} = \frac{\hat{f}_{\mathrm{fake}}}{f_{\mathrm{real}} - \hat{f}_{\mathrm{fake}}} \left(N^{\mathrm{loose}} f_{\mathrm{real}} - N^{\mathrm{tight}} \right) \tag{6.11}$$

The N^{tight} includes photons defined by the $t\bar{t}\gamma$ selection criteria.

6.3.2 Extraction of the multijet plus photon background

Kinematic-related and acceptance-based weights are applied to the $N^{\mathrm{tight}}_{\mathrm{fake}}$ sample, in order for the estimation to describe correctly the shape of reconstructed objects. However, the application

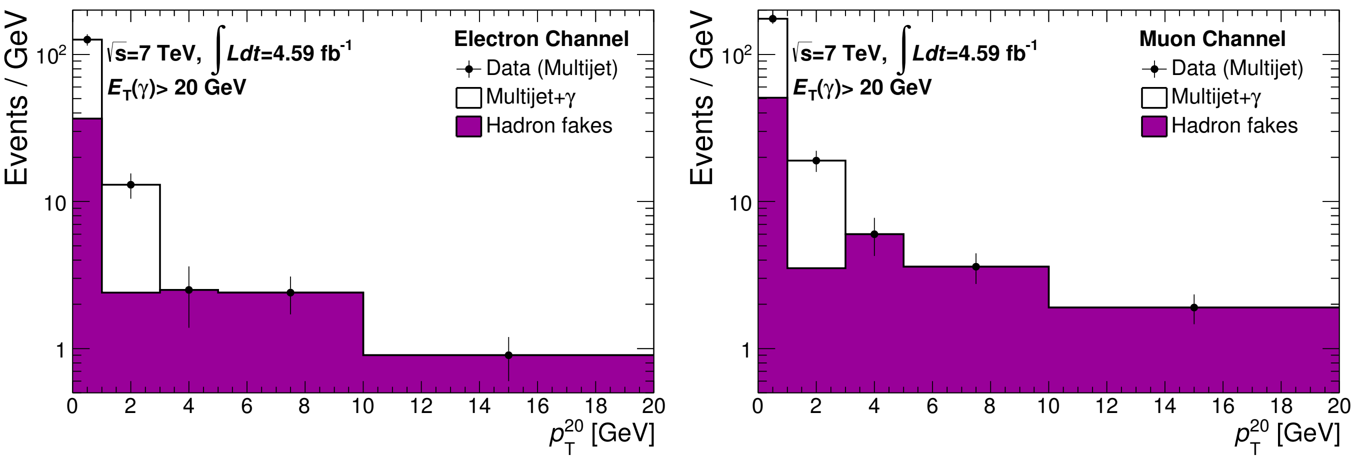

Figure 6.13: The extraction of the Multijet+γ background, with $E_{\mathrm{T}}(\gamma) > 20$ GeV, for the electron (muon) channel is shown on the left (right). The data points correspond to the events passing the loose selection requirements before application of kinematic and acceptance weights. The last bin contains any overflow.

Loose sample	***hadron-fakes* [events]**	**Fraction [%]**
Electron Channel	127.42 ± 27.89	71.59 ± 15.67
Muon Channel	246.88 ± 40.77	94.23 ± 15.56

Table 6.6: Estimates of hadron fakes within the loose sample selection. The fraction of hadron fakes for each channel is also shown. Uncertainties are statistical $\oplus$ systematic.

of event weights precludes the extraction of prompt-photons within the sample as it is based on the assumption that events in data are Poisson-distributed. Moreover, the validity of the asymptotic properties of the likelihood ratio method cannot be guaranteed for minimisations of binned distributions of small sizes.

The cut and count approach, described in App. D.5, is used instead. This approach determines the fraction of *hadron-fakes* from a given data binned distribution without constraining events within each bin to be Poisson-distributed. The cost of increased uncertainty, due to the chosen method, is overwhelmed by the statistical uncertainty, due to the small size of data candidates in this region.

At first, the fraction of hadron fakes within the control sample is estimated, see Tab. 6.6. The resulting $p_{\mathrm{T}}^{\mathrm{iso}}$ distributions are shown in Fig. 6.13. Secondly, the estimated fractions are applied to the reweighed candidates of the Multijet+γ.

The total multijet plus photon background is estimated to be 3.9 ± 1.7 events in the electron channel and 1.6 ± 2.8 events in the muon channel.

Systematic Uncertainties

Systematic uncertainties for the Multijet+γ background comprise a 50% and 20% uncertainty in the electron and muon channels respectively, and are driven by the uncertainty of the matrix method [150]. The uncertainty on the extraction of prompt-photons is estimated to be 9.1% and

4.3% for the electron and muon channels respectively. It is determined from the fluctuations of the $p_{\mathrm{T}}^{\mathrm{iso}}$ distribution for the *hadron-fakes*, details are given in App. D.5. Overall, the statistical uncertainty dominate across the entire $E_{\mathrm{T}}(\gamma)$ range.

6.4 Estimation of other processes with prompt-photons

The processes $Z+\text{jets}$, dibosons, and single top production can also feature final state photons from lepton final state radiation, jet fragmentation or from photon production in the ME. In comparison to the other backgrounds these contributions are expected to be small. They are determined from simulation, the cross section uncertainty is included in the predicted event yields for each background component. These uncertainties range from a few percentiles to at most 10%. However poor simulation statistics under the $t\bar{t}\gamma$ selection criteria overwhelm the total uncertainty. Numbers are summarised in Tab. 6.7.

	Estimation [events]	
Process	**Electron channel**	**Muon channel**
$Z\gamma+\text{jets}$	2.92 ± 0.89	3.14 ± 0.99
Dibosons+γ	0.09 ± 0.06	0.42 ± 0.11
Single top+γ	1.77 ± 0.26	3.75 ± 0.36

Table 6.7: Simulation based estimation of background process with additional photons. Numbers are given for the range $E_{\mathrm{T}}(\gamma) > 20$ GeV, the errors are statistical$\oplus$systematic.

6.5 Summary

This chapter summarised the methods used for extracting the background contributions in data within the $t\bar{t}\gamma$ fiducial phase-space. For the most significant backgrounds the extraction was derived from data, thus reducing the model dependency of the measurement. The smaller contributions were determined using simulations, but the induced model dependency of the measured $t\bar{t}\gamma$ cross section is expected to be very small, due to both their small size and their large uncertainties.

The estimation was performed both in the inclusive $E_{\mathrm{T}}(\gamma) > 20$ GeV as well as in exclusive $E_{\mathrm{T}}(\gamma)$ bins. Each section summarised the total contribution for each background, the complete breakdown is shown in Tab. 6.8. The estimation was performed independently in the inclusive and differential ranges as event migrations in $E_{\mathrm{T}}(\gamma)$ bins and correlations of systematic uncertainties may contribute differently. However, the sum of all backgrounds from all $E_{\mathrm{T}}(\gamma)$ bins was found to be in good agreement with the estimation from the inclusive $E_{\mathrm{T}}(\gamma) > 20$ bin.

Electron channel						
	e/γ **backgrounds [events]**					
$E_{\mathrm{T}}(\gamma)$ [GeV]	e-**fakes**	$W\gamma+$ **jets**	**Multijets**$+\gamma$	$Z\gamma+$ **jets**	**Dibosons**$+\gamma$	**Single top**$+\gamma$
$]20, 30[$	7.23 ± 1.11	0.02 ± 0.01	1.23 ± 1.10	1.24 ± 0.72	0.01 ± 0.02	0.61 ± 0.14
$[30, 40[$	4.55 ± 0.75	0.93 ± 0.14	0.01 ± 0.79	0.40 ± 0.28	0.01 ± 0.02	0.20 ± 0.07
$[40, 50[$	4.97 ± 0.71	0.02 ± 0.00	0.01 ± 0.32	0.40 ± 0.28	0.01 ± 0.02	0.39 ± 0.13
$[50, 70[$	4.15 ± 0.57	1.01 ± 0.14	0.55 ± 0.56	0.82 ± 0.58	0.01 ± 0.02	0.35 ± 0.14
$[70, 120[$	4.48 ± 0.57	1.82 ± 0.29	1.66 ± 1.18	0.75 ± 0.38	0.01 ± 0.02	0.01 ± 0.08
$[120, 180[$	0.92 ± 0.27	2.27 ± 0.47	0.32 ± 0.61	< 0.01	0.10 ± 0.06	0.19 ± 0.14
$[180, 250[$	0.20 ± 0.12	0.01 ± 0.02	0.11 ± 0.16	< 0.01	< 0.01	< 0.01
$[250, 300[$	0.20 ± 0.12	0.01 ± 0.02	0.01 ± 0.09	< 0.01	< 0.01	< 0.01
$[300, \infty[$	< 0.01	2.84 ± 1.40	< 0.01	< 0.01	< 0.01	< 0.01
Muon channel						
	e/γ **backgrounds [events]**					
$E_{\mathrm{T}}(\gamma)$ [GeV]	e-**fakes**	$W\gamma+$ **jets**	**Multijets**$+\gamma$	$Z\gamma+$ **jets**	**Dibosons**$+\gamma$	**Single top**$+\gamma$
$]20, 30[$	9.95 ± 1.24	0.89 ± 0.06	0.52 ± 0.18	0.29 ± 0.29	0.02 ± 0.02	1.16 ± 0.19
$[30, 40[$	7.53 ± 0.96	1.20 ± 0.10	0.21 ± 0.12	0.68 ± 0.34	0.15 ± 0.06	0.55 ± 0.14
$[40, 50[$	6.45 ± 0.78	1.05 ± 0.12	0.19 ± 0.12	0.01 ± 0.02	0.01 ± 0.02	0.42 ± 0.12
$[50, 70[$	5.62 ± 0.69	2.11 ± 0.24	0.09 ± 0.10	0.84 ± 0.60	0.06 ± 0.04	1.21 ± 0.24
$[70, 120[$	7.44 ± 0.77	0.01 ± 0.01	0.40 ± 0.00	0.71 ± 0.50	0.19 ± 0.09	0.44 ± 0.12
$[120, 180[$	2.31 ± 0.42	1.61 ± 0.28	0.11 ± 0.07	< 0.01	0.01 ± 0.02	0.05 ± 0.02
$[180, 250[$	0.37 ± 0.15	0.23 ± 0.23	0.01 ± 0.02	< 0.01	< 0.01	< 0.01
$[250, 300[$	0.37 ± 0.15	0.01 ± 0.01	< 0.01	< 0.01	< 0.01	< 0.01
$[300, \infty[$	< 0.01	3.06 ± 1.84	< 0.01	< 0.01	< 0.01	< 0.01

Table 6.8: Summary of e/γ backgrounds in bins of $E_{\mathrm{T}}(\gamma)$. Components are shown for the electron (muon) channel on the top (bottom). Uncertainties include a statistical component and bin migration effects. For backgrounds that were evaluated to contribute less than < 0.01 events only an upper limit is shown.

CHAPTER 7

Systematic uncertainties

The methods of statistical inference used in this thesis are based upon a definition of the probability as being the limiting frequency (veryfying Kolmogorov's properties [123]) with increasing number of observations N. Therefore, the likelihood estimator should converge to the true value of any observed quantity with $N \to \infty$. However, complex deterministic or stochastic effects do not decrease with the increase of N. Their effect on the measurement of a natural quantity is to systematically bias the estimation. These effects are commonly referred as systematic uncertainties. It was shown in Chap. 5 that these biases are included into the likelihood estimator via parameters, so-called nuisance parameters, that increase the uncertainty on the final cross section estimation. The nuisance parameters are assumed to be *estimates* of observables (random variables) distributed according to probability density functions. The choice of each probability density function modelling each nuisance parameter depends upon the underlying mechanism that produces them. While Chap. 5 focused in the implementation of these bias corrections into the inference method, this chapter focuses on the study and the derivation of the sources of systematic uncertainty.

The determination of the signal efficiency was performed using simulations. These simulations are based upon assumptions that can potentially introduces biases that affect the way the signal ($\sigma_{t\bar{t}\gamma}$) is modelled. These uncertaintie are studied in Sec. 7.1.

The detector response is based upon calibrations of complex methods and can vary depending on the experimental conditions. Therefore, the detection and identification efficiency is known only to a certain degree of accuracy. The response is typically distorted by resolution and smearing effects on the observed distributions. These corrections introduce systematic biases and their effect on the measured cross section should incorporate them. Section 7.2 reviews these sources sorting them by the affected reconstructed objects used in this analysis.

Uncertainties may be correlated between channels and across the signal and the backgrounds; sec Sec. 7.5 reviews the treatment of these correlations.

7.1 Signal modelling

The choice to measure the $t\bar{t}\gamma$ cross section within the detector acceptance eliminates the uncertainty due to the extrapolation to a larger phase-space. However, the signal response in the detector was studied using two Leading-Order (LO) simulation programs, `WHIZARD` and `MadGraph`. It was shown that the efficiency (C) of detecting a $t\bar{t}\gamma$ event in the detector is independent of the simulation program used (see Sec. 4.3). In fact, in a fiducial measurement, these efficiencies depend uniquely on the detector response, *i.e.* trigger, identification and reconstruction efficiencies. However, event migrations to and from the detector phase-space can bias this efficiency determination. Therefore, a study of these possible biases is needed.

The `WHIZARD` and `MadGraph` simulation programs use complex and wide parameter sets. The study of the systematic uncertainty corresponding to the variation of those parameters is categorised in blocks of uncorrelated sets affecting collectively higher level observables. These are are: the choice of the Matrix-Element (ME) Monte Carlo (MC) generator, the effect of the choice of the renormalisation and factorisation scales, the choice of the parton showering technique, the approximations used to describe the parton density functions, the modelling of the Quantum Electrodynamics (QED) and Quantum Chromodynamics (QCD) radiation, the colour reconnection models used, and the parametrisation of the underlying event activity.

7.1.1 Monte Carlo generator

A wide range of parameters is used to model the $t\bar{t}\gamma$ singal LO contributions. These parameters range from physical quantities, like the particles masses, decay widths or phase-space requirements (mitigating divergencies), to the unique way the Feynman amplitudes are calculated numerically. An example of the different types of phase-space definition is given by the fact that `WHIZARD` uses invariant mass cuts while `MadGraph` uses angular separations. An example of the intrinsic generation treatment is given by the fact that `WHIZARD` uses a symbolic representation of the factored scattering amplitudes of all contributing subprocesses (using the optimised matrix element generator [88], see Sec. 3.2.1), while `MadGraph` uses a mapping between the subprocesses and the full phase-space for each generated event integration (see Sec. 3.2.2).

Given the wide range of parameter involved, the determination of he probability density function characterising each parameter, and its subsequent inclusion in the likelihood, would be in practice unachievable. A compound variation is used instead, and the effect is determined collectively. The majority of the physical constants used by the simulation programs are set to the same values, and effectively the variation includes only uncorrelated parameters.

The associated generator uncertainty is estimated by comparing selection efficiency by the two different LO generators, `WHIZARD` and `MadGraph` both interfaced with `HERWIG`. The comparison includes detector smearing and resolution effects as it is performed after full event reconstruction. The same reconstruction programs, with identical parameter settings, are used.

It is found that the selection efficiency varied by 2.1% and 0.7% for the electron and muon channels respectively. The photon track-isolation distributions are found to be in very good agreement with no distinguishable shape differences, as shown in Fig. 7.1 (top). Variations in the selection efficiency as a function of the photon's energy in the transverse plane are found to be within the statistical uncertainty of the efficiency calculation, as shown in Fig. 7.1 (bottom).

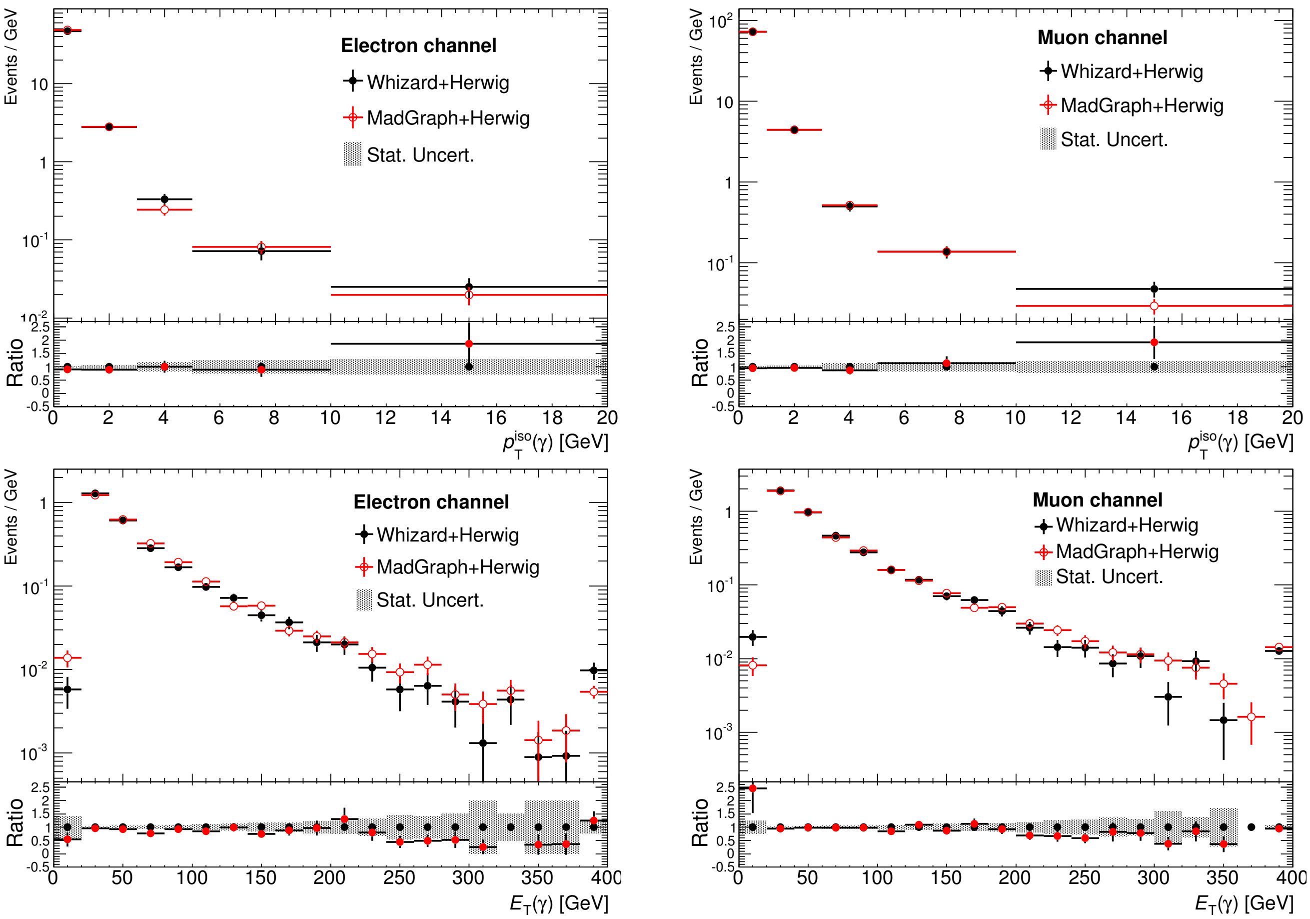

Figure 7.1: The shape differences for the photon track-isolation between `WHIZARD` and `MadGraph` are shown on the top. The distributions are shown after all reconstruction cuts for the electron (left) and muon (right) channels have been applied. The differences in the expected number of $t\bar{t}\gamma$ events as a function of the $E_{\mathrm{T}}(\gamma)$ is shown on the bottom, the electron channel is shown on the left while the muon channel is shown on the right. For both distributions the last bin contains any overflow.

7.1.2 Renormalistion and factorisation scales

As explained in Sec. 1.1 any cross section calculation has to be performed at a given value of the renormalisation (μ_{R}) and factorisation (μ_{F}) scales. The effect is estimated by comparing three different $t\bar{t}\gamma$ `MadGraph` samples interfaced to `PYTHIA`, where μ_R and μ_F have been set to m_t, $m_t/2$ and $2m_t$. The systematic uncertainty is evaluated from the shape difference of the following kinematic variables: $p_{\mathrm{T}}^{\mathrm{iso}}(\gamma)$, $E_{\mathrm{T}}(\gamma)$, $\eta(\gamma)$, $\phi(\gamma)$, $p_{\mathrm{T}}(\ell)$ and $p_{\mathrm{T}}(j)$. As an example, Fig. 7.2 compares the photon track isolation and the photon's transverse energy for the samples generated with different scales.

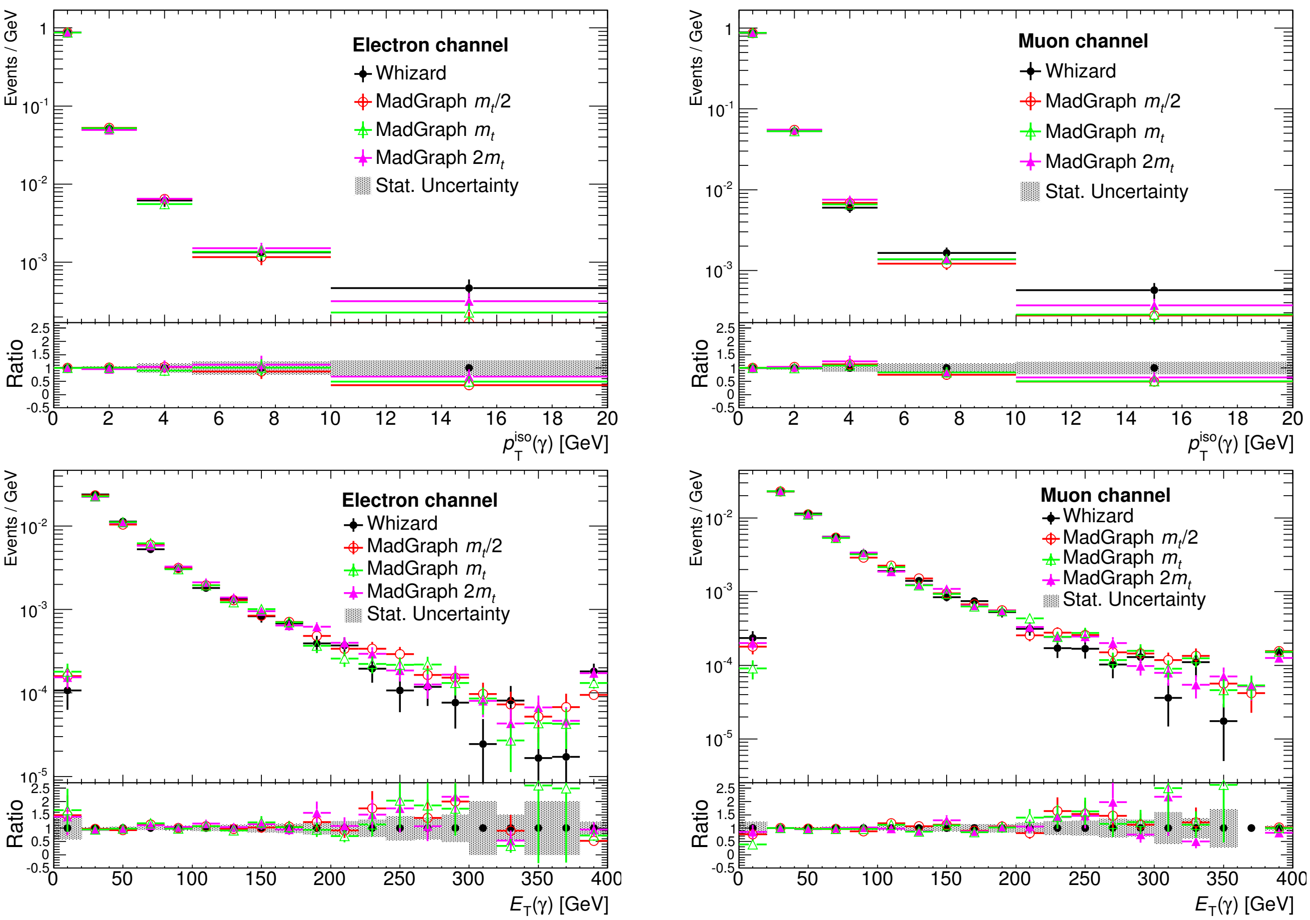

Figure 7.2: Top: Shape differences for the photon track isolation; Bottom shape differences as a function of the $E_T(\gamma)$. The plots compare samples with different scales after all reconstruction cuts for the electron (left) and muon (right) channels. For illustrative purposes, the results obtained with WHIZARD have been also included. Because of the different cross sections, the samples are normalised to their area. In each plot, the bottom pad shows the ratio of each sample with respect to the $t\bar{t}\gamma$ WHIZARD sample. The statistical uncertainty corresponds to the MadGraph sample.

For each kinematic variable, the distribution of the binned difference obtained from all permutations among the different MadGraph samples above is built, see Fig. 7.3. The uncertainty component is taken as the Root Mean Square of the resulting distribution. Table 7.1 shows the obtained uncertainties for all above mentioned variables. For each channel, the final uncertainty is taken as the maximal value among the different kinematic variables studied, reading 0.50% and 0.47% for the electron and muon channel respectively.

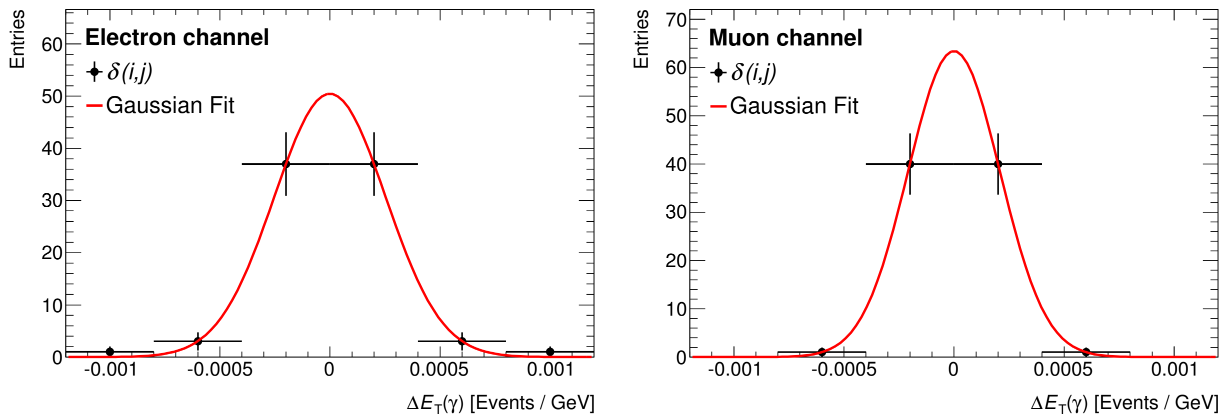

Figure 7.3: Distribution of differences in $E_\mathrm{T}(\gamma)$ from all permutations among the `MadGraph` samples generated with factorisation and renormalisation scales set at $m_t/2$, m_t and $2m_t$. Results are shown after full event reconstruction for the electron (muon) channel on the left (right).

Variable	Root mean square	
	Electron channel	**Muon channel**
$p_\mathrm{T}^\mathrm{iso}(\gamma)$	$(2.629 \pm 0.396) \times 10^{-3}$	$(3.568 \pm 0.538) \times 10^{-3}$
$p_\mathrm{T}(\gamma)$	$(4.685 \pm 0.366) \times 10^{-3}$	$(3.320 \pm 0.259) \times 10^{-3}$
$\eta(\gamma)$	$(4.899 \pm 0.500) \times 10^{-3}$	$(3.652 \pm 0.373) \times 10^{-3}$
$\phi(\gamma)$	$(4.257 \pm 0.365) \times 10^{-3}$	$(4.777 \pm 0.410) \times 10^{-3}$
$p_\mathrm{T}(\ell)$	$(2.732 \pm 0.109) \times 10^{-3}$	$(2.447 \pm 0.010) \times 10^{-3}$
$p_\mathrm{T}(\ell)$	$(4.287 \pm 0.227) \times 10^{-3}$	$(3.751 \pm 0.199) \times 10^{-3}$

Table 7.1: Root mean square of the distributions of the binned differences in several kinematic variables, as obtained from renornalization and factorization scale variations.

An alternative approach for the evaluation of the scale uncertainties has been also performed. From the `MadGraph` samples generated at different scales, signal templates are derived. Then, an ensemble of 10^4 pseudo-experiments is generated for each template and a template fit is performed for each pseudo-experiment. An uncertainty of 0.14% is derived by considering the maximal variation among the mean cross section yielded for each ensemble. Table 7.2 shows the relative uncertainties for different scale variations.

Input samples	$\delta\varepsilon/\varepsilon[\%]$
$\mu_\mathrm{F,R}(2m_t) - \mu_\mathrm{F,R}(m_t)$	0.13
$\mu_\mathrm{F,R}(m_t/2) - \mu_\mathrm{F,R}(m_t)$	0.14

Table 7.2: Relative uncertainties on $\sigma_{t\bar{t}\gamma}$ as yielded from ensemble tests based on templates of `MadGraph` samples for different scale variations. No direct comparison to the nominal cross-section is possible due to the different factorisation / renormalisation settings of the `WHIZARD` sample.

7.1.3 Parton Shower modelling

As discussed in Sec. 1.1.1, the time evolution of each Parton Density Function (PDF) is extracted from an iterative procedure on the splitting functions. This procedure is not unique and it is considered to be an approximation of an exact solution of the DGLAP equation. Two different procedures were applied to the $t\bar{t}\gamma$ sample, one implemented within the `HERWIG` simulation program and the other implemented within `PYTHIA` simulation program.

In `HERWIG` [90] the iterations are based upon the angle of emission (ξ) between the partons k, j emitted from a parton i ($\xi = (p_j \cdot p_k)/(E_j E_k)$). ξ is distributed according to the Sudakov form factors. At each iteration step ξ gets smaller and the algorithm terminates at an arbitrary cutoff value[1].

In `PYTHIA` parton showers are treated as radiation (either photon or gluon) and each gluon (or photon) emission is characterised by the splitting functions (see Sec. 1.1.1). The algorithm exploits the final state parton shower time dependence (for each branching parton k its mass verifies $m_k^2 = E_k^2 - \boldsymbol{p}_k^2 \geq 0$) and, therefore, the ordering parameter is the invariant mass m_k. The algorithm starts for a value of m_k at an arbitrary scale Q^2_{max} evolving with lower values of m_k and it stops at a cutoff value.

Furthermore, emitted partons hadronise producing collimated sprays of particles (jets). The two simulation programs use different methods for modelling the hadronisation process.

In `HERWIG` the evolution of pairs of quark-antiquarks or diquark-antiquark is back-traced based upon their colour evolution [151]. Particles of the same colour are combined into colour singlet clusters. These colour clusters are allowed to evolve into mesons (baryons) composed of a quark-antiquark (diquark-antiquark) flavour mixture, which is chosen at random.

`PYTHIA` uses the Lund string model [133]. Gluon field lines are approximated by geometrical tubes of narrow width (strings) and their attractive force is approximated by the string's length. The strings are stretched to a breaking point beyond which they form quark-antiquark paris.

The uncertainty from the parton shower modelling is evaluated using $t\bar{t}\gamma$ samples generated with `MadGraph` interfaced to `HERWIG` and to `PYTHIA`. For both samples the comparison is made upon fully reconstructed quantities. This doing includes effects from events migrating in- and out- of the fiducial phase-space. Figure 7.4 shows the differences observed for the photon track isolation and the differences as a function of $E_{\mathrm{T}}(\gamma)$. These variations correspond to an efficiency variation of 8.0% and 5.6% in the electron and muon channels respectively. This is a rather large uncertainty component and the reason is the equal treatment of gluon and photon radiation in `PYTHIA`.

7.1.4 Final state photon radiation

The uncertainty associated to the modelling of photon radiation off leptons and photons from jet fragmentation needs also to be quantified. The different treatment of photons in `PYTHIA` and `HERWIG` is included in the parton shower related uncertainty. However, to complete the investigation `PYTHIA` parameters are varied in order to extract the uncertainty with respect to the photon radiation within a same simulation program. Two different simulations are considered. The first requests an angular separation of $\Delta R(\gamma, i) \geq 0.2$ between any parton (or lepton) i and the photon γ, and any additional radiation is handled by `PHOTOS` [92]. The second uses a relaxed angular requirement of $\Delta R(\gamma, i) \geq 0.05$, without any added radiation produced by `PHOTOS`.

[1]Specifically the termination occurs when $\xi < (m_i + Q_0)^2/E_i^2$, with Q_0 being a cutoff dependent on μ_{F} and m_i the mass of the i-th parton.

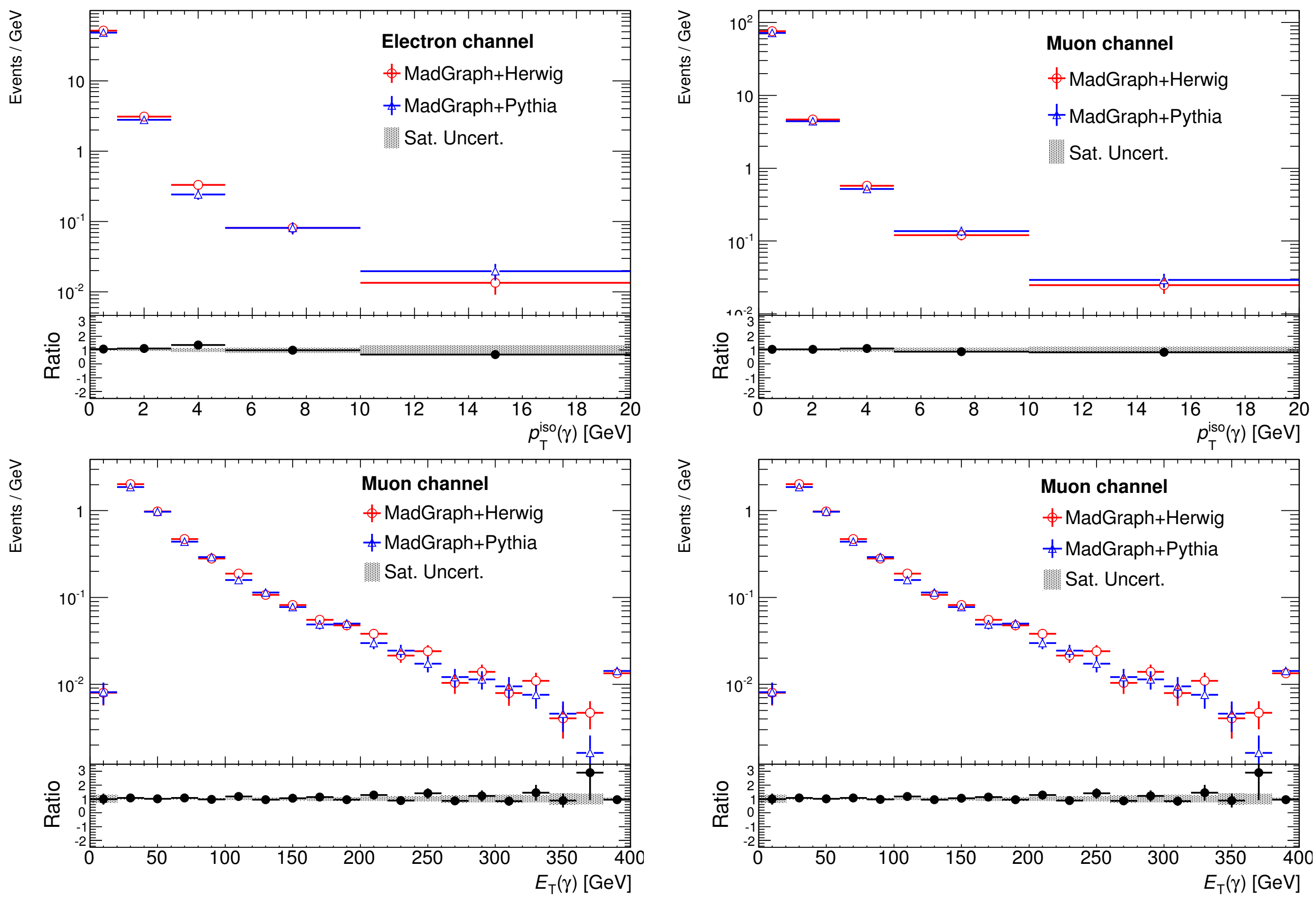

Figure 7.4: The photon track isolation (energy in the transverse plane) is shown on the top (bottom). The open circular markers correspond to the $t\bar{t}\gamma$ sample interfaced to `HERWIG`, while the triangular markers correspond to the $t\bar{t}\gamma$ sample interfaced to `PYTHIA`Ȧside from the overall normalisation difference the two E_T distributions show a good agreement in shape. Distributions for the electron (muon) channel are shown on the left (right). The last bin contains any overflow.

The differences in efficiency, after full reconstruction, are of 2.3% and 4.0% for the electron and muon channel respectively. It can bee seen that the first sample has a wider photon track isolation with respect to the second, as shown in Fig. 7.5 top. However, the shapes of the photon energy in the transverse plane are not discrepant with respect to each sample, see Fig. 7.5 bottom.

7.1.5 Parton distribution function

The uncertainty associated with the choice of the PDF is evaluated by re-weigthing the CTEQ6L1 LO PDF used in the generation of the $t\bar{t}\gamma$ `WHIZARD` sample to the CTEQ6.6, MSTW2008 and NNPDF2.0 NLO PDF sets as recommended by PDF4LHC working group [152]. The variation of the $t\bar{t}\gamma$ efficiency was estimated to be 1.3% and 0.1% for the electron and muon channels respectively [153].

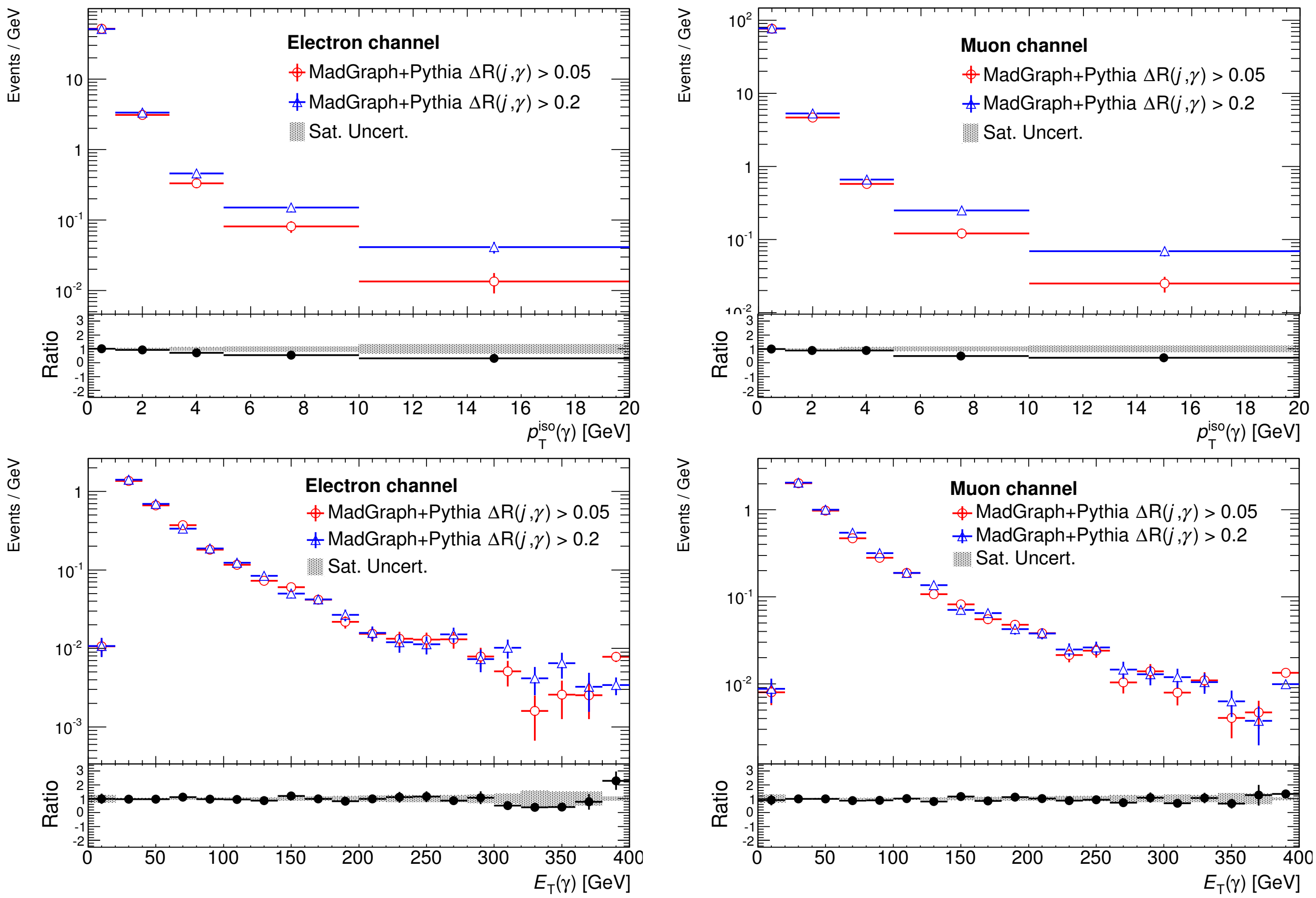

Figure 7.5: Shape differences for the photon track isolation (top) and for the photon energy in the transverse plane (bottom) among the samples with different scales after all reconstruction cuts for the electron (left) and muon (right) channels. For illustrative purposes, the results obtained with the `WHIZARD` MC have been also included. Because of the different cross-sections, samples are normalized to their area. In each plot, the bottom pad shows the ratio of each sample with respect to the $t\bar{t}\gamma$ `WHIZARD` sample. The statistical uncertainty corresponds to the `WHIZARD` sample.

7.1.6 Colour reconnection

Either parton shower algorithm has to iterate through the colour index of the generated particles in order to reconnect the final state hadrons to the partons. The authors of the simulation parameters values (tunes) suggest to the experiments the comparison of two different models [154]. Therefore, the uncertainty is extracted from comparisons of samples with the default modelling (`Perugia2011` tune) with respect to a model where the Lund string model is replaced by a p_{T}-ordering principle with no associated parton colour. This change appears as slightly harder $p_{\mathrm{T}}-$spectrum. The effect in the efficiency is estimated to be about 0.4% and it is obtained from comparisons of $t\bar{t}$ simulations with the `ACERMC` program (either using the default modelling (`Perugia2011` tune) or the p_{T}-ordering model (`Perugia2011 noCR` tune) [154].

Underlying event activity

Multiple hard scatterings can occur in pp collisions at the LHC. The uncertainty associated to the underlying event activity is estimated using $t\bar{t}$ simulations (`ACERMC` interfaced to `PYTHIA`). In particular, simulations with Λ_{QCD} set to 0.26 GeV (`Perugia2011 mpiHi`) are compared to that of the nominal settings (`Perugia 2011`) [154]. This results in a 0.6% and 0.2% efficiency change.

7.2 Detector modelling

Chapter 2 discussed how the ATLAS experiment detects particles trough their energy deposits within complex systems. The deposited energy corresponds to signals directly proportional to the energy loss, or the space-time characteristics, of the interacting particles. These signals are interpreted as sets of end-level objects with similar characteristics. The categorisation is based upon a close correspondence with the physical objects that the detection aims. These sets of reconstructed objects are therefore associated to leptons (electrons or muons), jets, missing energy in the transverse plane, etc. The detailed and formal definition of each reconstructed object was thoroughly detailed in Sec. 3.5. However, these definitions are subject to several uncertainties that arise from the detection processes which underpin their construction. A complex set of parameters is used for calibrating the reconstructed objects in order to provide the response with respect to the input signals. The knowledge of the detector response is included in complex simulations that are compared with respect to data for well known physical phenomena. Data-to-simulation differences define the level of this knowledge. The following sections discuss how the effect of those differences is included as input on the statistical model which extracts the $t\bar{t}\gamma$ cross section.

7.2.1 Leptons

Simulation-to-data differences obtained for the lepton trigger, reconstruction and identification efficiencies are corrected by applying scale factors. The scale factors are determined from data as a function of the lepton kinematics. The trigger uncertainty on the efficiency is extracted using a Tag and Probe technique on data from $Z(\rightarrow \ell\bar{\ell})$ and $W(\rightarrow e\nu)$ decays. The trigger efficiencies are given as a function of the different single lepton triggers or run periods [155]. The impact on the $t\bar{t}\gamma$ selection efficiency is determined using simulations. Varying the scale factor values (within 1σ of their uncertainty) determines the effect on the $t\bar{t}\gamma$ selection efficiency.

The accuracy of the lepton scale and lepton resolution has been studied in data from $Z(\rightarrow \ell\bar{\ell})$ decays. In the case of electrons, smearing corrections to the energy scale in data and to the energy resolution in simulations are applied [107]. For muons, both momentum scale and smearing corrections are applied in the simulation [112]. The impact of the electron (muon) energy (momentum) scale on the efficiency is evaluated by shifting up and down the electron (muon) energy (momentum) by the corresponding relative scale uncertainty. The effect is document in Fig. 7.6. The same procedure is applied to evaluate the systematic uncertainty associated with the lepton resolution. Both lepton scale and resolution uncertainties are propagated to the calculation of $E_{\mathrm{T}}^{\mathrm{miss}}$.

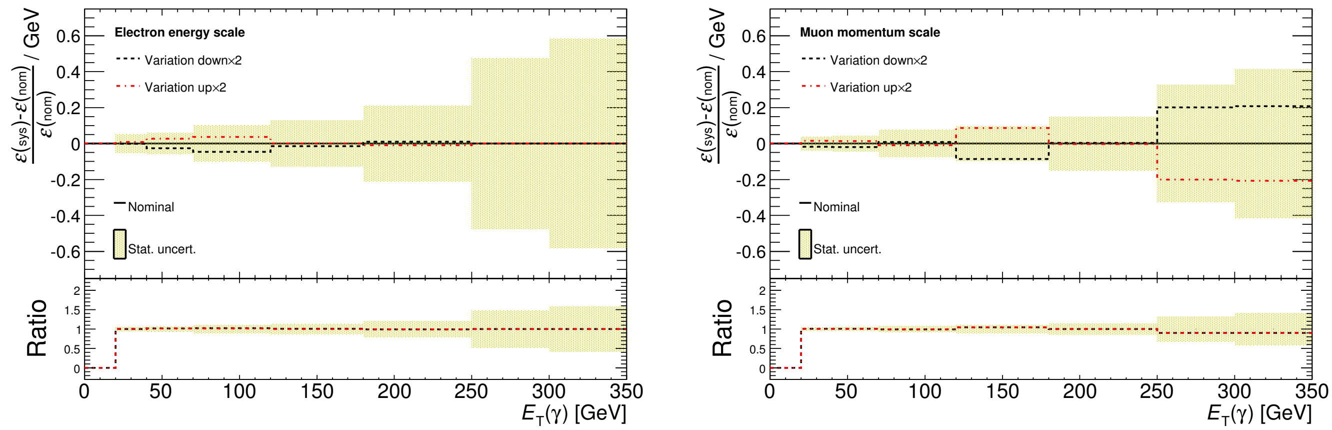

Figure 7.6: Electron (muon) energy (momentum) scale variations as a function of the photon energy in the transverse plane. In each frame the top distributions show the normalised difference of the up (dotted line) and down (dashed line) variation with respect to the nominal $t\bar{t}\gamma$ sample (continuous line). The filled histogram corresponds to the statistical uncertainty of the simulated sample. The last bin contains any overflow.

7.2.2 Photons

Photons share similar properties with that of electrons. Correction factors are applied to the simulated samples based upon measurements in data of well known radiative phenomena. These factors are varied within the measured uncertainties.

Photon identification efficiency

The accuracy of the photon identification has been studied from radiative $Z(\rightarrow \ell\bar{\ell}\gamma)$ decays. These decays offer the possibility to study the extrapolation from the electron objects to the photon objects [111].

Photon energy scale and resolution

In the same way as done for electrons, normalisation corrections to the photon energy scale are applied. Data-to-simulation discrepancies are corrected by applying correction factors [156]. The corresponding systematic uncertainties on $t\bar{t}\gamma$ selection efficiency are estimated by varying the photon energy scale and energy resolution scale factors according to their uncertainties. Figure 7.7 shows the effect of the variations to the photon energy scale correction factors. Figure 7.8 shows the effect of the variation of the photon energy resolution correction factors within their uncertainties.

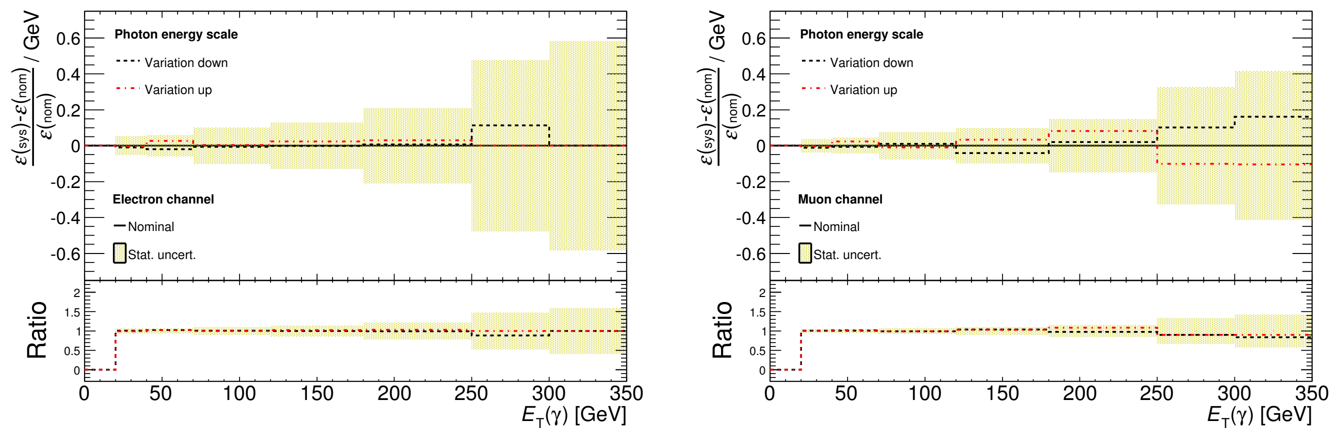

Figure 7.7: Effect of the photon energy scale in the $t\bar{t}\gamma$ selection efficiency as a function of the photon energy in the transverse plane. The distribution on the left (right) shows the effect in the electron (muon) channel. The last bin contains any overflow.

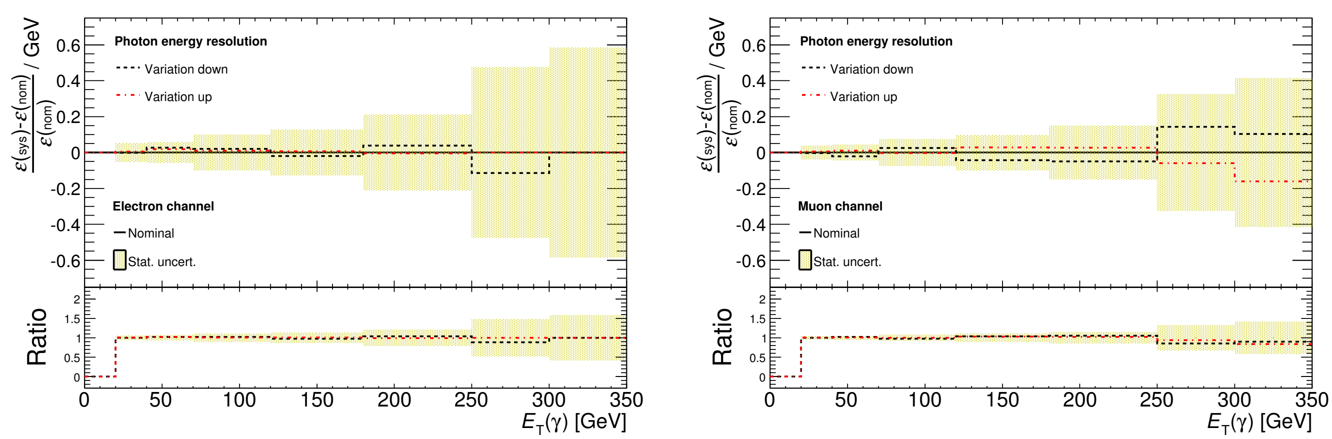

Figure 7.8: Effect of variations of the photon energy resolution in the $t\bar{t}\gamma$ selection efficiency as a function of the photon energy in the transverse plane. The distribution on the left (right) shows the effect in the electron (muon) channel. The last bin contains any overflow.

7.2.3 Jets

Jet reconstruction efficiency

The jet reconstruction efficiency is measured as the fraction of jets built from tracks reconstructed by the Inner Detector (ID) matched to jets reconstructed by the calorimeters using an *in-situ* Tag and Probe technique. The efficiencies measured in a sample of minimum bias events shows a good agreement overall between data and simulations except at low $p_{\mathrm{T}}(j)$. The systematic uncertainty from the *in-situ* determination (2% for $p_{\mathrm{T}}(j) < 30$ GeV and negligible for higher momenta [113]) is larger than the observed shift. The observed difference between data and simulations is applied (to simulations) by discarding randomly a fraction of the jets taken within the inefficiency range. The effect as a function of the photon energy in the transverse plane is shown in Fig. 7.9. It can be seen that the effect is small but not negligible. In the range $E_{\mathrm{T}}(\gamma) > 20$ GeV it corresponds to a < 1% and 0.1% uncertainty on the selection efficiency in the electron and muon channels respectively.

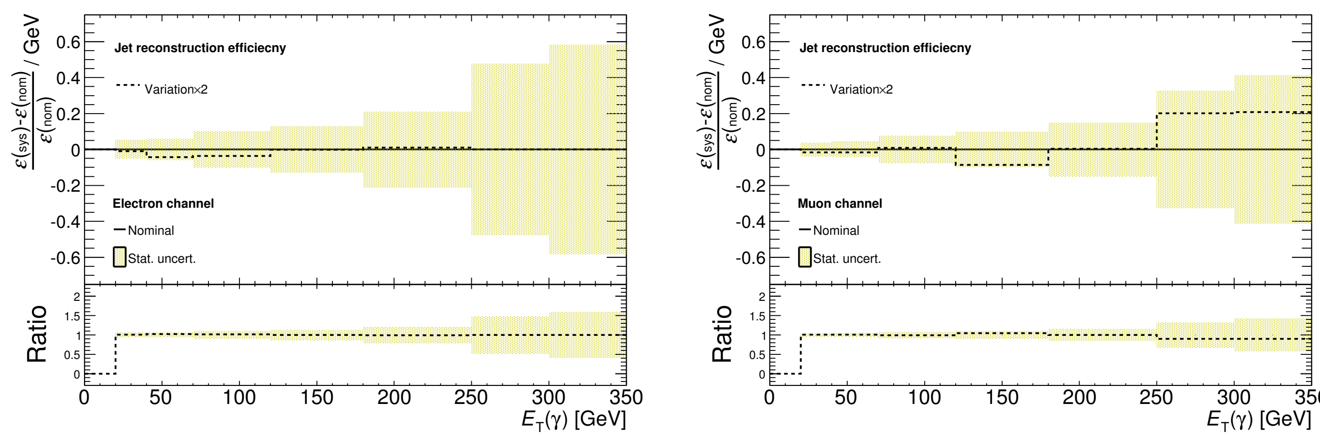

Figure 7.9: Differences of track based each frame the top distributions show the normalised difference of the up (down) variation with respect to the nominal $t\bar{t}\gamma$ sample in a dotted (dashed) line. The dashed area corresponds to the statistical uncertainty of the simulated sample. The last bin contains any overflow.

Jet energy scale

The jets used in this analysis are calibrated at the EM scale with the EM+JES scheme [157]. The jet calibration corrects for detector effects on the jet energy measurement as non compensating calorimeter, dead material, leakage and out-of-calorimeter jet cone. The calibration is implemented as energy correction factors (so called jet response factors) derived from simulations in different pseudorapidity regions. The uncertainty on the jet energy scale is derived by combining informations from the single hadron response measured with *in-situ* techniques and with single pion test-beam measurements. They include uncertainties on the amount of material, the description of the electronic noise and the simulation choice [113]. The application of the uncertainty includes terms for flavour composition, flavour response and close-by jets. The effect on the $t\bar{t}\gamma$ selection efficiency as a function of $E_{\mathrm{T}}(\gamma)$, see Fig. 7.10, is estimated on $t\bar{t}\gamma$ simulations by shifting the

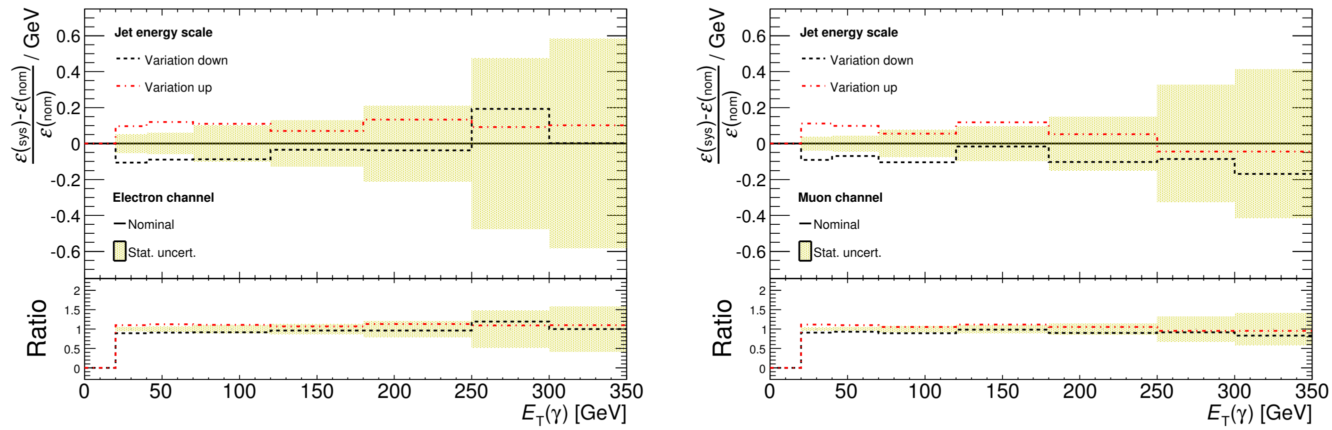

Figure 7.10: Effect of shifted values for the jet response factors within their uncertainty on the photon energy in the transverse plane. The effect on the electron (muon) channel is shown on the left (right). The last bin contains any overflow.

correction factors within their uncertainties.

Jet energy resolution

Dijet balance and bi-sector techniques [2] show a good agreement between data and simulations [158]. The jet energy resolution systematic uncertainty to the $t\bar{t}\gamma$ selection efficiency is evaluated by smearing the simulated jets by one sigma around the systematic uncertainties of the measured resolution, see Fig. 7.11.

Jet vertex fraction

The systematic uncertainty associated to the cut on the jet vertex fraction ($P_{\mathrm{JVF}}(\mathrm{PV})$), see Eq. 3.3, is obtained by applying simultaneously up and down variations to the nominal scale factors [3].

7.2.4 Missing energy in the transverse plane

The uncertainties on the energy scale and resolution of leptons, jets and photons are propagated to the $E_{\mathrm{T}}^{\mathrm{miss}}$calculation. Two additional sources, and specific to the $E_{\mathrm{T}}^{\mathrm{miss}}$, are considered.

Soft jets and cell out terms

The systematic uncertainty associated with these $E_{\mathrm{T}}^{\mathrm{miss}}$ components is estimated by varying the energy scale of soft jets ($7\,\mathrm{GeV} < p_{\mathrm{T}}(j) < 20\,\mathrm{GeV}$) and calorimeter clusters or cells not associated with any reconstructed object (cell out) within their respective uncertainties. These two terms are fully correlated and thus no distinction is made. The effects of the up and down jet energy scale

[2] These techniques involve the decomposition of the highest-p_{T} jets in four-vector projections orthogonal to each jet's η, ϕ plane.

[3] These are the the jet selection efficiency and inefficiency, the pile-up jet rejection efficiency and inefficiency.

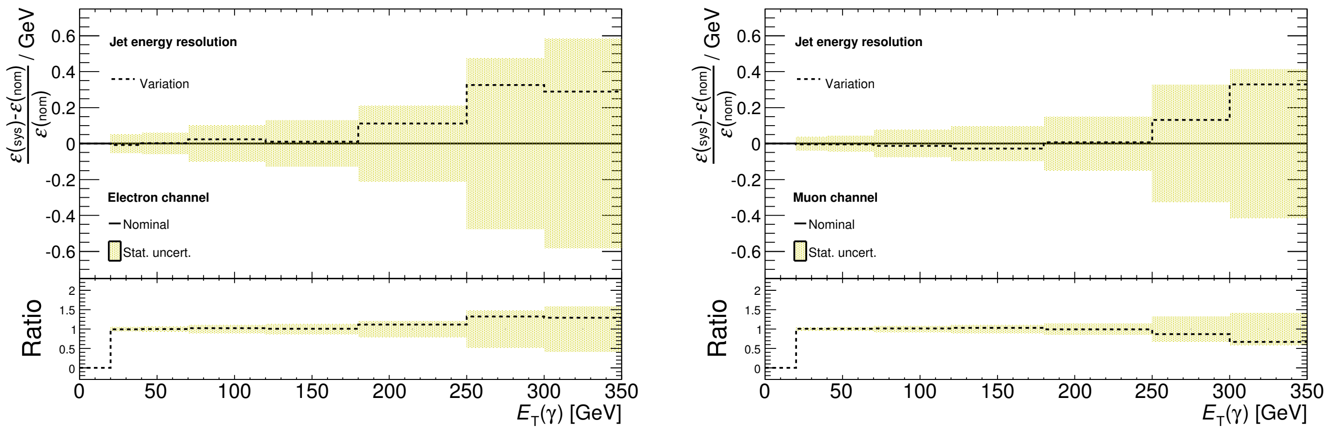

Figure 7.11: Estimation of the effect on the $t\bar{t}\gamma$ selection by smearing the simulated jet resolution by one sigma around the measured energy resolution in dijet balance an bi-sector techniques. The effect of the electron (muon) channel is shown on the left (right). The last bin contains any overflows.

variations on the $t\bar{t}\gamma$ selection efficiency is shown on Fig. 7.12. The effect is small across all $E_{\mathrm{T}}(\gamma)$ ranges, and overall is found to be 0.2% in the electron channel and 0.1% in the muon channel.

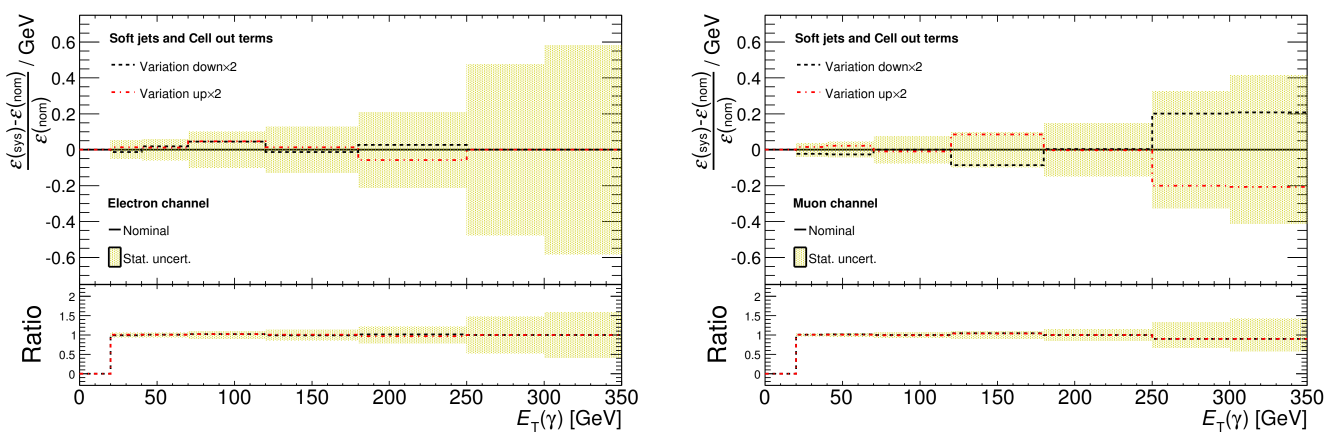

Figure 7.12: Effect of the jet energy scale up and down variations for jets with 7 GeV $< p_{\mathrm{T}}(j) <$ 20 GeV. as a function of the photon energy in the transverse plane. The effect on the electron (muon) channel is shown on the left (right). The last bin contains any overflow.

Pile-up

The systematic uncertainty in the $E_{\mathrm{T}}^{\mathrm{miss}}$ due to multiple interactions per bunch crossing (pile-up) is computed by varying the jet, soft jet and cell out terms by 6.6%. The latter uncertainty has been determined by comparing the sum of the MET soft-terms (by excluding events with jets with $p_T > 20$ GeV) for data and MC in $Z \to \mu\mu$ decays in different η regions. The effect is small and it is summarised in Fig. 7.13 for both electron and muon channels independently.

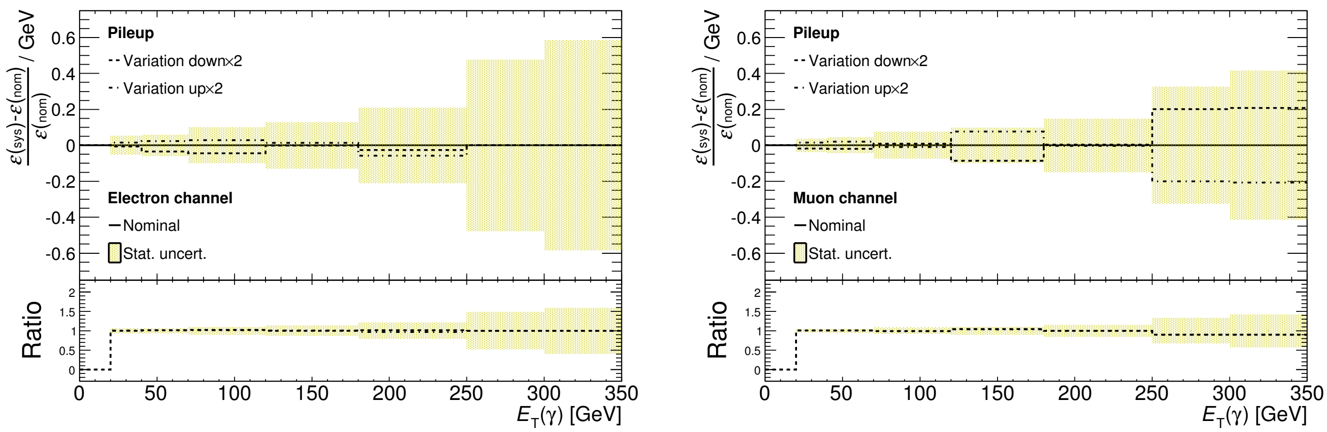

Figure 7.13: Dependence of the $E_{\mathrm{T}}^{\mathrm{miss}}$ calculation to pileup conditions as a function of $E_{\mathrm{T}}(\gamma)$. The plot on the left (right) shows the dependance in the electron (muon) channel. The last bin contains ay overflow.

7.2.5 Heavy flavour jet identification.

The algorithms identifying the jet flavour (b-tagging) associate a jet as being originated from a b-quark with a given efficiency, see Sec. 3.6. The efficiency and the probability of mis-tagging a light jet as a b-jet (mistag rate) are extracted from data with different complementary methods. The MV1 b-tagging mathod is based on a neural network using the output weights of multiple b-tagging algorithms [4]. Data-to-simulations discrepancies are corrected with the applications of scale factors [115, 116]. The uncertainty on the $t\bar{t}\gamma$ selection efficiency is determined from simulations by varying these scale factors within their uncertainties and it is found to be around 5% of the efficiency.

7.3 Templates modelling

Both the prompt photon and the *hadron-fake* templates incorporate within their modelling the dependence upon the kinematic variables of the photon. For the determination of the inclusive cross section the nuisance parameters modelling these kinematic dependencies do not allow for a shape change in the corresponding template. Their net effect is purely to widen the likelihood, thus to increase the uncertainty on the $t\bar{t}\gamma$ cross section. On the contrary, in the differential measurement, the dependence in photon transverse momentum can contribute to bin-by-bin cross section variations. In that case the corresponding nuisance parameters modelling the E_{T}-dependence are allowed to change the template shape and they can vary within the widths of the Gaussian probability density function (pdf) constraining them. In each E_{T}-bin the templates are shaped (*morphed*) with variations (modelling a positive and negative change in $E_{\mathrm{T}}(\gamma)$) with respect to

[4] JetFitter+IP3D, IP3D and SV1, see Sec. 3.6.

the "nominal" template in that bin. Section 5.5.1 and Sec. 5.5.1 explain in detail how the E_{T}-modelling is achieved in the likelihood model for the prompt photon and *hadron-fake* templates respectively.

Dependencies in pseudorapidity were found to be small for both the inclusive and differential measurements, and no *morphing* is included as the result is inclusive in η.

In what follows a description of the uncertainties affecting the signal template (Sec. 7.3.1) and the hadron-fake template (Sec. 7.3.2) is given with greater detail.

7.3.1 Signal template modelling

The nominal prompt photon template ($T_{\mathrm{sig}}^{\mathrm{data},\gamma}$) is derived by extrapolating the electrons (from $Z(\to e^+e^-)$ decays) to photons. Possible biases due to the electron-to-photon extrapolation are investigated by comparing ensembles (of 10^4 pseudo-experiments) using a simulation based template to ensembles using $T_{\mathrm{sig}}^{\mathrm{data},\gamma}$. Furthermore, the effect of the different event topologies in $t\bar{t}\gamma$ decay to that of $Z(\to e^+e^-)$ decays is estimated by comparing ensembles using a template from $Z(\to e^+e^-)+\geq 4$ jets and to that with $T_{\mathrm{sig}}^{\mathrm{data},\gamma}$.

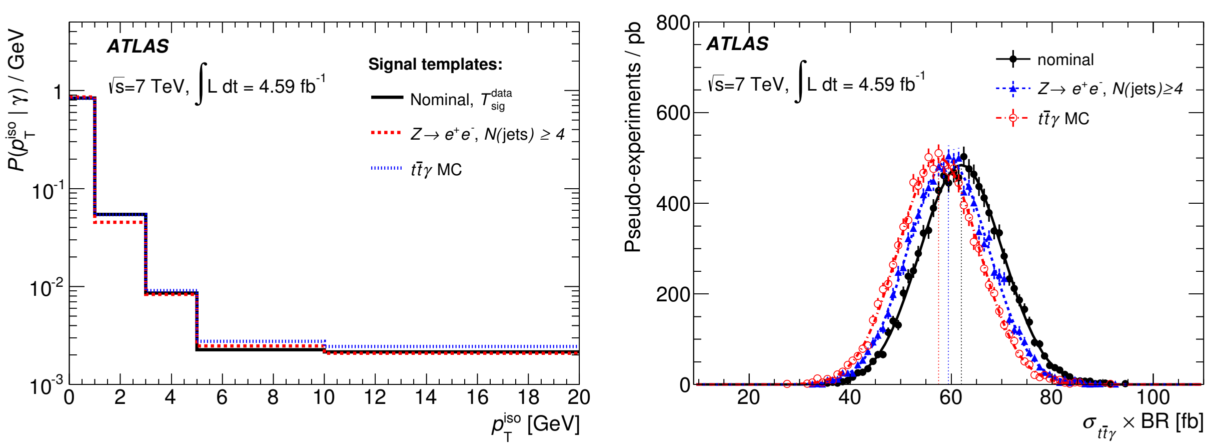

Figure 7.14: Left: comparison of the signal template obtained with the nominal $Z(\to e^+e^-)$ selection (solid line), with the subsequent electron to photon extrapolation and (dashed lines): the template obtained from a $Z(\to e^+e^-)+\geq 4$ jets selection without the electron to photon extrapolation and the template obtained from `WHIZARD` simulations. Right: effect on the cross section of ensemble tests, 10^4 pseudo experiments, using the nominal template $T_{\mathrm{sig}}^{\mathrm{data,e}}$, the template obtained from $Z(\to e^+e^-)+\geq 4$ jets decays without the electron to photon extrapolation and the $t\bar{t}\gamma$ MC template.

Figure 7.14 shows both nominal and uncorrected signal templates as well as the distributions from the pseudo-experiments. Results are summarised in Tab. 7.3 and the subsequent systematic uncertainty is assigned based on the largest deviation among these comparisons.

The effect of additional multjet production into the signal template has been addressed by performing a selection with the requirement of at least three reconstructed jets. The same jet defintion as in the case of the $t\bar{t}\gamma$ full event selection is applied [5]. After the E_{T} and η reweighting

[5]Calibrated jets at the EM+JES scale and reconstructed with the anti-k_{T} algorithm with R=0.4, $p_{\mathrm{T}}(j) > 25$ GeV, $|\eta(j)| < 2.5$ and $|P(\mathrm{JVF})_{\mathrm{PV}}| > 0.75$.

Template type	$\delta\sigma_{t\bar{t}\gamma}/\sigma_{t\bar{t}\gamma}$ [%]
$Z(\rightarrow e^+e^-)+\geq 4$ jets	3.6
Extrapolation to $t\bar{t}\gamma$ simulation	2.2

Table 7.3: Table summarising the effect on the cross section from ensemble tests on different signal templates. Differences with respect the nominal result are shown.

procedure using the corresponding spectrums of the $t\bar{t}\gamma$ simulations the differences in the template shapes between the nominal and modified selections are found to be less than 1%.

7.3.2 Hadron fake template

As explained in section 5.4, the *hadron-fake* templates obtained are reweighted as a function of the E_T and η distributions obtained from data (three η-bins, E_T-spectrum fitted to an exponential function). Systematic templates are obtained by shifting within their error the extrapolation weights in η and E_T. The largest variation with respect to the nominal templates is less than 0.5%. The uncertainty on the cross section from these varied templates is found to be negligible.

The fraction of prompt photons (f) contaminating the *hadron-fake* template is parameterised by the nuisance parameter α_fake, determining the strength of the correction. The uncertainty on α_fake is included in the likelihood function.

7.4 Luminosity

The luminosity was estimated with three Van der Meer scans [159–161] performed in the horizontal and vertical directions [73]. The beam characteristic for each scan are shown in Tab. 7.4. The measurement principle relays on the simultaneous measurements of the collision rates with zero beam crossing angles, the corresponding charge of the colliding proton bunches and the beam profile (horizontally and vertically). The leading systematic uncertainty (10%) on the determination of the luminosity originates from the uncertainty on the measurement of the charge of the colliding proton bunches (number of protons). Smaller contributions comprise uncertainties on the dependence on the number of interactions per bunch crossing (2%), uncertainties on the beam crossing angles (2%), on the transverse emmitance growth (3%), and the uncertainty on the step size during the scan (2%). The total relative uncertainty on the luminosity was estimated to be 1.8% [73].

7.5 Correlations and likelihood modelling

The uncertainties described in this chapter may affect simultaneously the signal or the background for either a single lepton channel or both channels. Therefore, they may be correlated between the different terms in the likelihood. As explained in Sec. 5.5.5, correlations between nuisance parameters are included via the implementation of a transfer function. The uncertainties estimated in this chapter are inputs to the likelihood modelling. The choice of correlations and propagation of the uncertainties is based upon the detector response, as well upon the the derivation method for each component. A summary of the final correlations and propagations of uncertainties included in the likelihood is given in Tab. 7.5, while a detailed explanation is given below.

Parameter	**Scan I**	**Scans II and II**
Scan directions	One horizontal, One vertical	Two horizontal, Two vertical
Scan steps per plane	27	54
Step duration	30 s	
n_{b}	1	
$< N_{\mathrm{b}} >$	0.1×10^{11} protons	0.2×10^{11} protons
$\beta^{\star}$	2 m	
μ	0.03 interactions/ bunch crossing	0.11 interactions/ bunch crossing

Table 7.4: Beam characteristics during the Van Der Meer scans [73].

Signal modelling

Although some of the signal modelling uncertainties may have uncorrelated parameters between the electron and muon channels, the methods with which they are derived remain the same for both channels. Furthermore, electron and muon channel $t\bar{t}\gamma$ simulated cross section are the same. Therefore, these uncertainties are treated as **fully correlated** between the electron and muon channel and affect only the $t\bar{t}\gamma$ cross section.

Signal template modelling

These uncertainties affect only the signal and irreducible backgrounds (e/γ which distribute on $p_{\mathrm{T}}^{\mathrm{iso}}$as the signal) and are kept treated as **fully correlated** across the two channels and across the irreducible backgrounds. In fact, the template derivation is channel independent.

“Background" template modelling (hadrons misidentified as γ)

These uncertainties affect only the hadrons misidentified as photons background and are kept treated as **fully correlated** across channels. The isolation of the hadron-fakes is assumed to to be independent per lepton flavour, and the derived uncertainties are the same for both electron and muon channels.

Lepton modelling

These uncertainties are kept treated as **uncorrelated** across channels. As both channels use statistically independent data samples, there is no cross effect of the electron (muon) properties affecting the muon (electron) channel.

Jet modelling

These uncertainties are treated as **fully correlated** across channels and affect both signal and backgrounds components. In fact, the correction factors applied to simulations for the jet energy scale, jet energy resolution and jet reconstruction efficiency are estimated inclusively for both lepton channels.

Soft terms/cell-out

These uncertainties are treated as **fully correlated** across channels and affect both signal and backgrounds components. As these uncertainties are obtained by variation of correction factors applied to the jet modelling (see above item), they affect both lepton channels simultaneously.

b-tagging

These uncertainties are treated as **fully correlated** across channels and affect both signal and backgrounds components. The input weights to the b-tagging algorithms are, in fact, the same for both channels.

Photon modelling

These uncertainties are treated as **fully correlated** across channels and affect both signal and backgrounds components. Although photon uncertainties are derived using similar methods as for the electrons, their modelling is chosen to be the same for both channels.

Prompt γ backgrounds

The uncertainties upon the estimation of the background to $t\bar{t}$ production with an additional photon feature uncertainties affecting simultaneously both estimates for the electron and muon channels respectively. In all cases the statistical uncertainty is always assumed to be uncorrelated, as the electron and muon channel selections determine statistically independent ensembles. The treatment of each one of those components is summarised below.

- $Z\gamma+$jets, dibosons$+\gamma$, and single top $+\gamma$: The statistical uncertainties are **uncorrelated** . The simulation-based cross section uncertainties, that in principle should be treated as fully correlated, are not included as they are negligible with respect to the statistical uncertainty.
- $W\gamma+$jets: The $W+$jets flavour composition and $W+$jets jets normalisation for different jet multiplicities are kept as **fully correlated**. Statistical uncertainties are kept as **uncorrelated**.
- Mulitjets$+\gamma$: As the uncertainties on the *matrix method* are obtained independently from the electron and muon channels the corresponding nuisance parameters are kept **uncorrelated**.
- $e \to \gamma$ fakes: uncertainties are treated as **fully correlated**, as the $f.r.(e \to \gamma)$ affect simultaneously both lepton channels. The statistical uncertainties are kept **uncorrelated**.

Luminosity

This uncertainty is kept treated as **fully correlated**.

Uncertainty	**Channel correlation**	**Parameters affected**
Signal modelling	full	$\sigma_{t\bar{t}\gamma}$
	Templates modelling	
Prompt photon template	full	$\sigma_{t\bar{t}\gamma}$ and all e/γ bck.
hadron-fake template	full	*hadron-fakes* bck.
	Detector modelling	
Lepton	none	all
Jet	full	all
Soft term/cell-out	full	all
b-tagging	full	all
Photons	full	all
	e/γ backgrounds	
Statistical $Z\gamma$ + jets, dibosons+γ and single top+γ	none	respective bck. parameters
Statistical $W\gamma +$ jets	none	respective bck. parameters
Systematic $W\gamma +$ jets	full	respective bck. parameters
Statistical $e \to$ misidentification	none	respective bck. parameters
Systematic $e \to$ misidentification	full	respective bck. parameters
Luminosity	full	$\sigma_{t\bar{t}\gamma}$, $Z\gamma +$ jets, dibosons+γ and single top+γ

Table 7.5: Summary of correlations between nuisance parameters.

CHAPTER 8

Results

The measurement of the $t\bar{t}\gamma$ cross section is performed in a fiducial phase-space within the detector acceptance defined in terms of the kinematic properties of jets, lepton and photons. The likelihood model, incorporating the background expectation and the systematic uncertainties on the measurement, is used to extract the cross section and its uncertainty. The measurement in the $E_{\mathrm{T}}(\gamma) > 20$ GeV bin is discussed from Sec. 8.1 to Sec. 8.3 and the significance of the observation of the $t\bar{t}\gamma$ process is quantified. Section 8.4 presents the $t\bar{t}\gamma$ differential cross section with respect to the photon transverse energy. Finally in Sec. 8.5 an interpretation, in terms of constraints on the top-photon coupling values is attempted.

8.1 Fiducial cross section

In this section the result of the $t\bar{t}\gamma$ fiducial cross section measurement is reviewed. The likelihood is minimised simultaneously for both the electron and the muon channels and the fiducial cross section ($\sigma^{\mathrm{fid}}_{t\bar{t}\gamma}$) is extracted.

Totals of 140 and 222 $t\bar{t}\gamma$ candidate data events are observed in the electron and muon channels respectively. The numbers of background events extracted from the combined likelihood fit are 79 ± 26 for the electron channel and 120 ± 39 for the muon channel. Using the values of the efficiency (ε) for each lepton channel ($\ell = e, \mu$) and the integrated luminosity ($\mathcal{L}$), the combined cross section is projected in terms of signal events ($N_s^{\ell} = \sigma^{\mathrm{fid}}_{t\bar{t}\gamma} \cdot \varepsilon^{\ell} \cdot \mathcal{L}$). They are determined to be $N_s^e = 52 \pm 14$ and $N_s^{\mu} = 100 \pm 28$, the numbers include statistical and systematic uncertainties [132]. Table 8.1 compares, for each lepton flavour, the expectation of backgrounds and the number of signal events. It is found that the sums of the extracted contributions is in good agreement with the number of candidate events.

The $p_{\mathrm{T}}^{\mathrm{iso}}$ distributions, as extracted from the likelihood fit, are shown in Fig. 8.1. It can be seen that, within the statistical fluctuations, the resulting distributions are in good agreement with the data candidate events.

Contribution	Electron channel	Muon channel	Total
Signal	52 ± 14	100 ± 28	152 ± 31
Hadron-fakes	38 ± 26	55 ± 38	93 ± 46
e/γ objects	41 ± 5	65 ± 9	106 ± 10
Total background	79 ± 26	120 ± 39	199 ± 47
Total signal plus background	131 ± 30	220 ± 48	351 ± 59
Data candidates	140	222	362

Table 8.1: Number of $t\bar{t}\gamma$ signal and background events extracted from the likelihood fit, which is performed for the electron and muon channels simultaneously. The uncertainties are statistical and systematic. The total number of $t\bar{t}\gamma$ candidate events observed in data is also shown [132].

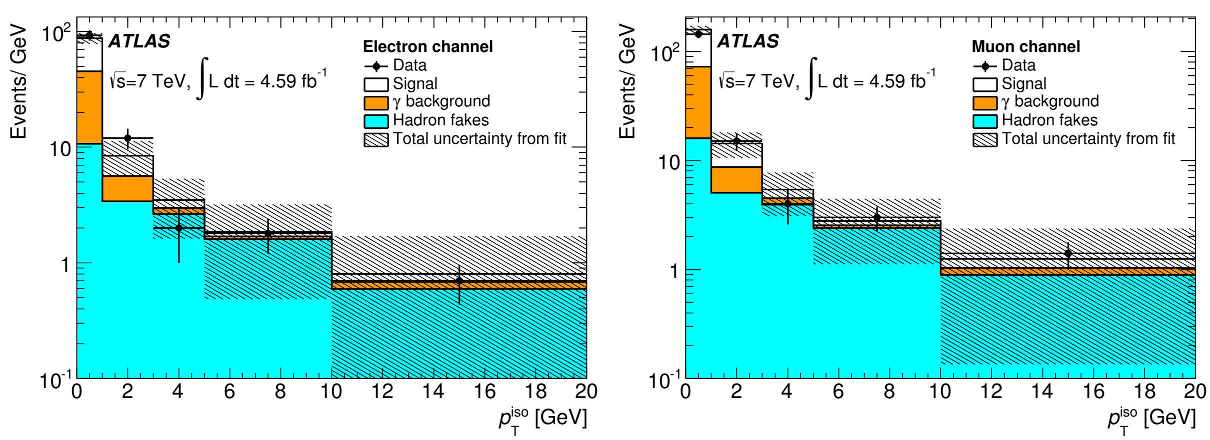

Figure 8.1: Results of the combined likelihood fit using the track-isolation ($p_{\mathrm{T}}^{\mathrm{iso}}$) distributions as the discriminating variable for the electron (left) and muon (right) channels. The contribution from $t\bar{t}\gamma$ events is labeled as "Signal", prompt-photon background is labeled "γ backgrounds", the contribution from hadrons misidentified as photons (as estimated by the template fit) is labeled as "Hadron fakes" [132]

.

The $t\bar{t}\gamma$ cross section together with its total uncertainty obtained from the profile likelihood ratio fit (see Fig. 8.2), is found to be 63^{+19}_{-16} fb. The total systematic component of the uncertainty is extracted from

$$\sqrt{(\sigma_{\mathrm{syst}\oplus\mathrm{stat}})^2 - \sigma^2_{\mathrm{stat}} - \sigma^2_{\mathcal{L}}} =^{+17}_{-13} \text{ fb} \tag{8.1}$$

where $\sigma_{\mathcal{L}}$ is the luminosity uncertainty; σ_{stat} is the pure statistical uncertainty, evaluated from the profile likelihood without including nuisance parameters; $\sigma_{\mathrm{syst}\oplus\mathrm{stat}}$ is the total uncertainty extracted from the 68% CL of the profile likelihood fit (including nuisance parameters).

The statistical uncertainty has been cross checked with that obtained from ensemble tests from the unconstrained likelihood. The resulting width of the distribution of the cross section estimates,

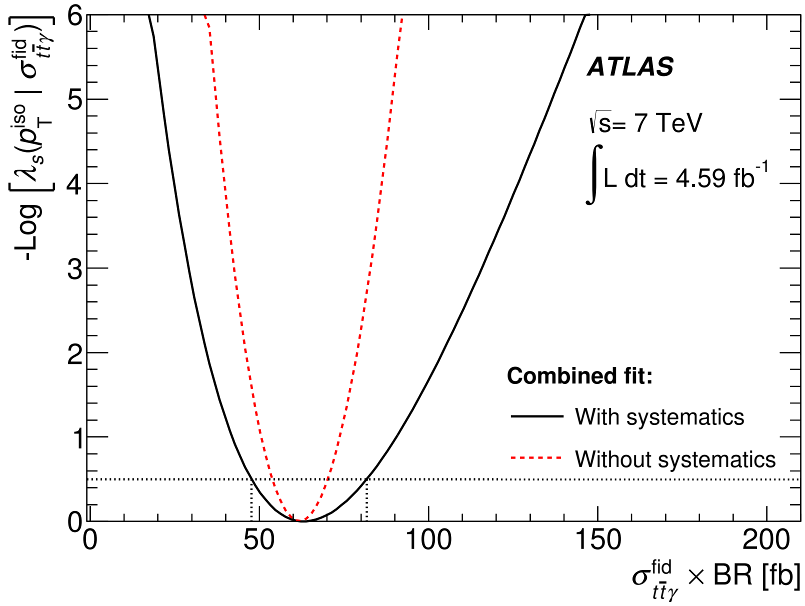

Figure 8.2: Negative logarithm of the profile likelihood as a function of the $t\bar{t}\gamma$ fiducial cross section $\sigma_{t\bar{t}\gamma} \times$ BR with (solid line) and without (dashed line) free nuisance parameters associated with the systematic uncertainties. The horizontal dotted line corresponds to a value of $-\log\left[\lambda_s(p_{\mathrm{T}}^{\mathrm{iso}}\,|\,\sigma_{t\bar{t}\gamma})\right] = 0.5$. Intersections of this line with the solid (dashed) curve give the $\pm 1\sigma$ total (statistical only) uncertainty interval to the measured fiducial $t\bar{t}\gamma$ cross section.

see Fig. 8.3, is in excellent agreement with that obtained from the fit on data.

The $t\bar{t}\gamma$ cross section times the Branching Ratio (BR) per lepton flavour, as defined in Chap. 4, is determined to be

$$\sigma_{t\bar{t}\gamma} \times \mathrm{BR} = 63\,\pm 8(\mathrm{stat.})\,{}^{+17}_{-13}\,(\mathrm{syst.}) \pm 1\,(\mathrm{lumi.})\,\mathrm{fb} \tag{8.2}$$

where BR is the $t\bar{t}\gamma$ branching ratio in the single-electron or single-muon final state. A good agreement is found with the predicted cross sections [54, 56] of 48 ± 10 fb and 47 ± 10 fb obtained from the `WHIZARD` and `MadGraph` Monte Carlo generators respectively after normalisation by the corresponding NLO/LO k-factors.

8.1.1 Systematic uncertainties

The total effect of each systematic uncertainty on the cross section is evaluated using ensemble tests with the method described in App. D.1.3. For each systematic uncertainty i, pseudo-data are generated from the full likelihood while keeping all parameters fixed to their maximum likelihood estimates values except for the nuisance parameter associated to the systematic uncertainty source of interest. For each ensemble, a template fit is performed allowing all parameters of the likelihood (nuisance parameters, signal cross section) to vary. The variance of the obtained distribution of cross sections gives the uncertainty due to the i-th systematic uncertainty. This method has been validated against several others, which are thoroughly described in App. D.1. In the following, the effect on the cross section of each systematic component is reviewed in more details, while a summary of the breakdown is shown in Tab. 8.2.

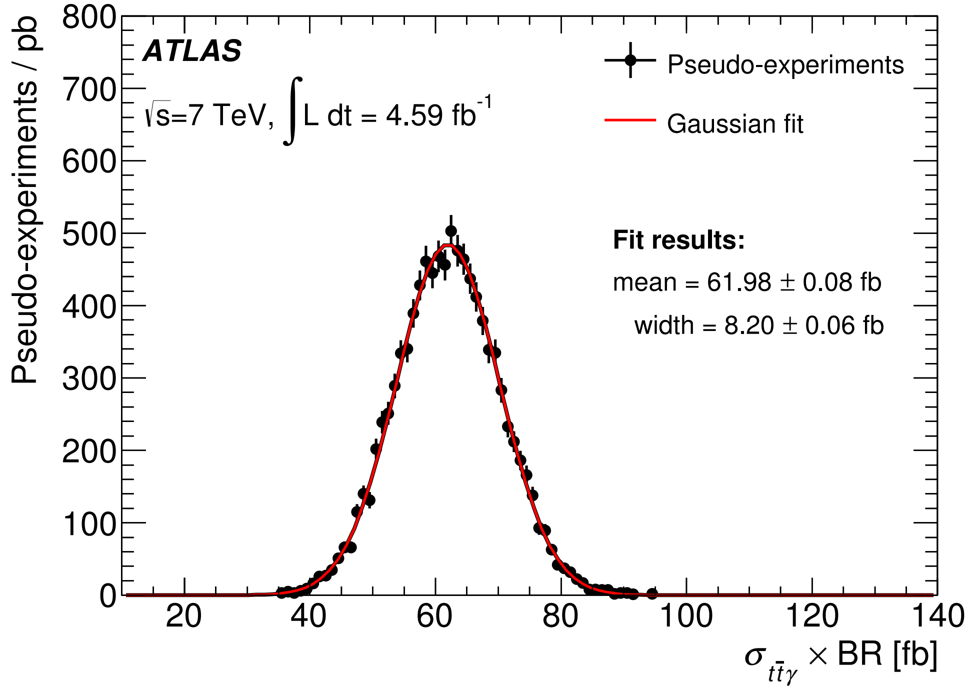

Figure 8.3: Verification of the estimation of the statistical uncertainty on the cross-section measurement. Cross-section estimates are obtained from a set of 10^4 pseudo-experiments performed without the inclusion of systematic sources. Each pseudo-experiment is generated with the same amount of data as the dataset analyzed. The statistical uncertainty on the cross-section measurement is extracted from the width of a Gaussian fit (solid line).

Template modelling

The contribution to the systematic uncertainty on $\sigma_{t\bar{t}\gamma}$ due to the template shape modelling amounts to 7.6% in total. Of this, the background template shape modelling uncertainty amounts to 3.7% of the cross section, and the prompt-photon template uncertainty amounts to 6.6%.

Signal modelling

The uncertainty on the $t\bar{t}\gamma$ cross section due to the modelling of the signal is estimated to be 8.4%. It is seen that the differences between `MadGraph` and `WHIZARD` amount to 1.7% of the total uncertainty, while the component of uncertainty due to the QED radiation modelling amounts to 1.7%. The effect of varied renormalisation and factorisation scales leads to an uncertainty of 1.1% on the cross section. The effect on the choice of the Parton Shower (PS) model impacts the cross section with a 7.3% uncertainty. Smaller contributions due to the choice of colour reconnection model (0.2%) and underlying event (0.9%) settings are also included into the total uncertainty.

Systematic source	**Uncertainty, %**
Template modelling	
Bck. template modelling: γ leakage	3.7
Signal template modelling	6.6
Signal modelling	
MC generator	1.7
PDF	1.1
Parton shower	7.3
QED FSR	3.4
Colour reconnection	0.2
Underlying event	0.9
Ren/Fac. scale	1.1
Photon modelling	
Photon identification efficiency	7.3
Photon scale	2.7
Photon resolution	4.0
Electron modelling	
Trigger efficiency	0.3
Reconstruction efficiency	0.5
Identification efficiency	1.2
Energy scale	0.3
Energy resolution	0.1
Muon modelling	
Trigger efficiency	1.7
Reconstruction efficiency	0.4
Identification efficiency	1.0
Momentum scale	0.3
Momentum resolution	0.7
Jet modelling	
Jet reconstruction efficiency	0.1
Jet energy scale	15.0
Jet energy resolution	6.5
Jet vertex fraction	2.6
***b*-tagging**	
b-tag efficiency	8.1
Mistag rate	1.1
$E_{\mathrm{T}}^{\mathrm{miss}}$**modelling**	
Soft-jets and Cell-Out terms	0.3
Pile-up	0.9
Luminosity	1.8
Background contributions	
e-fakes	5.0
QCD multijets+γ	1.5
W+jets+γ	5.4
Z+jets+γ	1.3
Dibosons+γ	0.4
Single top+γ	0.4

Table 8.2: Summary of the different systematic uncertainty contributions to the $\sigma_{t\bar{t}\gamma}$ cross section as obtained from ensemble tests.

Detector modelling

The systematic uncertainty on the cross section due to photon modelling is 8.8%. It is estimated from the photon identification (7.3%) [111], the electromagnetic energy scale (2.7%) and the resolution (4.0%) systematic uncertainties [156].

The systematic uncertainty on the cross section due to lepton modelling is 2.5%. It is estimated separately for the electron and muon channels from the lepton trigger (0.3% and 1.7%), reconstruction (0.5% and 0.4%) and identification (1.2% and 1.0%) efficiency uncertainties, as well as from those on the energy scale (0.3% and 0.3%) and resolution (0.1% and 0.7%).

The systematic uncertainty on the cross section due to jet modelling is 16.6%. It is estimated taking into account the following contributions. The largest effect comes from the energy scale (15.0%) uncertainty. The jet energy resolution uncertainty is estimated to 6.5% of the cross section. The uncertainty on jet reconstruction efficiency (1.0%) and the jet vertex fraction uncertainty (2.6%) are also included.

The systematic uncertainty on the cross section due to b-tagging modelling is 8.2%. It is dominated by the contribution due to the efficiency (8.1%) with a small contribution due to the mistag probability (1.1%).

Systematic uncertainties on the energy scale and resolution of leptons, jets and photons are propagated to $E_{\mathrm{T}}^{\mathrm{miss}}$. Additional contributions from low-p_{T} jets (Soft terms) and from energy in calorimeter cells that are not included (Cell out) in the reconstructed objects (0.3%), as well as any dependence on pile-up (0.9%) are estimated to impact the cross section to 0.9% in total.

The effect of the luminosity uncertainty on the cross section amounts to 1.8%.

Background contributions

The total systematic uncertainty originating from processes that constitute a background to $t\bar{t}$ production with an additional final state photon as well as electrons misidentified as photons is estimated to be 7.7%. This uncertainty includes the following: electrons misidentified as photons (5.0%), $W\gamma+$ jets (5.4%), as well as multijet+γ (1.5%), $Z\gamma+$ jets (1.3%), diboson (0.4%) and single top+γ (0.4%) processes.

For background *estimates* obtained using simulation, uncertainties on the cross section predictions are taken into account. For $Z\gamma$+jets, single-top and diboson contributions the cross section systematic uncertainty is negligible with respect to the statistical uncertainty.

8.1.2 Channel independent cross sections

The cross section measurements are performed separately in the electron and muon channels. The results are

$$\sigma_{t\bar{t}\gamma} \times \mathrm{BR} = 76^{+16}_{-15}(\mathrm{stat.})\,^{+22}_{-17}\,(\mathrm{syst.}) \pm 1(\mathrm{lumi.})\,\mathrm{fb} \tag{8.3}$$

for the electron channel and

$$\sigma_{t\bar{t}\gamma} \times \mathrm{BR} = 55^{+10}_{-9}(\mathrm{stat.})\,^{+14}_{-11}\,(\mathrm{syst.}) \pm 1(\mathrm{lumi.})\,\mathrm{fb} \tag{8.4}$$

for the muon channel.

Figure 8.4 compares the channel dependent results with that obtained from the combined fit and with the prediction from theory. It can bee seen that although the cross section for the electron channel is slightly larger than the theoretical prediction, overall all results agree within one gaussian standard deviation.

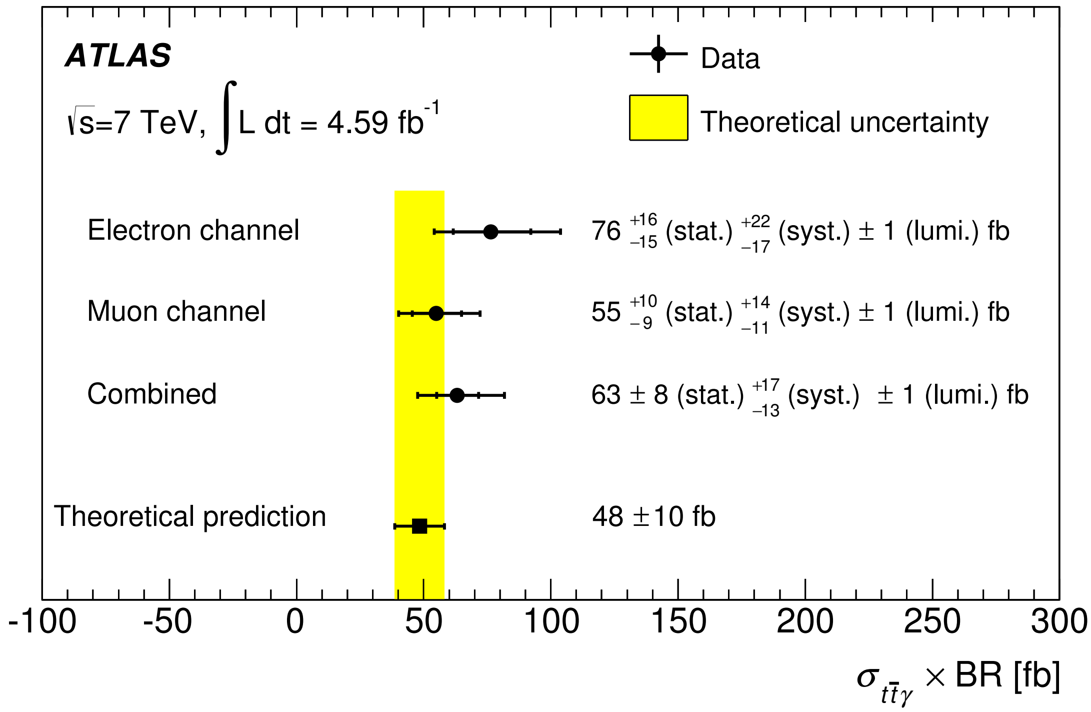

Figure 8.4: Fit results are shown for the combined fit, as well as for the electron and muon channels separately. The filled area represents the uncertainty on the theoretical prediction.

The number of events extracted from the channel independent estimations are also compared with those obtained from the combined fit. Table 8.3 shows that the sums for each signal and background component from the two channels is close to the signal and background estimations from the combined fit.

	Single channel fit			**Combined fit**
	Electron channel	**Muon channel**	**Total**	
Signal events	62 ± 20	87 ± 25	149 ± 32	152 ± 31
Had. Fakes	34 ± 24	58 ± 40	92 ± 53	93 ± 46
Prompt-photons	41 ± 6	66 ± 8	107 ± 10	106 ± 10
Total Background	75 ± 25	125 ± 40	199 ± 48	199 ± 47

Table 8.3: Comparison of the number of signal and background events resulting from fits performed in each lepton channel separately and from the combined fit.

8.1.3 Significance

Under regularity conditions the distribution of $-2\ln[\lambda(\sigma_{t\bar{t}\gamma})]$ relates asymptotically to a distribution of $\chi^2(1)$ (Wilk's theorem [130]). In the asymptotic scenario, the χ^2 can be used for testing two different hypothesis of $\sigma_{t\bar{t}\gamma}$. The validity of the likelihood used in this analysis (Eq. 5.32) is tested under such hypothesis by means of ensemble tests. A set of 1000 pseudo-experiments are generated by fixing the value of $\sigma_{t\bar{t}\gamma}$ to its upper limit and randomising $p_{\mathrm{T}}^{\mathrm{iso}}$ and constraints observables. The resulting distribution is compared to a χ^2 as shown in Fig. 8.5. The pull between the two overlaid distributions doesn't show any significant discrepancies.

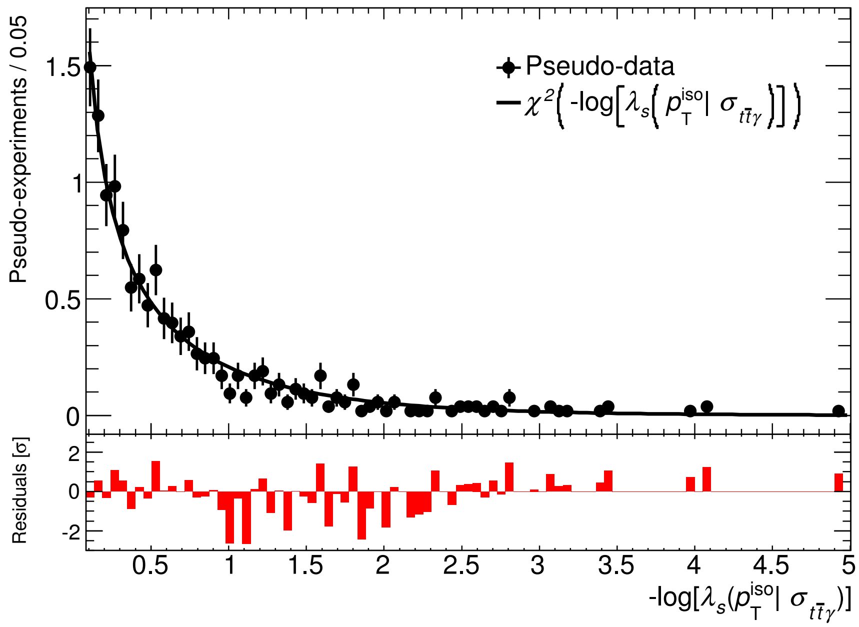

Figure 8.5: Comparison of a $\chi^2(1)$ distribution with the distribution of $-2\ln[\lambda(\sigma_{t\bar{t}\gamma})]$ under the conditional hypothesis of $\sigma_{t\bar{t}\gamma} = \hat{\sigma}_{t\bar{t}\gamma} + \delta\hat{\sigma}_{t\bar{t}\gamma}$ from a set of 1000 pseudo-experiments. No significant discrepancies are visible.

A quantification of the probability of an observation of the null hypothesis ($\sigma_{t\bar{t}\gamma} = 0$) over the alternate ($\sigma_{t\bar{t}\gamma} \neq 0$) is made by calculating the integral of a χ^2 from the observed $-2\ln[\lambda(\sigma_{t\bar{t}\gamma})]$ value to infinity. Table 8.4 shows the full set of p-values obtained with and without the inclusion of the systematic terms in the likelihood.

	Observed $-2\ln[\lambda(\sigma_{t\bar{t}\gamma})]$	p_0	**Significance**
No systematics	36.8	$p_0^{\mathrm{obs}} = 4.73 \times 10^{-18}$	8.6 σ
All systematics	14.1	$p_0^{\mathrm{obs}} = 5.73 \times 10^{-8}$	5.3 σ

Table 8.4: Observed likelihood ratios, p-values and Gaussian deviations of the null and alternate hypothesis, with and without systematics.

The test statistic for the no-signal hypothesis is extrapolated to the likelihood ratio value observed in data (14.1) to determine the p-value of $p_0^{\mathrm{obs}} = 5.73 \times 10^{-8}$. The process $t\bar{t}\gamma$ in the lepton-plus-jets final state is thus observed with a significance of 5.3 σ away from the no-signal hypothesis.

8.2 Constraint from parameters

The constraint of nuisances to the value (and the uncertainty) of the fit can be assessed by means of the pull:

$$\text{Pull}(\theta) = \frac{\theta - \hat{\theta}}{\sigma_\theta} \tag{8.5}$$

where θ is the fitted nuisance, $\hat{\theta}$ is its nominal value and σ_θ is the input error of the constraint. An over-constrain from the data to the estimation of θ occurs when its normalised error is < 1. The totally unconstrained limit is obtained when all pulls are centred around 0 and have widths equal to 1. Although a maximal constraint leads to significantly reduced errors, the parametrisation of the nuisances and their corresponding constraining probability density function (pdf) were chosen to minimise such effect for the reasons explained in Sec. 5.5. The resulting pulls from nuisance parameters are shown in Fig. 8.6. A negligible constraint on the error of each nuisance with respect to its input is observed.

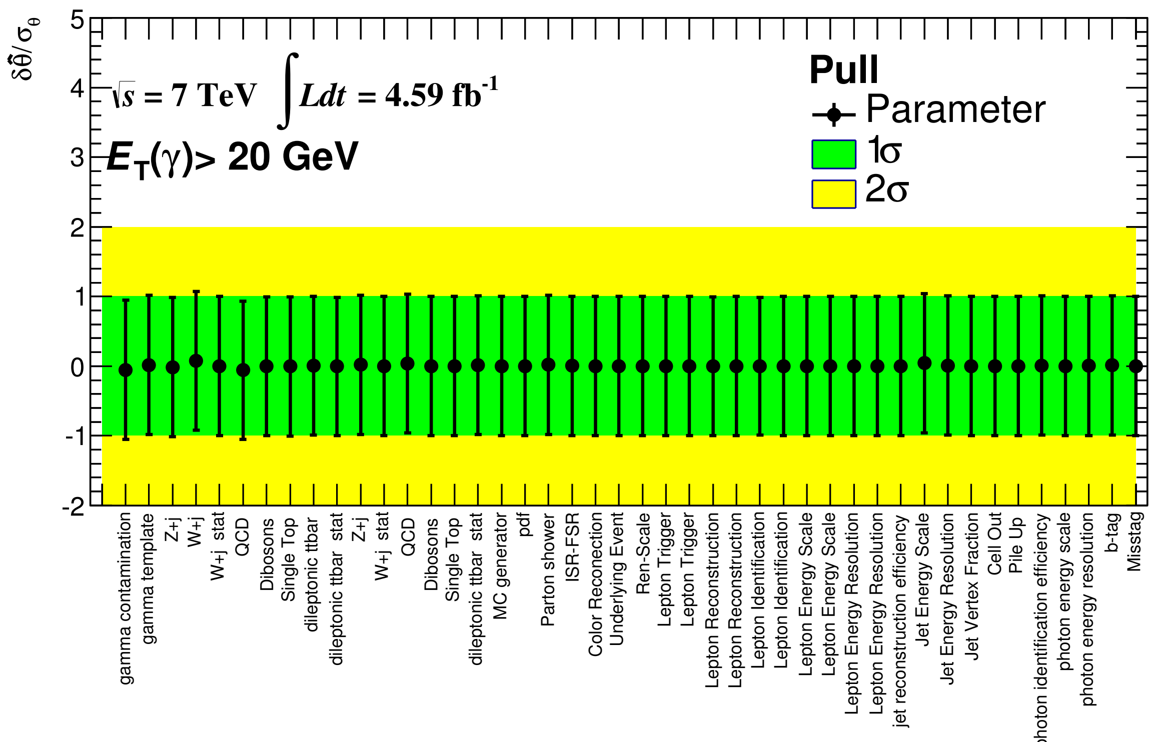

Figure 8.6: Pull of nuisances representing systematic uncertainties after incorporation of correlations across channels for detector systematics as described in Sec. 5.5.5. All points are consistent with mean 0 and error of one gaussian standard deviation.

8.3 Robustness of the result

A wide range of tests has been performed in order to consolidate the robustness of the extracted cross section result. A summary is presented here, whilst the detailed description can be found in App. D.

i) **Stability with respect to background fluctuations**

The stability of the result against background fluctuations has been tested by performing subsequent fits after removing a given background component. The observed variations in the cross section are consistent with the expectation. The removal of small backgrounds (dibosons+γ and single top+γ) results into smaller variations of the cross section compared to the removal of more important background contributions ($e \to \gamma$ misidentification and $W\gamma$ + jets). Furthermore, the difference in number of signal events of the i-th fit to the nominal is in good agreement with the contribution of the i-th omitted background. A detailed description of the test is given in App. D.2.1.

ii) **Linear response from the fit as a function of the efficiency**

While the likelihood fit extracts the cross section, the number of signal events is calculated *post*-fit. Cross section variations are expected to be linear with respect to efficiency changes. Ensemble tests show that an excellent linearity is achieved. See App. D.2.2 for details.

iii) **Total cross section uncertainty variation with respect to the source**

Because of its impact on the significance of the measurement, it is of interest to study how the cross section uncertainty varies with respect to different types of errors on the nuisance parameters. Subsequent fits, varying the uncertainty on only one nuisance parameter at each stage, are performed. The results show, as expected, an approximatively quadratic increase of the total cross section uncertainty for all type of variations, see Fig. 8.7 left. However, the rate of increase is specific to each type (of uncertainty). The corresponding decrease in significance is shown in Fig. 8.7 right. Details are given in App. D.2.3.

iv) **Anomalous constraints from the simultaneous fit**

While performing a simultaneous fit the correlations of nuisance parameters should not absorb differences between the two channels that can appear in the data distribution of $p_{\mathrm{T}}^{\mathrm{iso}}$. Absorptions in cross section variations can by symptoms of an anomalous modelling of the response function of Eq. 5.28. Results of an anomalous modelling and results from different cross sections for each channel (for example, because of the small size of data) can be difficult to disentangle. An anomalous behaviour of likelihood modelling has been excluded performing fits in the combination of the two channels, while leaving the electron channel cross section and muon channel cross section free to float independently to each other. The results, see App. D.2.4, show the absence of absorptions in nuisance parameters of statistical fluctuations.

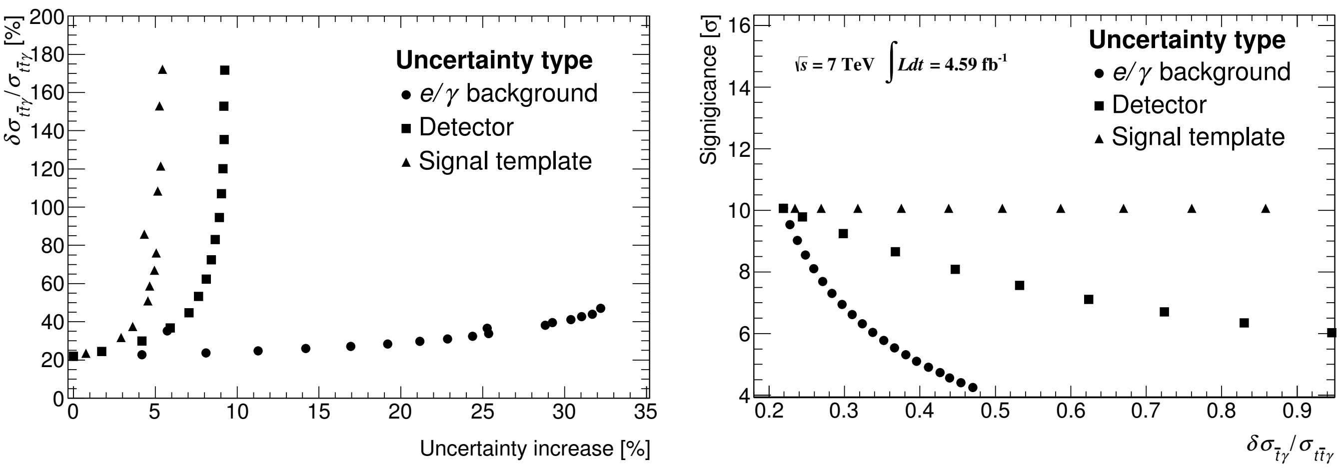

Figure 8.7: The relative cross section uncertainty as a function of the input uncertainty is shown on the left. The signal significance as a function of the increase of the cross section uncertainty is shown on the right. Round markers correspond to the prompt-photon background uncertainty. Square markers correspond the detector-type uncertainty (for example jet energy scale or the photon identification efficiency). Triangular markers correspond to the uncertainty on the signal template (this is the prompt-photon template while being set to affect only the signal yield).

v) **Closure**

Intrinsic biases of the likelihood modelling are excluded by means of a closure test, see Sec. D.2.5. The test is performed on ensembles of pseudo data by successive randomisation and fit of all parameters of the likelihood. The distribution of the *estimates* of the cross section is consistent with a Gaussian pdf of mean 0 and variance 1.

vi) ***Estimator* choice**

The choice of the estimator (`MINOS` minimisation of the profile likelihood ratio) has been tested by comparing the result to that of a *Bayesian* marginalisation using the Markov Chain Monte Carlo technique [162]. Appendix D.4 details the method and shows the results of the comparison. It is found that both estimations are in excellent agreement.

vii) **Cut and count technique**

The result is compared to that of a simplified model that does not use any template information. The method imposes a cut on the $p_{\mathrm{T}}^{\mathrm{iso}}$ distribution and distinguishes two regions in data: one below the cut (dominated by prompt-photons) and an other above the cut (dominated by *hadron-fakes*). The amount of *hadron-fakes* leaking into the prompt-photon region is extrapolated from the region above the cut. Although this method comes with increased uncertainty, the result of the cross section is consistent with that obtained from the likelihood fit. Appendix D.5 compares extensively both methods.

8.4 Differential measurement

The e/γ backgrounds and the systematic uncertainties have been also determined as a function of the photon transverse energy. Therefore, an extraction of the $\sigma_{t\bar{t}\gamma}$ differentially is also possible.

Nine exclusive $E_{\mathrm{T}}(\gamma)$ bins have been selected. Because the $E_{\mathrm{T}}(\gamma)$ spectrum decreases exponentially the bins are increasingly coarser. The measurement stops for photons with $E_{\mathrm{T}}(\gamma) > 300$ GeV for which un upper limit at 95% Confidence Level (CL) on the $t\bar{t}\gamma$ final state is derived.

The same procedure, used for deriving the inclusive cross section, has been applied in each $E_{\mathrm{T}}(\gamma)$ bin, extracting the $\sigma_{t\bar{t}\gamma}$ by minimising the likelihood ratio of Eq. 5.34.

The number of signal and background events extracted form the likelihood fit in each $E_{\mathrm{T}}(\gamma)$ bin are shown in Fig. 8.8. It can be seen that the total number of events (signal plus backgrounds) is in good agreement with the number of candidate events. Because of the small size of data some fluctuations are present, but overall the fluctuations are within one gaussian standard deviation.

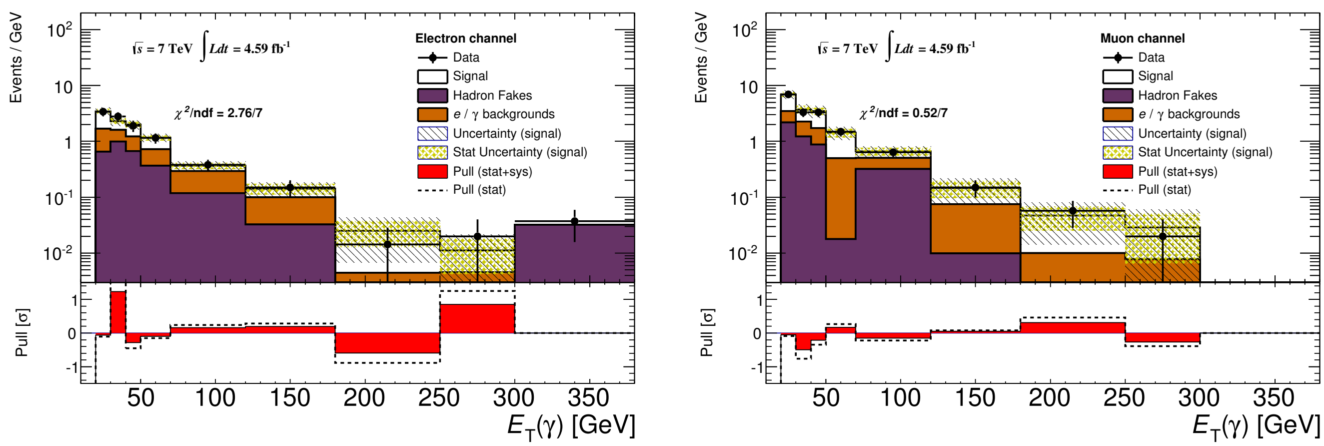

Figure 8.8: Number of signal and background events as extracted from the likelihood fit and as a function of the photon transverse energy. Results are projected to the electron (left) and muon (right) channels respectively. The number of candidate events is shown with filled markers. The white histogram indicates the number of signal events. The filled histograms show the number of hadron fakes and the number of e/γ background events respectively. The uncertainties on the number of signal events are shown with two bands. The dashed band corresponds to the stat$\oplus$uncertainty, while the hatched band corresponds to the statistical uncertainty. The bottom plot in each figure shows the normalised residuals (Pull) of the total number of events extracted from the fit to the number of data candidates. The filled area corresponds to the inclusion of systematic uncertainties in the calculation of the residuals.

The extracted $t\bar{t}\gamma$ cross sections are summarised in Tab. 8.5. The systematic component of the uncertainty is comparable to the statistical component for the first $E_{\mathrm{T}}(\gamma)$ bins, however, the measurement is rapidly dominated by the statistical uncertainty.

The addition of the $\sigma_{t\bar{t}\gamma}$ measurements in all $E_{\mathrm{T}}(\gamma)$ bins gives a value of 66 fb which is close to that obtained in Eq. 8.2.

$E_{\mathrm{T}}(\gamma)$ **range [GeV]**	$\sigma_{t\bar{t}\gamma}$ **[fb]**
$]20, 30[$	$30.56\ ^{+6.36}_{-6.18}(\mathrm{stat})\ ^{+5.94}_{-4.78}(\mathrm{syst})$
$[30, 40[$	$10.10\ ^{+4.01}_{-3.68}(\mathrm{stat})\ ^{+2.50}_{-1.95}(\mathrm{syst})$
$[40, 50[$	$9.35\ ^{+2.90}_{-2.66}(\mathrm{stat})\ ^{+2.14}_{-1.78}(\mathrm{syst})$
$[50, 70[$	$9.35\ ^{+2.60}_{-2.36}(\mathrm{stat})\ ^{+1.82}_{-1.26}(\mathrm{syst})$
$[70, 120[$	$3.63\ ^{+2.46}_{-2.27}(\mathrm{stat})\ ^{+1.38}_{-1.06}(\mathrm{syst})$
$[120, 180[$	$1.91\ ^{+1.42}_{-1.21}(\mathrm{stat})\ ^{+0.58}_{-0.38}(\mathrm{syst})$
$[180, 250[$	$0.97\ ^{+0.63}_{-0.53}(\mathrm{stat})\ ^{+0.32}_{-0.23}(\mathrm{syst})$
$[250, 300[$	$0.40\ ^{+0.52}_{-0.33}(\mathrm{stat})\ ^{+0.21}_{-0.15}(\mathrm{syst})$
$[300, \infty)$	< 1.45 fb at 95% CL
Total	$66.3\ ^{+9.1}_{-8.5}(\mathrm{stat})$

Table 8.5: Summary of $\sigma_{t\bar{t}\gamma}$ as a function of $E_{\mathrm{T}}(\gamma)$. The entry labelled by "Total" corresponds to the sum of all components, statistical have ben added quadratically.

8.4.1 Uncertainties

The determination of the relative strength of each component of the systematic uncertainty to the cross section was evaluated using the same method as for the inclusive measurement. The full breakdown is presented in Tab. 8.6, while a a condensed version is shown in Fig. 8.9.

The low-$E_{\mathrm{T}}(\gamma)$ range ($20 \rightarrow 50$ GeV) is dominated by the uncertainty on parton shower modelling (0.65 %/GeV), on the signal template modelling (0.60%/GeV), on the photon identification (0.41%/GeV) and on the modelling of the QED radiation (0.40%/GeV). The same uncertainties remain important with increasing $E_{\mathrm{T}}(\gamma)$, however the uncertainty on $e \rightarrow \gamma$ increases its contribution to the total.

Component	$E_\mathrm{T}(\gamma)$ **range [GeV]**							
	$]20,30[$	$[30,40[$	$[40,50[$	$[50,70[$	$[70,120[$	$[120,180[$	$[180,250[$	$[250,300[$
	Signal modelling [%/GeV]							
MC generator	0.13	0.15	0.13	0.07	0.05	0.02	0.04	0.05
PDF	0.07	0.09	0.08	0.05	0.04	< 0.01	< 0.01	< 0.01
Parton shower	0.65	0.83	0.67	0.38	0.23	0.18	0.10	0.49
QED radiation	0.38	0.50	0.42	0.24	0.14	0.11	0.13	0.45
Colour reconnection	0.03	0.10	0.06	0.04	0.13	< 0.01	< 0.01	< 0.01
Underlying event	0.04	0.11	0.09	0.05	0.13	0.22	< 0.01	< 0.01
Ren./Fac. scale	0.05	0.08	0.07	0.05	< 0.01	< 0.01	< 0.01	< 0.01
	Lepton modelling [%/GeV]							
Trigger efficiency	0.12	0.17	0.15	0.09	0.05	0.05	0.03	0.09
Reconstruction efficiency	0.06	0.08	0.10	0.06	0.01	0.01	< 0.01	< 0.01
Identification efficiency	0.15	0.16	0.11	0.16	0.06	0.13	0.10	0.03
Energy scale	0.08	0.10	0.21	0.05	0.13	< 0.01	< 0.01	< 0.01
Energy resolution	0.08	0.12	0.17	0.04	0.02	0.22	< 0.01	< 0.01
	Jet modelling [%/GeV]							
Reconstruction efficiency	0.13	0.10	0.23	0.16	0.05	0.12	0.10	< 0.01
Energy Scale	0.17	0.09	0.16	0.19	0.07	0.14	0.14	0.51
Energy resolution	0.03	0.10	0.08	0.04	0.07	< 0.01	0.10	0.34
Vertex fraction	0.14	0.19	0.17	0.10	0.06	0.06	0.08	0.26
	$E_\mathrm{T}^\mathrm{miss}$ **modelling [%/GeV]**							
Cell out and soft terms	0.08	0.16	0.15	0.19	0.05	0.12	0.10	< 0.01
Pile-up	0.03	0.11	0.09	0.04	0.13	< 0.01	< 0.01	< 0.01
	Photon modelling [%/GeV]							
Identification efficiency	0.41	0.53	0.44	0.25	0.15	0.12	0.14	0.45
Energy scale	0.12	0.14	0.24	0.20	0.04	0.10	0.14	0.12
Energy resolution	0.12	0.13	0.25	0.12	0.05	0.10	0.08	0.34
	b**-tagging [%/GeV]**							
b-tag. efficiency	0.48	0.61	0.52	0.30	0.17	0.14	0.14	0.47
Mistag rate	0.04	0.11	0.09	0.05	0.13	0.22	< 0.01	< 0.01
	e/γ **backgrounds [%/GeV]**							
$Z\gamma+$jets	0.13	0.14	0.12	0.11	0.06	< 0.01	< 0.01	< 0.01
$W\gamma+$jets	0.04	0.10	0.07	0.07	0.05	0.10	< 0.01	< 0.01
Multijets+γ	0.20	0.11	0.06	0.09	0.17	0.13	0.10	0.44
Dibosons+γ	0.04	0.08	0.07	0.07	0.01	< 0.01	< 0.01	< 0.01
Single top+γ	0.25	0.48	0.34	0.15	0.15	0.13	< 0.01	0.51
$e \to \gamma$ missidentification	0.21	0.32	0.24	0.09	0.08	0.06	0.13	0.49
	Templates modelling [%/GeV]							
Prompt photons	0.60	0.61	0.55	0.32	0.12	0.12	0.12	0.48
Hadron-fakes	< 0.01	0.35	0.14	0.05	0.08	0.05	< 0.01	< 0.01

Table 8.6: Breakdown of systematic uncertainties on $\sigma_{t\bar{t}\gamma}$ as a function of the energy in the transverse plane of the photon.

The observed increase of the detector modelling systematics is associated with the increase of statistical component of each uncertainty. In fact, these uncertainties have been determined from simulations, for which the amount of simulated $t\bar{t}\gamma$ events decreases with increasing $E_\mathrm{T}(\gamma)$.

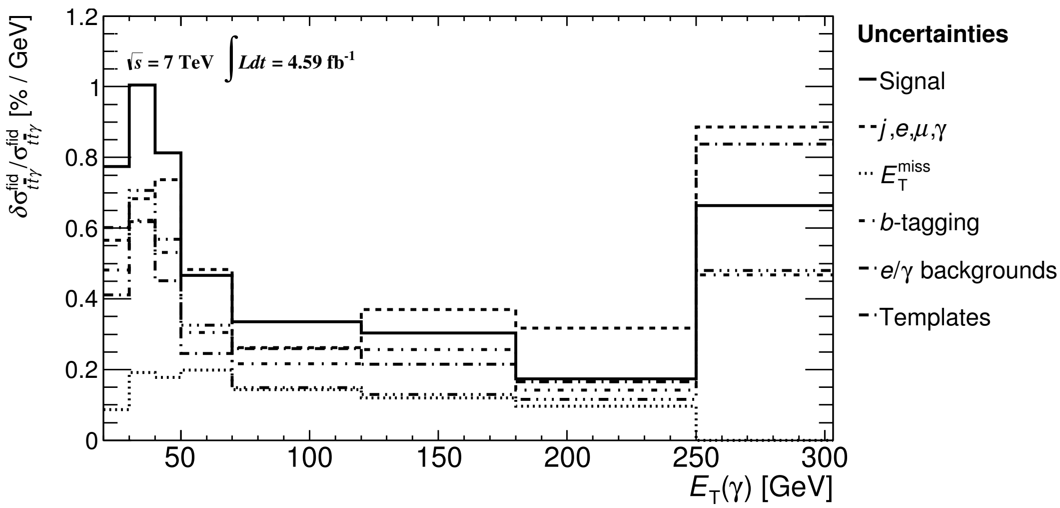

Figure 8.9: Relative strength to the cross section of each component of systematic uncertainty.

8.4.2 Comparison with the theoretical prediction

The results have been compared to that of the Next-to-Leading-Order (NLO) theoretical prediction. Three Leading-Order (LO) calculations, normalised to the same NLO/LO fraction are used in the comparison. The LO prediction are obtained with `WHIZARD` interfaced to `HERWIG` with `MadGraph` interfaced to two different PS programs, `PYTHIA` and `HERWIG`. The comparison is shown in Fig. 8.10. It can bee seen that, overall, the agreement is good and it increases with the photon-E_T. For low-E_T photons ($E_T(\gamma) < 30$ GeV) the comparison shows consistent discrepancies with all predictions. However, the statistical fluctuations may contribute considerably to those discrepancies.

The (small) difference with respect to the theoretical prediction of the cross section seen in the inclusive measurement can be, thus, attributed to the low-E_T region. In this region, the definition of the photon isolation may play a more important role. In fact, the NLO calculation uses a different definition of photons with respect to that used in the experimental measurement. The main difference arises in the treatment of collinear and *infra*-red divergencies. The theory uses a clustering algorithm to define the photon which is considered to be *infra*-red safe. The photon definition used in this analysis uses a minimum-p_T requirement upon the tracks entering in the p_T^{iso} calculation. Therefore, it cannot be excluded these differences are due to this different definition of photons.

8.5 Interpretation of the results

It was shown in Sec. 1.3 that the $t\bar{t}\gamma$ production cross section is sensitive to the top-quark's electric charge (Q_t) and in particular to anomalous couplings of the top quark to the photon. It is expected that the relation between $\sigma_{t\bar{t}\gamma}$ and Q_t is, approximatively quadratic. It was also shown that, besides a difference with respect to the inclusive cross section, shape differences in the $\sigma_{t\bar{t}\gamma}$ spectra with respect to the photon kinematic variables are sensitive to anomalous $t\gamma$ couplings,

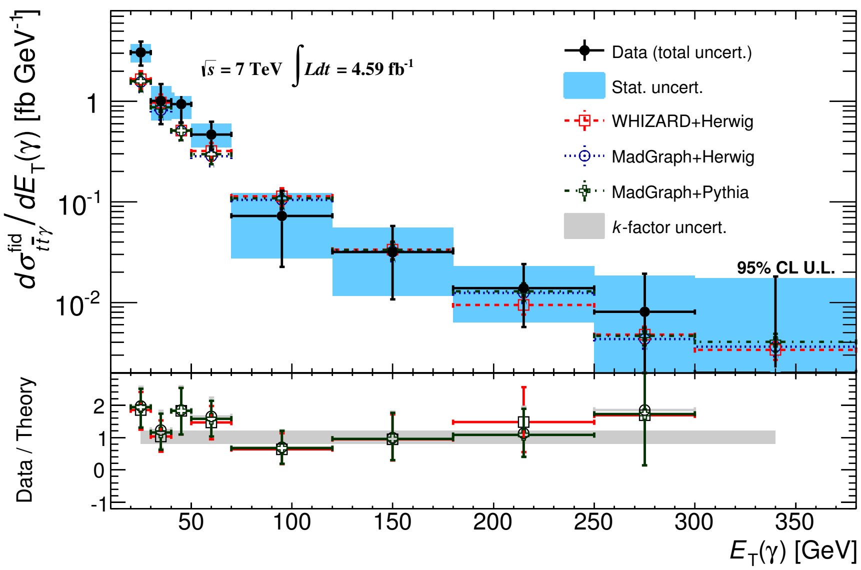

Figure 8.10: Comparison of the measured $t\bar{t}\gamma$ cross section spectrum in $E_{\mathrm{T}}(\gamma)$ with the prediction obtained different simulation programs. The measured spectrum (filled dots) includes the stat$\oplus$sys uncertainties, while the statistical uncertainty is overlaid (hatched area). All predictions are normalised to the same k-factor. The leading order predictions, obtained from `WHIZARD` interfaced to `HERWIG` (squared markers), `MadGraph` interfaced to `HERWIG` (open dots) and from `MadGraph` interfaced to `PYTHIA`(crosses) are normalised to the same k-factor. The dashed area in the ratio plot (shown on the bottom) corresponds to the theoretical k-factor uncertainty.

and specifically to anomalous values of Q_t. It is, in principle, possible to exploit the measured differential cross section in order to make an inference on the $t\gamma$ vertex, and specifically on Q_t.

At first it is of interest to inspect the fraction of photons radiated off top-quarks ($\sigma^{\mathrm{prod.}}_{t\bar{t}\gamma}$) or off top decay products ($\sigma^{\mathrm{decay}}_{t\bar{t}\gamma}$). These two quantities are shown, as evaluated from simulations, in Fig. 8.11. It can be seen that a sizeable fraction of $\sigma^{\mathrm{prod.}}_{t\bar{t}\gamma}$ is contained within $\sigma_{t\bar{t}\gamma}$. However, it can also be seen that non negligible interferences (both constructive and destructive) between $\sigma^{\mathrm{decay}}_{t\bar{t}\gamma}$ and $\sigma^{\mathrm{prod.}}_{t\bar{t}\gamma}$ affect the $\sigma_{t\bar{t}\gamma}$. From Fig. 8.11 it can be seen that for $E_{\mathrm{T}}(\gamma) > 40$ GeV, in the fiducial phase-space, the interferences seem to be only constructive. These interferences seem to be more prominent for lower than for higher values of $E_{\mathrm{T}}(\gamma)$. The increase of $\sigma^{\mathrm{prod.}}_{t\bar{t}\gamma}$ with respect to the $\sigma^{\mathrm{decay}}_{t\bar{t}\gamma}$ was already observed by the theoretical prediction, see Fig. 8.12.

Therefore, because of the interferences, that should be taken into account, a determination of $\sigma^{\mathrm{prod.}}_{t\bar{t}\gamma}$ experimentally is not straightforward. However, the shape dependence of the $\sigma_{t\bar{t}\gamma}$ to Q_t can be exploited. As no distinction with respect to $\sigma^{\mathrm{prod.}}_{t\bar{t}\gamma}$ or $\sigma^{\mathrm{decay}}_{t\bar{t}\gamma}$ is made, all final state interferences are included in the dependence. Different values of $\sigma_{t\bar{t}\gamma}$ are obtained using `MadGraph` interfaced to `PYTHIA` with varying values for the $t\gamma$ coupling (Q_t). Table 8.7 summarises the LO cross sections as estimated with `MadGraph`. For consistency with the baseline `MadGraph` simulations, the same settings with respect to the phase-space definition are used (see Sec. 3.2.2).

A total of 5×10^4 events are generated for each Q_t value. The phase space cuts defining the

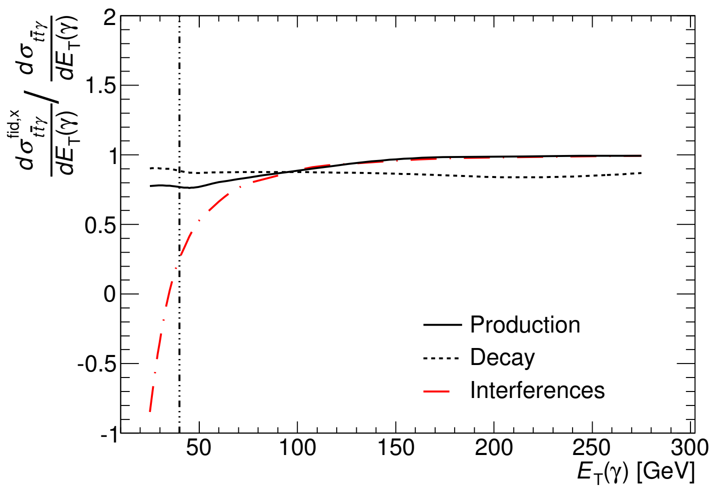

Figure 8.11: Fraction to the total $t\bar{t}\gamma$ predicted cross section for photons radiated off top-quark (labelled "Production", drawn with a solid line) and for photons radiated off decay products of the top-quark (labelled "Decay", drawn with a dashed line). The phase-space corresponds to that of the measured $\sigma_{t\bar{t}\gamma}$ and the calculation was performed using `MadGraph` normalised to the NLO/LO theory prediction.

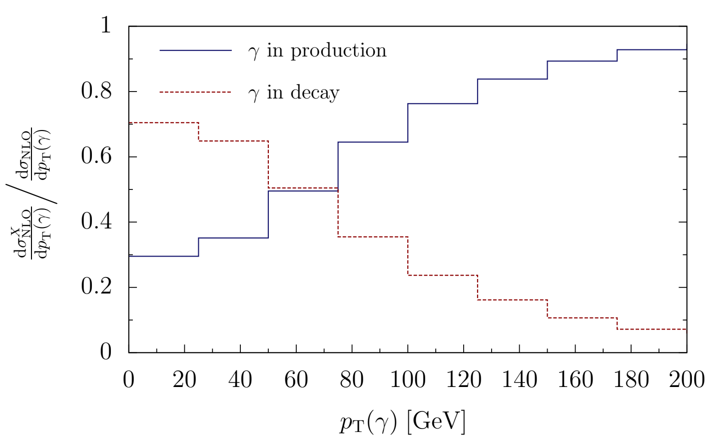

Figure 8.12: Next-to-leading ordered computation of the fraction to the total $t\bar{t}\gamma$ predicted cross section for photons radiated off top-quark (labelled "γ in production", drawn with a solid line) and for photons radiated off decay products of the top-quark (labelled "γ in decay", drawn with a dotted line) [56].

cross section measurement are applied to the new simulations, thus obtaining the $\sigma_{t\bar{t}\gamma}$ cross section in fiducial phase-space, also shown in Tab. 8.7. About 17% (for each lepton flavour) of the events are generated within the detector acceptance. Since the results of Sec. 8.4 are already corrected for detector resolution and smearing effects, no detector simulation is applied to the `MadGraph` samples with varied $t\gamma$ couplings. Finally, only the $F^{\gamma}_{1,\mathrm{V}}$ (see Eq. 1.7) was varied, with all other couplings set to their Standard Model (SM) value. The magnetic and electric dipole factors are

Q_t/Q_t^{SM}	$\sigma(pp \to \ell\nu_\ell q\bar{q}'b\bar{b}, \ell\nu_\ell\ell'\nu_{\ell'}b\bar{b}\gamma)^{\mathrm{LO}}$ **[pb]**	$\sigma^{\mathbf{fid,NLO}}_{t\bar{t}\gamma}$ **[fb]**
0.25	0.4370 ± 0.002	28.1 ± 0.1(stat) ± 5.6(theor)
0.50	0.4569 ± 0.002	32.0 ± 0.1(stat) ± 6.4(theor)
0.75	0.5085 ± 0.002	40.3 ± 0.2(stat) ± 8.0(theor)
1.00	0.5870 ± 0.002	50.9 ± 0.2(stat) ± 10.2(theor)
1.25	0.6979 ± 0.002	66.5 ± 0.3(stat) ± 13.3(theor)
1.50	0.8357 ± 0.001	87.1 ± 0.4(stat) ± 17.4(theor)
2.50	1.6890 ± 0.001	207.0 ± 0.9(stat) ± 41.5(theor)

Table 8.7: Summary of cross sections generated with `MadGraph` interfaced to `PYTHIA` for the $t\bar{t}\gamma$ process ($\sigma(pp \to \ell\nu_\ell q\bar{q}'b\bar{b}, \ell\nu_\ell\ell'\nu_{\ell'}b\bar{b}\gamma)^{\mathrm{LO}}$, $\ell = e, \mu, \tau$). Uncertainties for the generated cross sections at LO are statistical only. The prediction in the fiducial phase-space ($\sigma^{\mathrm{fid,NLO}}_{t\bar{t}\gamma}$) is also given.

set to zero. The LO simulations are normalised to the same NLO calculation with respect to which the $\sigma_{t\bar{t}\gamma}$ is compared. It is important to stress at this point that these simulated samples do not correspond necessarily to valid theoretical models, but the unitarity of the Matrix-Element (ME) is imposed at a later stage.

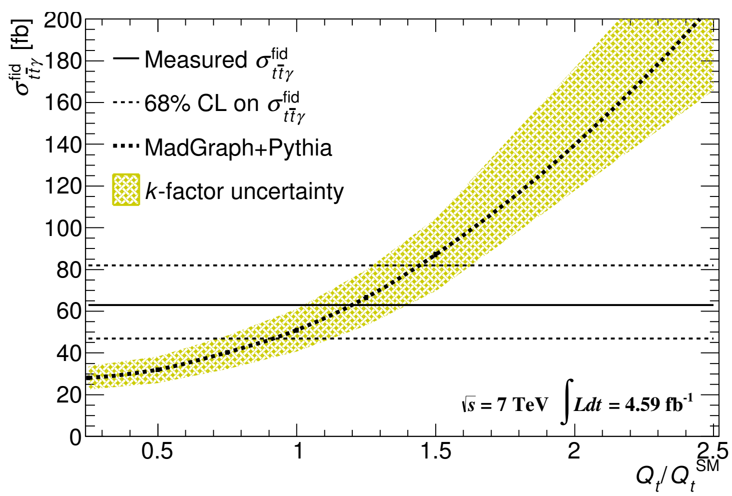

Figure 8.13: Simulated cross section for the $t\bar{t}\gamma$ process as a function of different values for Q_t. The measured $t\bar{t}\gamma$ cross section (see Sec. 8.1) is shown with a horizontal continuous line. The two dotted horizontal lines correspond to the upper and lower limit of the 68% CL on $\sigma_{t\bar{t}\gamma}$ respectively. The filled are corresponds to the k-factor uncertainty as estimated from the theoretical calculation.

Figure 8.13 shows the relation of the simulated $t\bar{t}\gamma$ cross sections (in the fiducial region) as a function of the varied Q_t values. It can be seen that the relation is, as expected, quadratic. Values of $\frac{Q_t}{Q_t^{\mathrm{SM}}} > 1.4$ and values of $\frac{Q_t}{Q_t^{\mathrm{SM}}} < 0.7$ are incompatible with the measured cross section.

From each $E_{\mathrm{T}}(\gamma)$ spectrum, corresponding to a value of Q_t, templates are constructed. In oder to estimate the values of the $E_{\mathrm{T}}(\gamma)$ spectrum in between the simulated values of Q_t, a linear interpolation was used [139]. The generated templates are shown in Fig. 8.14. It can be seen, as expected from the theory, that the spectrum becomes harder with increasing values of Q_t.

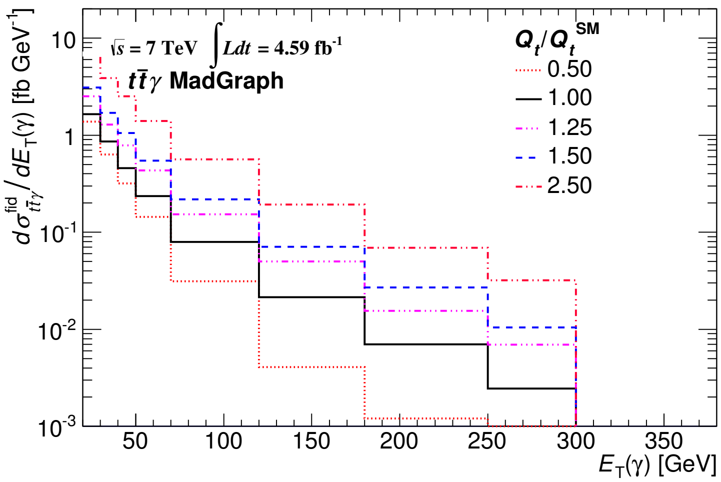

Figure 8.14: Simulated $E_{\mathrm{T}}(\gamma)$ spectra of $\sigma_{t\bar{t}\gamma}$ for different values of Q_t.

The value of Q_t is extracted from the differential $t\bar{t}\gamma$ cross section by maximising a likelihood function. Statistical uncertainties on $t\bar{t}\gamma$ as a function of $E_{\mathrm{T}}(\gamma)$ are treated as uncorrelated, the systematic uncertainty is kept as fully correlated across all $E_{\mathrm{T}}(\gamma)$ bins. Figure 8.15 shows the minimised negative logarithm of the likelihood for both estimations with and without systematic uncertainties.

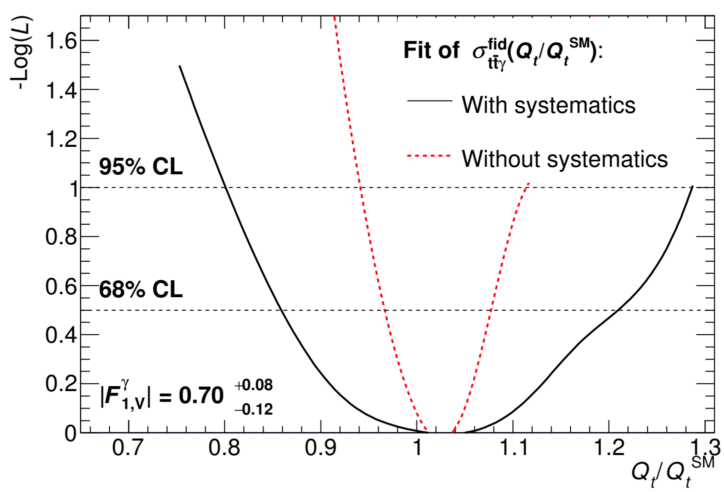

Figure 8.15: Minimised negative logarithm of the likelihood used to extract the ratio Q_t/Q_t^{SM}. The dotted curve corresponds to statistical variations on the measured $d\sigma_{t\bar{t}\gamma}/E_{\mathrm{T}}(\gamma)$ while the continous line includes both statistical and systematic uncertainties. The two horizontal lines indicate the intervals at the 68% and 95% confidence level.

The extracted value of Q_t at a 68% CL is:

$$|Q_t| = |F^{\gamma}_{1,\mathrm{V}}| = 0.70\ ^{+0.05}_{-0.02}\ (\mathrm{stat})\ ^{+0.11}_{-0.08}\ (\mathrm{syst}) \tag{8.6}$$

which is in excellent agreement with the standard model value of the top charge. From Fig. 8.15 it can be seen that the upper limit on Q_t at 95% CL corresponds to 0.79. This suggests that new physics induced by an anomalous vector real coupling of the $t\gamma$ vertex can be excluded as a function of the scale of the new phenomena and the partonic centre-of-mass-energy ($\sqrt{\hat{s}}$).

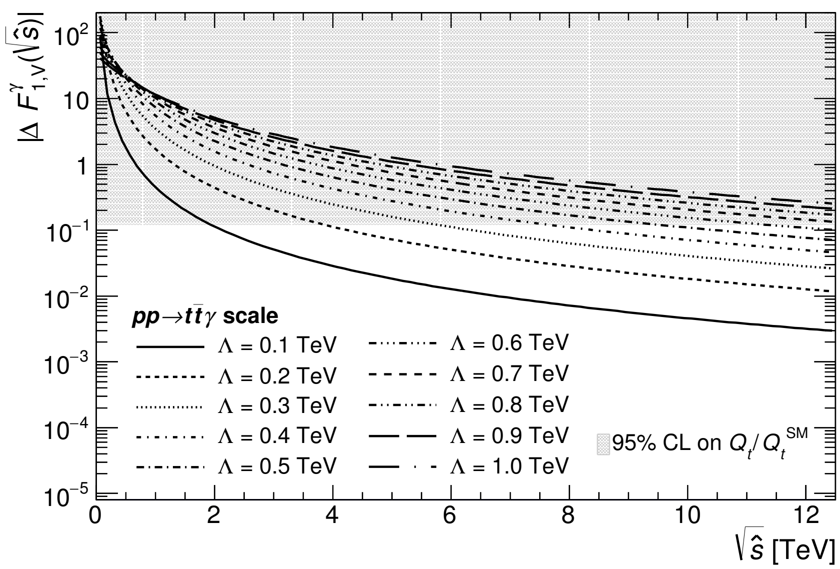

Figure 8.16: Evolution of the unitarity contraint on anomalous $t\bar{t}\gamma$ couplings as a function of the partonic centre of mass energy ($\sqrt{\hat{s}}$). Unitarity of the S-matrix allows for deviations of the SM couplings in the regions below the curves. The curves are parametrised with respect to the scale of new physics (Λ). Limits are deduced from Eq. 1.10 and Eq. 1.11, which are based on the calculation derived elsewhere [12]. Allowed regions $|\Delta F^{\gamma}_{1,\mathrm{V}}|$ are shown by the curves, while the excluded region by the extracted value of Q_t is indicated by the grey area.

Combining the unitarity constraint on the ME for the $t\bar{t}\gamma$ process, which was shown in Fig. 1.7 of Chap. 1, to those of Eq. 8.6 it is possible to extract such limits, which are shown in Figure 8.16. Exact values are shown in Tab. 8.8 summarising both the lower and the upper limits derived on $|\Delta F^{\gamma}_{1,\mathrm{V,A}}(0)|$ (see Eq. 1.10).

$\|\Delta F^{\gamma}_{1,\mathrm{V}}\| \leq 0.79$										
Λ [TeV]	0.1	0.2	0.3	0.4	0.5	0.6	0.7	0.8	0.9	1.0
$\sqrt{\hat{s}}$ **[TeV]**	1.95	3.9	5.8	7.7	9.5	11.4	13.2	15.0	16.8	18.6

Table 8.8: Experimental constrain on the unitarity of the matrix element as derived from the upper limit on on $|\Delta F^{\gamma}_{1,\mathrm{V,A}}(0)|$. The constrain is shown as a function of the the scale of new physics (Λ) and as a function of the partonic centre-of-mass energy ($\sqrt{\hat{s}}$).

Although event generation at Next-to-Leading-Order has become available, recently, in programs such as `MadGraph5@MCNLO` [163], it is important to remind the reader that these limits use information from simulations evaluated at LO. In fact, the $E_{\mathrm{T}}(\gamma)$ spectra with varied Q_t are normalised to the same NLO prediction. Since the NLO corrections of $\sigma_{t\bar{t}\gamma}$ to Q_t^{SM} are non negligible, it is not possible to exclude a k-factor shape dependance with different values of Q_t. In terms, these dependencies can alter the value of the limits. However, the interpretation of the result shows that at leading order data are well compatible with the prediction from the standard model.

Conclusion

The top quark (t), because of its large mass, is speculated to play a crucial role in the electroweak symmetry braking mechanism that underpin the Standard Model of particle physics. Many of the properties of the top quark are yet to be fully constrained by the experiment and fully understood from the theory. The couplings of the top quark to vector gauge bosons (W, Z, γ) are yet to be measured with precision. At hadron colliders, and in particular at the Large Hadron Collider (LHC), the production of top anti-top pairs ($t\bar{t}$) in association with a final state photon ($t\bar{t}\gamma$) is sensitive to the electromagnetic couplings of the $t\gamma$ vertex.

It was discussed in Chap. 1 that a direct measurement of the coupling constants of quarks to gauge bosons has not been performed yet. Because of its narrow decay width, the top quark decays before hadronising into bound states, therefore a study of the $t\bar{t}\gamma$ production provides the framework for a direct measurement of the $t\gamma$ vertex, and in particular a direct measurement of the top quark's electric charge (Q_t). A determination of Q_t through for a direct observation is of great importance because, from one side, it can provide an indisputable proof of the fractional nature of the quark's electric charge, from the other side, anomalous and small deviations off the SM value of Q_t can be an indicator of undiscovered phenomena appearing at a higher energy scales.

In this thesis the $pp \to t\bar{t}\gamma$ production cross section ($\sigma_{t\bar{t}\gamma}$) was studied with 4.59 fb^{-1} of LHC proton proton collision data recoreded by the ATLAS detector. The study focused on the final states determined by a single lepton (electron or muon), at least four jets, large transverse missing momentum and a final state photon.

The $\sigma_{t\bar{t}\gamma}$ was defined in a phase-space within the kinematic and geometrical detector acceptance. The definition of particles belonging to the phase-space was motivated by imposing experimentally observable selection criteria. This definition diminishes the model-dependency and augments the reproducibility of the result.

In the $t\bar{t}$ decay channel scrutinised by this analysis, the final states of $t\bar{t}\gamma$ production are indistinguishable from the production of $W+$jets, $Z+$jets, single top, and diboson which may also feature a final state energetic photon. Furthermore, the experimental response of leptons reconstructed as jets with an additional photon radiation and the experimental response of electrons reconstructed as photons (mainly W-boson leptonic decays) are also indistinguishable from the $t\bar{t}\gamma$ final states. These process constitute a background to the measurement of the $\sigma_{t\bar{t}\gamma}$. Their contribution was estimated using techniques based on data and on well known phenomena, reducing the simulation-induced model-dependency of the result.

Furthermore, the response for hadrons, or hadron decay products ($\pi^0 \rightarrow \gamma\gamma$) is close to that of real photon objects. A discrimination between the two is possible exploiting the differences in shapes of showers developed by either hadrons or photons. Showers initiated by hadrons have a larger longitudinal and lateral profile. The fine granularity of the ATLAS electromagnetic calorimeter of the detector rejects the bulk of hadrons identified as photons. Residual hadrons, or hadron decay products, identified as photons constitute also an important background for the $t\bar{t}\gamma$ process and for the background processes with an additional photon. The final extraction of the $t\bar{t}\gamma$ signal was performed exploiting the isolation variable, defined as the sum momenta of all particles within a cone around the photon direction. The isolation distribution for hadrons, which are accompanied by hadronic activity, peaks at larger values than for photons. Therefore, in isolation terms, detector responses are categorised in two categories. The prompt-like objects, which are photons and electrons misidentified as photons, and non-prompt objects, which are hadrons misidentified as photon.

A likelihood model was created modelling all detector responses for $t\bar{t}\gamma$ events, background processes with additional prompt-like objects, hadrons misidentified as photons and their corresponding systematic uncertainties. The $\sigma_{t\bar{t}\gamma}$, and its spectrum in E_{T} were extracted by maximising the profile likelihood ratio of such model and they were determined for photons with $E_{\mathrm{T}}(\gamma) > 20$ GeV and $|\eta| < 2.37$. The extracted cross section times the BR per lepton flavour is:

$$\sigma_{t\bar{t}\gamma} \times \mathrm{BR} = 63 \pm 8(\mathrm{stat.})\,^{+17}_{-13}\,(\mathrm{syst.}) \pm 1\,(\mathrm{lumi.})\,\mathrm{fb}$$

where the leading systematic uncertainties arise from the jet detector response and the identification of b-flavoured jets. A Similar strength of systematic uncertainties was seen in result as a function of $E_{\mathrm{T}}(\gamma)$.

The significance of the signal with respect to background fluctuations was determined to be 5.3σ, making this measurement the first observation of the $t\bar{t}\gamma$ process.

The results of $\sigma_{t\bar{t}\gamma}$ as a function of $E_{\mathrm{T}}(\gamma)$ were interpreted, exploiting the E_{T} spectra for different values $t\gamma$ coupling values, and a direct inference on Q_t was derived. The inferred top quark charge is

$$|Q_t| = 0.70\ ^{+0.05}_{-0.02}\ (\mathrm{stat.})\ ^{+0.11}_{-0.08}\ (\mathrm{syst.}),$$

being in excellent agreement with the fractional quark hypothesis of the SM. Furthermore this value was used for deriving upper limits (at a 95% confidence level) for new physics phenomena associated with anomalous coupling values of the $t\gamma$ vertex. These interpretations showcase that the results presented in this thesis can make an important step towards the experimental determination of the top quark's properties.

Appendices

APPENDIX A

Photon shower shapes

In this section the shower shape variables for *tight* and *loose* photons are shown for converted and unconverted photons separately.

A.1 Unconverted photons

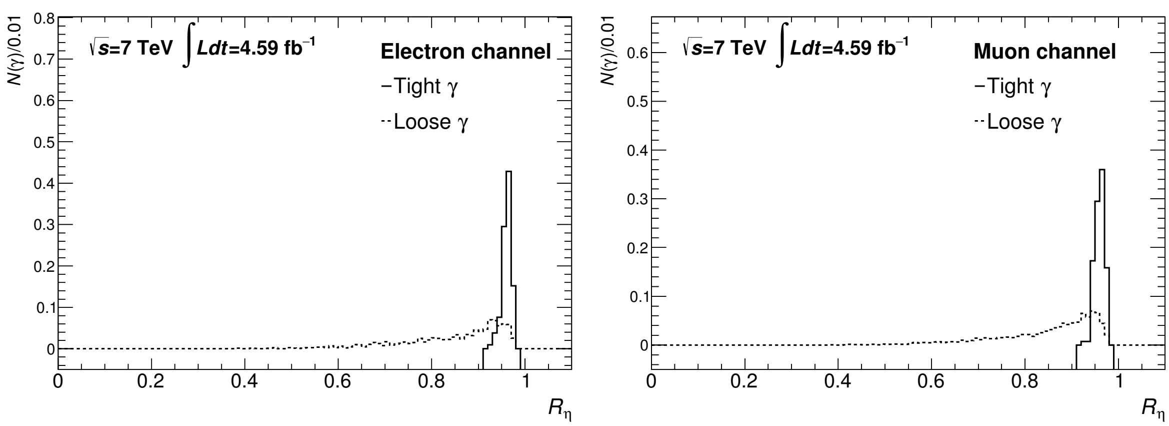

Figure A.1: R_η distributions for *tight* photons (continuous line) with respect to *loose* photons (dotted line). The distributions are obtained from data and are normalised to their area. The left (right) plot shows distribution for the electron channel (muon) channel.

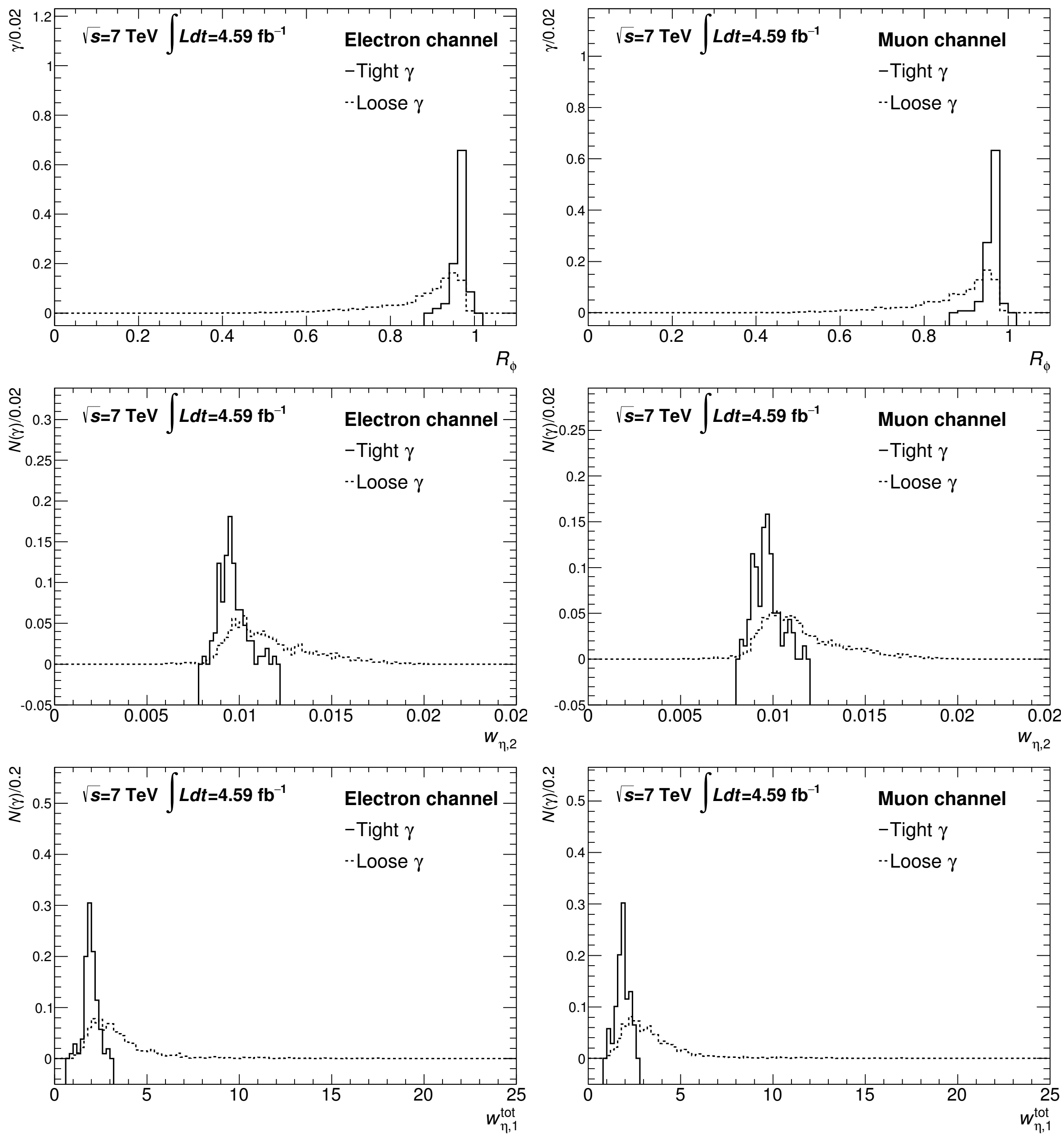

Figure A.2: R_ϕ, w_{η_2} and $w_{s_{1\ \mathrm{tot}}}$ distributions for *tight* photons (continuous line) with respect to *loose* photons (dotted line). The distributions are obtained from data and are normalised to their area. The left (right) plot shows distribution for the electron channel (muon) channel.

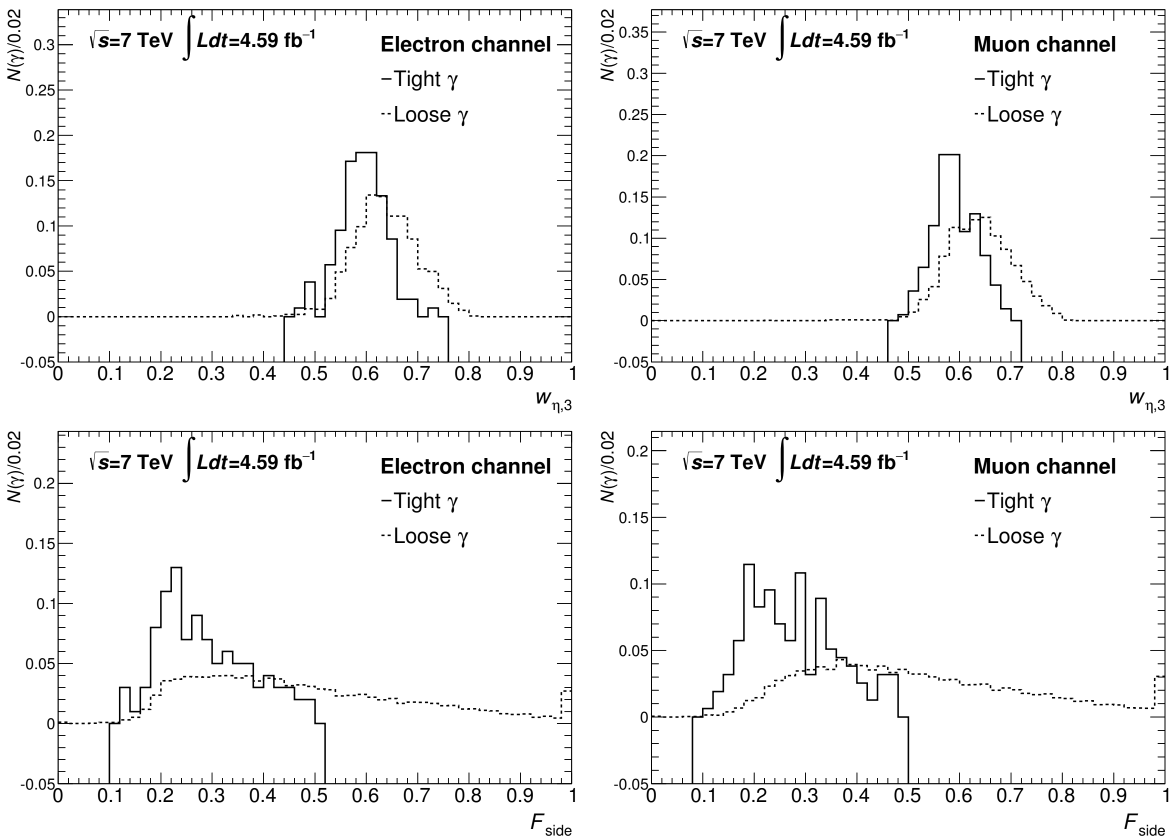

Figure A.3: w_{s_3} and F_{side} distributions for *tight* photons (continuous line) with respect to *loose* photons (dotted line). The distributions are obtained from data and are normalised to their area. The left (right) plot shows distribution for the electron channel (muon) channel.

A.2 Converted photons

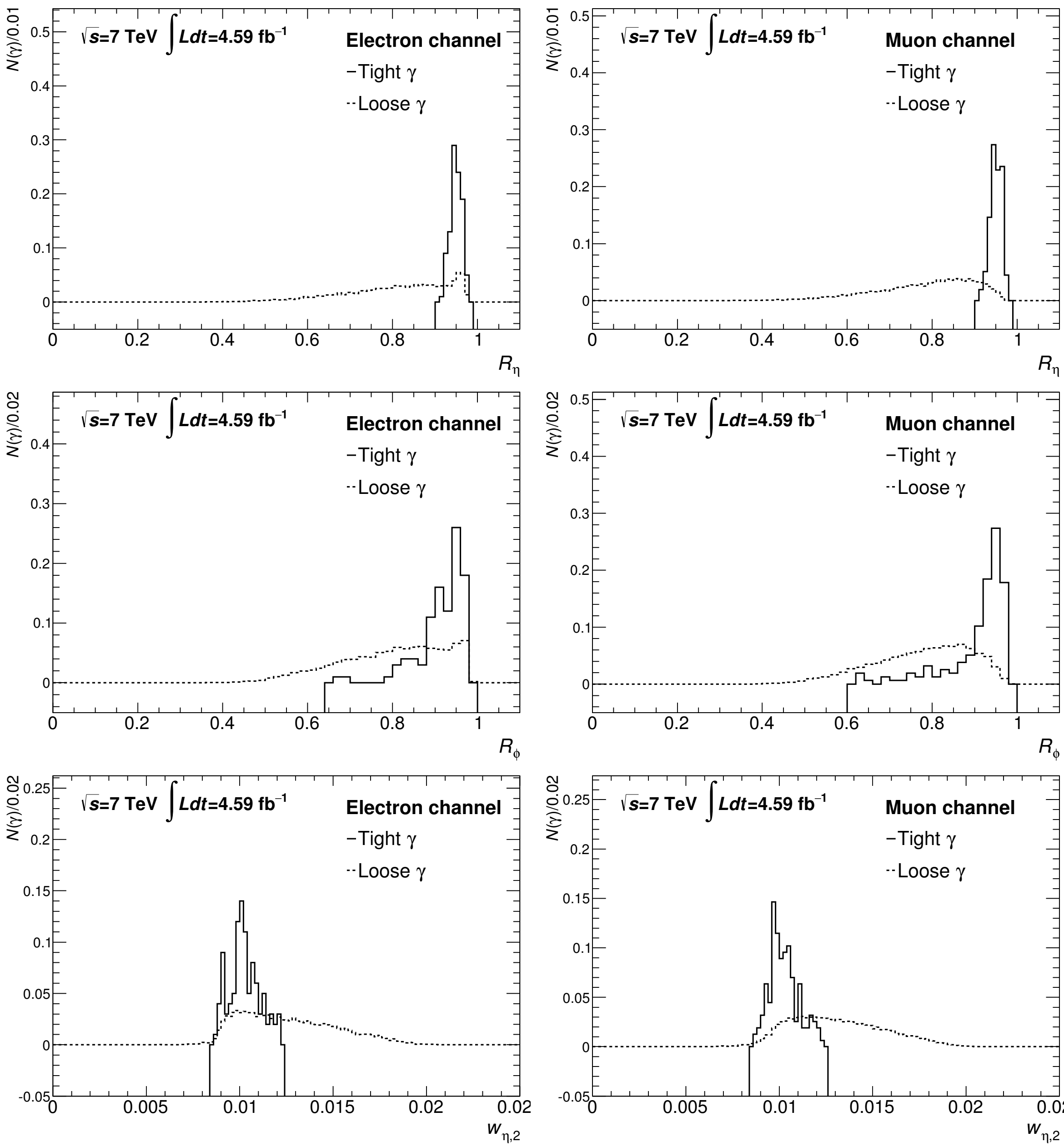

Figure A.4: R_η, R_ϕ, and $w_{s_{\rm tot}}$ distributions for *tight* photons (continuous line) with respect to *loose* photons (dotted line). The distributions are obtained from data and are normalised to their area. The left (right) plot shows distribution for the electron channel (muon) channel.

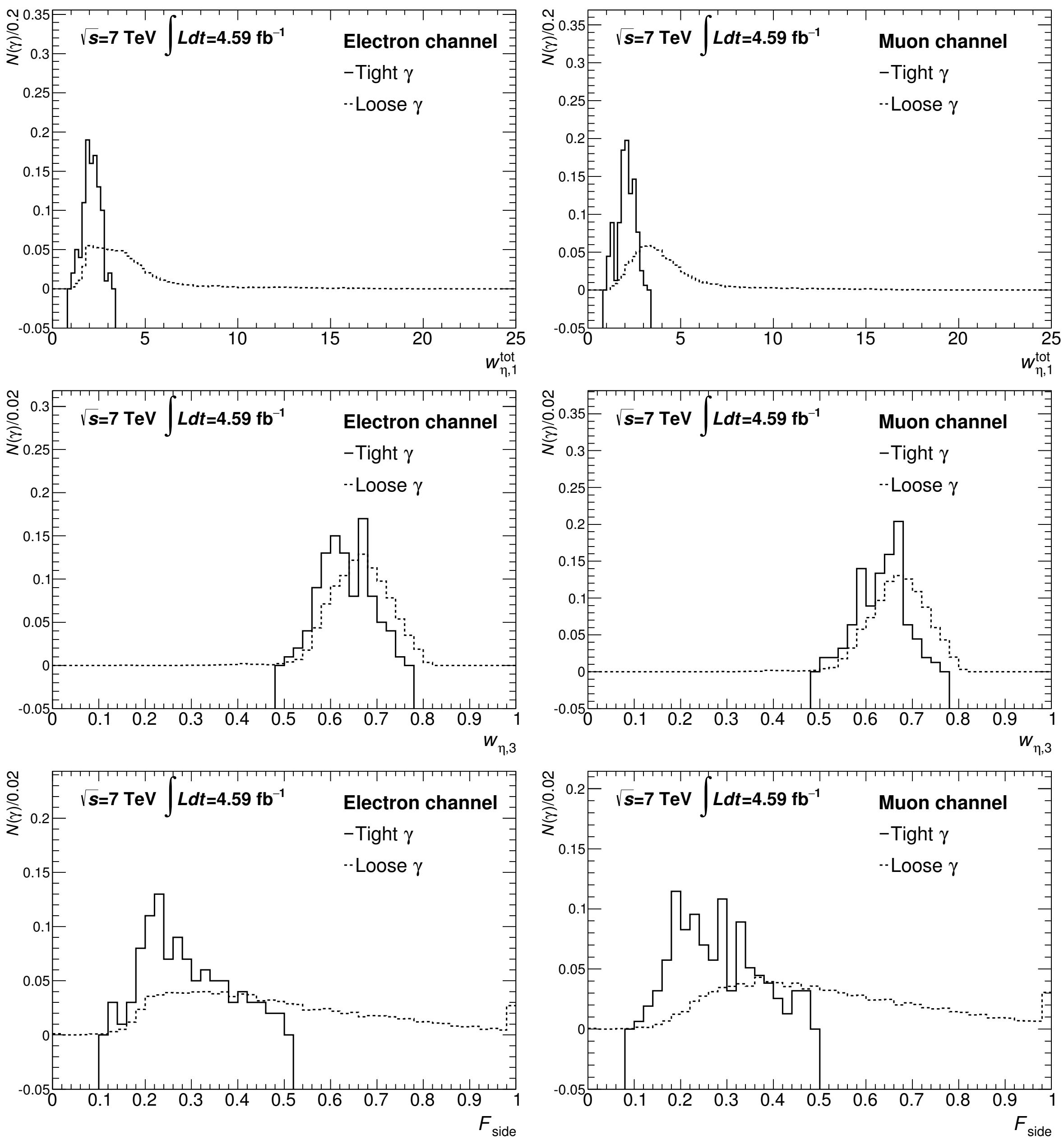

Figure A.5: $w_{s_{\rm tot}}$, w_{s3} and $F_{\rm side}$ distributions for *tight* photons (continuous line) with respect to *loose* photons (dotted line). The distributions are obtained from data and are normalised to their area. The left (right) plot shows distribution for the electron channel (muon) channel.

APPENDIX B

Data-to-simulation comparisons

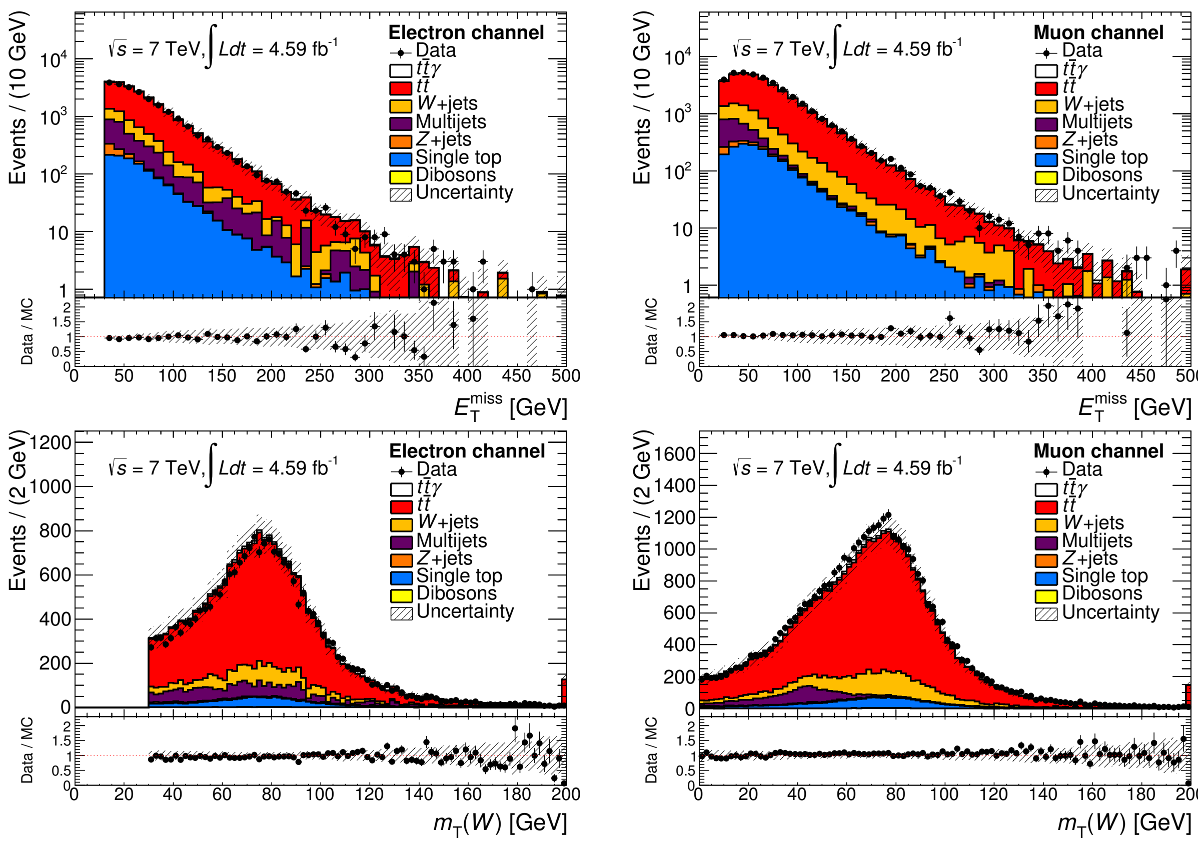

Figure B.1: Distributions for the missing transverse energy ($E_{\mathrm{T}}^{\mathrm{miss}}$) and the W-boson traverse mass ($m_{\mathrm{T}}(W)$). Distributions on the left (right) are for the electron (muon) channel. The band labelled "Uncertainty" includes sum in quadrature of the, simulation based, statistical and systematic uncertainties. The last bin includes any overflows.

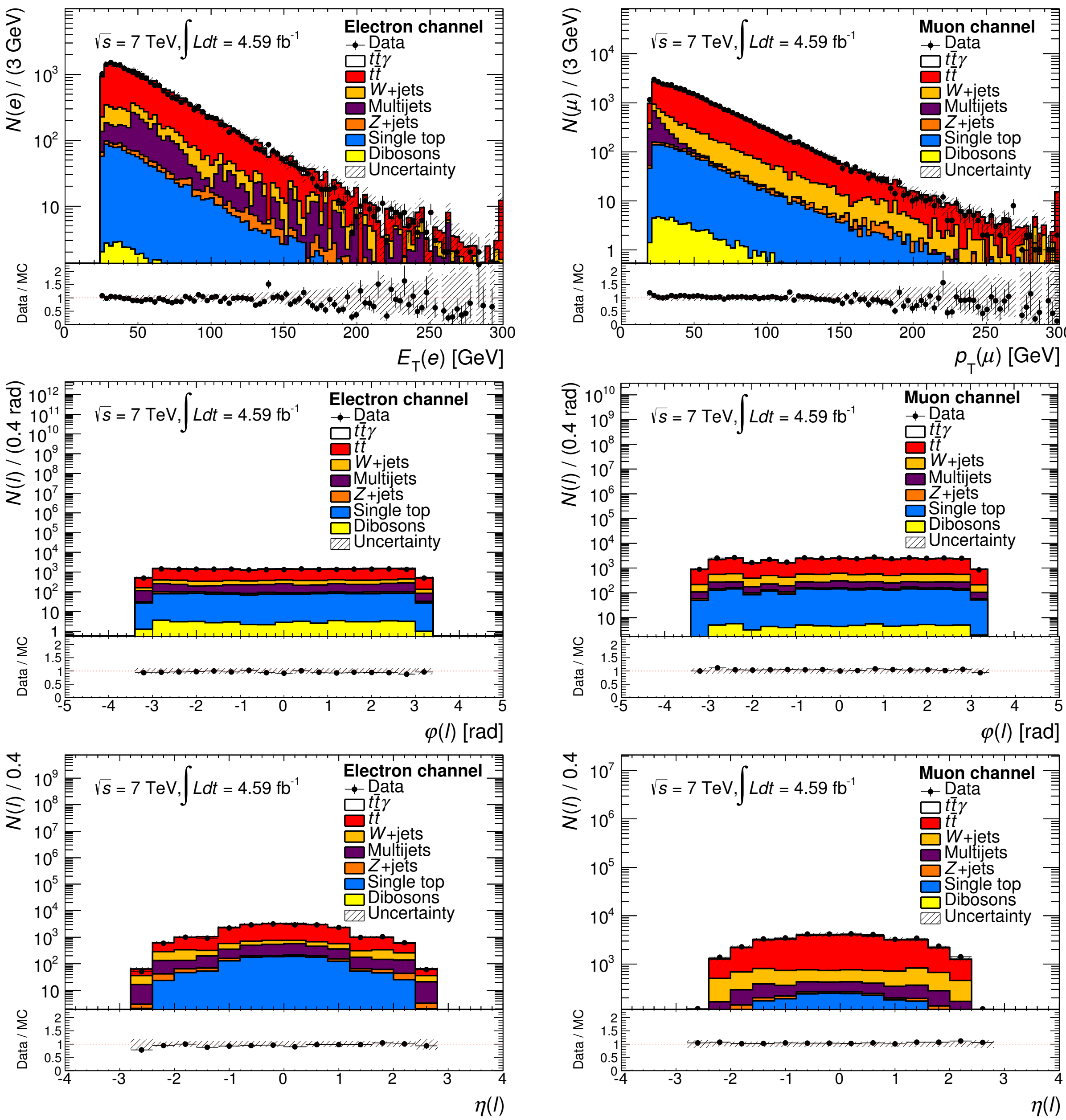

Figure B.2: Distributions for the electron transverse energy ($E_T(\gamma)$, the muon transverse momentum $p_T(\mu)$, lepton φ and η. Distributions on the left (right) are for the electron (muon) channel. The band labelled "Uncertainty" includes sum in quadrature of the, simulation based, statistical and systematic uncertainties. The last bin includes any overflows.

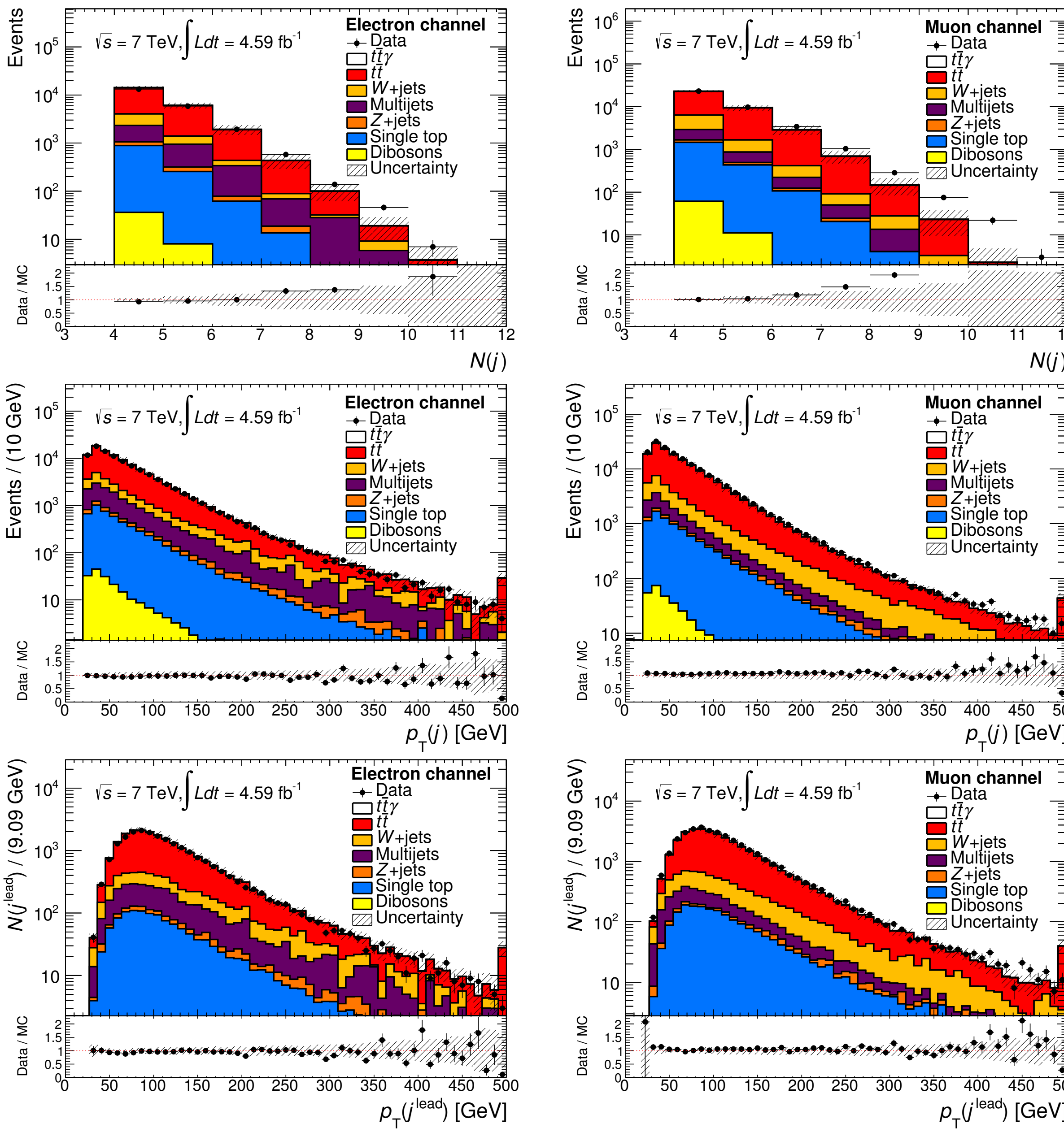

Figure B.3: Distributions for the jet multiplicity ($N(j)$), the transverse energy of the jet ($p_{\mathrm{T}}(j)$) and for the jet with highest-p_{T}in the event ($p_{\mathrm{T}}(j^{\mathrm{lead}})$). Distributions on the left (right) are for the electron (muon) channel. The band labelled "Uncertainty" includes sum in quadrature of the, simulation based, statistical and systematic uncertainties. The last bin includes any overflows.

APPENDIX C

Cross section and phase-space definition

This appendix contains additional plots and tables to the cross section phase-space definition.

C.1 Simulation to particle to reconstruction level comparisons

This section contains some additional particle- to reconstruction- level comparisons obtained with the `MadGraph` and `WHIZARD` simulation samples.

C.1.1 Leptons

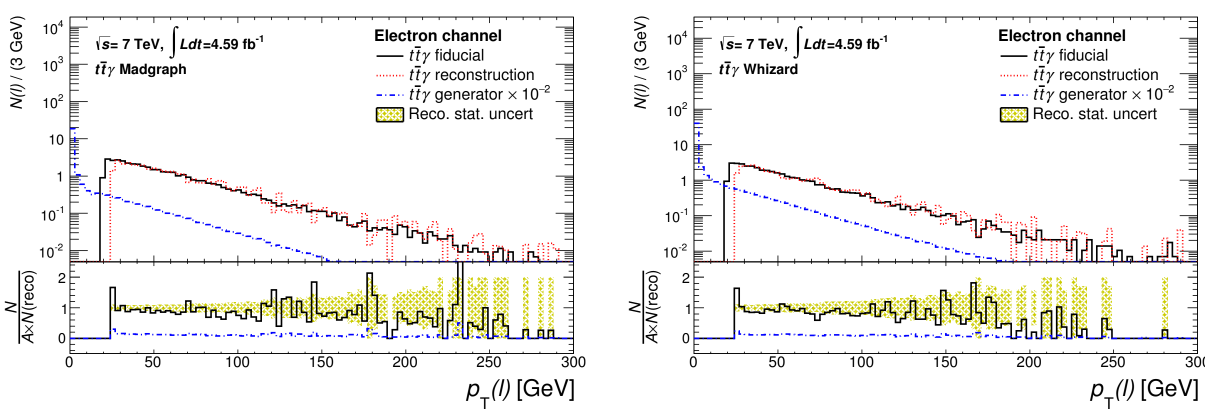

Figure C.1: Comparisons of kinematic distributions as defined at particle level (labelled “fiducial” and drawn with continuos line), at reconstruction level objects (labelled “reconstruction” and drawn with a dotted line) and in `WHIZARD` (labelled “generator” and drawn with a dashed line). Left distributions are for electrons while distributions on the right are for muons.

C.1.2 Leptons

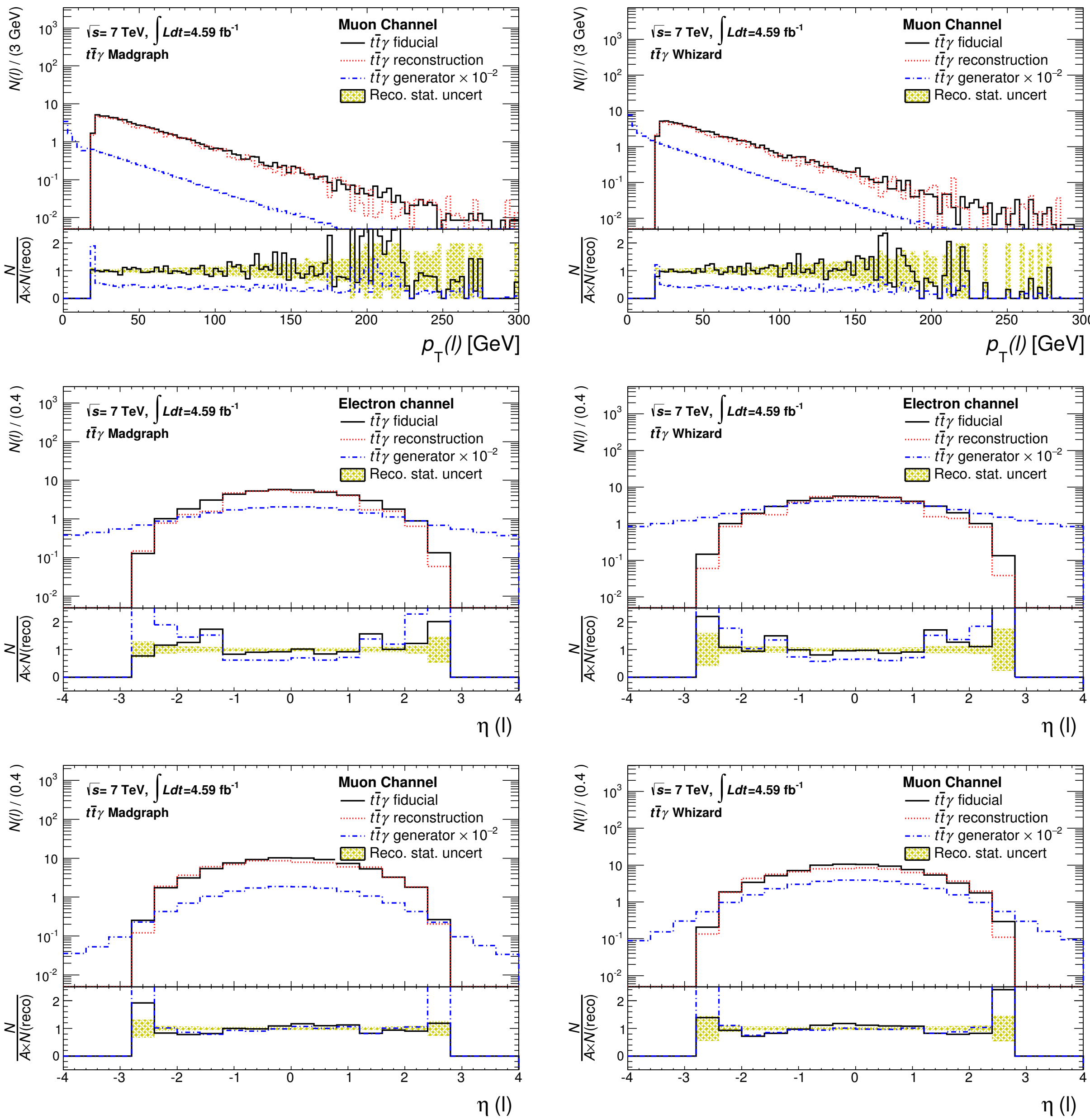

Figure C.2: Comparisons of kinematic distributions as defined at particle level (labelled "fiducial" and drawn with continuos line), at reconstruction level objects (labelled "reconstruction" and drawn with a dotted line) and in `WHIZARD` (labelled "generator" and drawn with a dashed line). Left distributions are for electrons while distributions on the right are for muons.

C.1.3 Jets

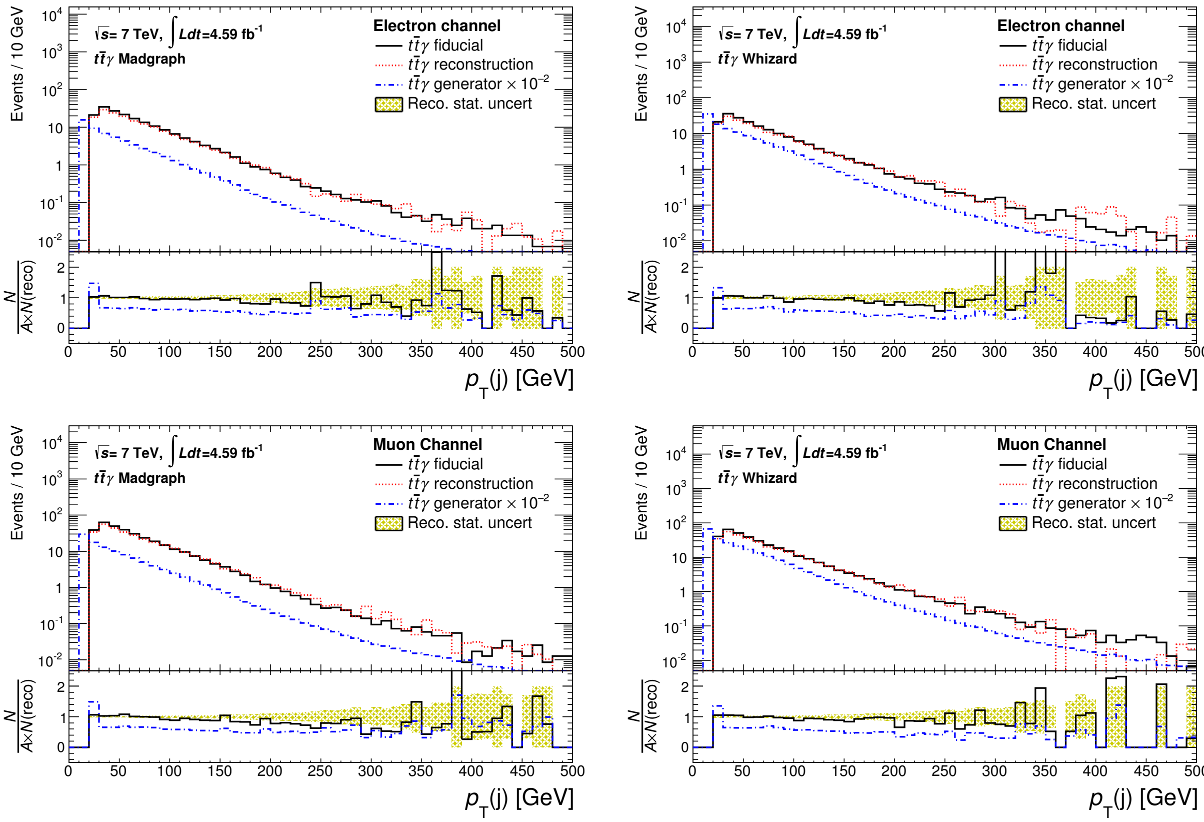

Figure C.3: Comparisons of kinematic distributions as defined at particle level (labelled “fiducial” and drawn with continuos line), at reconstruction level objects (labelled “reconstruction” and drawn with a dotted line) and in `WHIZARD` (labelled “generator” and drawn with a dashed line). Left distributions are for electrons while distributions on the right are for muons.

C.2 Photons

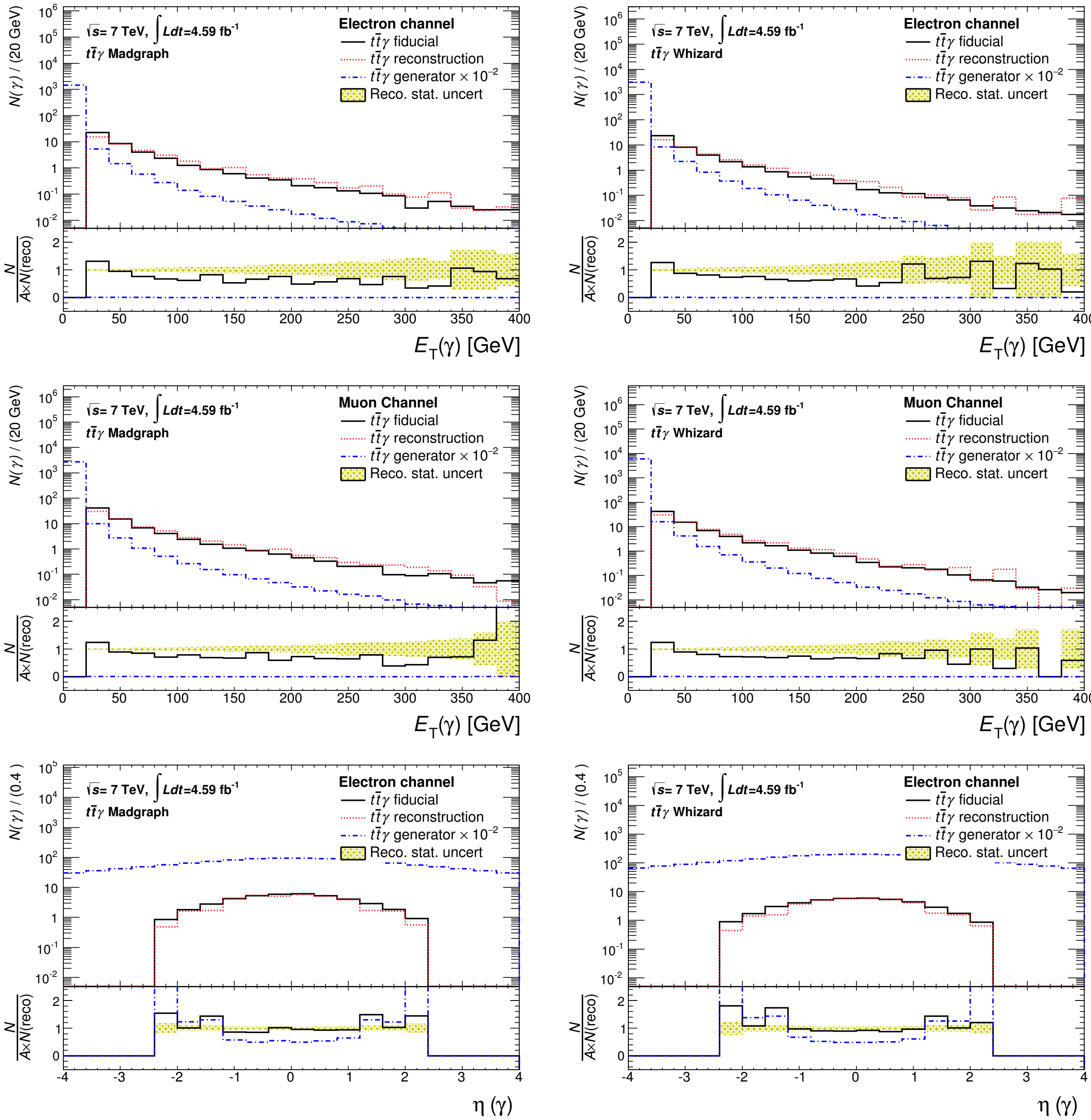

Figure C.4: Comparisons of kinematic distributions as defined at particle level (labelled "fiducial" and drawn with continuos line), at reconstruction level objects (labelled "reconstruction" and drawn with a dotted line) and in `WHIZARD` (labelled "generator" and drawn with a dashed line). Left distributions are for electrons while distributions on the right are for muons..

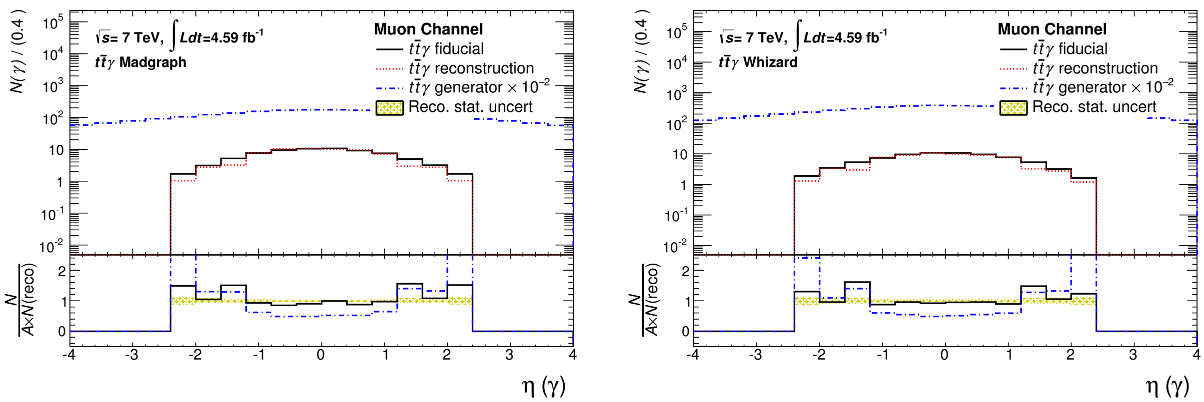

Figure C.5: Comparisons of kinematic distributions as defined at particle level (labelled "fiducial" and drawn with continuos line), at reconstruction level objects (labelled "reconstruction" and drawn with a dotted line) and in `WHIZARD` (labelled "generator" and drawn with a dashed line). Left distributions are for electrons while distributions on the right are for muons.

C.3 Selection requirements

This section contains additional particle- to reconstruction-level comparisons when the selection requirements are applied.

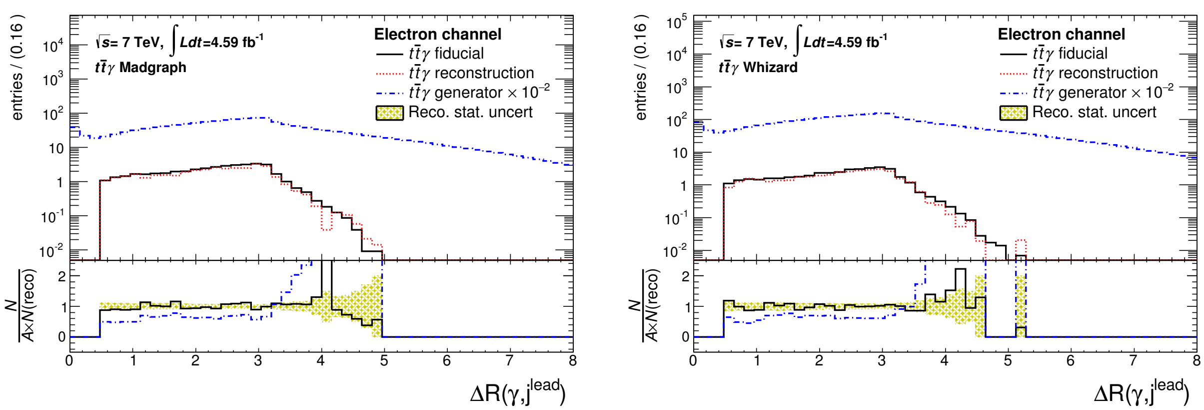

Figure C.6: Comparisons of kinematic distributions as defined at particle level (labelled "fiducial" and drawn with continuos line), at reconstruction level objects (labelled "reconstruction" and drawn with a dotted line) and in `WHIZARD` (labelled "generator" and drawn with a dashed line). Left distributions are for electrons while distributions on the right are for muons.

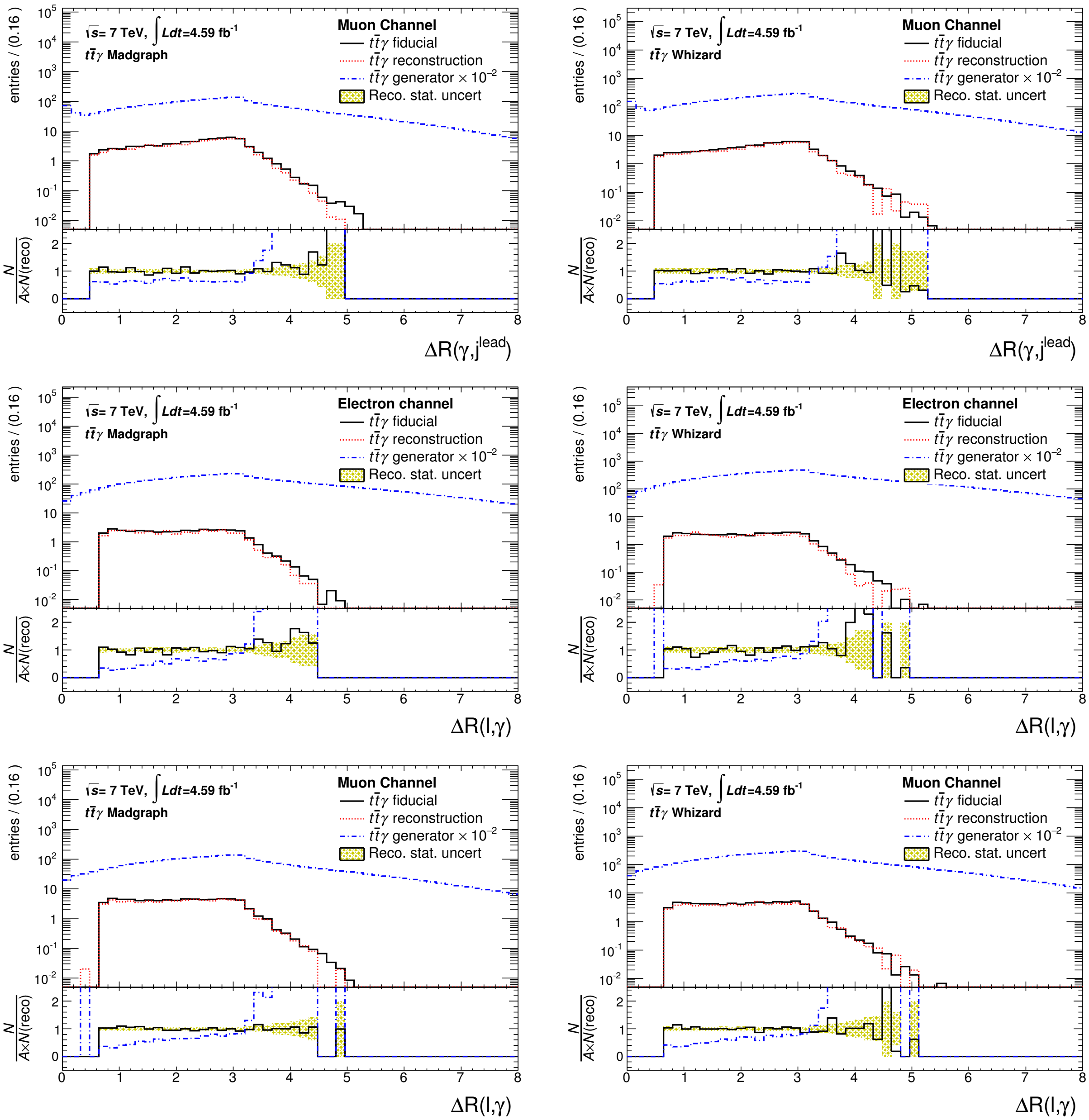

Figure C.7: Comparisons of kinematic distributions as defined at particle level (labelled "fiducial" and drawn with continuos line), at reconstruction level objects (labelled "reconstruction" and drawn with a dotted line) and in WHIZARD (labelled "generator" and drawn with a dashed line). Left distributions are for electrons while distributions on the right are for muons.

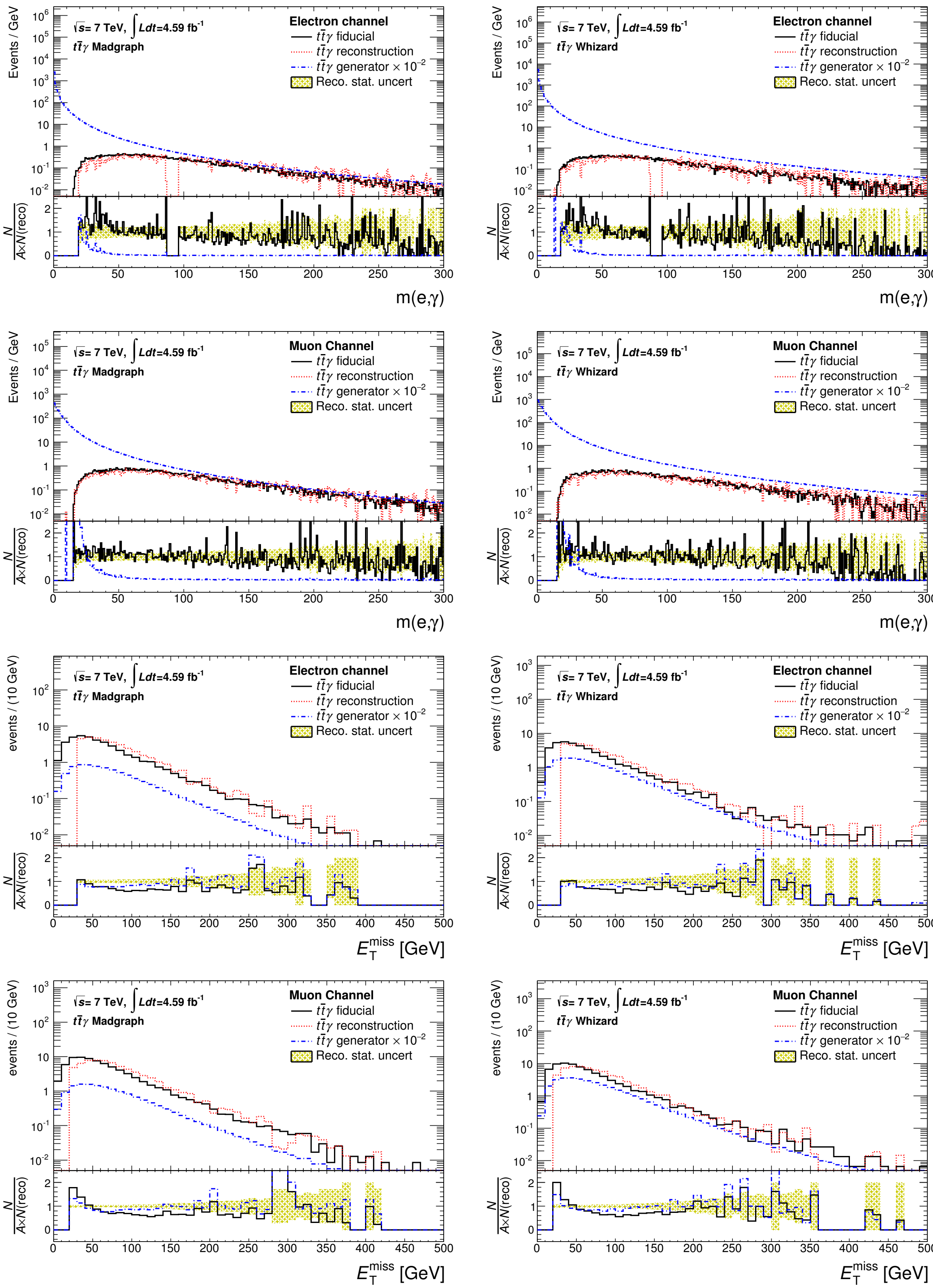

Figure C.8: Comparisons of kinematic distributions as defined at particle level (labelled "fiducial" and drawn with continuos line), at reconstruction level objects (labelled "reconstruction" and drawn with a dotted line) and in WHIZARD (labelled "generator" and drawn with a dashed line). Left distributions are for electrons while distributions on the right are for muons.

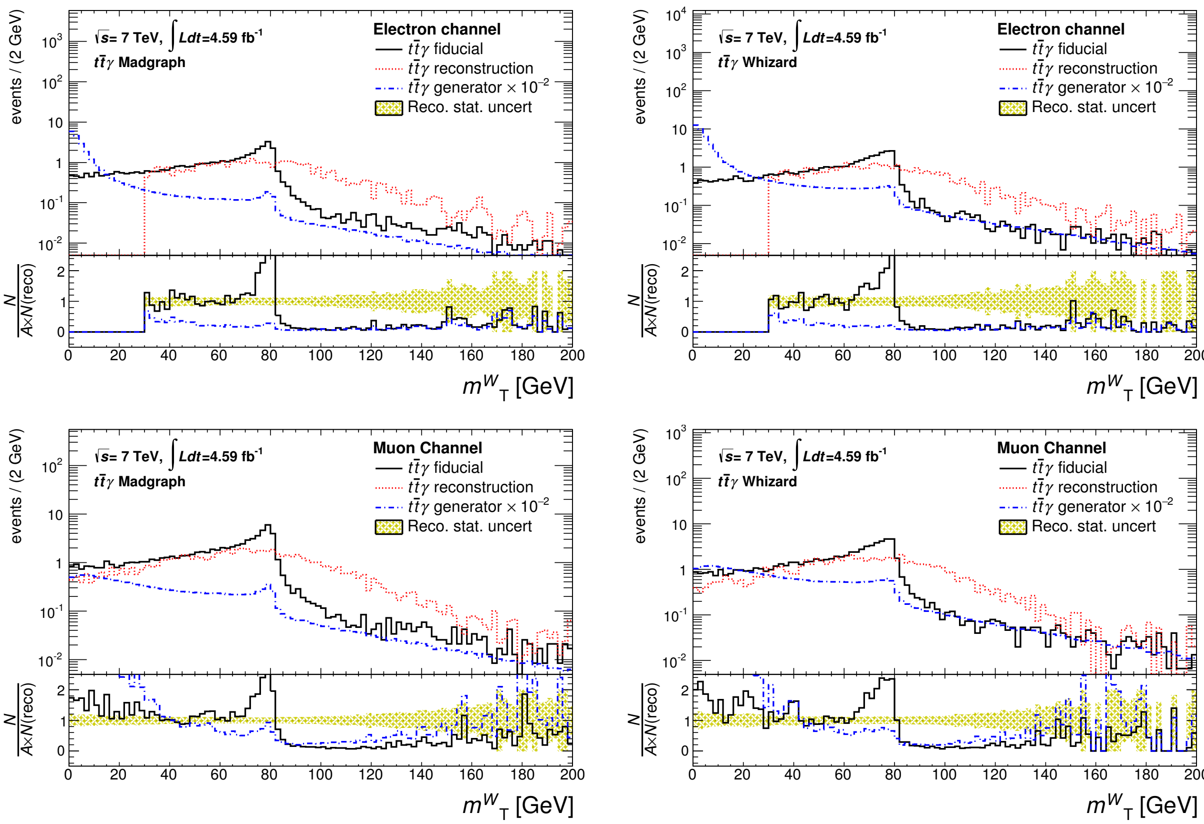

Figure C.9: Comparisons of kinematic distributions as defined at particle level (labelled “fiducial” and drawn with continuos line), at reconstruction level objects (labelled “reconstruction” and drawn with a dotted line) and in `WHIZARD` (labelled “generator” and drawn with a dashed line). Left distributions are for electrons while distributions on the right are for muons.

C.4 Particle to reconstruction correlations

This section contains correlation histograms between objects defined ad particle-level and objects defined at reconstruction level.

C.4.1 Leptons

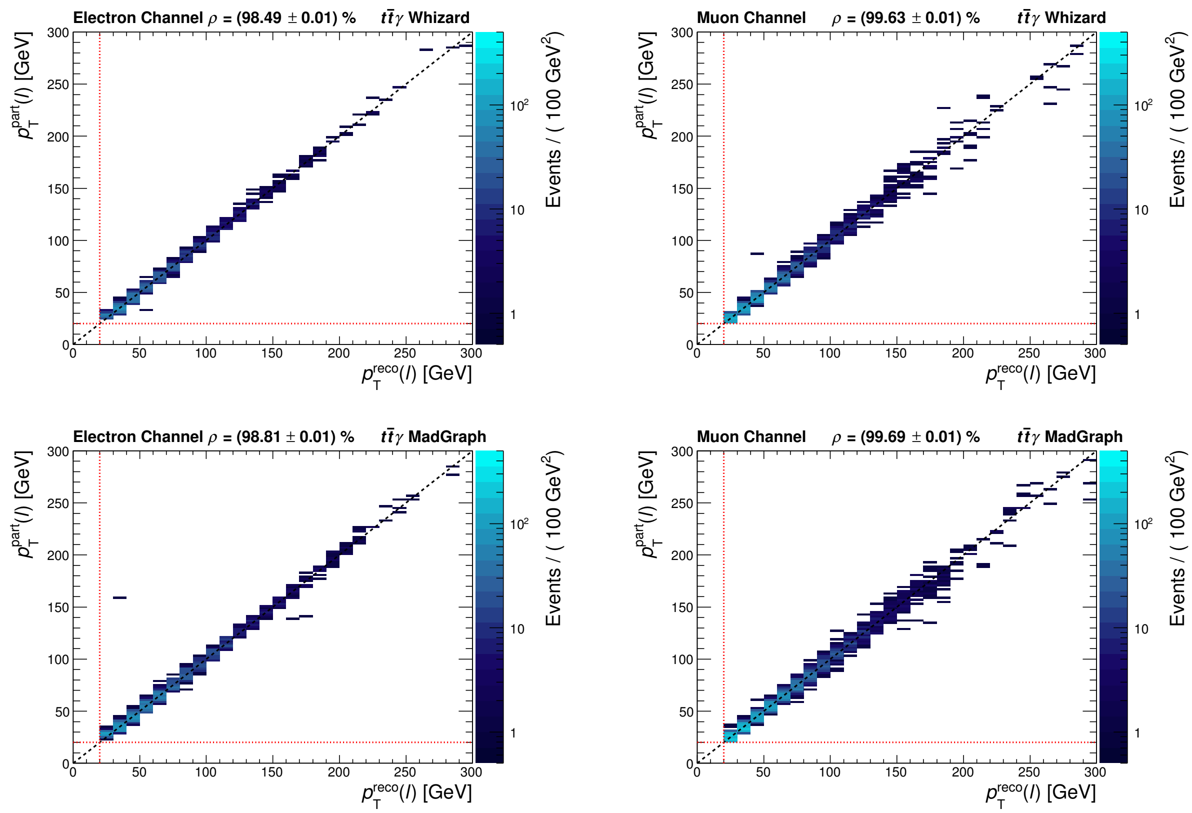

Figure C.10: Correlation histogram between reconstructed and particle level $p_{\mathrm{T}}(\ell)$. The dotted vertical line shows the reconstruction level cut, while the dotted horizontal line shows the cut at particle level. For both leptons (electrons shown on the left and muon on the right) a correlation above 90% is observed and the spread between the two quantities remains along the diagonal.

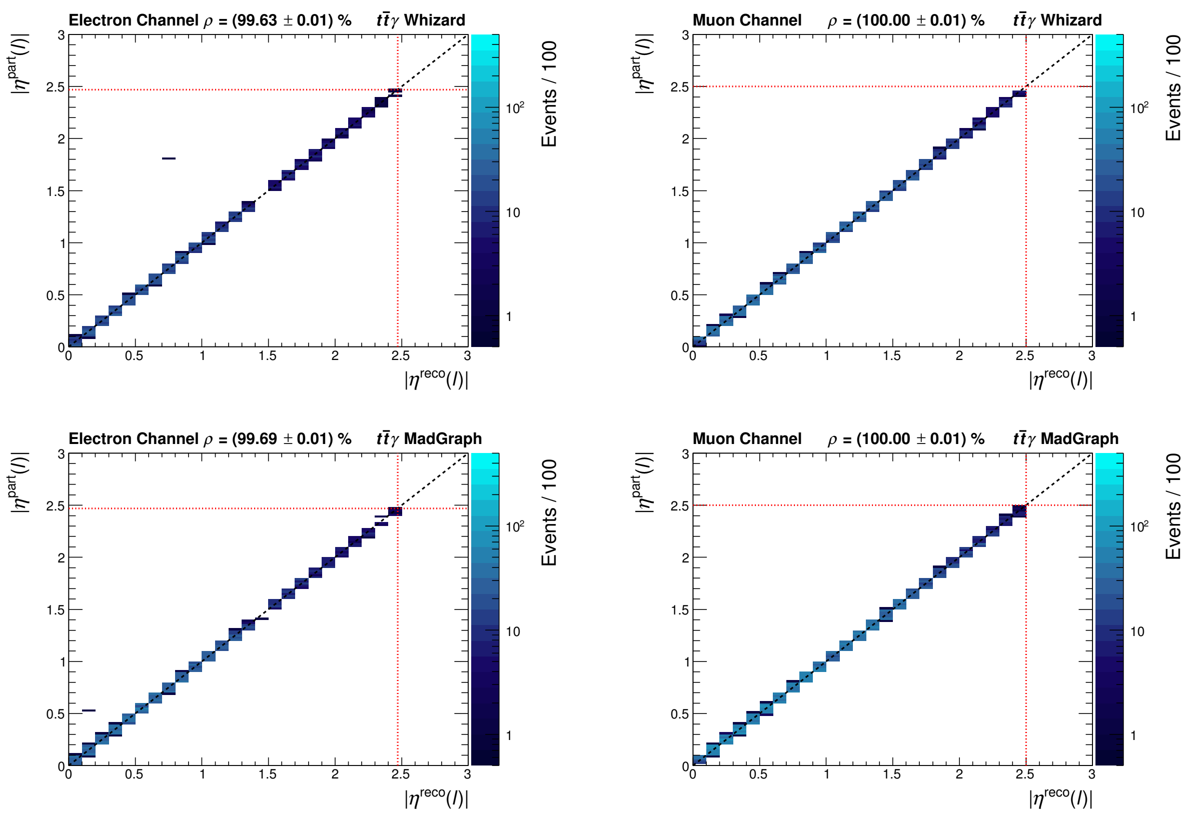

Figure C.11: Correlation histogram between reconstructed and particle level $\eta(\ell)$. The dotted vertical line shows the reconstruction level cut, while the dotted horizontal line shows the cut at particle level. For both leptons (electrons shown on the left and muon on the right) a correlation above 90% is observed and the spread between the two quantities remains along the diagonal.

C.4.2 Jets

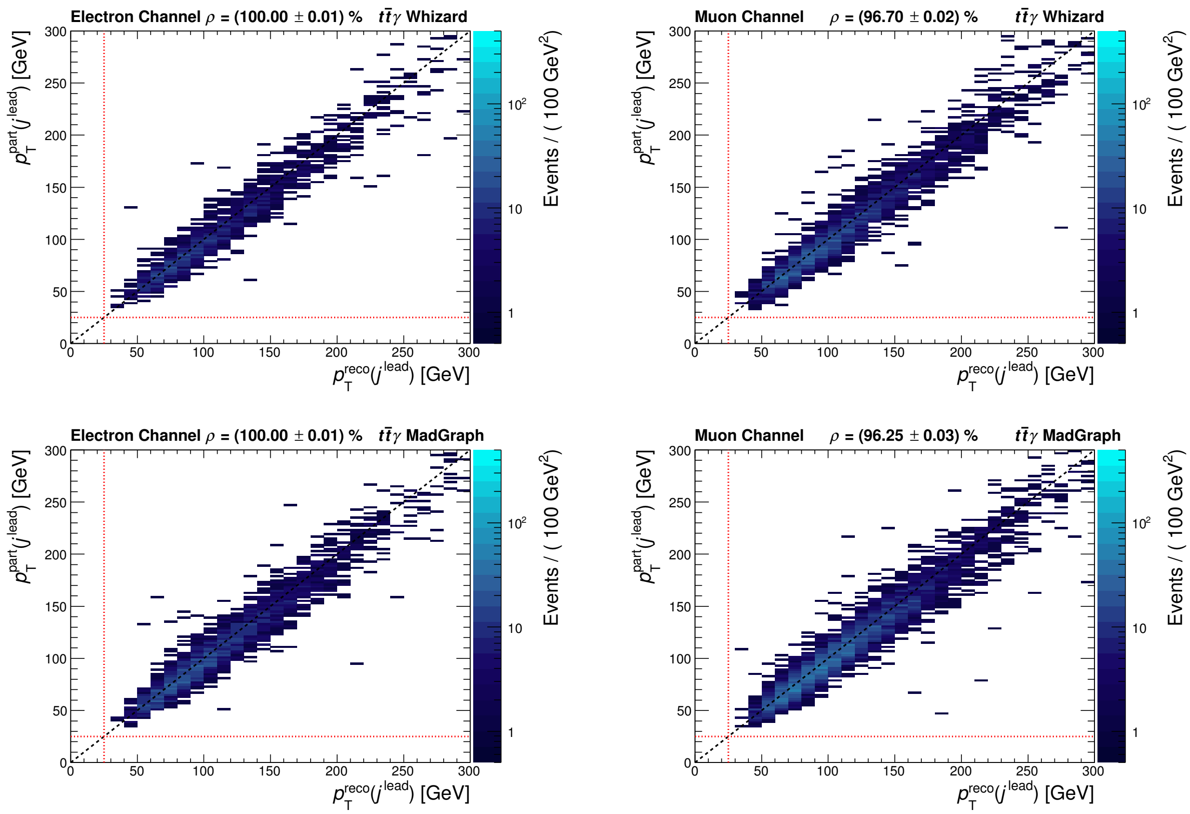

Figure C.12: Correlation histogram between reconstructed and particle level $p_{\mathrm{T}}(jl)$. The dotted vertical line shows the reconstruction level cut, while the dotted horizontal line shows the cut at particle level. For both leptons (electrons shown on the left and muon on the right) a correlation above 90% is observed and the spread between the two quantities remains along the diagonal.

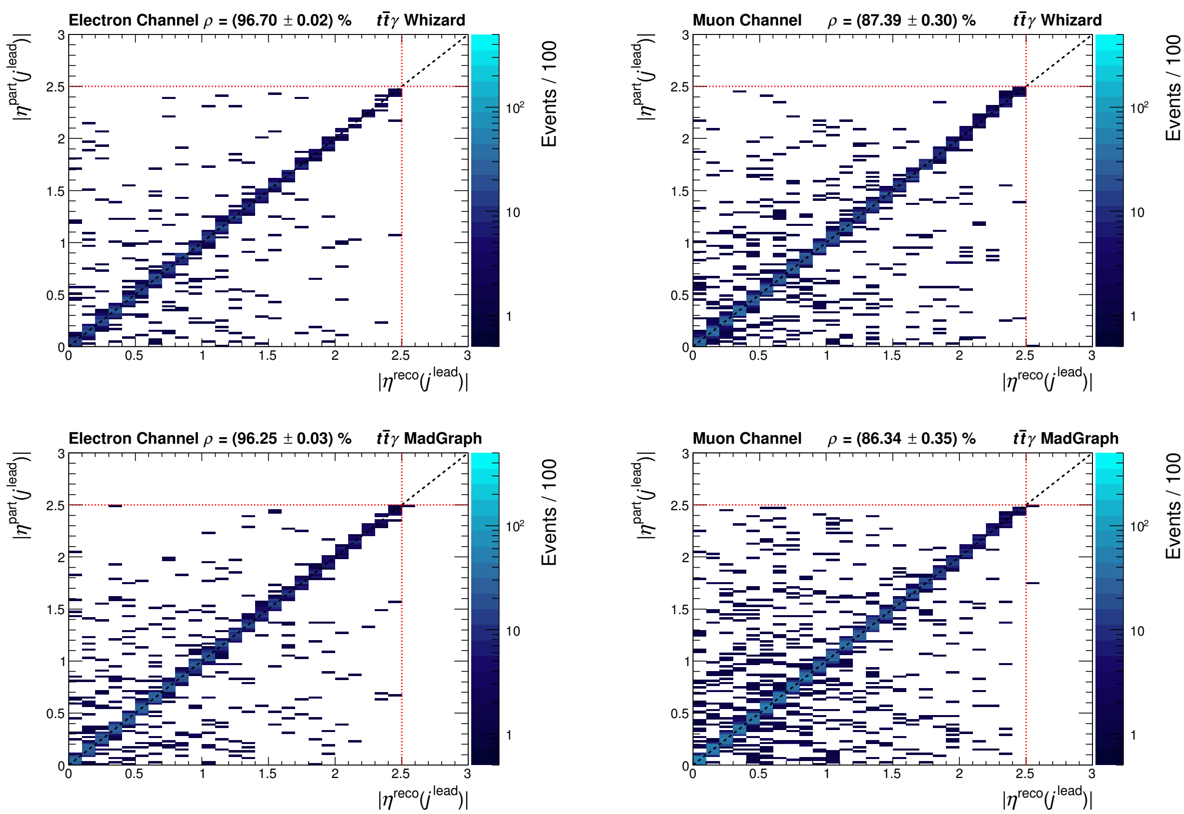

Figure C.13: Correlation histogram between reconstructed and particle level $\eta(j)$. The dotted vertical line shows the reconstruction level cut, while the dotted horizontal line shows the cut at particle level. For both leptons (electrons shown on the left and muon on the right) a correlation above 90% is observed and the spread between the two quantities remains along the diagonal.

C.4.3 Photons

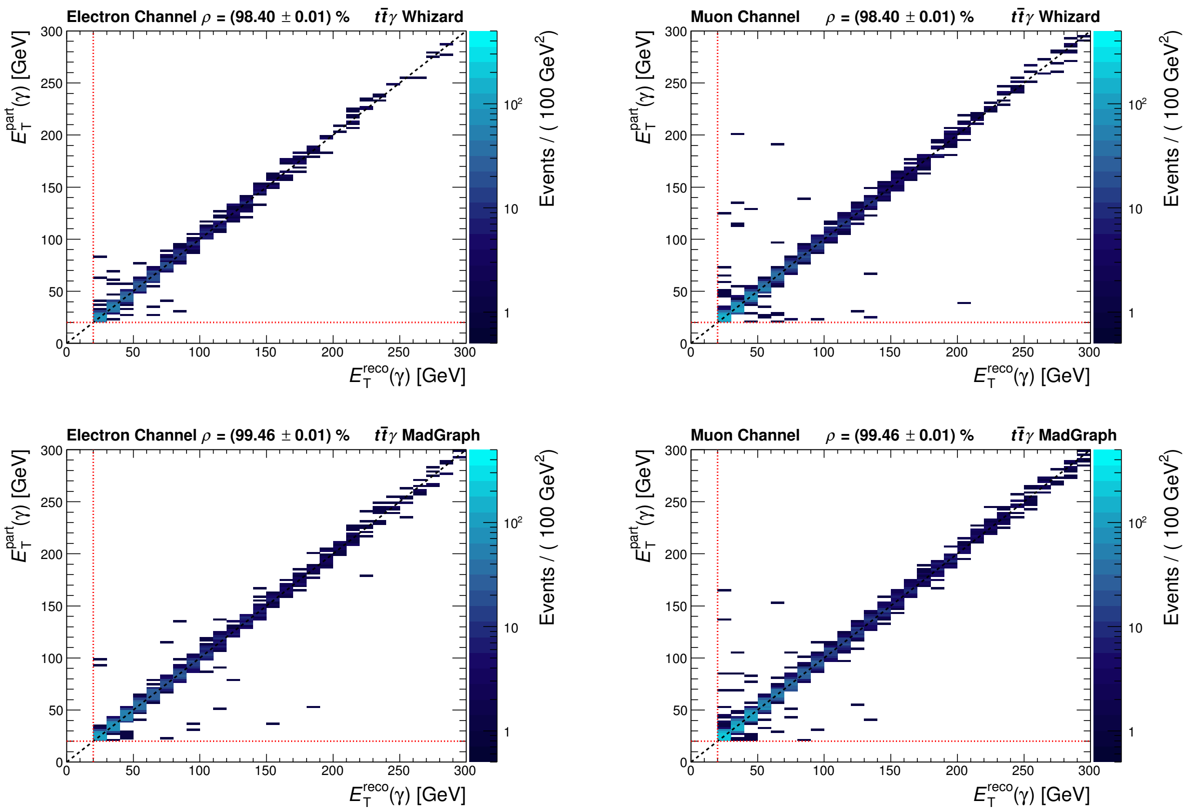

Figure C.14: Correlation histogram between reconstructed and particle level for photon kinematics. The dotted vertical line shows the reconstruction level cut, while the dotted horizontal line shows the cut at particle level. For both leptons (electrons shown on the left and muon on the right) a correlation above 90% is observed and the spread between the two quantities remains along the diagonal.

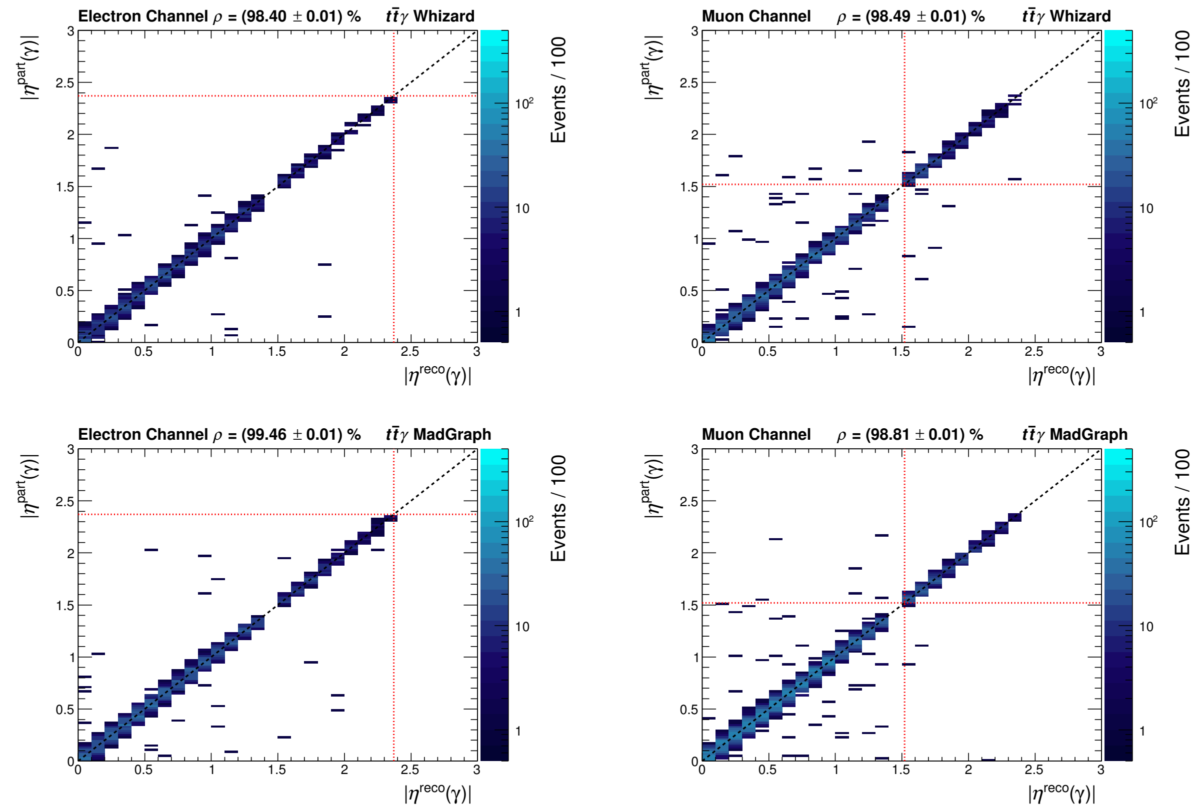

Figure C.15: Correlation histogram between reconstructed and particle level for photon kinematics. The dotted vertical line shows the reconstruction level cut, while the dotted horizontal line shows the cut at particle level. For both leptons (electrons shown on the left and muon on the right) a correlation above 90% is observed and the spread between the two quantities remains along the diagonal.

C.5 Efficiencies and event migrations

C.5.1 Efficiencies evaluated with The WHIZARD simulation sample

Range 20GeV $< E_{\mathrm{T}}(\gamma) \leq$ 30GeV

$$\left(\begin{array}{c|cc} - & \text{Pass Reco} & \text{Fail Reco} \\ \hline \text{Pass Particle} & 0.347\%(e)\ 0.642\%(\mu) & 4.07\%(e)\ 3.51\%(\mu) \\ \text{Fail Particle} & 0.178\%(e)\ 0.353\%(\mu) & 95.4\%(e)\ 95.7\%(\mu) \end{array}\right) \tag{C.1}$$

Range 30GeV $< E_{\mathrm{T}}(\gamma) \leq$ 40GeV

$$\left(\begin{array}{c|cc} - & \text{Pass Reco} & \text{Fail Reco} \\ \hline \text{Pass Particle} & 0.462\%(e)\ 0.918\%(\mu) & 3.97\%(e)\ 3.34\%(\mu) \\ \text{Fail Particle} & 0.239\%(e)\ 0.426\%(\mu) & 95.3\%(e)\ 95.5\%(\mu) \end{array}\right) \tag{C.2}$$

Range 40GeV $< E_{\mathrm{T}}(\gamma) \leq$ 50GeV

$$\left(\begin{array}{c|cc} - & \text{Pass Reco} & \text{Fail Reco} \\ \hline \text{Pass Particle} & 0.549\%(e)\ 1.07\%(\mu) & 3.53\%(e)\ 3.21\%(\mu) \\ \text{Fail Particle} & 0.273\%(e)\ 0.552\%(\mu) & 95.7\%(e)\ 94.9\%(\mu) \end{array}\right) \tag{C.3}$$

Range 50GeV $< E_{\mathrm{T}}(\gamma) \leq$ 70GeV

$$\left(\begin{array}{c|cc} - & \text{Pass Reco} & \text{Fail Reco} \\ \hline \text{Pass Particle} & 0.666\%(e)\ 1.11\%(\mu) & 4.02\%(e)\ 3.34\%(\mu) \\ \text{Fail Particle} & 0.336\%(e)\ 0.722\%(\mu) & 95\%(e)\ 94.7\%(\mu) \end{array}\right) \tag{C.4}$$

Range 70GeV $< E_{\mathrm{T}}(\gamma) \leq$ 120GeV

$$\left(\begin{array}{c|cc} - & \text{Pass Reco} & \text{Fail Reco} \\ \hline \text{Pass Particle} & 1.01\%(e)\ 1.68\%(\mu) & 5.09\%(e)\ 3.91\%(\mu) \\ \text{Fail Particle} & 0.442\%(e)\ 0.85\%(\mu) & 93.5\%(e)\ 93.6\%(\mu) \end{array}\right) \tag{C.5}$$

Range 120GeV $< E_{\mathrm{T}}(\gamma) \leq$ 180GeV

$$\left(\begin{array}{c|cc} - & \text{Pass Reco} & \text{Fail Reco} \\ \hline \text{Pass Particle} & 1.57\%(e)\ 3\%(\mu) & 6.77\%(e)\ 5.49\%(\mu) \\ \text{Fail Particle} & 0.768\%(e)\ 1.24\%(\mu) & 90.9\%(e)\ 90.1\%(\mu) \end{array}\right) \tag{C.6}$$

Range 180GeV $< E_{\mathrm{T}}(\gamma) \leq$ 250GeV

$$\left(\begin{array}{c|cc} - & \text{Pass Reco} & \text{Fail Reco} \\ \hline \text{Pass Particle} & 1.87\%(e)\ 3.8\%(\mu) & 7.31\%(e)\ 6.38\%(\mu) \\ \text{Fail Particle} & 0.878\%(e)\ 1.52\%(\mu) & 89.9\%(e)\ 87.5\%(\mu) \end{array}\right) \tag{C.7}$$

Range 250GeV $< E_{\mathrm{T}}(\gamma) \leq$ 300GeV

$$\left(\begin{array}{c|cc} - & \text{Pass Reco} & \text{Fail Reco} \\ \hline \text{Pass Particle} & 0.924\%(e)\ 5.08\%(\mu) & 10.4\%(e)\ 6.7\%(\mu) \\ \text{Fail Particle} & 1.15\%(e)\ 1.39\%(\mu) & 87.5\%(e)\ 88\%(\mu) \end{array}\right) \tag{C.8}$$

Range $E_{\mathrm{T}}(\gamma) >$ 300GeV

$$\left(\begin{array}{c|cc} - & \text{Pass Reco} & \text{Fail Reco} \\ \hline \text{Pass Particle} & 3.12\%(e)\ 5.04\%(\mu) & 9.59\%(e)\ 6.24\%(\mu) \\ \text{Fail Particle} & 1.44\%(e)\ 1.2\%(\mu) & 85.9\%(e)\ 88.2\%(\mu) \end{array}\right) \tag{C.9}$$

APPENDIX D

Statistics and method validation

D.1 Breakdown of systematic uncertainties

The profile likelihood ratio $\lambda_s(p_{\mathrm{T}}^{\mathrm{iso}} \,|\, \sigma_{t\bar{t}\gamma})$ as defined in eq. 5.34 includes the correlation between the different systematic uncertainties and the confidence interval is extracted for the total amount of uncertainty. However, it is of interest to determine the relative strength of each systematic component to the total uncertainty of the cross section.

D.1.1 Naive approach

The first approach to be considered is the most naive. Only the unconstrained likelihood is considered, *i.e.* no nuisance parameters are included. The signal efficiency (or the corresponding background yield, or any template) is shifted by $\pm 1\sigma$ of corresponding uncertainty. Ensemble tests are created using pseudo-experiments, in order to minimise the stochastic fluctuations. The mean of the distribution of *estimates* is considered for the ensembles with varied parameters (μ_{sys}) as well as the mean from the ensembles with nominal parameter values (μ_{nom}). The component uncertainty is measured as the difference $\mu_{\mathrm{sys}} - \mu_{\mathrm{nom}}$. Figure D.1 shows the estimated effect of two uncertainties (jet energy scale and photon energy scale).

However, this breakdown does not correspond to the modelling (propagations and correlations) included in the likelihood and provides only the total uncorrelated effect of the uncertainties. The correlated effect could be obtained by analytical evaluation of all correlations *post* estimation. This has shortcomings, as the correlation between parameters is not simple and the phase-space dependence on $p_{\mathrm{T}}^{\mathrm{iso}}$ of each variable has to be determined. While this type of breakdown remains useful for an eventual combination with another measurement, it fails to give the total strength of each uncertainty to the cross section. Therefore, this naive method is discarded.

D.1.2 Likelihood approach

An approach, including all parameter correlations, is possible. Two initial cases were considered, but finally discarded for the reasons explained below. In the two cases considered, the evaluation

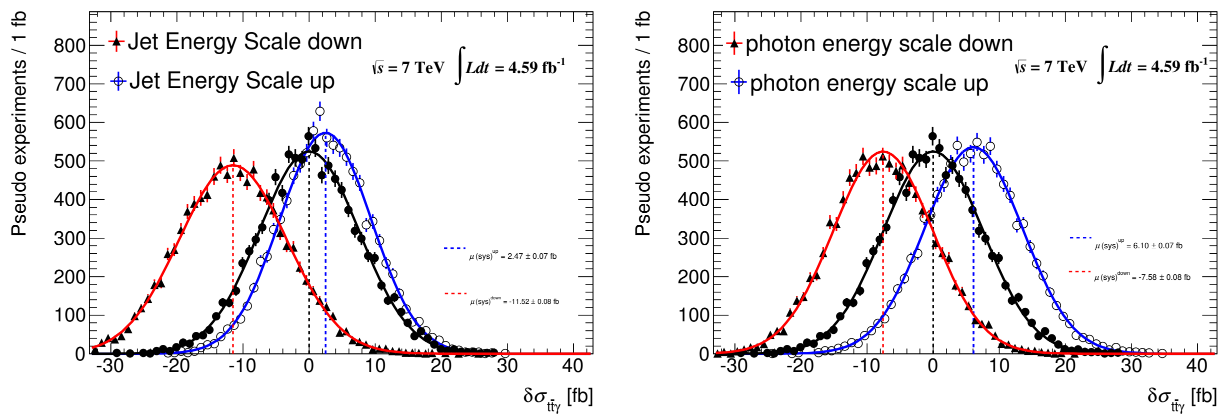

Figure D.1: Estimation of the strength of the jet (photon) energy scale uncertainty. The estimation was performed using pseudo-experiments and by shifting the $t\bar{t}\gamma$ efficiency to the corresponding uncertainty. The closed round markers correspond to the statistical uncertainty on $\sigma_{t\bar{t}\gamma}$. For all distribution the continuous lines correspond to a normal distribution best fit. The vertical dotted lines correspond to the mean as estimated from the fit. The half difference to the nominal mean corresponds to the effect of the systematic variation to the cross section.

was be based on data and not on pseudo-experiments.

For the first method, the breakdown is achieved by minimising a new profile likelihood ratio for each systematic component, in which the corresponding nuisance parameter is kept fixed to its maximum likelihood estimate from the nominal fit (where the nuisance has been of course kept free to float). The 68% C.L. of each of these fits would then correspond to the total uncertainty excepting that of the systematic source associated to the fixed nuisance parameter. Denoting by $\delta\sigma^{\mathrm{tot}}_{t\bar{t}\gamma}$ the total uncertainty on the cross section, and by $\delta\sigma^{i}_{t\bar{t}\gamma}$ the total uncertainty excepting that of i-th systematic source, the breakdown of the latter $\delta\sigma^{\mathrm{syst},i}_{t\bar{t}\gamma}$ would correspond to :

$$\delta\sigma^{\mathrm{syst},i}_{t\bar{t}\gamma} = \sqrt{(\delta\sigma^{\mathrm{tot}}_{t\bar{t}\gamma})^2 - (\delta\sigma^{i}_{t\bar{t}\gamma})^2} \tag{D.1}$$

In each i-th fit, the remaining nuisances are allowed to float. Therefore, absorbing the correlation with the i-th nuisance parameter, which is fixed. The quadratic summation of all terms is possible. Although fixing multiple nuisances at once (by defining groups of mostly correlated parameters) is possible, it was chosen to fix only one nuisance parameter in each fit for simplicity. An example of the complete breakdown in shown in Fig. D.2. The total systematic uncertainty from this profile approach, calculated as the quadratic sum of all terms, corresponds to the total uncertainty of the cross section.

However, this method has a shortcoming. While the breakdown is, statistically speaking, correct, it does not have a physical meaning. Each extracted component corresponds to an uncertainty, of which its definition is hidden. For example, the extracted decomposition of the jet energy scale uncertainty corresponds to the effect of the jet energy scale plus some phase-space dependence.

The phase-space of some uncertainties have similar, or identical, dependence on $p_{\mathrm{T}}^{\mathrm{iso}}$. Anti-correlations between the (remaining) nuisance parameters corresponding to uncertainties with similar shape can absorb portion of the differences. For example, a downwards shift of one compo-

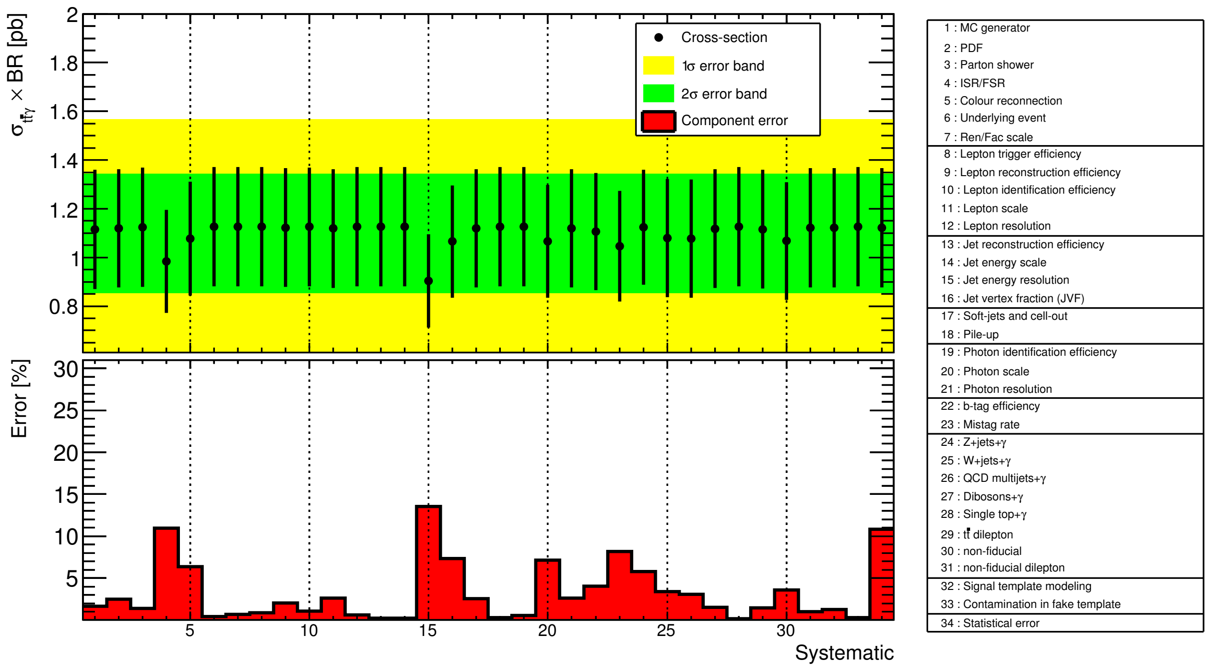

Figure D.2: Breakdown of systematic components via the profile likelihood method.

nent is compensated by an upwards shift of another one. The vast majority of nuisance parameters considered here are of a normalisation type, therefore their dependence on $p_{\mathrm{T}}^{\mathrm{iso}}$ is identical [1]

This is not necessarily a problem, since the quadrature sum of all components corresponds to the total, but the meaning of each component is dependent upon the parametrisation. However, this method demonstrates that the total uncertainty remains stable with respect to any arbitrarily chosen component breakdown.

For the second method, the breakdown is achieved by fixing in the likelihood all nuisance parameters but the one the strength of which needs determination. Each fit on data provides the quadrature sum of the statistical uncertainty and the component uncertainty. This method eliminates the phase-space dependence observed in the previous. Examples of the likelihood parabolas for different uncertainties are shown in Fig. D.3.

However, this method has also shortcomings. At each evaluation stage a different likelihood is used (all nuisance parameters, but the tested one, are fixed). This does not reflect the final likelihood, and some hidden model dependencies can be introduced. Also, this method is evaluated on data, and the statistical component needs to be quadratically extracted. This is feasible for uncertainties which have a large contribution, but for small variations the precision of the extracted component is degraded.

D.1.3 Final breakdown

The final method for determining the systematics breakdown while using the full likelihood, including all correlations is the following.

[1]The choice for the majority of uncertainties to be of a normalisation type is done on purpose, in order to avoid over constraints from the nuisance parameters themselves.

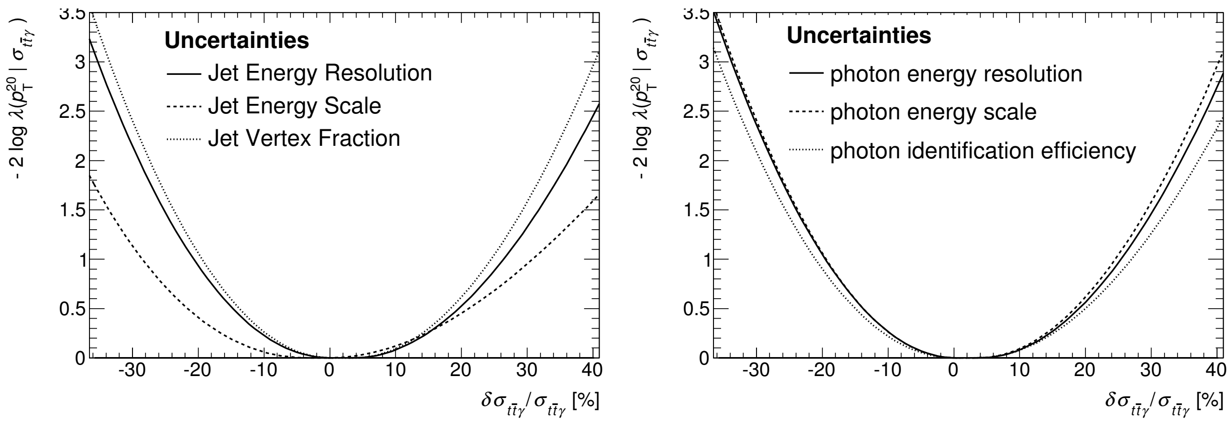

Figure D.3: Likelihood parabolas as evaluated with the inclusion of only a portion of nuisance parameters. Jet-related uncertainties are shown on the let. Photon-related uncertainties are shown on the right.

For each systematic i pseudo-data are generated from the full likelihood while keeping all parameters fixed (to their maximum likelihood *estimate*) but the $\theta_i(\alpha_i)$ corresponding nuisance parameter.

For each pseudo-data ensemble full fit is performed, in which all components are allowed to fluctuate. The variance of the distribution of the cross section *estimates* the sizes the effect of the component uncertainty. The distribution of the cross section *estimates* is typically a Gaussian probability density function (pdf) , but the construction remains valid without any assumption on the distribution type. The uncertainty extracted, because of the Gaussian approximation, is symmetric by construction. As an example, the extraction of the uncertainties related to the jet energy scale and to the photon energy scale are shown in Fig. D.4.

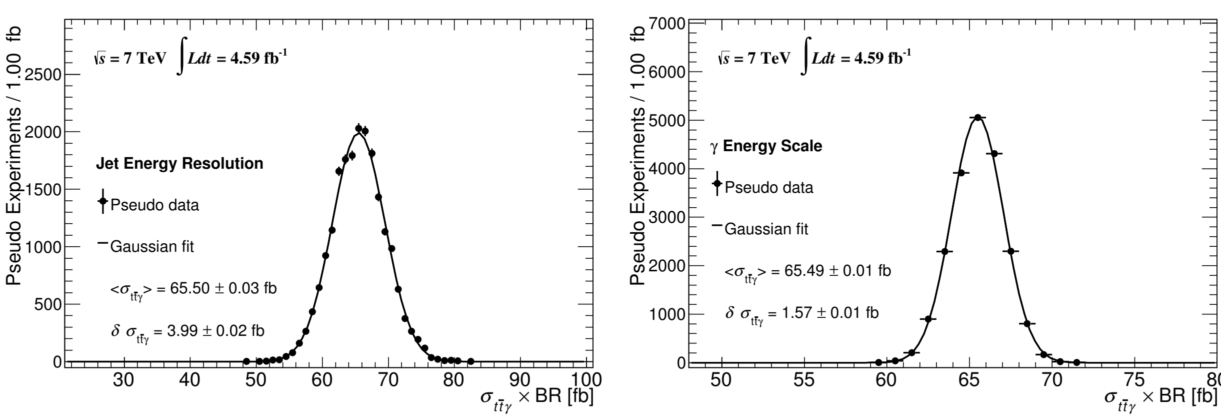

Figure D.4: Estimation of the strength of the jet (photon) energy scale uncertainty. The variance of each distribution corresponds to the uncertainty on the cross section of the component being evaluated.

It is found, that using this method, the quadratic sum of all components is about 21% which the same as the total uncertainty as extracted from the fit on data.

Component	**Uncertainty [%]**	
	Final method	**Naive**
Signal modelling		
Monte carlo generator	1.00	0.88
Parton density function	0.59	0.43
Parton shower	4.7	5.1
QED radiation	2.6	2.7
Colour reconnection	0.2	0.056
Underlying event	0.35	0.36
Renormalisation / factorisation scales	0.42	0.51
Lepton modelling		
Lepton trigger	0.86	0.74
Lepton reconstruction	0.47	0.39
Lepton identification	1.00	0.98
Lepton energy scale	0.33	0.27
Lepton energy resolution	0.19	0.09
Jet modelling		
Jet reconstruction efficiency	0.19	0.03
Jet energy scale	6.10	6.60
Jet energy resolution	2.90	1.80
Jet vertex fraction	1.10	1.10
$E_{\mathrm{T}}^{\mathrm{miss}}$ **modelling**		
Cell out	0.2	0.03
Pileup	0.27	0.25
Photon modelling		
Photon identification efficiency	3.0	3.3
Photon energy scale	1.1	1.2
Photon energy resolution	1.6	1.7
b**-tagging modelling**		
b-tagging efficiency	3.4	3.6
Misstag probability	0.29	0.26
e/γ **background modelling**		
$Z\gamma + \text{jets}$	2.60	0.78
$W\gamma + \text{jets}$	2.90	3.00
Multijets+γ	1.20	0.98
Single top+γ	1.30	0.28
Dibosons+γ	0.20	0.19
$e \to \gamma$ missidentification	3.50	2.70
Template modelling		
Hadron fake template	3.50	3.70
Prompt photon template	8.10	6.60
Total Systematic	14.6	13.4
Statistical	11.6	
Total Stat$\oplus$ Sys	18.6	17.7

Table D.1: Comparison of the systematic component break down using the profiled approach and the "naive" approach of Sec. D.1.1. The propagation and correlation of the nuisance parameters in the profiled approach is set to match that of Sec. D.1.1. The total uncertainty, as a quadrature sum of all components, is in good agreement between the two methods.

As a validation test, this method has been applied to a likelihood with no constraints. The results are compared to that of the naive method. The quadrature sum of all components for each method is found to be in agreement. The full comparison can be found in Tab. D.1

D.2 Fit method validation

In this section, a series of validations tests are presented, which are meant to prove the robustness of the result.

D.2.1 Stability with respect to background fluctuations

An interesting cross-check on the fit stability against small background changes has been done by performing subsequent fits after removing a particular background component. Table D.2 shows the variation of the resulting cross section after removal of a specific background with respect to the nominal fit (all other background sources remain included).

Omitted background	$\delta\sigma_{t\bar{t}\gamma}/\sigma_{t\bar{t}\gamma}$ **[%]**	**Significance [σ]**	$\widetilde{N}^i_{\mathrm{b}}$ **[events]**	N^i_{b} **[events]**
$t\bar{t}(e \to \gamma$ misidentification)	24.0 ± 0.2	6.8	34.8	38.6
$W\gamma + \text{jets}$	15.8 ± 0.2	6.3	21.7	26.0
Multijets+γ	2.5 ± 0.17	5.3	4.6	4.0
Single top+e/γ	7.7 ± 0.16	5.9	7.7	8.7
Dibosons+e/γ	0.4 ± 0.17	5.1	0.7	0.4
Ze/γ+jets	17.3 ± 0.15	6.5	13.6	11.0

Table D.2: Cross section variations by subsequently removing an e/γ background component. The biggest effect is reached for $W\gamma + \text{jets}$ and for the $e \to \gamma$ misidentification. For the smallest contributions such as single top+γ, dibosons+γ the effect remains negligible. The difference of the extracted number of signal events with respect to the nominal fit result ($\widetilde{N}^i_{\mathrm{b}}$) is compared with respect to the omitted background component (N^i_{b}).

In each fit, all systematics uncertainties have been included excepting those associated with the omitted background. The observed variations in the cross section are consistent with the expectations: small background contributions (dibosons+γ, multijets+γ) result in small variations in the cross section while the largest variations result from the dominant backgrounds ($W\gamma + \text{jets}$ and $e \to \gamma$). Furthermore, the omitted background $\widetilde{N}^i_{\mathrm{b}}$, as estimated from the extracted cross section difference with respect to the nominal, corresponds to the omitted input (within statistical uncertainties).

D.2.2 Linear response from the fit as a function of the efficiency

The template likelihood fit extracts the cross section as determined in Eq. 5.32. The number of signal events is extracted *post*-fit. The output of the cross section is expected to be linear with respect to the efficiency. This was tested using ensemble tests. Sets of independent events were generated using pseudo-experiments. For each ensemble the efficiency is increased by a constant factor. The mean cross section for each ensemble is extracted from a gaussian pdf fit on the distribution of the cross section *estimates.* Figure D.5 compares the relative cross section increase with respect to the increase of the efficiency. It can be seen that the relation is indeed linear.

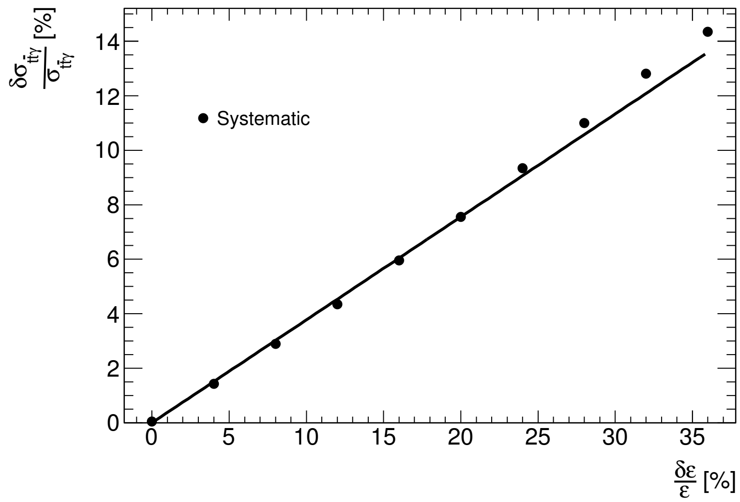

Figure D.5: Linear response of uncertainty on cross section against and increase of the efficiency. Each point corresponds to ensemble tests on 10^4 pseudo-experiments. The results are compared to a linear relationship (solid line).

D.2.3 Total cross section uncertainty variation with respect to the source

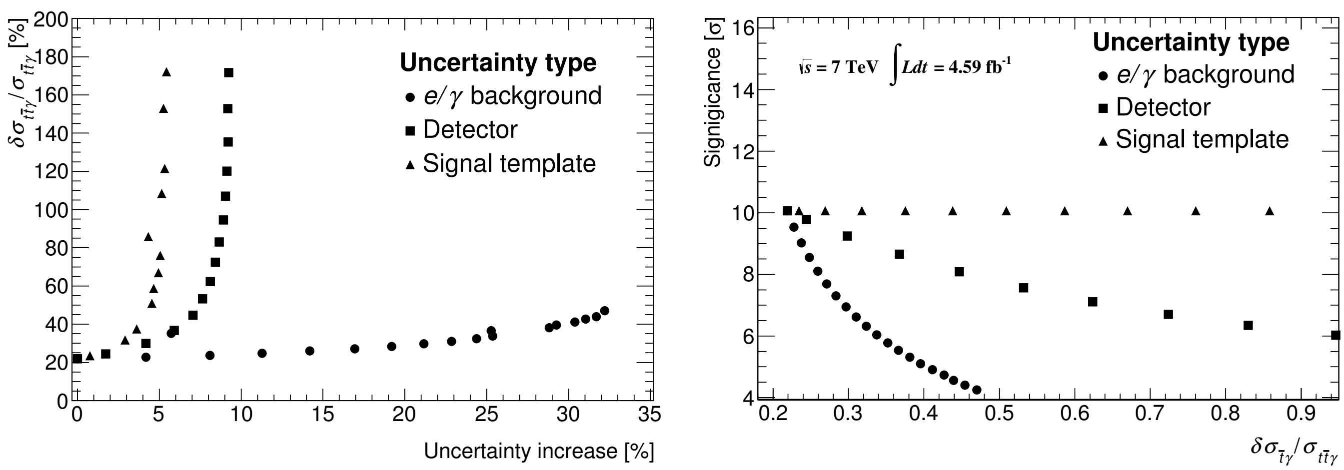

Figure D.6: The increase of the relative cross section uncertainty compared to the increase of the input uncertainty is shown on the left. The decrease of the signal significance with respect to the increase of the cross section uncertainty is shown on the right. Round markers correspond to an increase of the prompt-photon background uncertainty. Square markers correspond to an increase of the detector-type uncertainty (for example jet energy scale or the photon identification efficiency). Triangular markers correspond to an increase in uncertainty on the signal template (this is the prompt-photon template while being set to affect only the signal yield).

Because of its impact on the significance of the measurement, it is of interest to study how the cross section uncertainty varies with respect to different types of errors on the nuisance parameters.

The estimation of the cross section is repeated several times. At each step the input uncertainty on only a type of nuisance parameters is gradually increased. Three type of nuisance parameters are selected. The first corresponds to an increase to the uncertainty associated with the prompt like background (e/γ). The second corresponds to an increase of the detector related uncertainties. The third corresponds to an increase of the uncertainty affecting the prompt-photon template. For the last case, the propagation of the corresponding nuisance parameter is set to affect only the cross section, thus neglecting its effect on background-related parameters. This is done in order to see the uncorrelated effect of the signal template uncertainty on the cross section [2]. For this test no ensemble tests were performed, but each estimation was performed on the same data set. The statistical component of the uncertainty is not considered as it remains the same for each variation.

It can be seen in Fig. D.7 that the uncertainty on the cross section increases, as excepted, parabolically with respect to the increase of the input. However, the rate of increase is very different when comparing the three types of varied uncertainties. The rate is higher for the prompt-photon template and for the detector type of systematics. The e/γ backgrounds contribute in a less significant manner. However, when looking at the effect on the significance the situation is different (see Fig. D.7 right). There is no decrease in significance corresponding to an increase of the prompt-photon template systematic. This is excepted; when testing the no signal hypothesis $\sigma_{t\bar{t}\gamma} = 0$, any uncertainty affecting only the signal does not enter into consideration. The fastest rate of significance decrease is seen with the increase of the e/γ background uncertainty. This is also expected. The significance (Z), when signal and background have equal distributions, goes as

$$Z \simeq N_s \Big/ \sqrt{\sum_i N_{b_i} + \sigma_{b_i}} \tag{D.2}$$

with σ_{b_i} being the uncertainty on N_{b_i}. The signal and e/γ background distribute according to the same template shape and their distribution is concentrated ($> 80\%$) in the low $p_{\mathrm{T}}^{\mathrm{iso}}$ region. Therefore, a higher decrease in significance is expected from the uncertainty on the e/γ background than from the uncertainty affecting the entire $p_{\mathrm{T}}^{\mathrm{iso}}$ range.

Figure D.7 shows the relative increase of width of the likelihood parabola as for the three types of uncertainty considered in this test. It can be seen that in all cases the shape of the likelihood remains parabolic and the minima are all consistent with zero. This means that the increase of uncertainty does not bias the result.

D.2.4 Anomalous constraints from the simultaneous fit

Under the hypothesis that the $t\bar{t}\gamma$ cross section is the same for the electron channel and the muon channel, the likelihood of Eq. 5.32 extracts a common cross section simultaneously from both channels. Statistical fluctuations between the $p_{\mathrm{T}}^{\mathrm{iso}}$ distributions in the two channels, because of the small size of data, should not bias the cross section *estimate*. This has to be tested without any loss in the generality of the likelihood modelling, *i.e.* it must not be assumed *a priori* that the cross section for the two channels is the same. Several sources of systematic uncertainties are treated as being (fully) correlated between the two channels. However, a constraint on a nuisance parameter from one channel (and from data) should not absorb variations of the cross section. In other terms, the modelling of correlations between nuisance parameters should not absorb differences between the two channels in the observed distribution of $p_{\mathrm{T}}^{\mathrm{iso}}$ in data. The results reproduced by an

[2]This is not the case in the nominal fitting procedure, as changes in the prompt-photon template affect also the e/γ backgrounds.

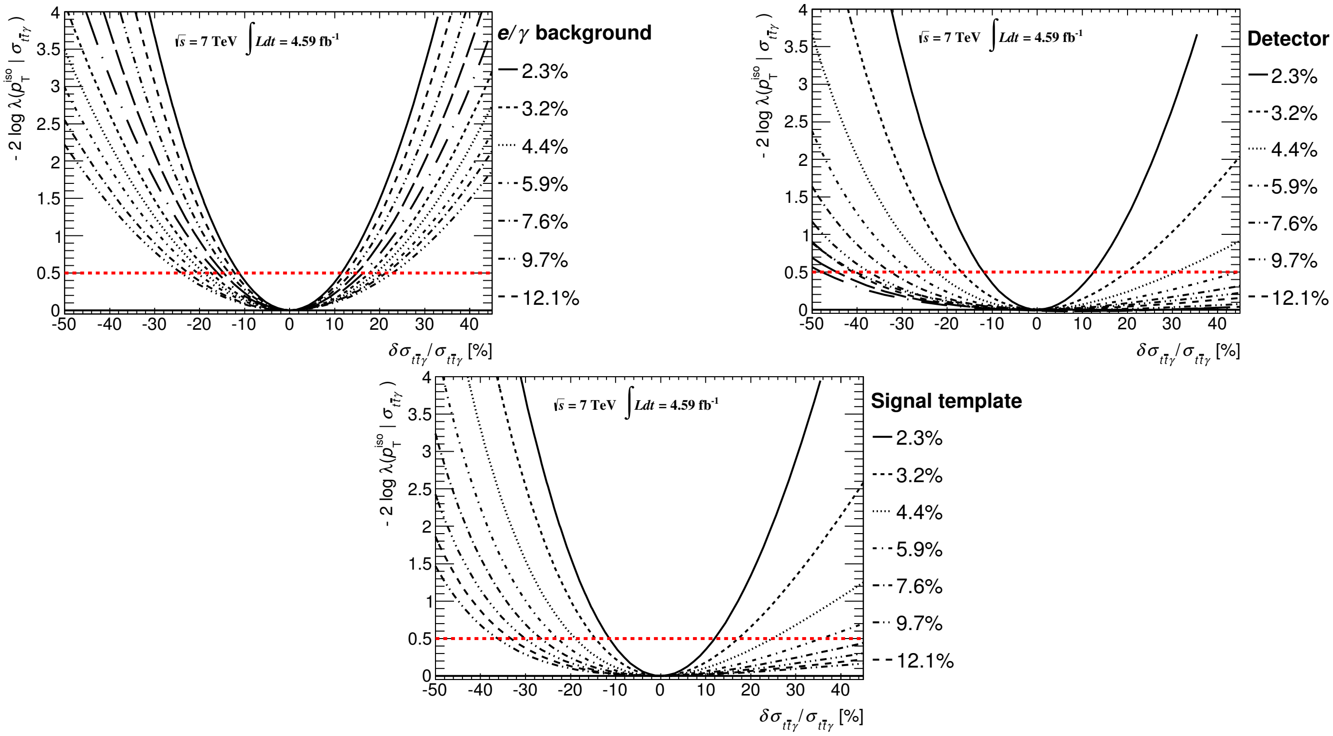

Figure D.7: Negative logarithm of the likelihood ratio as a function of the relative uncertainty on the cross section. Each plot shows the increase of the confidence interval with respect to an increase in uncertainty of each (labelled) nuisance parameter.

anomalous modelling of the response function of Eq. 5.28 can be very similar to that of a different cross section for each channel. This has to be tested while including the full likelihood function with all nuisance parameters (that are allowed to vary) in their final configuration. Testing this can be difficult to achieve *per-se* because shape differences in the $p_{\mathrm{T}}^{\mathrm{iso}}$ data distribution originated by statistical fluctuations can mask both an irregular modelling of the likelihood and a difference in the cross sections.

An informative test is a fit in the combination of the two channels while leaving both the electron channel cross section and the muon channel cross section free to float.

The test is based upon the comparison from (i) the channel independent fits, (ii) a simultaneous fit to both channels with a common cross section, and (iii) a simultaneous fit with two independent cross sections. All the of the above estimations are performed by both excluding variations due to systematic uncertainties (by fixing the nuisance parameters to their nominal value) and including systematic uncertainties (by allowing the nuisance parameters them to vary). Table D.3 shows the extracted cross sections and the number of events from the different type of fits.

Channel independent fits without the inclusion of systematics have no constrain. Channel independent fits with the inclusion of systematics have an increased constrain on the cross section (because of the nuisance parameters) but no constrain between channels. Simultaneous fits without the inclusion of systematic uncertainties have only a constraint from data between channels, because of the shape differences of the track-isolation distribution. The simultaneous fit with the inclusion of systematic uncertainties, but with to independent cross sections has an constrain

			Electron channel						
Case			Signal		Backgrounds		Totals		
Simultaneous	$\sigma^{e}_{t\bar{t}\gamma} = \sigma^{mu}_{t\bar{t}\gamma}$	**Has Sys**	$\sigma_{t\bar{t}\gamma}$ [fb]	N_{s} [events]	$N_{\mathrm{b}}^{e/\gamma}$ [events]	$N_{\mathrm{b}}^{\mathrm{had.\ fakes}}$ [events]	$\sum_i N_{\mathrm{b^i}}$ [events]	N
✓	✓	✓	63	52	41	38	79	131
✓	Two equal parameters	✓	63	52	41	38	79	131
✓	✗	✓	79	65	40	34	74	139
✓	✗	✗	77	63	41	33	74	137
✓	✓	✗	62	50	41	38	79	129
✗	✗	✓	76	62	41	34	74	137
✗	✗	✗	77	63	41	33	74	137
Data candidates			-	-	41	-	-	140
			Muon channel					
Case			**Signal**		**Backgrounds**		**Totals**	
Simultaneous	$\sigma^{e}_{t\bar{t}\gamma} = \sigma^{mu}_{t\bar{t}\gamma}$	**Has Sys**	$\sigma_{t\bar{t}\gamma}$ [fb]	N_{s} [events]	$N_{\mathrm{b}}^{e/\gamma}$ [events]	$N_{\mathrm{b}}^{\mathrm{had.\ fakes}}$ [events]	$\sum_i N_{\mathrm{b^i}}$ [events]	N
✓	✓	✓	63	100	65	55	120	220
✓	Two equal parameters	✓	63	100	65	55	120	220
✓	✗	✓	57	90	65	58	123	214
✓	✗	✗	55	87	66	58	124	211
✓	✓	✗	62	98	66	54	121	218
✗	✗	✓	55	87	66	58	124	211
✗	✗	✗	55	87	66	58	124	211
Data candidates			-	-	66	-	-	222

Table D.3: Results from the channel independent and simultaneous fits, with and without the inclusion of systematic uncertainties and with and without a common parameter for the cross section. The results are shown separately for the electron (top) and muon (bottom) channels. For each channel the first line shows the result from the nominal likelihood fit. The remainder items are shown with decreasing (cross channel) constrain to the cross section.

across channels, but the added degree of freedom (two independent cross sections) has to absorb eventual differences in $p_{\mathrm{T}}^{\mathrm{iso}}$. The results are shown with decreasing order of modelling constraint. It can be seen in Tab. D.3 that with increasing constraint the results evolve accordingly without an absorption of changes due to nuisance parameters shifts.

The absence of absorption from the nuisance parameters can be also seen in Fig. D.8, where the pull of nuisance parameters is consistent with mean zero and variance one. It was concluded that the fit is very stable since no differences on the extracted cross sections were seen.

D.2.5 Closure

The binning of the track isolation distributions is optimised based on the expected statistical uncertainty on the number of $t\bar{t}\gamma$ events for different binning options, see App. D.2.6. The final choice of five binsis however not sufficient for a complete goodness of fit test.

In order to conclusively check for any existing bias in the fit procedure, a closure test is performed using ensemble tests. A set of 10^4 pseudo-experiments, each containing the same amount of event candidates as observed in data, was generated. Nuisance parameters are smeared randomly according to their defining pdf. This is achieved by randomising the corresponding observable (for example,θ_i for $\hat{\theta}_i$). For each pseudo-experiment, template fits are performed and a $t\bar{t}\gamma$ cross section is calculated. Fig. D.9 shows the pull distribution of the cross-section, with the

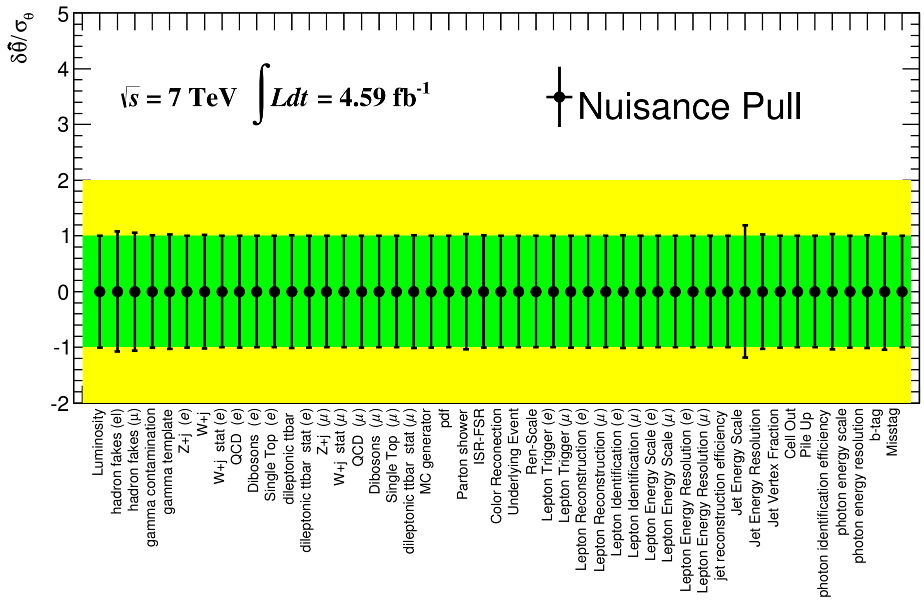

Figure D.8: Pull of nuisance parameters representing systematic uncertainties after incorporation of correlations across channels while performing a fit with an independent cross sections for each channel. All points are consistent with mean 0 and error of one gaussian standard deviation

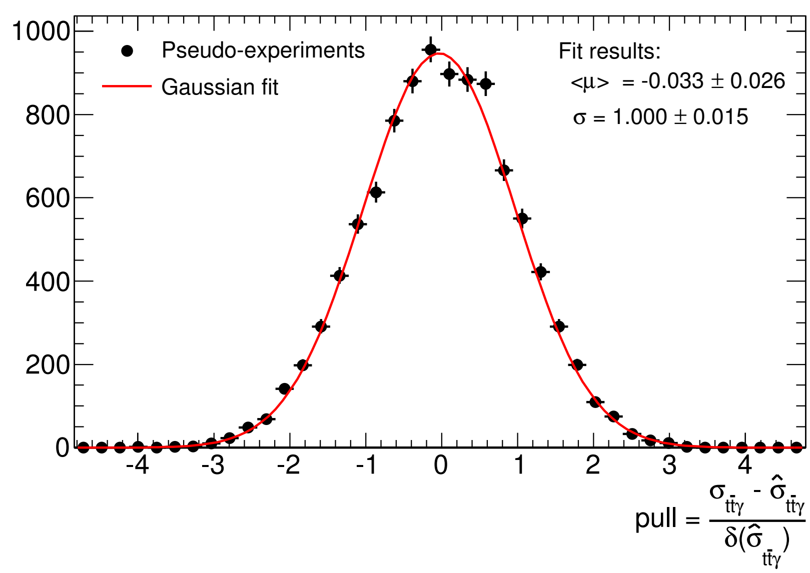

Figure D.9: Pull of the $t\bar{t}\gamma$ cross-section as obtained from 10^4 pseudo-experiments.

pull being defined for each pseudo-experiment as

$$\text{pull}\left(\sigma_{t\bar{t}\gamma}\right) = \frac{\sigma^{\star}_{t\bar{t}\gamma} - \hat{\sigma}_{t\bar{t}\gamma}}{\delta(\hat{\sigma}_{t\bar{t}\gamma})}$$

where $\sigma^{\star}_{t\bar{t}\gamma}$ is the generated cross section, and $\hat{\sigma}_{t\bar{t}\gamma}$ and $\delta(\hat{\sigma}_{t\bar{t}\gamma})$ are respectively its estimate and uncertainty as extracted from the combined likelihood fit. The resulting distribution is well compatible with a Gaussian of zero mean and unit width.

D.2.6 Track-isolation distribution binning.

The choice of the binning of $p_{\mathrm{T}}^{\mathrm{iso}}$ may potentially influence the sensitivity of the extracted cross section. The binning was chosen [164] such that the number of *hadron-fakes* is equal in each bin with $p_{\mathrm{T}}^{\mathrm{iso}} > 3$ GeV. It is $[0,1[$ GeV, $[1,3[$ GeV, $[3,5[$ GeV, $[5,10[$ GeV, and $[10\ \mathrm{GeV},\infty[$.

However, different binning options were considered [86]. Ensembles of 10^4 pseudo experiments were generated and the statistical uncertainty on the cross section was compared for different binning choices. Results are shown in Tab. D.4.

Binning		$\delta\sigma_{t\bar{t}\gamma}/\sigma_{t\bar{t}\gamma}[\%]$ **stat**
Type	**Width [GeV]**	
Uniform	1	9.4%
Uniform	2	9.3%
Uniform	4	9.9%
Uniform	5	10.8%
Uniform	10	15.4%
Variable	$[0,1[$, $[1,2[$, $[2,3[$, $[3,5[$, $[5,10[$, $[10,\infty$	9.1%
Variable	$[0,1[$, $[1,3[$, $[3,5[$, $[5,10[$, and $[10,\infty[$	8.9%

Table D.4: The statistical uncertainty on $\sigma_{t\bar{t}\gamma}$ is compared to various binning options for $p_{\mathrm{T}}^{\mathrm{iso}}$ [86].

The statistical uncertainty increases with a coarser binning. It can also be seen that the final choice corresponds to the smallest uncertainty.

D.3 Photon isolation and template truncation

Although theoretical calculations of the cross section typically request photons being isolated objects [122], introducing in this analysis an explicit cut on the photon isolation would eliminate the shape discrimination between signal and background templates, thus rendering the signal extraction via the profile likelihood impossible. In this section an alternative solution is investigated. The signal binned probability is reformulated by setting the probability of observing a photon with an isolation higher than a given cut value, $C(p_{\mathrm{T}}^{\mathrm{iso}})$, equal to zero:

$$T_{\mathrm{sig}}^{\mathrm{trunc}}(p_{\mathrm{T}}^{\mathrm{iso}}|\gamma) = \begin{cases} \dfrac{T_{\mathrm{sig}}^{\mathrm{nom}}(p_{\mathrm{T}}^{\mathrm{iso}}|\gamma)}{\int_0^C T_{\mathrm{sig}}^{\mathrm{nom}}(p_{\mathrm{T}}^{\mathrm{iso}}|\gamma)\, dp_{\mathrm{T}}^{\mathrm{iso}}} & \text{if} \quad 0\ \mathrm{GeV} < p_{\mathrm{T}}^{\mathrm{iso}} \leq C \\ 0 & \text{if} \quad p_{\mathrm{T}}^{\mathrm{iso}} > C \end{cases} \tag{D.3}$$

where $T_{\mathrm{sig}}^{\mathrm{nom}}(p_{\mathrm{T}}^{\mathrm{iso}})$ is the nominal signal template. The truncated template is equivalent to an isolation cut, however applied for prompt-photons only. Hadrons, and hadron decay products, possess a distribution different that zero across the entire $p_{\mathrm{T}}^{\mathrm{iso}}$ range. Therefore, the usage of the truncated signal template allows for a signal to background shape discrimination. The number of signal events as extracted from the fit are considered (by construction) isolated.

D.3.1 Results

The extracted number of signal and background events are presented in table D.5. As expected, by using the truncated template the number of signal events decreases. The relative change of ∼10% in the signal events directly translates into an increase in the number of background events by roughly this same amount. When using the truncated template, the cross section decreases by ∼9% with respect to the cross section obtained with the nominal template.

Parameter	**Truncated template**	**Nominal template**
N_s	183 ± 19 events	201 ± 21 events
$\sum_i N_{b_i}$	237 ± 16 events	213 ± 17 events
$\sigma_{t\bar{t}\gamma}$	$1.15 \pm 0.12\,[\mathrm{pb}]$	$1.26 \pm 0.14\,[\mathrm{pb}]$

Table D.5: Number of signal and background events, and $\sigma_{t\bar{t}\gamma}$ cross section, as obtained with both the nominal and truncated signal templates. All uncertainties are statistical.

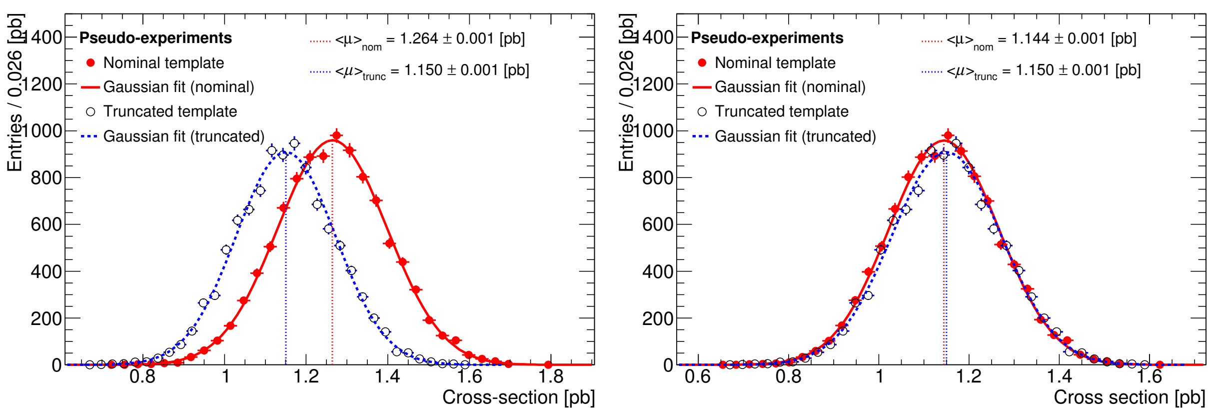

Figure D.10: Left: Cross section as obtained from pseudo-experiments with the truncated signal template and with the nominal template. Right: cross section with and without the inclusion of $C_{\mathrm{iso}\gamma}$ scale factor. In each case, the dotted line indicates the mean of the corresponding gaussian fit.

Due to the existing correlations on the fit results (both fits with the truncated and nominal templates are performed on the same dataset), a study using pseudo-experiments was performed. A set of 10^3 pseudo-experiments matching the data statistics was generated with both the truncated and the nominal signal templates. Fig. D.10 left shows the resulting cross sections. A shift of ∼9.5% corresponding to the mean difference of the Gaussian fits to the distributions is observed. This shift is in agreement with the results obtained while fitting on data (although correlated).

Figure D.11 shows the results from this study on the number of *hadron-fakes* as extracted from each template fit. In this case, a shift of ∼16% is observed. This is an expected consequence of the template truncation and poses a question of the physical interpretation of the events that would have been extracted as prompt-photons if using the nominal template instead. The categorisation of non-isolated ($p_{\mathrm{T}}^{\mathrm{iso}} > 3$ GeV) photons as background events is thus not fully correct, and consequently one needs to redefine the cross section taking into account the signal truncation to extract isolated photons.

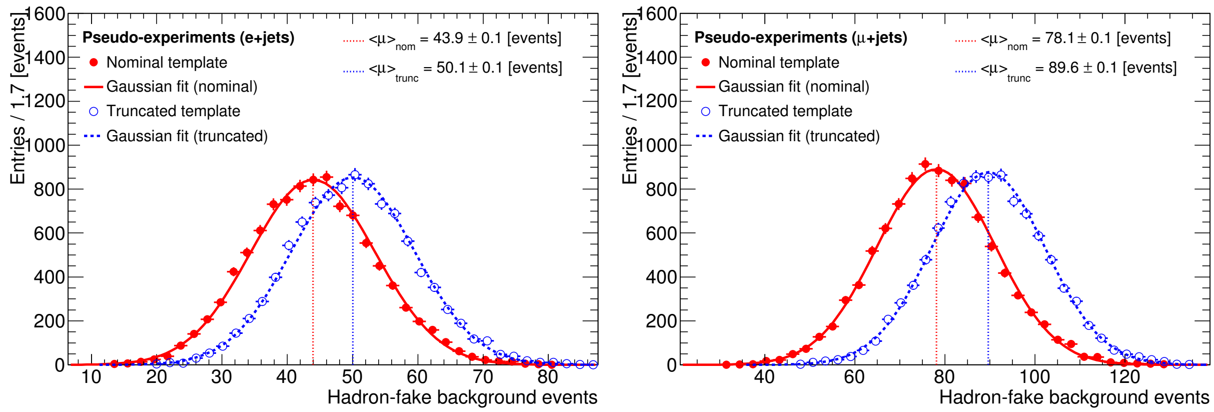

Figure D.11: Number of hadron-fake background events from pseudo-experiments for the electon (left) and muon (right) channels, as obtained with the truncated signal template and with the nominal template in the full isolation range. In each case, the dotted line indicates the mean of the corresponding Gaussian fit.

	Nominal template	**Truncated template**	**Shift [%]**
$N^{\mu}_{hadron\text{-}fakes}$	89.03 ± 0.45 events	101.32 ± 0.42 events	13.8
$N^{e}_{hadron\text{-}fakes}$	41.14 ± 0.30 events	47.84 ± 0.31 events	16.3
$\delta\sigma_{t\bar{t}\gamma}$	10.36 ± 0.03 %	10.26 ± 0.03 %	0.1%

Table D.6: Table showing the results from ensemble tests using the nominal and the truncated signal template

D.3.2 Cross section definition for "isolated" photons

The cross section for "isolated" photons, arbitrarily defined as those having $p_{\mathrm{T}}^{\mathrm{iso}} \leq 3$ GeV, can be written as

$$\sigma^{\mathrm{iso}}_{t\bar{t}\gamma} = C_{\mathrm{iso}\gamma} \times \sigma_{t\bar{t}\gamma} \tag{D.4}$$

where $\sigma_{t\bar{t}\gamma}$ is the nominal fiducial cross section (obtained with the full signal template in the entire $p_{\mathrm{T}}^{\mathrm{iso}}$ range), and $C_{\mathrm{iso}\gamma}$ is a scale-factor defined as

$$C_{\mathrm{iso}\gamma} = \frac{N^{\mathrm{trunc.}}_{\mathrm{sig}}}{N^{\mathrm{nom.l}}_{\mathrm{sig}}} = 1.111 \pm 0.003 \tag{D.5}$$

with $N^{\mathrm{trunc}}_{\mathrm{sig}}$ and $N^{\mathrm{nom}}_{\mathrm{sig}}$ being the mean number of signal events extracted from pseudo-experiment using the truncated and nominal signal templates, respectively. Figure D.10 left shows the resulting cross section as obtained with the truncated template and with the full template in combination with the $C_{\mathrm{iso}\gamma}$ factor. The mean cross sections are in good agreement within statistical uncertainties (both Gaussians are centred around the same mean). For both channels, the same difference in the number of background events between the truncated and the full-template with $C_{\mathrm{iso}\gamma}$ is observed.

In conclusion, with this method it is shown that a photon definition based upon an isolation ($p_{\mathrm{T}}^{\mathrm{iso}} < 3$ GeV) cut would correspond to about 90% of that of currently used in the analysis. However, this is not used in the final result, as the photon at particle level would need to be redefined in that way and event migration to- and from-this definition would need studying.

D.4 Bayesian estimator approach

The nominal estimator method used in this analysis was compared with a *Bayesian* based *estimator* [86] used in a previous measurement [164, 165]. The *Bayesian* method also uses a binned likelihood as the estimator of choice. Events are also assumed to be Poisson distributed within each $p_{\mathrm{T}}^{\mathrm{iso}}$ bin [165].

The *Bayesian* method relies in the extraction of the signal and background distributions using the *Bayes Theorem*. The true signal (and background) is identified as a *posterior* probabilities. Added knowledge and assumptions on the estimator parameters have to multiply the likelihood function in terms of *prior* probabilities. Each *prior* indicates the unconditional knowledge on each likelihood parameter known *a priori* of the measurement. The *prior* probabilities were chosen to be the Dirac delta functions for the e/γ background parameters and a uniform probability over the $p_{\mathrm{T}}^{\mathrm{iso}}$ range for the probabilities of the signal and *hadron-fakes*. In the *Bayesian* picture these *priors* correspond to no additional knowledge about the parameters, but their range. The extraction of the number of signal events are marginalised by integration over all parameters in their phase-space. The integration is performed numerically using the Markov Chain Monte Carlo technique [162]. The uncertainty on the *estimates* is determined by computing the smallest interval containing the 68% around the of the posterior density.

Because of the fact that the *Bayesian* method extracts only the statistical component of the error, only the unconstrained likelihood default method was used in the comparison. In the unconstrained method the nuisance parameters are not allowed to vary and therefore do not contribute to the total uncertainty.

The templates used in this comparison were not the final templates used in the analysis, but just meant to validate the two fitting approaches against each other. The expected numbers of background events with prompt-photons and electrons misidentified as photons was fixed to a arbitrary number and only treated as one parameter taking into account both contributions for each channel. Also the comparison was not performed using the final $t\bar{t}\gamma$ selection criteria, but on a region with relaxed selection criteria.

A binned likelihood fit was performed and the number of events in each bin i of the signal template distribution relates to the number of signal events s by

$$s_i = \varepsilon_i \cdot s \,, \tag{D.6}$$

where ε_i describes the acceptance and selection, and the probability to end up in bin i. For each background j, the respective contribution in the bin i of $p_{\mathrm{T}}^{\mathrm{iso}}$ b_i^j is modelled by a template Hence, the sum of all contributions in each bin reads:

$$\lambda_i = s_i + \sum_{j=1}^{N_{\text{bkg}}} b_i^j \,. \tag{D.7}$$

The following likelihood was then maximised in the fit using Markov Chain Monte Carlo implemented in the *Bayesian* Analysis Toolkit [162]

$$L = \prod_{i=1}^{N_{\text{bins}}} P(N_i|\lambda_i) \cdot \prod_{j=1}^{N_{\text{bkg}}} P(b^j) \cdot P(s)\,, \tag{D.8}$$

where N_i is the number of observed events in bin i of$p_{\text{T}}^{\text{iso}}$. $P(N_i|\lambda_i)$ is the poisson distributed probability to observe N_i events given an expectation of λ_i. $P(b^j)$ is the probability for the j-th background contribution, and $P(s)$ is the probability for the signal contribution.

The background probabilities were either chosen to be constant in a range $[b^j_{\text{min}}, b^j_{\text{max}}]$, if the background yield was treated as a free parameter

$$P(b^j) = \begin{cases} \frac{1}{b^j_{\text{max}} - b^j_{\text{min}}}\,, & b^j_{\text{min}} \leq b^j \leq b^j_{\text{max}} \\ 0, & \text{else} \end{cases}\,, \tag{D.9}$$

or fixed to a background estimate $\bar{b}^j$:

$$P(b^j) = \delta\left(\bar{b}^j - b^j\right)\,, \tag{D.10}$$

where $\delta(x)$ is the delta distribution. The uncertainty on the background estimate $\bar{b}^j$ was then treated as a source of systematic uncertainty.

Table D.7 gives an overview of the different parameters of the template fit and their respective probabilities: as already mentioned, the hadron fake contribution was treated as a free parameter, and a constant background probability was assigned to it covering the whole range of hadron fake contributions between 0% and 100%.

The $t\bar{t}\gamma$ signal contribution was also treated as a free parameter:

$$P(s) = \begin{cases} \frac{1}{s_{\text{max}} - s_{\text{min}}}\,, & s_{\text{min}} \leq s \leq s_{\text{max}} \\ 0, & \text{else} \end{cases}\,, \tag{D.11}$$

with s covering a range of signal fractions between 0% and 100%. The template fit was performed in both the electron channel (e) and the muon channel (μ) simultaneously. A combined likelihood was constructed in order to estimate the expected number of signal events s, which, combining Eq. D.6), Eq. D.7 and Eq. D.8, explicitly is :

$$L = \prod_{i=1}^{N_{\text{bins}}} P\left(N_{i,\text{e+jets}} \middle| \lambda_{i,\text{e+jets}} = \varepsilon_{i,\text{e+jets}} \cdot s + \sum_{j=1}^{N_{\text{bkg}}} b^j_{i,\text{e+jets}}\right) \cdot \prod_{j=1}^{N_{\text{bkg}}} P\left(b^j_{\text{e+jets}}\right) \cdot \tag{D.12}$$

$$\prod_{i=1}^{N_{\text{bins}}} P\left(N_{i,\mu\text{+jets}} \middle| \lambda_{i,\mu\text{+jets}} = \varepsilon_{i,\mu\text{+jets}} \cdot s + \sum_{j=1}^{N_{\text{bkg}}} b^j_{i,\mu\text{+jets}}\right) \cdot \prod_{j=1}^{N_{\text{bkg}}} P\left(b^j_{\mu\text{+jets}}\right) \cdot P(s) \tag{D.13}$$

Process	**Parameter**	**Parameter probability**
$t\bar{t}\gamma$ signal	Free	Constant
e/γ background	Fixed	Delta function
Hadron fakes	Free	Constant

Table D.7: Parameters and parameter probabilities for the signal and background contributions used in the *Bayesian* approach.

D.4.1 Results of the comparison

Two tests were performed: separate fits in the two lepton channels and a combined fit of both channels together. The results for the different parameters including the statistical uncertainties are presented in tables D.8. Fort the latter case, the fitted values for the number of $t\bar{t}\gamma$ events are 224.7 ± 18.9 for the default method and $224.6^{+19.6}_{-18.1}$ for the *Bayesian* approach. The agreement between methods is excellent upon the benchmark templates, as well as for the independent fits to each individual channel.

	Channel independent fit		**Simultaneous fit**	
	Result [events]		**Result [events]**	
Electron channel	**Default**	***Bayesian***	**Default**	***Bayesian***
Signal	$88.2^{+12.7}_{-12.1}$	$86.5^{+13.6}_{-11.0}$	224.6 ± 18.9	$224.6^{+19.6}_{-18.1}$
e/γ background	25.9			
Hadron-fakes background	65.5 ± 10.3	$65.6^{+10.6}_{-10.0}$	65.5 ± 9.7	$62.8^{+11.8}_{-7.8}$
Data candidates	178			
	Result [events]		**Result [events]**	
Muon channel	**Default**	***Bayesian***	**Default**	***Bayesian***
Signal	$137.3^{+14.6}_{-14.0}$	$137.2^{+15.6}_{-15.2}$	224.6 ± 18.9	$224.6^{+19.6}_{-18.1}$
e/γ background	12.9			
Hadron-fakes background	88.93 ± 11.99	$88.9^{+12.8}_{-10.9}$	92.1 ± 12.0	$91.8^{+12.2}_{-11.8}$
Data candidates	239			

Table D.8: Comparison of the template fits with the default method and the *Bayesian* approach. Results are shown for both channel independent and simultaneous fits.

D.5 Simplified model: cut and count

A cut and count cross check to the main method was also performed. A photon isolation cut $p_{\mathrm{T}}^{\mathrm{iso}} < 3$ GeV was introduced instead of the template fit.On this method no assumptions are made on the *hadron-fakes* track-isolation distribution nor on the prompt-photons isolation distributions.

All photon candidates with $p_{\mathrm{T}}^{\mathrm{iso}} > 3$ GeV are considered as background. The number of *hadron-fakes* leaking into the region with $p_{\mathrm{T}}^{\mathrm{iso}} \leq 3$ GeV needs to be determined. This is done using a *side-band* criterion. At first, an *estimator* (in this case, a weighted mean) determines the amount of *hadron-fakes* within the region $p_{\mathrm{T}}^{\mathrm{iso}} > 3$ GeV. Then this value is extrapolated in the region $p_{\mathrm{T}}^{\mathrm{iso}} \leq 3$ GeV.

e/γ backgrounds need to also be considered, each e/γ background is subtracted from from data. The reaming data candidates are considered considered to be the signal. Figure D.12 shows the resulting estimation for the electron and muon channel respectively. A systematic uncertainty on the extrapolation of the *hadron-fakes* must be introduced. It is estimated by calculating the root mean square for entries of $p_{\mathrm{T}}^{\mathrm{iso}} > 3$ GeV. Due to the low number of bins and relatively large fluctuations, this uncertainty is by large. It was estimated to be 8.3 fb for the electron channel and 10.2 fb for the muon channel. Uncertainties on the e/γ backgrounds are also considered with $W\gamma$ + jets and $e \to \gamma$ misidentification being the main ones. All Contributions are summarised in Tab. D.9.

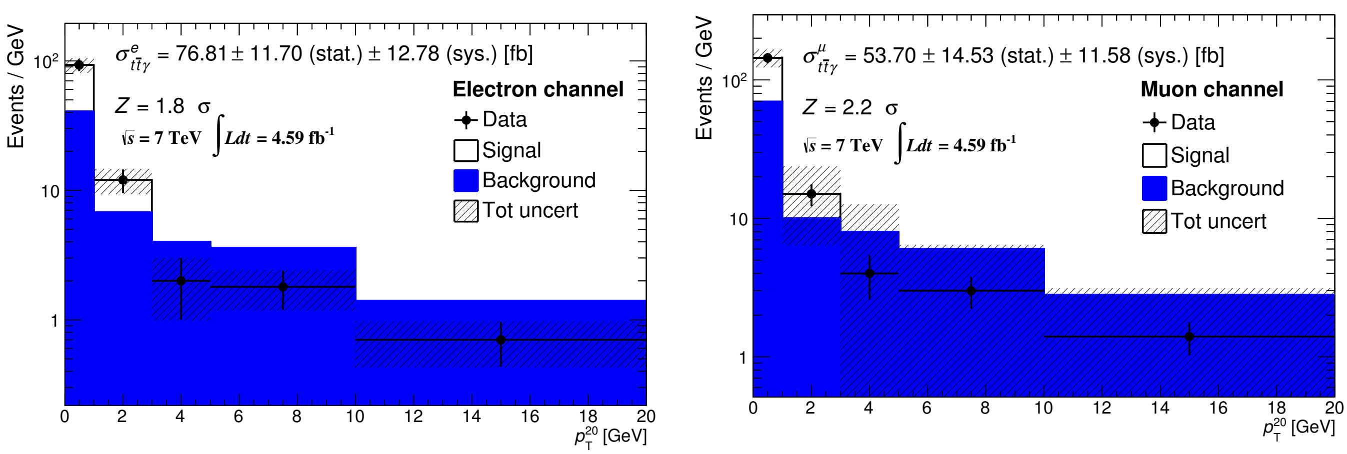

Figure D.12: Representation of isolation cut method performed on data. Results on the electron (muon) channel are shown on the left (right).

By construction this method extracts two independent cross sections. A combination is performed *post-estimation*, by averaging the two results. The significance for each channel is, respectively, computed by the approximation:

$$Z = \frac{N_s}{\sqrt{\sum_i^{\mathrm{Bck}} N_{b_i} + \sum_j^{\mathrm{Systs.}} \sigma_i^j + \sigma_j^{\mathrm{stat}}}} \tag{D.14}$$

and is found to be 1.8σ for the electron channel and 2.2σ for the muon channel respectively. The combined significance is expressed as the quadratic sum of both and it is 2.8σ.

Contribution	Electron channel [fb]	Muon channel [fb]
hadron-fakes	8.3	10.2
$Z\gamma + \text{jets}$	0.2	0.6
Single top+γ	0.1	0.2
Dibosons+γ	0.4	0.7
Multijets+γ	0.9	0.5
$W\gamma + \text{jets}$	0.2	0.5
$e \to \gamma$ misidentification	0.1	0.1
Total Systematic	12.8	11.6

Table D.9: Systematic contributions taken into account in the cut and count method.

Parameter	Electron channel	Muon Channel
Signal	57 ± 9 (stat) events	80 ± 22 (stat) events
Background	57 ± 9 (stat.) $\pm\, 10$ (sys.) events	96 ± 26 (stat.) $\pm\, 18$(sys.) events
$\sigma_{t\bar{t}\gamma}$	76.8±11.7 (stat.) ± 12.8 (sys.) fb	53.7±14 (stat) ± 11.6 (sys) fb
Combined $\sigma_{t\bar{t}\gamma}$	65 ± 14 (stat) ± 17 (sys) fb	

Table D.10: Signal and background estimations from the cut and count method

Detailed results are expressed in Tab. D.10 and are compatible within uncertainties [3] with the main fit. The total cross section estimated by this method is:

$$\sigma_{t\bar{t}\gamma} = 65 \pm 14 \text{ (stat)} \pm 17 \text{ (sys)fb} \tag{D.15}$$

and it is also compatible with the main result.

An alternative method to this, is the usage of template information without maximising a likelihood. Only the *hadron-fake* template needs to be used. The number of prompt-photons in each $p_{\mathrm{T}}^{\mathrm{iso}}$ bin is evaluated by subtracting the relative fraction of the *hadron-fake* template to distribution in data.

[3] The statistical uncertainty for this result and the ones from the main method are obviously correlated, and therefore are to be excluded from the comparison. The systematic uncertainties are independent.

D.6 Likelihood fits as a function of $E_{\mathrm{T}}(\gamma)$

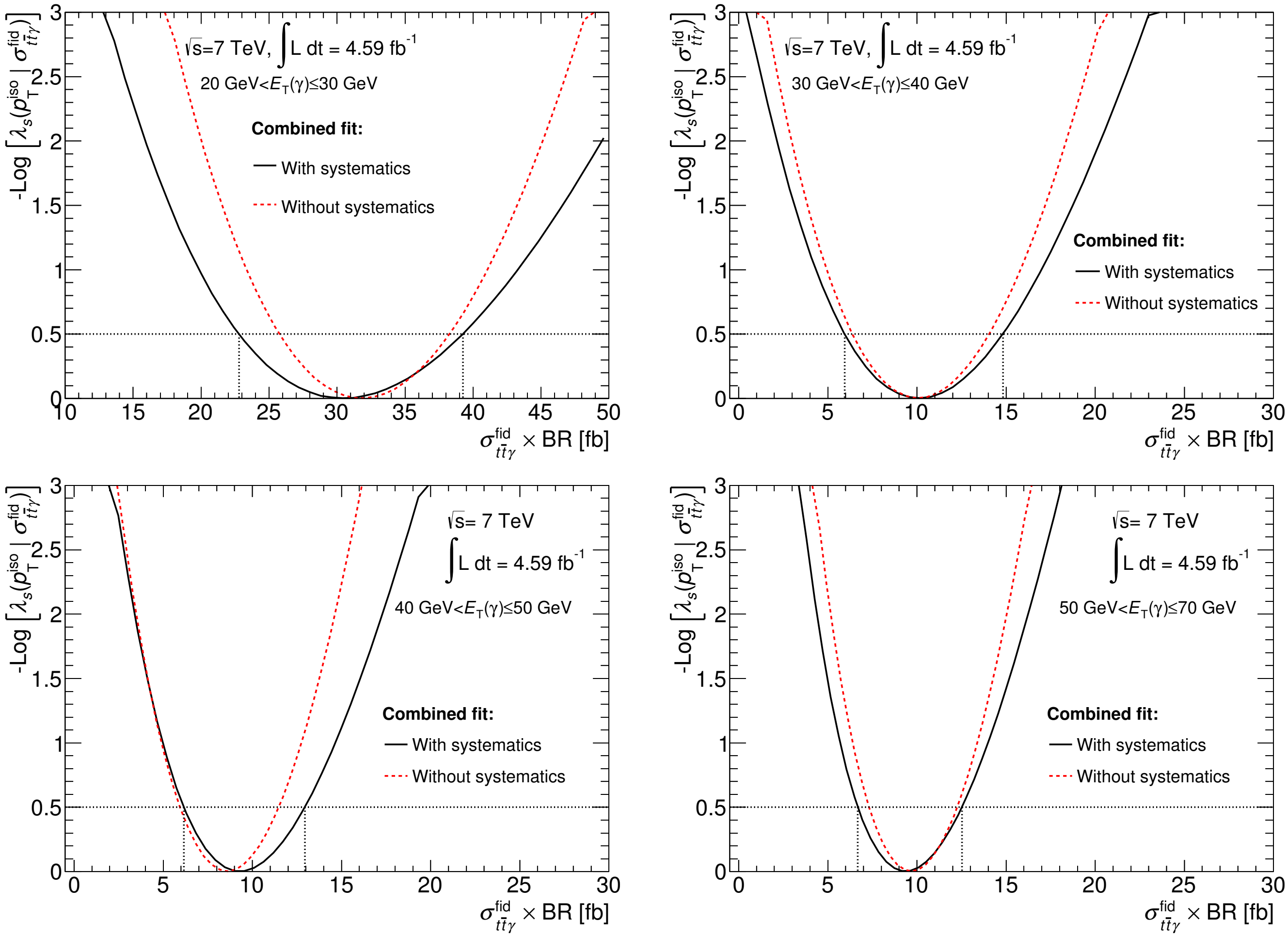

Figure D.13: Negative logarithm of the profile likelihood as a function of the fiducial cross section $\sigma^{\mathrm{fid}}_{t\bar{t}\gamma}\times$ BR with (solid line) and without (dotted line) free nuisance parameters associated with systematic uncertainties in different $E_{\mathrm{T}}(\gamma)$ ranges. The horizontal corresponds to a value of $-\log\left[\lambda_s(p_{\mathrm{T}}^{\mathrm{iso}}, |\sigma^{\mathrm{fid}}_{t\bar{t}\gamma}\right)\right] = 0.5$. Intersections of this line with the curves give the total (statistical only) $\pm 1\sigma$ uncertainty on the cross section.

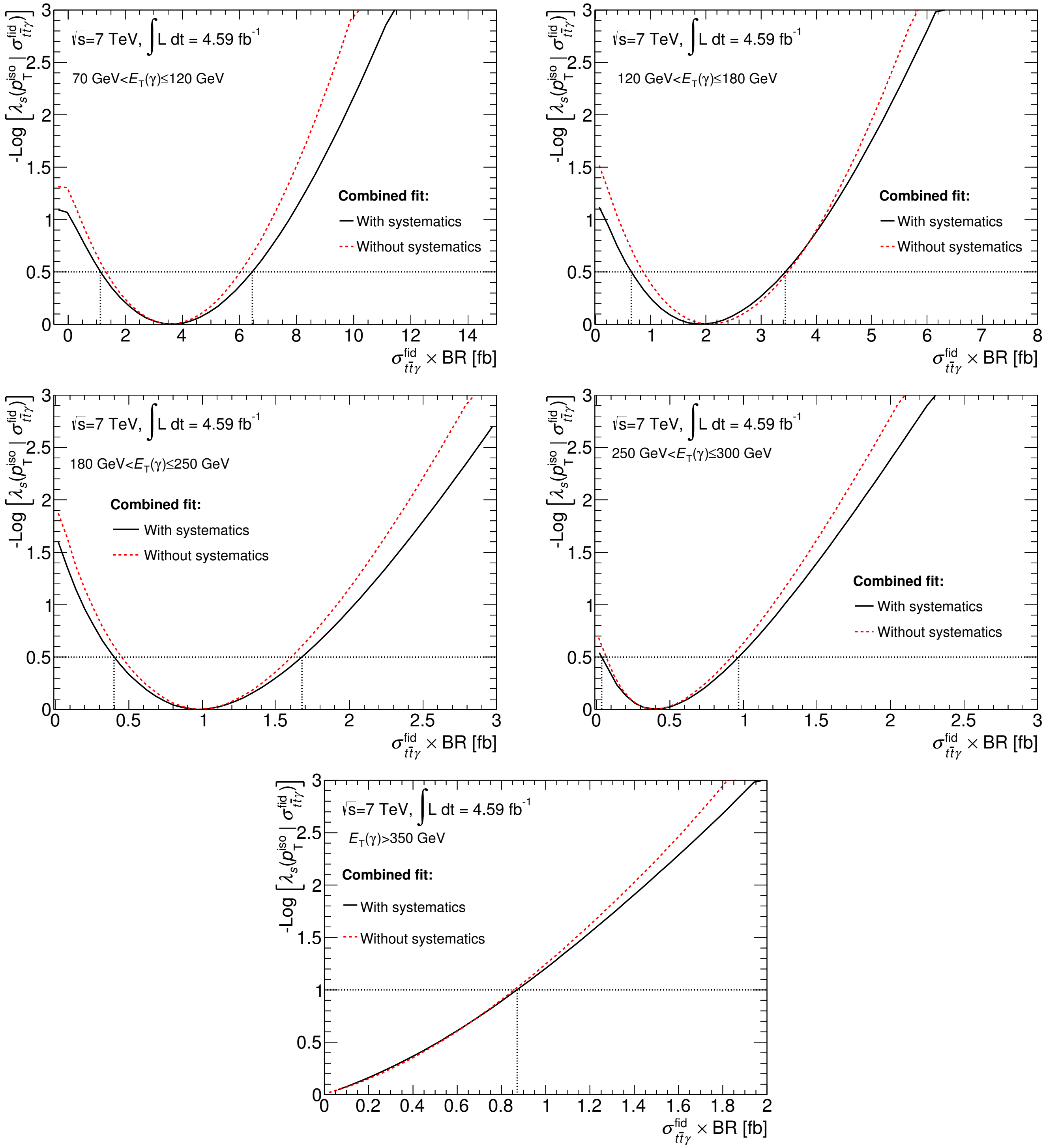

Figure D.14: Negative logarithm of the profile likelihood as a function of the fiducial cross section $\sigma^{\mathrm{fid}}_{t\bar{t}\gamma}\times$ BR with (solid line) and without (dotted line) free nuisance parameters associated with systematic uncertainties in different $E_{\mathrm{T}}(\gamma)$ ranges. For the two top plots (bottom one) the horizontal line corresponds to a value of $-\log\left[\lambda_s(p_{\mathrm{T}}^{\mathrm{iso}},|\sigma^{\mathrm{fid}}_{t\bar{t}\gamma})\right] = 0.5$ (1). Intersections of this line with the curves give the total (statistical only) $\pm1\sigma$ and upper limit the cross section respectively.

D.7 Constraint from nuisance parameters

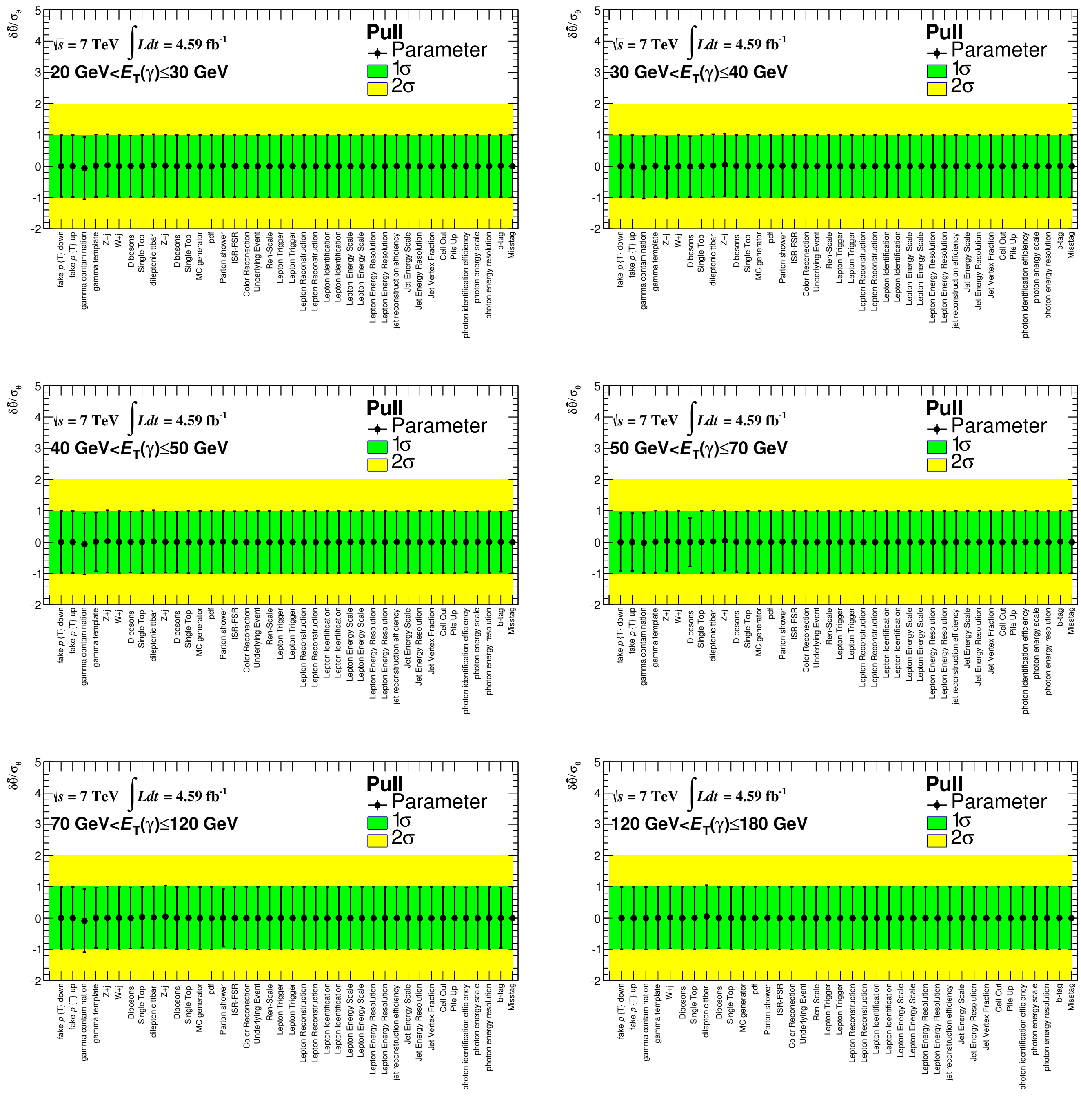

Figure D.15: Representation of isolation cut method performed on data. Results on the electron (muon) channel are shown on the left (right).

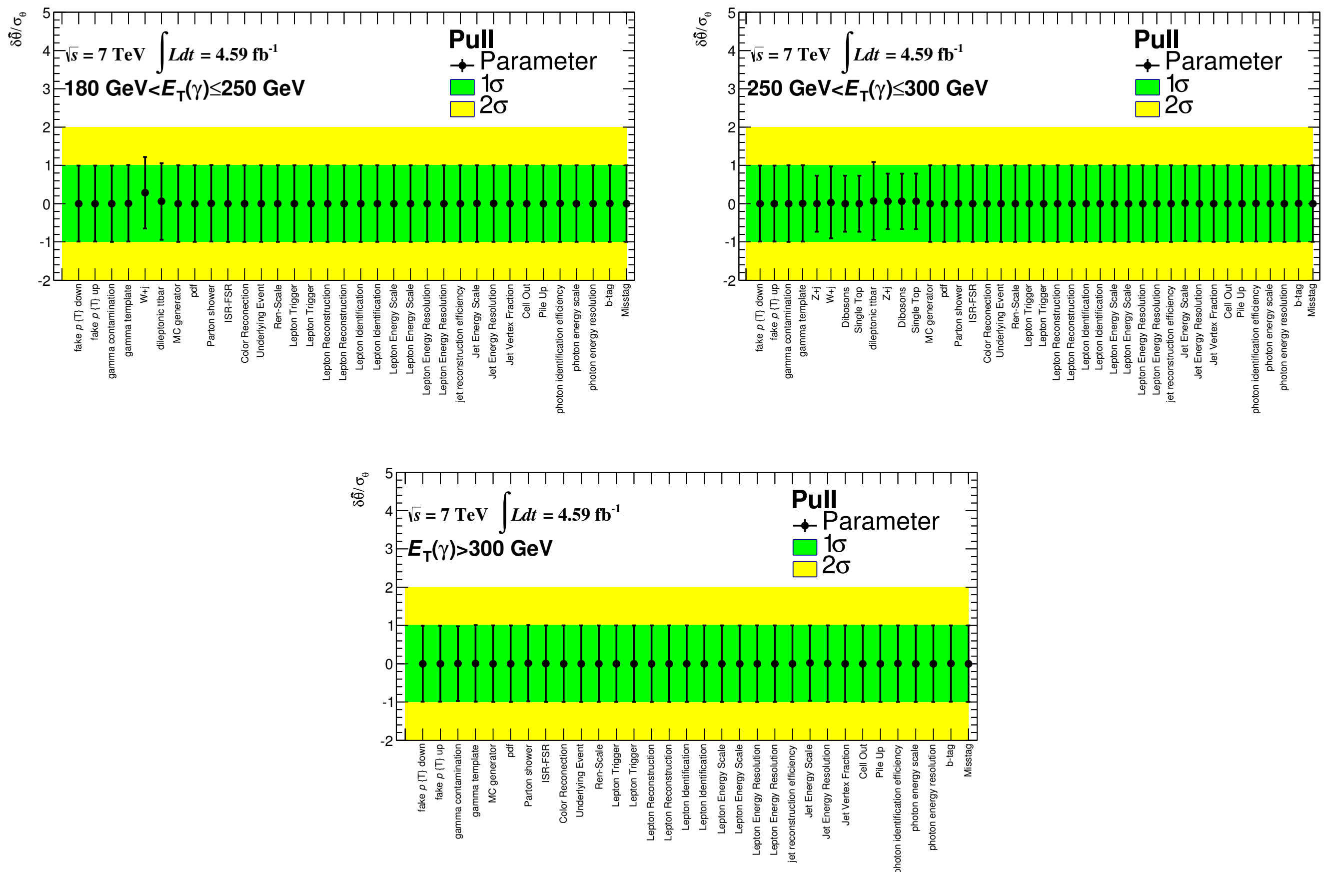

Figure D.16: Representation of isolation cut method performed on data. Results on the electron (muon) channel are shown on the left (right).

References

[1] F. Abe *et al.*, *Observation of top quark production in $\bar{p}p$ collisions*, PRL **74** (1995) 2626–2631, `arXiv:9503002 [hep-ex]`.

[2] S. Abachi *et al.*, *Observation of the top quark*, PRL **74** (1995) 2632–2637, `arXiv:9503003 [hep-ex]`.

[3] Particle Data Group Collaboration, K. A Olive *et al.*, *Review of particle physics*, Chin. Phys. C **38** (2014) 090001.

[4] B. Lillie, J. Shu, and T.M.P. Tait, *Top compositeness at the tevatron and LHC*, JHEP (2008) 087, `arXiv:0712.3057 [hep-ph]`.

[5] The CDF Collaboration, *Evidence for $t\bar{t}\gamma$ production and measurement of $\sigma_{t\bar{t}\gamma}/\sigma_{t\bar{t}}$*, Phys. Rev. D **84** (2011) 031104, `arXiv:1106.3970 [hep-ex]`.

[6] E. L. Ibanez, *Grand unification with local supersymmetry*, Nucl. Phys. B **218** (1983) 514.

[7] J. Ellis *et al.*, *Grand unification in simple supergravity*, Phys. Lett. **121** (1983) 123.

[8] L. Alvarez-Gaume, J. Polchinski, and M.B. Wise, *Minimal low-energy supergravity*, Nucl. Phys. B **221** (1983) 495.

[9] R. S. Chivukula, E. Simmons and J. Terning, *A heavy top quark and the Z b anti-b vertex in noncommuting extended technicolor*, Phys. Lett. B **331** (1994) 383–389, `arXiv:9404209 [hep-ph]`.

[10] D. Chang W.F. Changd and E. Ma, *Alternative interpretation of the Tevatron top events*, Phys. Rev. D **59** (1999) 091503, `arXiv:9810531 [hep-ph]`.

[11] D. Choudhury, T.P.M Tait and C.E.M. Wagner, *Beautiful mirrors and precision electroweak data*, Phys. Rev. D **65** (2002) 053002, `arXiv:0109097 [hep-ph]`.

[12] U. Baur, *et al.*, *Probing electroweak top quark couplings at hadron colliders*, Phys. Rev. D **71** (2005) 054013, `arXiv:0412021 [hep-ph]`.

[13] R. D. Field and R. P. Feynman , *A Parametrization of the properties of quark jets*, Nucl. Phys. B **136** (1978) 1.

[14] R. Barate *et al.*, *Determination of $A - b$(FB) using jet charge measurements in Z decays*, Phys. Lett. B **426** (1998) 217–230.

[15] G. Aad *et al.*, *Measurement of the top quark charge in pp collisions at $\sqrt{s} = 7$ TeV with the ATLAS detector*, JHEP **1311** (2013) 031, `arXiv:1307.4568 [hep-ex]`.

[16] D. Chakraborty J. Konigsberg and D. L. Rainwater, *Review of top quark physics*, Ann. Rev. Nucl. Part. Sci. **53** (2003) 301–351, `arXiv:0303092 [hep-ph]`.

[17] S. Frixione, P. Nason and B. R. Webber, *Matching NLO QCD and parton showers in heavy flavor production*, JHEP **0308** (2003) 007, `arXiv:0305252 [hep-ph]`.

[18] S. Frixione *et al.*, *Single top production in MC@NLO*, JHEP **0603** (2006) 092, `arXiv:0512250 [hep-ph]`.

[19] S. Frixione *et al.*, *Single-top hadroproduction in association with a W-boson*, JHEP **0807** (2008) 029, `arXiv:0805.3067 [hep-ph]`.

[20] G. Altarelli and G. Parisi, *Asymptotic freedom in parton language*, Nucl. Phys. B **126** (1977) 298.

[21] Y. L. Dokshitzer, *Calculation of the structure functions for deep inelastic scattering and e^+e^- annihilation by perturbation theory in quantum chromodynamics.*, Sov. Phys. JETP **46** (1977) 641–653.

[22] V. N. Gribov and L. N. Lipatov, *Deep inelastic e-p scattering in perturbation theory*, Sov. J. Nucl. Phys. **15** (1972) 438–450.

[23] CTEQ Collaboration, R. Brock *et al.*, *Handbook of perturbative QCD: Version 1.0*, Rev. Mod. Phys. **67** (1995) 157–248.

[24] A. D. Martin *et al.*, *Parton distributions for the LHC*, Eur. Phys. J. **63** (2009) 189–285, `arXiv:0901.0002 [hep-ph]`.

[25] A. D. Martin *et al.*, *Uncertainties on α_S in global PDF analyses and implications for predicted hadronic cross sections*, Eur .Phys. J. C **64** (2009) 653–680, `arXiv:0905.3531 [hep-ph]`.

[26] A. D. Martin *et al.*, *Heavy-quark mass dependence in global PDF analyses and 3- and 4-flavour parton distributions*, Eur. Phys. J. **70** (2010) 51–72, `arXiv:1007.2624 [hep-ph]`.

[27] A. Buckley, *et al.*, *General-purpose event generators for LHC physics*, Phys. Rept. **504** (2011) 145–233, `arXiv:1101.2599 [hep-ph]`.

[28] C. J. Collins, *Sudakov form-factors*, Adv. Ser. Direct. High Energy Phys. **5** (1989) 573–614, `arXiv:0312336 [hep-ph]`.

[29] J. Pumplin *et al.*, *New generation of parton distributions with uncertainties from global QCD analysis*, JHEP **07** (2002) 012, `arXiv:hep-ph/0201195`.

[30] M.L. Mangano *et al.*, *Matching matrix elements and shower evolution for top-quark production in hadronic collisions*, JHEP **0701** (2007) 013, `arXiv:0611129 [hep-ph]`.

[31] S. Catani *et al.*, *QCD matrix elements + parton showers*, JHEP **0111** (2001) 063, `arXiv:0109231 [hep-ph]`.

[32] Fermilab-Serpukhov-Moscow-Michigan Collaboration, J.P. Berge *et al.*, *Net charge in deep inelastic anti-neutrino -nucleon scattering*, Phys .Lett. B **91** (1980) 311.

[33] Aachen-Bonn-CERN-Munich-Oxford Collaboration, P. Allen *et al.*, *Multiplicity Distributions in neutrino - hydrogen interactions*, Nucl. Phys. B **181** (1981) 385.

[34] Aachen-Bonn-CERN-Munich-Oxford Collaboration, P. Allen *et al.*, *Charge properties of the hadronic system in neutrino p and nnti-neutrino p interactions*, Phys. Lett. B **112** (1982) 88.

[35] M. Y. Han and Y. Nambu, *Three triplet model with double $SU(3)$ Symmetry*, Phys. Rev. B **139** (1965) 1006–1010.

[36] M. Gell-Mann, *A schematic model of baryons and mesons*, Phys. Lett. **8** (1964) 214–215.

[37] G. Zweig, *An $SU(3)$ model for strong interaction symmetry and its breaking; Version 2*, . Version 1 is CERN preprint 8182/TH.401, Jan. 17, 1964.

[38] F. Gursey and L.A. Radicati, *Spin and unitary spin independence of strong interactions*, PRL **13** (1964) 173–175.

[39] W. Pauli, *The connection between spin and statistics*, Phys. Rev. **58** (1940) 716–722.

[40] A. I. Sanda, *A QCD determination of quark charges: sum of quark charges squared*, tech. rep., 1979.

[41] G.Hanson *et al.*, *Evidence for jet structure in hadron rroduction by e^+e^- annihilation*, PRL **35** (1975) 1609–1612, `10.1103/PhysRevLett.35.1609`.

[42] G.Hanson *et al.*, *Hadron production by e^+e^- annihilation at center-of-mass energies between 2.6 GeV and 7.8 GeV. Part 2. Jet structure and related inclusive distributions*, Phys. Rev. D **26** (1982) 991, `10.1103/PhysRevD.26.991`.

[43] J. Bonner, C. Fisher and E. Michael, *Linear magnetic chains with anisotropic coupling*, Phys. Rev. A **135** (Aug, 1964) 640–658, `10.1103/PhysRev.135.A640`.

[44] I. S. Gerstein and M.L Whippman, *Strong-interaction symmetries based upon rank-three Lie groups*, Phys. Rev. B **137** (Mar, 1965) 1522–1529, `10.1103/PhysRev.137.B1522`.

[45] B. Iijima and R.L. Jaffe, *Can quarks have integer charge?*, Phys. Rev. D **24** (1981) 177–184, `10.1103/PhysRevD.24.177`.

[46] W. O. Greenberg, *Spin and unitary spin independence in a paraquark model of baryons and mesons*, PRL **13** (1964) 598–602.

[47] W. O. Greenberg and D. Zwanziger, *Saturation in triplet models of hadrons*, Phys. Rev. **150** (1966) 1177–1180.

[48] P. Achard *et al.*, *Inclusive π^0 and K^0_S production in two photon collisions at LEP*, Phys. Lett. B **524** (2002) 44–54, `arXiv:0109037 [hep-ex]`.

[49] J. Pati, C. Jogesh and A. Salam, *Unified lepton-hadron symmetry and a gauge theory of the basic interactions*, Phys. Rev. D **8** (1973) 1240–1251.

[50] J. LaChapelle, *Quarks with integer electric charge*, `arXiv:0408305 [hep-ph]`.

[51] W. Hollik *et al.*, *Dipole form-factors and loop induced CP violation in supersymmetry*, Nucl. Phys. B **557** (1999) 407, `arXiv:9808408 [hep-ph]`.

[52] W. F. L. Hollik, *Radiative corrections in the Standard Model and their role for precision tests of the electroweak theory*, Fortsch. Phys. **38** (1990) 165–260, `10.1002/prop.2190380302`.

[53] P.F. Duan *et al.*, *QCD corrections to associated production of $t\bar{t}\gamma$ at hadron colliders*, Phys. Rev. D **80** (2009) 014022.

[54] K. Melnikov and M. Schulze, *Private communication*, .

[55] U. Baur *et al.*, *Direct measurement of the top quark charge at hadron colliders*, Phys. Rev. D **64** (2001) 094019, `arXiv:0106341 [hep-ph]`.

[56] K. Melnikov, M. Schulze and A. Scharf, *QCD corrections to top quark production in association whith a photon at hadron colliders*, Phys. Rev. D **83** (2011) 074013, `arXiv:1102.1967 [hep-ph]`.

[57] V. Fadin *et al.*, *Interference radiative phenomena in the production of heavy unstable particles*, Phys. Rev. D **49** (1994) 2247–2256.

[58] K. Melnikov and O. I. Yakovlev, *Top near threshold: all α_S corrections are trivial*, Phys. Lett. B **324** (1994) 217–223, `arXiv:9302311 [hep-ph]`.

[59] K. Melnikov and O. I Yakovlev, *Final state interaction in the production of heavy unstable particles*, Nucl. Phys. **471** (1996) 90–120, `arXiv:9501358 [hep-ph]`.

[60] G. Barone, *ATLAS silicon microstrip tracker operation and performance*, NIM A **732** (2013) 57–60.

[61] L. Evans and P. Bryant, *LHC Machine*, JINST **3** (2008) S08001.

[62] J. Haffner, *The CERN accelerator complex. Complexe des accélérateurs du CERN*, . `https://cds.cern.ch/record/1621894`. General Photo.

[63] LHC Study Group Collaboration, T. S. Pettersson and P. Lefèvre, *The Large Hadron Collider: conceptual design*, Tech. Rep. CERN-AC-95-05 LHC, CERN, Geneva, Oct, 1995.

[64] M. Lamont, *Status of the LHC*, J. Phys. Conf. Ser. **455** (2013) 012001.

[65] CERN, *3rd Evian workshop on LHC beam operation.* CERN, Geneva, 2011.

[66] G. Aad *et al.*, *ATLAS experiment at the CERN Large Hadron Collider*, JINST **3** (2008) S08003, `doi:10.1088/1748-0221/3/08/S08003`.

[67] G. Aad *et al.*, *The ATLAS inner detector commissioning and calibration*, Eur. Phys. J. C **70** (2010) 787–821, arXiv:1004.5293 [physics.ins-det].

[68] E. Abat *et al.*, *The ATLAS Transition Radiation Tracker (TRT) proportional drift tube: Design and performance*, JINST **3** (2008) P02013.

[69] G. Aad *et al.*, *Particle identification performance of the ATLAS Transition Radiation Tracker*, Tech. Rep. ATLAS-CONF-2011-128, CERN, Geneva, Sep, 2011.

[70] G. Aad *et al.*, *ATLAS liquid-argon calorimeter: technical design report.* Technical Design Report ATLAS. CERN, Geneva, 1996.

[71] *Twiki page: Trigger Operations Public Results*, https://twiki.cern.ch/twiki/bin/view/AtlasPublic/TriggerOperationPublicResults.

[72] *Twiki page: Data Quality Conditions for 2012*, https://twiki.cern.ch/twiki/bin/view/AtlasPublic/LuminosityPublicResults.

[73] G. Aad *et al.*, *Luminosity determination in pp collisions at* $\sqrt{s} = 7$ *TeV using the ATLAS detector at the LHC*, Eur. Phys. J. C **71** (2011) 1630, arXiv:1101.2185 [hep-ex].

[74] *Twiki page: Data Quality Conditions for 2011*, https://twiki.cern.ch/twiki/bin/view/AtlasPublic/RunStatsPublicResults2010#2011.

[75] *Twiki page: Data Quality Conditions for 2012*, https://twiki.cern.ch/twiki/bin/view/AtlasPublic/RunStatsPublicResults2010#2012.

[76] A. Ahmad *et al.*, *The silicon microstrip sensors of the ATLAS semiconductor tracker*, NIMA A **578** (2007) 98–118, 10.1016/j.nima.2007.04.157.

[77] S. D'Auria, *The ATLAS semiconductor tracker: operations and performance*, Tech. Rep. ATL-INDET-PROC-2012-027, CERN, Geneva, Nov, 2012.

[78] *Twiki page: Data Quality Conditions for 2012*, https://twiki.cern.ch/twiki/bin/view/AtlasPublic/InDetTrackingPerformanceApprovedPlots.

[79] Aad, Georges and others, *Study of alignment-related systematic effects on the ATLAS inner detector tracking*, Tech. Rep. ATLAS-CONF-2012-141, CERN, Geneva, Oct, 2012.

[80] G. Aad *et al.*, *Operation and performance of the ATLAS semiconductor tracker*, arXiv:1404.7473 [hep-ex].

[81] A. Ferrari *et al.*, *FLUKA: A multi-particle transport code (Program version 2005)*, .

[82] S. Agostinelli *et al.*, *GEANT4 - A Simulation Toolkit*, NIM A **506** (2003) 250.

[83] *Twiki page: Top GoodRunList - Final 2011 data (release 17)*, https://twiki.cern.ch/twiki/bin/viewauth/AtlasProtected/TopGRLs.

[84] R. Brun and F. Rademakers, *ROOT–an object oriented data analysis framework*, NIM A **389** (1997) . http://root.cern.ch/.

[85] G. Duckeck *et al.*, *ATLAS computing: technical design report*, .

[86] G. Barone *et al.*, *Measurement of the total inclusive $t\bar{t}$+photon cross section in the single lepton channel at $\sqrt{s}$ = 7 TeV in 4.7 fb^{-1} of pp collision data collected with the ATLAS detector*, Tech. Rep. ATL-COM-PHYS-2012-1632, CERN, Geneva, Nov, 2012.

[87] W. Kilian, T. Ohl. and J. Reuter, *WHIZARD: simulating multi-particle processes at LHC and ILC*, Eur. Phys. J. C **71** (2011) 1742, `arXiv:0708.4233 [hep-ph]`.

[88] M. Moretti, T. Ohl, and J. Reuter, *O'Mega: an optimizing matrix element generator*, LC-TOOL-2001-040-rev (2001) , `arXiv:0102195 [hep-ph]`.

[89] F. Maltoni and T. Stelzer, *MadEvent: automatic event generation with MadGraph*, JHEP (2003) 027, `arXiv:0208156 [hep-ph]`.

[90] G. Corcella *et al.*, *HERWIG 6: an event generator for hadron emission reactions with interfering gluons (including supersymmetric processes)*, JHEP **0101** (2001) 010, `arXiv:0011363 [hep-ph]`.

[91] J. Butterworth *et al.*, *Multiparton interactions in photoproduction at HERA*, Z. Phys. C **72** (1996) 637–646, `arXiv:9601371 [hep-ph]`.

[92] P. Golonka and Z. Was, *PHOTOS Monte Carlo: a Precision tool for QED corrections in Z and W decays*, Eur. Phys. J. C **45** (2006) 97, `arXiv:0506026 [hep-ph]`.

[93] S. Frixione and B.R. Webber, *Matching NLO QCD computations and parton shower simulations*, JHEP **0206** (2002) 029, `arXiv:0204244 [hep-ph]`.

[94] P. M. Nadolsky *et al.*, *Implications of CTEQ global analysis for collider observables*, Phys. Rev. D **78** (2008) 013004, `arXiv:0802.0007[hep-ph]`.

[95] M. *et al.*, *ALPGEN, a generator for hard multiparton processes in hadronic collisions*, JHEP **0307** (2003) 001, `arXiv:0206293 [hep-ex]`.

[96] T. Gleisberg *et al.*, *Event generation with SHERPA 1.1*, JHEP **0902** (2009) 007.

[97] H.L. *et al.*, *New parton distributions for collider physics*, Phys. Rev. D **82** (2010) 074024, `arXiv:1007.2241 [hep-ph]`.

[98] *Twiki page: Heavy Flavor Overlap Removal Tool*, `https://twiki.cern.ch/twiki/bin/view/AtlasProtected/HforTool`.

[99] J. P. Archambault *et al.*, *The simulation of the ATLAS liquid argon calorimetry*, .

[100] W. Lampl *et al.*, *Calorimeter clustering algorithms: description and performance*, .

[101] S. Ellis, D. Soper and E. Davison, *Successive combination jet algorithm for hadron collisions*, Phys. Rev. D **48** (1993) 3160–3166, `arXiv:9305266 [hep-ph]`.

[102] Y. Dokshitzer *et al.*, *Better jet clustering algorithms*, JHEP **9708** (1997) 001, `arXiv:9707323 [hep-ph]`.

[103] M. Cacciari, G. P. Salam and G. Soyez, *The anti-k_T jet clustering algorithm*, JHEP (2008) 063, `arXiv:0802.1189 [hep-ph]`.

[104] D. *et al.*, *Jet-vertex association algorithm*, ATL-COM-PHYS-2008-008 (2008) .

[105] G. Aad *et al.*, *Expected electron performance in the ATLAS experiment*, Tech. Rep. ATL-PHYS-PUB-2011-006, CERN, Geneva, Apr, 2011. `http://cds.cern.ch/record/1345327`.

[106] G. Aad *et al.*, *Expected performance of the ATLAS Experiment- detector, trigger and physics*, `arXiv:0901.0512 [hep-ex]`.

[107] G. Aad *et al.*, *Muon reconstruction efficiency and momentum resolution of the ATLAS experiment in proton-proton collisions at $\sqrt{s}$=7 TeV in 2010*, Eur. Phys. J. C **74** (2014) 3034, `arXiv:1404.4562 [hep-ex]`.

[108] G. Aad *et al.*, *Muon performance in minimum bias pp collision data at $\sqrt{s}$ = 7 TeV with ATLAS*, .

[109] B. *et al.*, *Object selection and calibration, background estimations and MC samples for the Automn 2012 top quark analyses with 2011 data*, ATL-COM-PHYS-2012-499 (2012) .

[110] G. Aad *et al.*, *Expected photon performance in the ATLAS experiment*, ATL-PHYS-PUB-2011-007 (2011) . `http://cdsweb.cern.ch/record/1345329`.

[111] G. Aad *et al.*, *Measurements of the photon identification with the ATLAS detector using 4.9 fb^{-1} of pp collision data collected in 2011*, `ATLAS-CONF-2012-123`.

[112] G. Aad *et al.*, *Electron reconstruction and identification efficiency measurements with the ATLAS detector using the 2011 LHC proton-proton collision data*, Eur. Phys. J. C **74** (2014) no. 7, 2941, `arXiv:1404.2240 [hep-ex]`.

[113] G. Aad *et al.*, *Jet energy measurement with the ATLAS detector in proton-proton collisions at $\sqrt{s} = 7$ TeV*, Eur. Phys. J. C **73** (2013) no. 3, 2304, `arXiv:1112.6426 [hep-ex]`.

[114] G. Aad *et al.*, *Performance of missing transverse momentum reconstruction in proton-proton collisions at 7 TeV with ATLAS*, Eur. Phys. J. C **72** (2012) 1844, `arXiv:1108.5602 [hep-ex]`.

[115] G. Aad *et al.*, *Calibrating the b-Tag efficiency and mistag rate in 35 pb^{-1} of data with the ATLAS Detector*, `ATLAS-CONF-2011-089`.

[116] G. Aad *et al.*, *Measurement of the mistag rate with 5 fb^{-1} of Data Collected by the ATLAS Detector*, Tech. Rep. ATLAS-CONF-2012-040, CERN, Geneva, Mar, 2012.

[117] G. Aad *et al.*, *Expected performance of the ATLAS Experiment - Detector, trigger and physics,* pp. 870-883, `arXiv:0901.0512 [hep-ex]`.

[118] G. Aad *et al.*, *Measurement of the $t\bar{t}$ production cross-section as a function of jet multiplicity and jet transverse momentum in 7 TeV proton-proton collisions with the ATLAS detector*, JHEP **1501** (2015) 020, `arXiv:1407.0891 [hep-ex]`.

[119] J. Erdmann *et al.*, *A likelihood-based reconstruction algorithm for top-quark pairs and the KLFitter framework*, NIM A **748** (2014) 18–25, `arXiv:1312.5595 [hep-ex]`.

[120] M. Dobbs and J. B. Hansen, *The HepMC C++ Monte Carlo event record for high energy physics*, Comput. Phys. Commun. **134** (2001) 41–46, `10.1016/S0010-4655(00)00189-2`.

[121] T. Carli *et al.*, *Draft proposal for truth particle definitions used in ATLAS*, Tech. Rep. ATL-COM-PHYS-2014-439, CERN, Geneva, May, 2014.

[122] S. Frixione, *Isolated photons in perturbative QCD*, Phys. Lett. D **429** (1998) 369, `arXiv:9801442`.

[123] F. James, *Statistical methods in experimental physics*, .

[124] J. Neyman, *Outline of a theory of statistical estimation based on the classical Theory of probability*, Philosophical Transactions of the Royal Society of London. Series A, Mathematical and Physical Sciences **236** (1937) 333–380.

[125] G. J. Feldman and R. D. Cousins, *Unified approach to the classical statistical analysis of small signals*, Phys. Rev. D **57** (1998) 3873.

[126] R. Fisher, *Statistical methods for research workers.* Cosmo study guides. Cosmo Publications, 1925.

[127] R. Fisher., *The design of experiments.* Hafner Pub. Co., 1966.

[128] C. Fourgeaud and A. Fuchs, *Statistique: Préface de R. Fortet.* Collection universitaire de mathematiques. Dunod, 1967.

[129] F. James, and M. Roos, *Minuit: a system for function minimization and analysis of the parameter errors and correlations*, Comput. Phys. Commun. **10** (1975) 343–367.

[130] S. S. Wilks, *The large-sample distribution of the likelihood ratio for testing composite hypotheses*, Annals Math. Statist. **9** (1938) no. 1, 60, `doi:10.1214/aoms/1177732360`.

[131] G. Cowan *et al.*, *Asymptotic formulae for likelihood-based tests of new physics*, Eur. Phys. J. C **71** (2011) 1554, `arXiv:1007.1727 [physics.data-an]`.

[132] G. Aad *et al.*, *Observation of top-quark pair production in association with a photon and measurement of the $t\bar{t}\gamma$ production cross section in pp collisions at $\sqrt{s} = 7$ TeV using the ATLAS detector*, Phys. Rev. D **91** (2015) , `arXiv:1502.00586 [hep-ex]`.

[133] B. Andersson *et al.*, *Parton fragmentation and string dynamics*, Phys. Rept. **97** (1983) 31–145.

[134] G. Aad *et al.*, *Measurement of multi-jet cross sections in proton-proton collisions at a 7 TeV center-of-mass energy*, Eur. Phys. J. C **71** (2011) 1763, `arXiv:1107.2092 [hep-ex]`.

[135] ROOT Collaboration, K. Cranmer *et al.*, *HistFactory: a tool for creating statistical models for use with RooFit and RooStats*, Tech. Rep. CERN-OPEN-2012-016, New York U., New York, Jan, 2012.

[136] C. Stein, *A bound for the error in the normal approximation to the distribution of a sum of dependent random variables.* University of California Press, Berkeley, Calif., 1972. `http://projecteuclid.org/euclid.bsmsp/1200514239`.

[137] James, Fred and Winkler, Matthias, *MINUIT user's guide*, .

[138] F. James, *MINUIT function minimization and error analysis: reference Manual version 94.1*, .

[139] W. Verkerke and D. Kirkby, *The RooFit toolkit for data modeling*, Tech. Rep. SLAC, Stanford, CA (2003) , `arXiv:physics/0306116 [physics.data-an]`.

[140] L. *et al.*, *The RooStats project*, PoS ACAT2010 (2010) , `arXiv:physics/1009.1003 [physics.data-an]`.

[141] M. Oreglia, *A Study of the reactions $\psi' \to \gamma\gamma\psi$*, Ph.D. Thesis, SLAC-236 (1980) . Appendix D., SLAC.

[142] J. Gaiser, *Charmonium spectroscopy from radiative decays of the J/ψ and ψ'*, Ph.D. Thesis, SLAC-R-255 (1982) . Appendix F., SLAC.

[143] *Twiki page: MCTruthClassifier*, `https://twiki.cern.ch/twiki/bin/viewauth/AtlasProtected/MCTruthClassifier`.

[144] G. Aad *et al.*, *Measurements of normalized differential cross sections for $t\bar{t}$ production in pp collisions at $\sqrt{s} = 7$ TeV using the ATLAS detector*, Phys. Rev. D **90** (2014) no. 7, 072004, `arXiv:1407.0371 [hep-ex]`.

[145] C-H. Kom and W. J. Stirling, *Charge asymmetry in $W+$ jets production at the LHC*, Eur. Phys. J. C **69** (2010) 67–73, `arXiv:1004.3404 [hep-ph]`.

[146] K, Melnikov and F. Petriello, *Electroweak gauge boson production at hadron colliders through $O(alpha_s^2)$*, Phys. Rev. D **74** (2006) 114017, `arXiv:0609070 [hep-ph]`.

[147] G. Aad *et al.*, *Measurement of the muon reconstruction performance of the ATLAS detector using 2011 and 2012 LHC proton-proton collision data*, Eur. Phys. J. C **74** (2014) no. 11, 3130, `arXiv:1407.3935 [hep-ex]`.

[148] F. A. Berends *et al.*, *On the production of a W and jets at hadron colliders*, Nucl. Phys. B **357** (1991) 32–64.

[149] G. Aad *et al.*, *Measurement of the top quark-pair production cross section with ATLAS in pp collisions at $\sqrt{s} = 7$ TeV*, Eur. Phys. J. C **71** (2011) 1577, `arXiv:1012.1792 [hep-ex]`.

[150] G. Aad *et al.*, *Measurement of the top quark pair production cross-section with ATLAS in the single-lepton channel*, Phys. Lett. B **711** (2012) 244–263, `arXiv:1201.1889 [hep-ex]`.

[151] G. Marchesini and B.R. Webber, *Simulation of QCD jets including soft gluon interference*, Nucl. Phys. B **238** (1984) 1, `10.1016/0550-3213(84)90463-2`.

[152] M. Botje *et al.*, *The PDF4LHC Working Group Interim Recommendations*, `arXiv:1101.0538 [hep-ph]`.

[153] M. Rammes, *Measurement of the inclusive $t\bar{t}\gamma$ cross section at $\sqrt{s} = 7$ TeV with the ATLAS detector*. PhD thesis, Universität Siegen, 2012. Presented 2012.

[154] P. Z. Skands, *Tuning Monte Carlo generators: the Perugia tunes*, Phys. Rev. D **82** (2010) 074018, `arXiv:1005.3457[hep-ph]`.

[155] G. Aad *et al.*, *Performance of the ATLAS trigger system in 2010*, Eur. Phys. J. C **72** (2012) 1849, `arXiv:1110.1530 [hep-ex]`.

[156] G. Aad *et al.*, *Electron performance measurements with the ATLAS detector using the 2010 LHC proton-proton collision data*, Eur. Phys. J. C **72** (2012) 1909, `arXiv:1110.3174 [hep-ex]`.

[157] G. Aad *et al.*, *Jet energy measurement and its systematic uncertainty in proton-proton collisions at $\sqrt{s} = 7$ TeV with the ATLAS detector*, Eur. Phys. J. C **75** (2015) no. 1, 17, `arXiv:1406.0076 [hep-ex]`.

[158] G. Aad *et al.*, *Jet energy resolution in proton-proton collisions at $\sqrt{s} = 7$ TeV recorded in 2010 with the ATLAS detector*, Eur. Phys. J. C **73** (2013) no. 3, 2306, `arXiv:1210.6210 [hep-ex]`.

[159] H. Burkhardt and P. Grafström, *Absolute luminosity from machine parameters*, Tech. Rep. LHC-PROJECT-Report-1019. CERN-LHC-PROJECT-Report-1019, 2007. `http://cds.cern.ch/record/1056691`.

[160] W. Kozanecki *et al.*, *Interaction-point phase-space characterization using single-beam and luminous-region measurements at PEP-II*, NIM A **607** (2009) 293–321.

[161] S. van der Meer, *Calibration of the effective beam height in the ISR*, Tech. Rep. CERN-ISR-PO-68-31. ISR-PO-68-31, CERN, Geneva, 1968.

[162] A. Caldwell, D. Kollar and K. Kroninger, *BAT - The Bayesian Analysis Toolkit*, Comput. Phys. Commun. **180** (2009) 2197–2209, `arXiv:08082552 [hep-ex]`.

[163] J. Alwall, *et al.*, *The automated computation of tree-level and next-to-leading order differential cross sections, and their matching to parton shower simulations*, JHEP **07** (2014) 079, `arXiv:1405.0301 [hep-ph]`.

[164] G. Aad *et al.*, *Measurement of the inclusive* $t\bar{t}\gamma$ *cross section at* $\sqrt{s} = 7$ TeV *with the ATLAS detector*, ATLAS-CONF-2010-153 (2011).

[165] J. Erdmann, *Measurement of the inclusive* $t\bar{t}\gamma$ *cross section at* $sqrts = 7\ TeV$ *with the ATLAS detector*, `arXiv:1206.5696 [hep-ex]`.